AD NUMBER

AD825616

NEW LIMITATION CHANGE

TO

Approved for public release, distribution unlimited

FROM

Distribution authorized to U.S. Gov't. agencies and their contractors; Critical Technology; MAY 1967. Other requests shall be referred to Air Force Cambridge Research Labs., Hanscom Field, MA.

AUTHORITY

AFCRL ltr, 22 Dec 1971

825616

AFCRL-67-0280 (Volume I)
MAY 1967
SPECIAL REPORTS, NO. 64 (I)

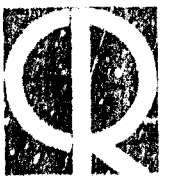

MICROWAVE PHYSICS LABORATORY PROJECT 4642

AIR FORCE CAMBRIDGE RESEARCH LABORATORIES

L. G. HANSCOM FIELD, BEDFORD, MASSACHUSETTS

Proceedings of the Third Symposium on the Plasma Sheath - Plasma Electromagnetics of Hypersonic Flight

Volume I. Radiation Characteristics of Plasma-Covered Antennas

W. ROTMAN
H. MOORE *
R. PAPA
J. LENNON
Editors

* Lowell Technological Institute Research Foundation, Lowell, Mass.

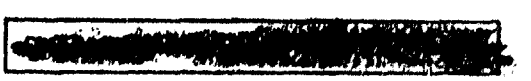

OFFICE OF AEROSPACE RESEARCH
United States Air Force

Abstract

This volume is a collection of the unclassified papers presented at the Third Symposium on the Plasma Sheath – Plasma Electromagnetics of Hypersonic Flight. This symposium consisted of the review of progress in reentry communication studies during the three year period since the prior meeting. The program of this symposium on plasma electromagnetics of hypersonic flight involves a wide range of scientific disciplines, including electromagnetics, aerodynamics, aerothermochemistry, plasma dynamics, electronics, and high-temperature phenomena. The papers were selected to explore as many of these facets of research, including the results of laboratory, flight, and system tests, as time permitted.

Preface

This volume is a collection of the unclassified papers presented at the Third Symposium on the Plasma Sheath - The Plasma Electromagnetics of Hypersonic Flight. The three day meeting, which examined the effects of ionized flow fields on the transmission, reception, and diffraction of radio waves from aerospace vehicles, was held in Boston, Massachusetts on September 21, 22 and 23, 1965, under the sponsorship of the Microwave Physics Laboratory of the Air Force Cambridge Research Laboratories, Air Force Office of Aerospace Research.

The term Plasma Sheath has been defined in the two prior symposia and through technical usage as an envelope of ionized gas that surrounds a space vehicle as it reenters the atmosphere at hypersonic velocities. Related topics which were considered to be within the scope of this symposium include other types of ionized flow fields, such as the exhausts of chemical, electrical, and nuclear rocket propulsion devices and the wakes of reentry vehicles. Also, the hypersonic velocities which may be attained during launch and guided flight of high-performance missiles and spacecraft give rise to similar ionization effects as the reentry plasma sheath. These ionized flow fields can all cause perturbation

or blackout of space-to-ground radio links and, therefore, are of concern in the design of aerospace communications, telemetry, reconnaissance, and electronic countermeasure systems. The related topics of radar cross-section and detectability of reentry bodies and their wakes were deliberately excluded from major consideration since these subjects are adequately treated in other specialized meetings.

A major goal of the Third Plasma Sheath Symposium was the review of progress in reentry communication studies during the three year period since the prior meeting. Several experimental reentry programs of the military and space agencies were initiated and brought to peak activityin this interval. Examples of these rocket programs include the Air Force's Advanced Ballistic Reentry Systems (ABRES) tests, flight studies of hypersonic lifting reentry vehicles under the Air Force's Projects ASSET and START and NASA's Project FIRE, and specific tests of reentry communication techniques under the Air Force's Trailblazer II flight program and NASA's Project RAM. These tests have demonstrated many important principles of reentry communication systems design, including the advantages of the higher microwave frequencies and

of chemical additives, and the development of techniques for optimum antenna design and location. Several other approaches for reducing reentry signal attenuation, such as techniques which use strong magnetic fields or electron beams, have been studied extensively in the laboratory, but have not yet been fully simulated or flight-tested. The substantiation of these techniques has been aided through the development of shock and wind tunnel facilities which permit realistic simulation of reentry conditions. Theoretical and laboratory programs have also advanced such topics as the radiative properties of plasma-covered antennas, nonlinear interactions of plasmas with high-power microwave signals, and non-equilibrium flow field calculations. However, the requirements of ballistic missile systems and manned space flight programs demand an even further increase in reentry communication and related research.

The program of this symposium on plasma electromagnetics of hypersonic flight involves a wide range of scientific disciplines, including electromagnetics, aerodynamics, aero-thermochemistry, plasma dynamics, electronics, and high-temperature phenomena. The papers were selected to explore as many of these facets of research, including the results of laboratory, flight, and system tests, as time permitted.

The papers presented in the various sessions are reported in the Symposium Proceedings. This consists of two separate sets of Air Force Cambridge Research Laboratories reports. The classified papers from the final session on Flight Tests and Alleviation Techniques are in a report which has already been distributed. Requests for additional copies of this SECRET document by agencies of the Department of Defense, their contractors, and other Government Agencies should be directed to the Defense Documentation Center, Cameron Station, Alexandria, Virginia, 22314. In ordering, Report Number AFCRL-66-608 (Special Reports #53, Aug 66) should be referenced. These present reports contain the unclassified papers from the other sessions. The papers are not presented in the same order as at the Symposium, although the papers in each section treat related topics. In addition, to assist the reader who is interested in the complete Proceedings, the unclassified titles and abstracts of the papers in the classified report are included here.

We wish to express our sincere thanks to those persons who helped to organize the symposium: to the members of the Technical Paper Committee, including Paul Huber, Theodore Sims,

and Robert Rawhauser, who undertook the difficult task of paper selection; to the Session Chairmen, Dr. Ronald Row, Dr. Tetsu Morita, Dr. Leopold B. Felsen, Dr, Warren McBee, Dr. Romayne F. Whitmer, Dr. Glen Pippert; to Mr. Charles E. Ellis, Symposium Director; and to Miss Alice Cahill for secretarial assistance.

Walter Rotman
Howard Moore
Robert Papa
John Lennon

Contents

PART ONE – Unclassified Abstracts for Classified Reports Included in the Classified Proceedings, Third Symposium on the Plasma Sheath 1

I. A STUDY OF THE MICROWAVE PROPAGATION CHARACTERISTICS OF A MODEL ENGINE EXHAUST USING A GELLED METALLIZED LIQUID FUEL by Compton 3

II. ANALYSIS OF COMMUNICATIONS ATTENUATION DATA FOR BLUNT AND SLENDER REENTRY VEHICLES IN FLIGHT by Edsall, Bisbing, and Numerich 4

III. ANALYSIS OF PLASMA-SHEATH ELECTRON DENSITY MEASUREMENTS AT ENTRY VELOCITIES by Grantham 6

IV. AN EXPERIMENTAL FEASIBILITY STUDY OF INJECTANT MATERIALS TO ALLEVIATE MARS ENTRY COMMUNICATIONS BLACKOUT by Kelly 7

V. DEPLETION OF FREE ELECTRONS DUE TO WATER INJECTION INTO HYPERSONIC FLOW FIELDS by Beckwith and Bushnell 9

VI. GEMINI REENTRY COMMUNICATIONS EXPERIMENT by Schroeder 11

VII. EFFECTS OF WATER DROPLETS ON REENTRY PLASMA SHEATHS by Kurzius and Ellison 12

Contents

PART TWO – Papers From the Session Directed by Dr. Leopold Felsen, Polytechnic Institute of Brooklyn, New York, N.Y. 13

I. WAVEGUIDE ADMITTANCE FOR RADIATION INTO PLASMA LAYERS – THEORY AND EXPERIMENT by Galejs and Mentzoni 15

II. ADMITTANCE OF A PLASMA-COVERED CYLINDRICAL ANTENNA by Meltz, Freyheit, and Lustig 39

III. RADIATION PATTERNS AND ADMITTANCE OF AN AXIAL SLOT ON A PLASMA COVERED CYLINDER by Knop, Swift, and Hodara 41

IV. THE RADIATION PATTERN OF AN ELECTRIC LINE CURRENT ENCLOSED BY AN AXIALLY SLOTTED PLASMA SHEATH by Olte 117

V. THE EFFECT OF A FINITE CONICAL PLASMA SHEATH ON THE RADIATION FIELD OF A DIPOLE by Pridmore-Brown 147

VI. PROPAGATION OF TRANSIENT SIGNALS IN PLASMAS by Case and Haskell 195

Index of Authors

	Volume	Page
Abele, M.	III	193
Antonucci, J.D.	III	107
Atallah, S.	III	319
Beckwith, I.E.	I	9
Bisbing, P.E.	I	4
Bredfelt, H.	II	125
Bushnell, D.M.	I	19
Calcote, H.F.	II	309
Caldecott, R.	III	69
Carswell, A.I.	III	281
Case, C.T.	I	195
Chown, J.B.	II	271
Clark, G.A.	III	131
Compton, R.E., Jr.	I	3
Daiber, J.W.	II	35
Dunn, M.G.	II	35
Eckert, H.U.	III	35
Edsall, R.H.	I	4
Ellison, R.	I	12
Epstein, M.	II	169
Evans, J.S.	III	343
Fox, J.F.	III	167
Freyheit, P.J.	I	39
Galejs, J.	I	15
Glatt, M.A.	III	1
Grantham, W.L.	I	6
Guthart, H.	II	125
Hartsel, J.E.	III	69
Haskell, R.E.	I	195
Hasserjian, G.	III	131
Hodara, H.	I	41
Huber, P.W.	II	1
Joerger, C.D.	III	1
Karas, N.V.	III	107
Kelly, A.J.	I	7
Knop, C.M.	I	41
Krause, P.M.	II	95
Kurzius, S.C.	I	12
Lordi, J.A.	II	35
Lustig, C.D.	I	39
Mates, R.E.	II	35
McPherron, T.R.	III	167
Medecki, H.	III	193
Medgyesi-Mitschang, L.N.	III	231

Authors

	Volume	Page
Meltz, G.	I	39
Mentzoni, M.H.	I	15
Morita, T.	II	125
	II	271
Mullen, J.H.	III	231
Nanevicz, J.E.	II	271
Numerich, F.H	I	4
Olte, A.	I	117
Papa, R.J.	II	203
Pergament, H.S.	II	309
Plugge, R.J.	III	259
Pridmore-Brown, D.C.	I	147
Richard, C.	III	281
Sanborn, W.A.	III	319
Scharfman, W.E.	II	125
Schroeder, L.C.	I	11
Sims, T.	II	1
Swift, C.T.	I	41
Taylor, W.C.	II	271
Vance, E.F.	II	271

Volume I

Part One

Unclassified Abstracts for Classified Reports Included in the Classified Proceedings, Third Symposium on the Plasma Sheath

I. A STUDY OF THE MICROWAVE PROPAGATION CHARACTERISTICS OF A MODEL ENGINE EXHAUST USING A GELLED METALLIZED LIQUID FUEL

R.E. Compton, Jr.
Electronics Department
Martin Company, Martin-Marietta Corporation
Denver Division
Denver, Colorado

This report describes a series of microwave attenuation measurements that were performed on an 11.6% scale model of an improved Titan II engine. The model engine burned Alumizine and nitrogen tetroxide and was fired into the atmosphere at an altitude of 6100 feet.

A microwave diagnostic scheme was utilized to determine the electron density and collision frequency of the exhaust plume at the exit plane and on axis of the exhaust. Measurements were recorded simultaneously at 16 and 21 Gc and the resulting attenuations in the order of 25 db were used to compute the plasma properites. Results of the measurements show that the free electron density and collision frequency are an order of magnitude higher than those results measured on a full scale, Titan II sustainer engine which uses similar liquid fuels without additives.

The addition of powdered aluminum to a liquid propellant engine creates a higher exit temperature and a gas-particle exhaust medium that is ionized to a high degree. Test results verify that high performance propellants increase the severity of microwave propagation through the exhaust plume. The improved Titan II plume characteristics are compared to other liquid and solid propellant rocket engines.

II. (U) ANALYSIS OF COMMUNICATIONS ATTENUATION DATA FOR BLUNT AND SLENDER REENTRY VEHICLES IN FLIGHT

R. H. Edsall
P. E. Bisbing
F. H. Numerich
General Electric Company
Philadelphia, Pennsylvania

The attenuation of communications signals transmitted from reentry vehicles in flight is assumed to be attributable to the effects of ionization formed in the flow field surrounding the vehicle. Theoretical analyses of hypersonic flow are given, including both viscous and inviscid flow regions. The effects of chemical nonequilibrium and heat shield contaminants are included in the analysis of flow field ionization. Nonequilibrium effects are found to predominate at high altitudes. On the other hand, the ionization in the flow field surrounding a slender vehicle at low altitudes is very strongly affected by the ablating heat shield material. The presence of alkali metals in trace quantities can significantly enchance the ionization relative to its corresponding level in pure air.

The attenuation of communications signals by the reentry induced plasma is treated theoretically by considering the problem of the interaction of plane electromagnetic waves with a one-dimensional non-uniform plasma. This approach is used in a general parametric study, since it is not subject to the geometry of the transmitting system. Parametric results have been obtained by numerical integration of Maxwell's equations through the plasma profiles obtained from the flow field studies, applying the required boundary conditions.

The results indicate in general that blunt vehicles are predominantly affected by the volume electron density in the shock layer; i.e., blackout occurs whenever the shock layer ionization is overdense. On the other hand, for the slender vehicles the plasma may be treated as a thin sheet, in which the surface density of electrons determines the propagation parameters. The latter result is a consequence of the fact that the flow field ionization is confined to a fraction of the thin viscous region (boundary layer) near the vehicle surface.

Experimental data from ballistic missile flights involving both slender and blunt reentry vehicles are analyzed. In the blunt body category, signal attenuation and ionization probe data from the Mark 6 are analyzed. Signal attenuation data for the RVX-2A vehicle are also analyzed. The slender vehicles included for analysis of flight data are REX, WAC, RMV, and TVX. In general, it is found that the important qualitative and quantitative characteristics of the theory are verified by the results of the flight experiments. In particular, it is found that the use of a non-ablating conical body reduces the signal attenuation to a negligible amount, for ICBM reentry conditions.

III. ANALYSIS OF PLASMA-SHEATH ELECTRON DENSITY MEASUREMENTS AT ENTRY VELOCITIES

William L. Grantham

Experimental results are given of a flight test designed to measure the electron density in the flow field of a hypersonic vehicle. A comparison is made of the flight measurements with nonequilibrium flow field calculations in order to assess the applicability of the flow field theory. The microwave reflectometer technique used to make the measurements is presented with attention given to measurement accuracy and resolution capability.

The experimental payload discussed was launched from the NASA Wallops Station, April 10, 1964, and achieved a maximum velocity of 18,143 ft/sec during the ascending portion of the flight. A three-frequency microwave reflectometer system in the payload measured the plasma-sheath electron density and standoff distance at discrete locations along the body. A heat-sink type of nose cone was used to keep the plasma free of ablation products during the data period.

IV. AN EXPERIMENTAL FEASIBILITY STUDY OF INJECTANT MATERIALS TO ALLEVIATE MARS ENTRY COMMUNICATIONS BLACKOUT*

Arnold J. Kelly
Jet Propulsion Laboratory, California Institute of Technology
Pasadena, California

A number of Mars lander mission profiles currently under consideration involve atmospheric braking and require that continuous communication be maintained with the spacecraft. For these missions to be successful therefore, requires that some means be provided to reduce the debilitating effects of shock produced ionization (expected to occur early in the entry maneuver) upon the fixed frequency telemetry signal.

An experimental program has been initiated to establish the feasibility of using appropriate materials, injected into the spacecraft wake, as a means of reducing the free electron density level sufficiently to eliminate its interference with telemetry. It has been determined that the flow conditions (pressure, temperature, electron density) anticipated behind the bow shock of a blunt Martian entry body can be accurately simulated by the plume from an energetic (Ducati type) arc.

Four such arcs, operating simultaneously in our vacuum facility, provide a large (~50 cm dia), uniform plume. Immersed in this plume, its upper surface parallel and contiguous with the centerline of the plume, is an aerodynamically "clean" flat plate, through which various electron-capture materials are injected into the str m. The electron density profile existing down stream of

this plate, with and without the presence of injectants, is determined by the use of a swinging microwave diagnostic arm. This microwave system, operating at a frequency of 24 GCPS, monitors electron densities in the range of 1 to 7 x 10^{12} cm^{-3} with a spatial resolution of~4 cm.

Electron density profiles data are obtained at several downstream stations for various injectant materials. From these initial tests it is possible to make estimates of the relative efficacy of the species used.

The results are classified and, therefore, the paper should be presented at the classified session.

---

* This work presents the results of one phase of research carried out at the Jet Propulsion Laboratory, California Institute of Technology, under Contract No. NAS7-100, sponsored by the National Aeronautics and Space Administration.

V. DEPLETION OF FREE ELECTRONS DUE TO WATER INJECTION INTO HYPERSONIC FLOW FIELDS

I.E. Beckwith and D.M. Bushnell
NASA - Langley Research Center

The results of the RAM B2 flight test of the effect of water injection on radio attenuation (NASA TM X989) are analyzed for electron depletion mechanisms. The mean concentrations of water droplets (or ice particles) in the flow field, as required in the analysis, are based on correlations of maximum spray penetration obtained from wind tunnel tests (NASA TMX-989). The initial mean droplet diameters are computed from correlations for cross-current breakup of liquid jets in airstreams (NACA TN 4087). A quasi-one-dimensional theory for the mean droplet motion and evaporation is described briefly and used to compute flow conditions and species concentrations downstream of the injection site. The analysis is limited to injection from the side ports of the RAM B2 vehicle.

Both equilibrium and finite rate homogeneous reactions are considered. In the equilibrium case, the only ionic reactions of any importance were the formation of NO^+ and OH^-. The free electron concentrations were generally below the critical value for VHF transmission (about 7×10^8 electrons per cm^3) at a distance of one foot downstream from the injection site as computed on the basis of equilibrium reactions.

Since equilibrium conditions are unlikely at the low densities encountered, the assumption of finite rate ionic reactions

should be more realistic. The concentrations of neutral species were assumed the same as for the equilibrium calculations and the only ionic reaction used was

$$N + O = NO^{+} + e^{-}$$

with the finite reaction rate coefficients taken from the data of Lin and Teare. Electron depletion due to this reaction was insufficient to account for the observed signal recovery even with the considerable cooling effect due to water evaporation.

This result suggests that heterogeneous ionic reactions (that is, those reactions that take place at or near the surface of the droplets) must have been responsbile for the observed effects of water injection. In the analysis of these possible heterogeneous reactions, the detailed mechanisms involved were not considered. The minimum water flow rates, injected during the flight test, were used to evaluate a factor which is considered to be the radius of an effective cross-section area for electron depletion associated with the individual droplets. The application of this factor, as derived from the RAM B2 results, to predicting injection flow requirements under other conditions is considered.

VI. (U) GEMINI REENTRY COMMUNICATIONS EXPERIMENT

L.C. Schroeder
NASA - Langley

This presentation will discuss a flight experiment in which water was injected from a Gemini spacecraft into the reentry plasma sheath to reduce the attenuation of RF communications and thereby increase the strength of the signals received at ground stations. Three different flow rates were pulsed into the flow field between the altitudes of 270 K ft. and 200 K ft. and effects on three frequencies, VHF Voice (296.8 mc), UHF TM (230.4 mc) and C-band (5690 mc) were observed. The origin, development and description of the experiment will be reviewed. A brief discussion of studies to determine penetration and flow requirements and to predict antenna patterns in the reentry plasma will be presented. Flight signal strength results will be analyzed as a function of water flow rate and aspect angle. Comparison will be made of measured with predicted antenna patterns and flow rates required to produce signal recovers.

VII. EFFECTS OF WATER DROPLETS ON REENTRY PLASMA SHEATHS

Shelby C. Kurzius and Roy Ellison
AeroChem Research Laboratories, Inc.
Princeton, New Jersey
a subsidiary of Pfaudler Permutit Inc.

Experimental studies of the effects of water sprays on suppressing ion and electron concentrations in seeded low-pressure combustion plasmas have been made to determine the mechanism by which water sprays are effective in restoring communications with blacked-out reentry vehicles. These studies were performed in hydrogen-hydrocarbon-air flames at pressures of from 10 to 100 Torr. Langmuir and ion mass spectrometric probes were employed to measure total ion and electron densities and to identify individual positive and negative ion species. Large decreases in plasma free electron concentrations were observed upon introducing water sprays to the plasmas studied. These decreases have been shown not to involve water vapor. Attachment processes involving droplets are similarly not involved in the mechanism--nor are negative ions. The results are compatible with a rapid recombination process involving droplets as sticky third bodies. Experimental observations of the effect of varying the mean droplet size and droplet concentration on enhanced recombination rates are interpreted in terms of theoretical predictions and the implications of these experiments to the alleviation of attenuation levels experienced in communications made through reentry plasma sheaths are discussed.

Volume I

Part Two

Papers From the Session Directed by Dr. Leopold Felsen, Polytechnic Institute of Brooklyn, New York, N.Y.

I. WAVEGUIDE ADMITTANCE FOR RADIATION INTO PLASMA LAYERS THEORY AND EXPERIMENT

by

Janis Galejs and Michael H. Mentzoni

Applied Research Laboratory
Sylvania Electronic Systems
A Division of Sylvania Electric Products, Inc.
Waltham, Massachusetts 02154

ABSTRACT

Measured admittance of an X-band waveguide radiating into dielectric and plasma layers is compared with variationally computed admittance figures.

The waveguide admittance measurements for polystyrene sheets of varying thicknesses compared closely with calculations. The admittance is computed first by assuming the principal waveguide mode and second by using a superposition of sine and shifted cosine waves as trial functions for aperture fields. Although the aperture fields are shown to differ significantly in the two cases, the computed admittance data are nearly the same because of the stationary character of the admittance expression.

The admittance measurements for plasma layers are made during the diffusion controlled afterglow of a pulsed discharge contained in a bell-shaped vessel. Thin Teflon sheets are used to confine the plasma layers to an approximate size of 5x5x 3/4 inches. The electron density of the plasma profile is measured by Langmuir probes at various times during the afterglow. The plasma density was measured over approximately 70 percent of the thickness of the plasma layers and was found to be nearly constant in this range which excluded regions near the boundary. Numerical solutions of the equations for ambipolar diffusion during the afterglow in a rectangular geometry show that the lateral plasma density variations are negligible in the vicinity of the waveguide. The measured admittance and plasma density data are shown to agree with calculations made for homogeneous plasma layers, if a correction is made for elevated ion temperatures for times of approximately 10 to 20 μs following the discharge. Several computational models consider plasma stratifications near the boundary of the plasma layer but they do not improve the agreement between measurement and calculations.

Research Report No. 451

WAVEGUIDE ADMITTANCE FOR RADIATION INTO PLASMA LAYERS THEORY AND EXPERIMENT

by

Janis Galejs and Michael H. Mentzoni

1. INTRODUCTION

In past slot antenna measurements in the presence of the plasma sheath [Cloutier and Bachynski, 1963] there have been no attempts to correlate measured impedances or reflection coefficients with theoretical calculations because of the lack of a suitable theoretical models. The analytical techniques for computing the admittance of slots radiating into layered plasmas have been developed recently for isotropic plasma that can be represented as a simple dielectric of a relative dielectric constant of less than unity [Galejs 1964, 1965a and b; Villeneuve, 1965]. This paper will attempt to correlate the above theoretical impedance calculations with laboratory measurements. The simplest measurements are possible with slots radiating into dielectric layers and after reviewing the theory in section 2, such measurements will be described in section 3. The experimental setup used for generating a plasma layer will be discussed in section 4. In section 5 the measured admittance figures will be compared with calculations.

2. REVIEW OF THEORY

Variational expressions have been derived for the slot admittance of waveguides radiating into plasma layers. The final expressions involve a double summation [Galejs 1965a], when enclosing the plasma layer by a large rectangular waveguide, or an infinite double integral for a plasma layer that is not bounded laterally [Villeneuve, 1965; Galejs, 1965b]. Both formulations have been shown to become equivalent with increasing size of the large waveguide.

The slot admittance is computed as a function of the aperture fields of the waveguide. The trial function for the fields and waveguide aperture is assumed to be a superposition of the sine and shifted cosine waves. For a rectangular waveguide aperture which is symmetrical with respect to the x and y coordinate axis the trial functions are of the form

$$f_A(x,y) = \sin[k(|x|-\ell)] \qquad (1)$$

$$f_B(x,y) = 1 - \cos[k(|x|-\ell)]$$

where k is an arbitrary parameter and 2ℓ is the length of the aperture. The amplitudes of the trial functions follow from the variational formulation and it is possible to compute an approximation to the field distribution in the waveguide aperture in terms of (1) and (2).

It is also possible to assume the principal waveguide mode as the aperture fields.

Impedance calculations will be reported using both the two-term trial functions (1) and (2) or the principal waveguide mode as the aperture fields.

3. IMPEDANCE FOR DIELECTRIC LAYERS

Impedance measurements are simplest to carry out for dielectric layers. At the same time this provides a non-trivial check of the theoretical developments. The presence of surface waves for dielectric layers of $\epsilon_p/\epsilon_o > 1$ causes additional singularities in the integrands of the admittance expression and the numerical evaluation of the integrals using a constant mesh size approximation can be expected to be less accurate than in the plasma case ($\epsilon_p/\epsilon_o < 1$) where there are no surface waves.

The admittance of an X-band waveguide radiating into plasma sheath of varying thickness d is shown in Figure 1. The measurements are made with a waveguide of aperture length x_i and width y_i. In the computational models

[Galejs, 1963a] the dielectric layer is assumed to be enclosed laterally by a large waveguide of inside dimensions of x_o and y_o. The calculations for this antenna geometry are made first with the principal waveguide mode as the electric aperture fields and also for a two-term trial function using the same value of k. ($k = 0.625\ k_o$, $k_o = \omega\sqrt{\mu_o \epsilon_o}$). The two sets of calculations agree closely except for sheath thicknesses of approximately 0.5 cm. The aperture field distribution which is computed with a two-term trial function is shown in Figure 2. It exhibits significant deviations from the principal waveguide mode. The field distribution is nearly triangular for $d \simeq 0.5$ cm, where the two sets of impedance computations shown in Figure 1 differ most. The impedance calculations have been repeated also for $k = k_o$ in the trial functions. These impedance computations do not differ from those with $k = 0.625\ k_o$, but there are minor differences in the computed field distributions although the same basic trend of the fields are observable. There are substantial deviations of the fields from those of the principal waveguide mode in the aperture. However, due to the stationary character of the admittance expressions the principal waveguide mode can be used as aperture fields for impedance calculations.

4. LABORATORY GENERATION OF A PLASMA LAYER

4.1 Experimental Arrangement

The plasma-covered slot antenna was simulated in a bell jar vacuum system as indicated in the diagram of Fig. 3. The X-band waveguide has a Mica vacuum window and is inserted through a vacuum seal at the base of the bell jar. This system could be pumped down to a pressure of about 10^{-6} torr before filling it with helium* gas of tank-grade quality. Aluminum blocks of 8 x 3/4 x 3/4 in.

* Argon was used initially, but it required approximately three times lower pressure for achieving a breakdown and hence it was more susceptible to system impurities.

were placed on top of the lower teflon sheet approximately 5 inches apart in a direction parallel to the short dimension of the rectangular waveguide opening. A plasma layer symmetrical with respect to a bisecting plane parallel to the ground plane is required for obtaining a predictable ambipolar diffusion profile. To achieve this, a teflon sheet was placed on top of the electrodes. This sheet also served as a support for a double Langmuir probe during electron-density measurements. Figure 4 shows a photograph of the bell jar and of the associated microwave circuitry. A photograph of the operating discharge is shown in Fig. 5. A teflon strip surrounds the electrodes in order to further confine the discharge to the space between electrodes. The plasma layer is generated in a bell jar during an active 2 μsec discharge and it declines thereafter according to the rate of electron removal from the afterglow. Both the electron density and the slot admittance were measured independently during the time following the active discharge.

4.2 Langmuir Probe Measurements

Electron and ion number densities and electron temperatures were measured as a function of time using a double Langmuir probe. The probe, shown in Fig. 6, consists of two 1 mm tungsten wires mounted 5 mm apart. The wires are beaded with pyrex glass and have polished planar collecting areas flush with the glass. To provide rf shielding the beaded wires are enclosed by a 5/8" pyrex tube, gold plated on the inside surface. All the external circuitry of the probe was housed in a Faraday cage. The probe, which was removed during antenna admittance measurements, was placed directly opposite to the waveguide aperture at various distances from it.

In reducing the double probe data the Equivalent Resistance Method described by Johnson and Malter [1950] was utilized. The number density of the positive ions, n_+, is given as

$$n_+ = \text{const.}\ (i_p/A)(M/T_+)^{1/2} \qquad (3)$$

where i_p = positive saturation current, A = effective collecting area, M = ionic mass, and T_+ = ionic temperatures. The electron density can be computed only when a quasi-neutrality is assumed and the ion temperature and mass is known. Our measurements showed that the log i_p vs voltage plot is linear. In this case the electron distribution is Maxwellian and the electron temperature, T_e, can be evaluated [Johnson and Malter, 1950]. Also the electron-atom momentum transfer collision frequency, ν_{em}, has been evaluated from published cross-section data. The contribution to the total collision frequency caused by electron-ion collisions ν_{ei} is small because T_e is high for high electron-ion densities and $\nu_{ei} \sim T_e^{-1.5}$ [Mentzoni, 1965].

The double Langmuir probe measurements yielded generally unambiguous probe characteristics with a surprisingly flat saturation curve and sharp "knees" as shown in Fig. 7 from which the values of ϵ_p and ν_m were computed. The scattering of experimental points shown in the figure is typical for most of the measurements. The electron energy in the early portion of the afterglow was quite high ranging from 4 to about 8 eV depending upon discharge current density. At 8 eV and p = .9 torr the electron collision frequency ν_m in helium is 1.5×10^9 sec^{-1} yielding a typical ratio $\nu_m/\omega \approx .025$ for frequencies in the X-band.

A typical electron density profile is shown in Fig. 8. The electron density is shown to be approximately constant for distances exceeding 1/8 in. from the insulating layer confining the discharge. No measurements were made for closer distances.

The variations of the electron density profile in the lateral direction have been estimated by solving the diffusion equation for the ambipolar case in discharge afterglow for the rectangular volume between the electrodes and the teflon plates [Mentzoni, 1963]. The electron density is nearly constant over approximately 80 percent of the area and the electron density gradient

appears to be negligible in the direction parallel to the aperture plane in the vicinity of the slot.

4.3 Admittance Measurements

The waveguide admittance was measured in the absence of plasma with standard slotted line techniques. A balanced microwave reflectometer bridge was used for the plasma measurements. A typical reflectometer output signal is shown in Fig. 9. The bridge is balanced to produce zero output in absence of plasma, and the output approaches again zero as electron density of the discharge decays.

The discharge was ignited 500 times per second. Using a pulsed signal that is triggered from a variable delay line at a time τ following the discharge, it is possible to display the reflectometer output at this time τ. After rebalancing the reflectometer with the aid of a precision attenuator and phase shifter the attenuation and phase shift settings along with the reflection coefficients that have been computed in the absence of plasma give the required inputs for an impedance calculation.

5. ADMITTANCE FOR PLASMA LAYER

It follows from the theory of a homogeneous plasma layer that the conductance of the slot is decreased and that the susceptance becomes more inductive with an increasing density of the plasma (increasing plasma frequency ω_p or decreasing dielectric constant ϵ_p). These changes are monotonic with increasing plasma density. In the experimental set-up shown in Fig. 3 it is necessary to have an insulating plate to isolate the discharge from the ground plane and also a second dielectric plate is required to limit the thickness of the plasma layer. The effects of these dielectric layers are illustrated for two sets of conditions in Fig. 10. An increasing electric thickness of the topplate tends to change the shape of the admittance curve. Even more marked

changes have been observed by increasing the electrical thickness of the bottom plate: a 1/8 inch thick pyrex glass sheet ($\epsilon_d/\epsilon_o = 4.52$) causes an increase of both the conductance and of the magnitude of the susceptance as ϵ_p/ϵ_o are decreased from 1.0 to 0.6. It is obviously desirable to keep the two dielectric plates as thin as possible in order to obtain approximately the same admittance behavior as for a plasma layer without the dielectric plates. Sheets of 15 and 31 mil teflon ($\epsilon_d/\epsilon_o = 2.08$) were selected as the bottom and top cover plates of the plasma layer. The effects of plasma stratification have been examined for the four geometries shown in Fig. 11. Measured plasma profiles showed an essentially constant plasma density for distances exceeding 1/8 in. from the dielectric boundaries, but there were no measurements made at closer distances. The plasma density will taper off near the boundaries and the geometries shown in Fig. 11 were examined as possible approximations to this taper. The comparisons include a homogeneous plasma layer of ϵ_p, a plasma layer of the same total thickness but with a 0.1 in. boundary layer of $(\epsilon_o + \epsilon_p)/2$ or ϵ_o, and a plasma layer with 0.05 in. boundary layer of ϵ_o. The corresponding admittance data are shown in Fig. 12. The decreasing plasma density near the dielectric boundaries increases the conductivity slightly, but it affects susceptance more significantly. The susceptance increases particularly for a larger discontinuity near the boundary (Model 3 of 0.1 inch boundary layer of ϵ_o).

The measured admittance data are shown in Fig. 13 together with the Model 1 of the homogeneous plasma layer, but the tapered plasma models would not improve the agreement with measurements. The solid dots are all computed with $T_+ = 300^\circ K$. The two experimental points corresponding to the smallest values of ϵ_p represent measurements made 10 and 20 microseconds after initiating the discharge. If these measurements are corrected for ion temperatures of

2000 and 600°K respectively the circles are obtained which yield good agreement both for C and B. Such elevated ion temperatures in the early discharge afterglow are not unreasonable.

There is a fair agreement between the theory and the experimental data. This theoretical work does not account for the reflections caused by discharge electrodes, reflections from the bell jar or for the finite size of the ground plane. In view of these uncertainties it is not expected to achieve a better agreement between measurements and theory using the present experimental procedure.

References

G.G. Cloutier and M.P. Bachynski (1963) "Antenna Characteristics in the Presence of a Plasma Sheath" in Electromagnetic Theory and Antennas, Ed. by E.C. Jordan, Pergamon Press, p. 537-548.

J. Galejs, (November 1964), "Slot Antenna Impedance for Plasma Layers" IEEE Trans. on Antennas and Propagation, Vol. AP-12, No. 6.,p.738-745.

J. Galejs, (January 1965a), "Admittance of a Waveguide Radiating into Stratified Plasma," IEEE Transactions on Antennas and Propagation, Vol. AP-13.,p.64-70.

J. Galejs (February 1965b), "Self and Mutual Admittances of Waveguides Radiating into Plasma Layers," RADIO SCIENCE, J.Res. NBS, Vol. 69D, No. 2.,p.179-189.

E.O. Johnson and L. Malter (October 1950), "A Floating Double Probe Method for Measurements in Gas Discharges," Physical Review, Vol. 80, p. 58.

M.H. Mentzoni, "Electron Density Profiles due to Ambipolar Diffusion," Research Note 438, Appl. Res. Lab., Sylvania Electronic Systems, Waltham, Mass. (Dec. 1963).

M.H. Mentzoni (February 1965) Momentum Transfer Collisions in Oxygen for Thermal Electrons, RADIO SCIENCE, J. Res. NBS, Vol. 69D.,p.213-217.

A.T. Villeneuve (Jan. 1965), "Admittance of Waveguide Radiating into Plasma Environment," IEEE Trans. on Antennas and Propagation, Vol. AP-13.,115-121.

3-1-0679

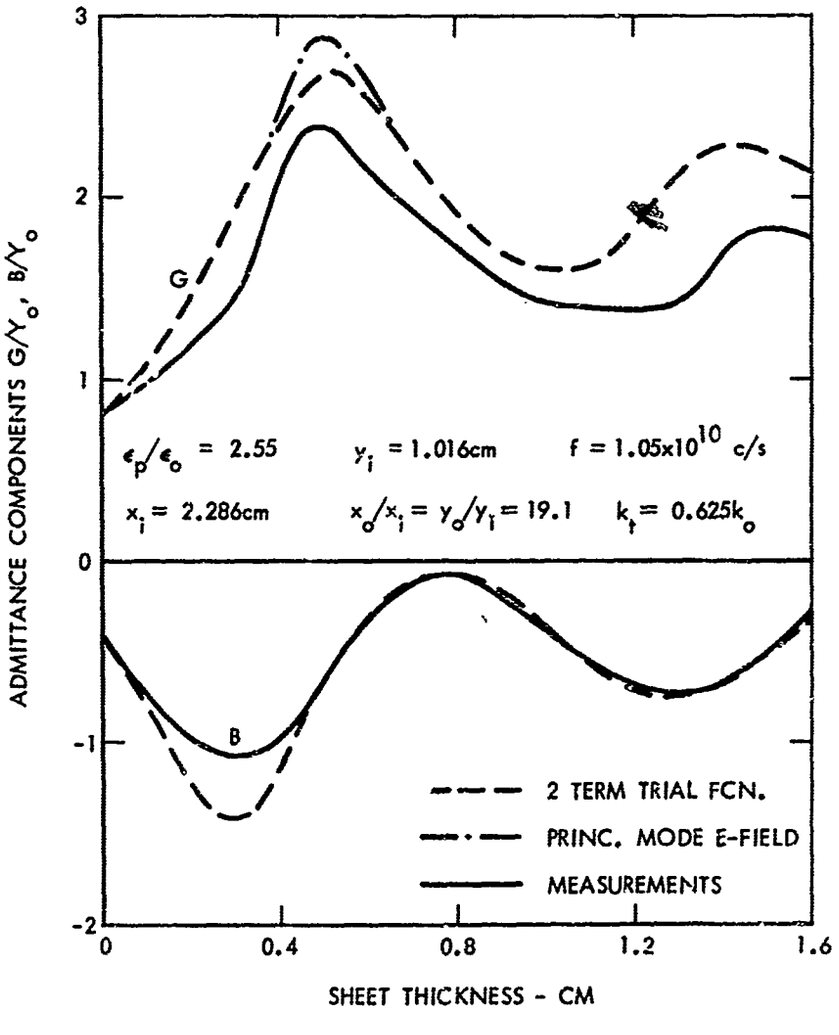

Figure 1

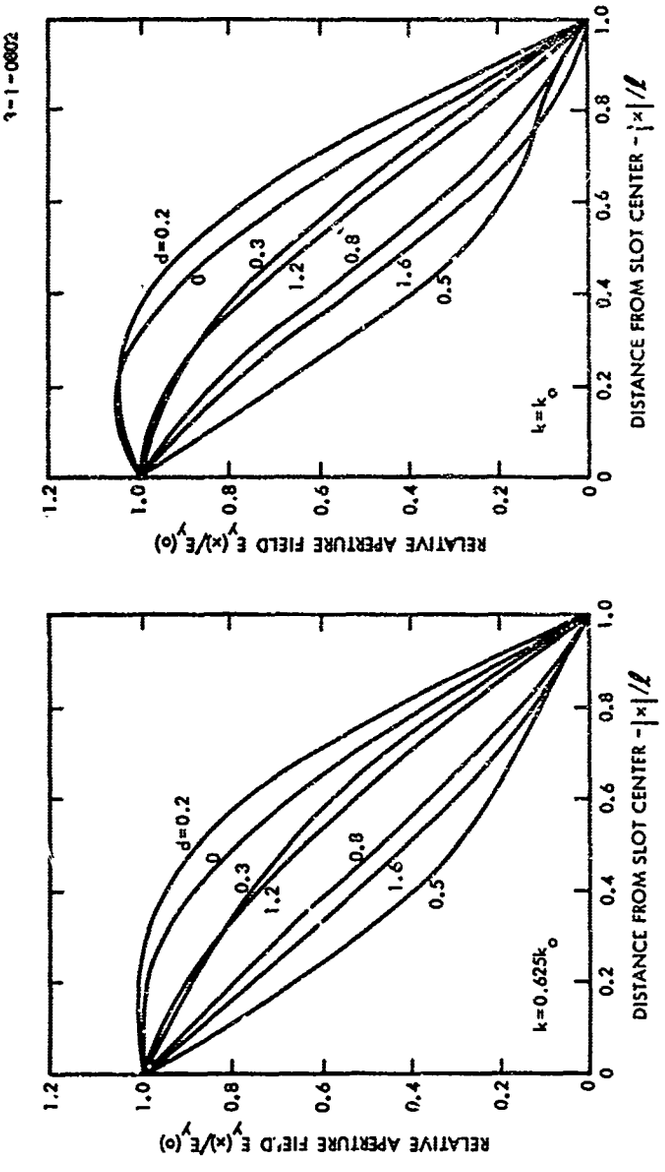
3-1-0802
RELATIVE APERTURE FIELD $E_y(x)/E_y(o)$
DISTANCE FROM SLOT CENTER - $|x|/\ell$
d=0.2
0
0.3
1.2
0.8
1.6
0.5
$k=k_o$
$k=0.625k_o$

Figure 2

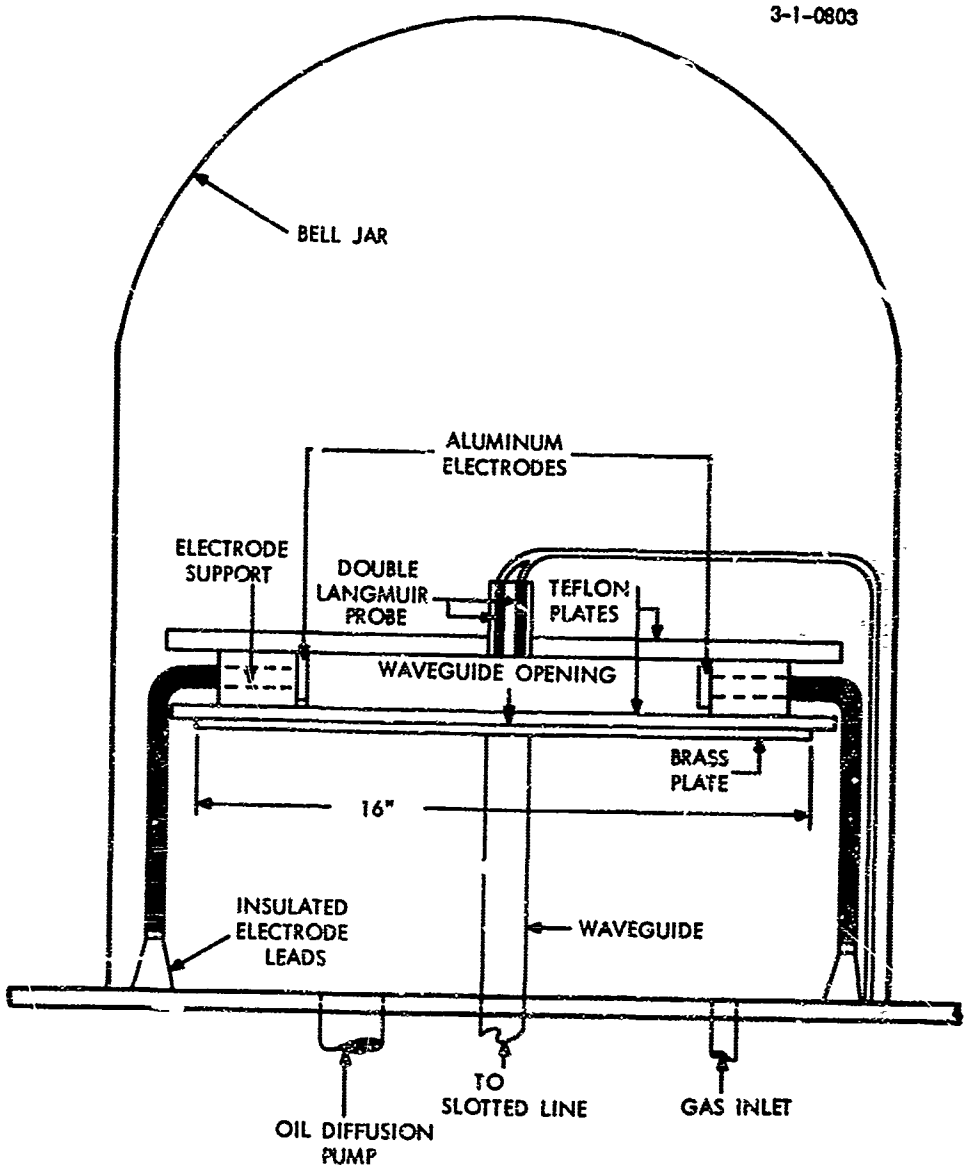
3-1-0803
BELL JAR
ALUMINUM ELECTRODES
ELECTRODE SUPPORT
DOUBLE LANGMUIR PROBE
TEFLON PLATES
WAVEGUIDE OPENING
BRASS PLATE
16"
INSULATED ELECTRODE LEADS
WAVEGUIDE
TO SLOTTED LINE
GAS INLET
OIL DIFFUSION PUMP

Figure 3

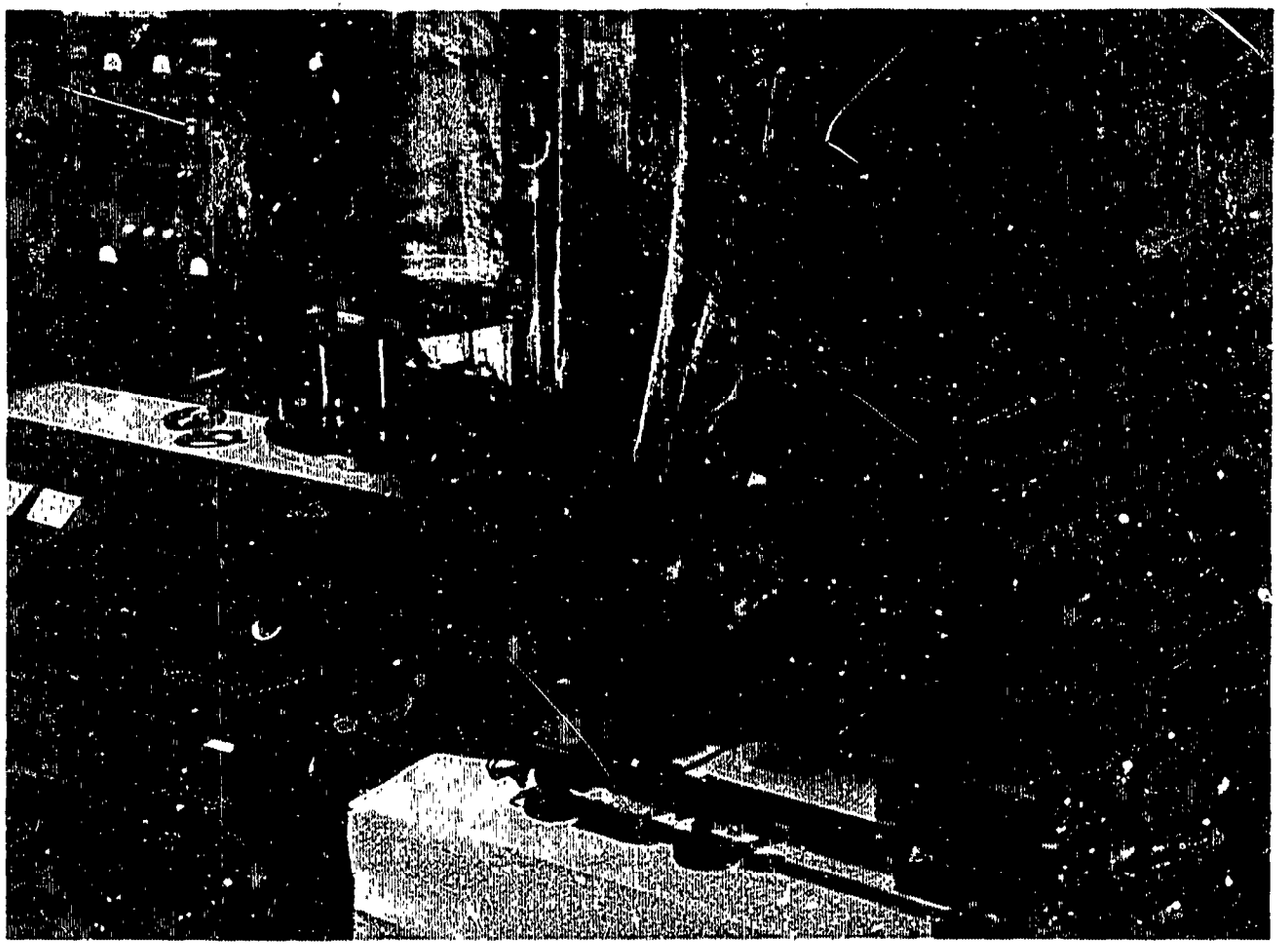

Figure 4

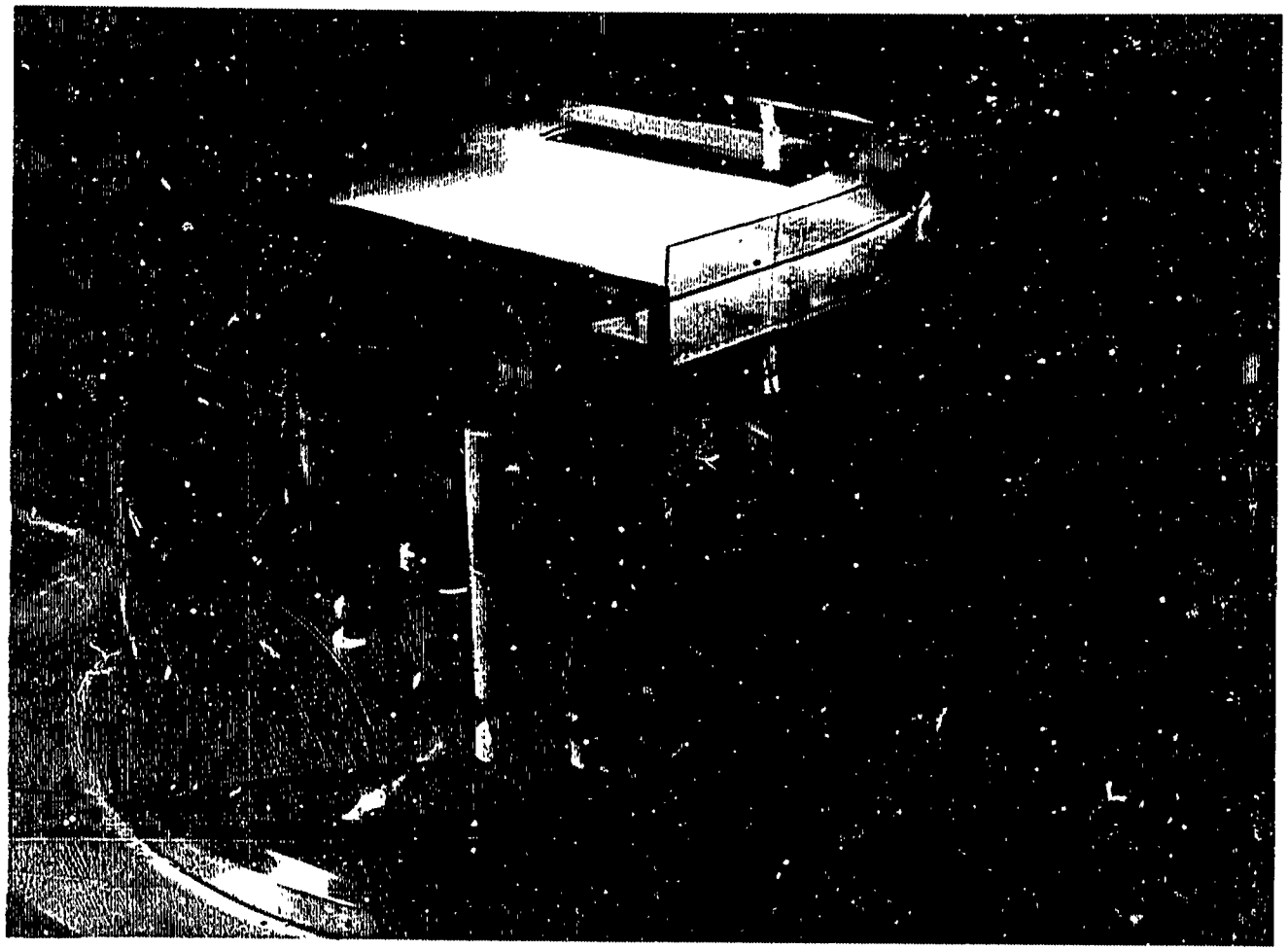

Figure 5

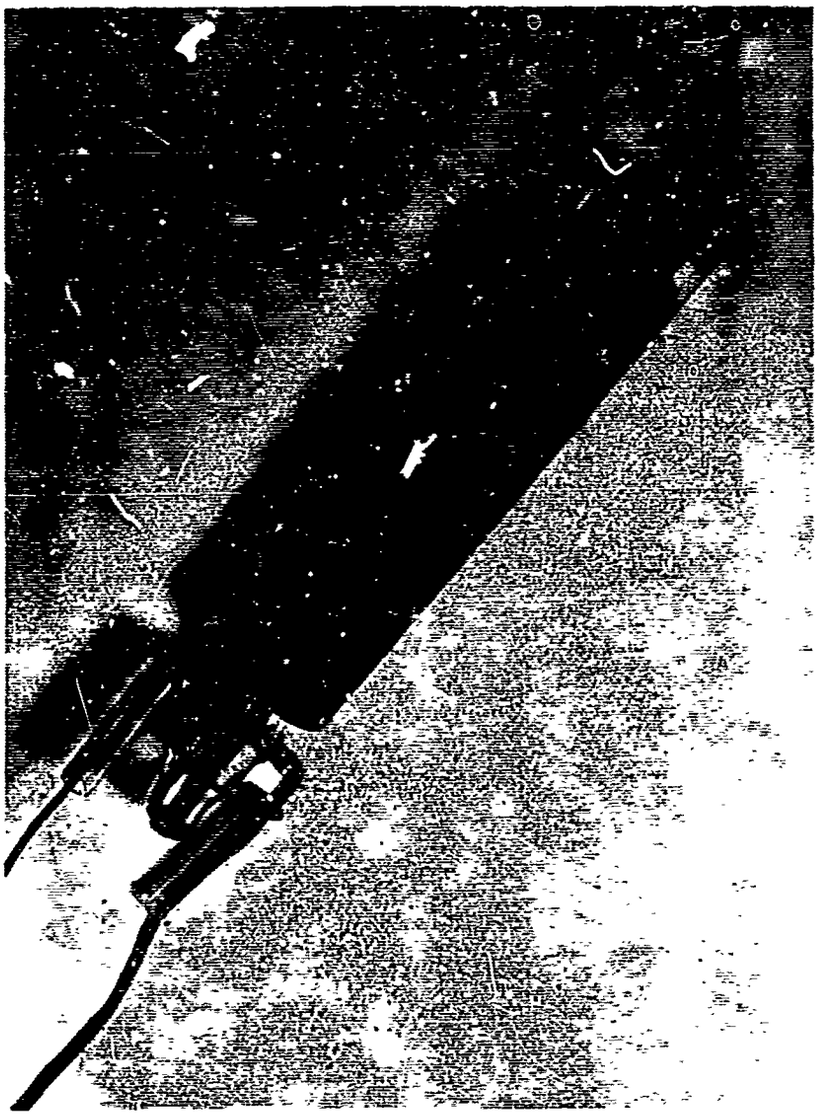

Figure 6

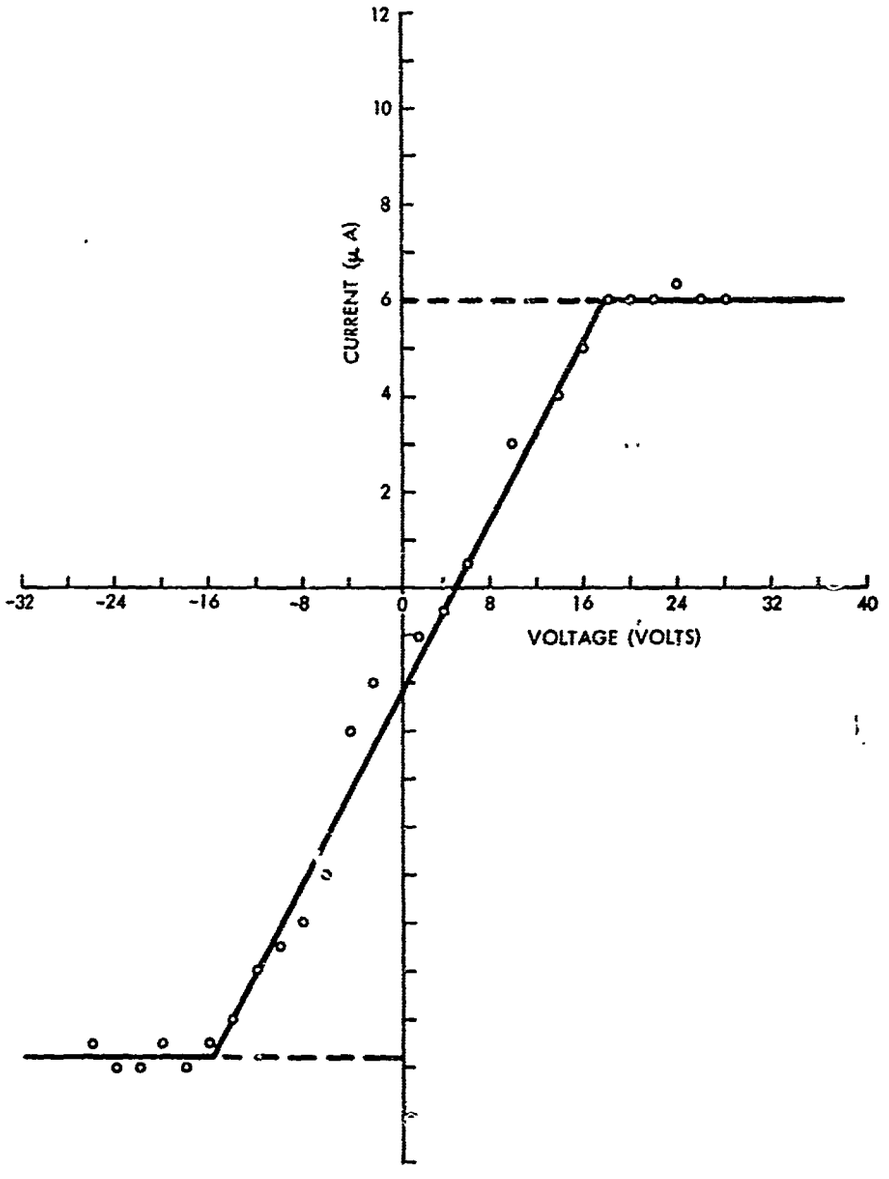

Figure 7

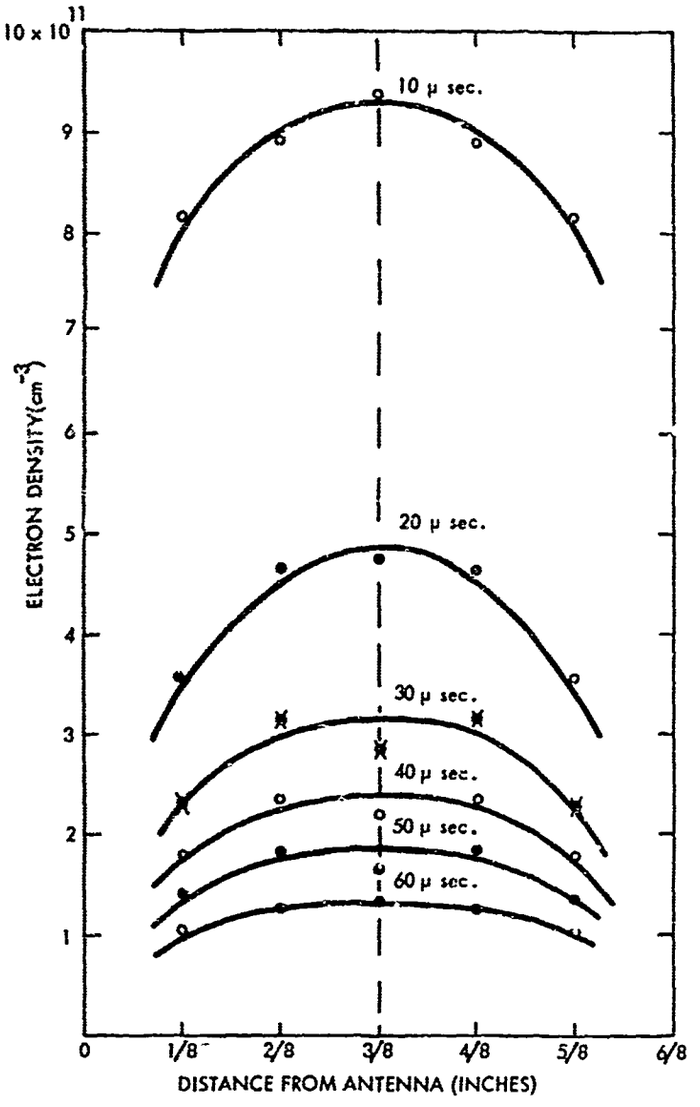
10 x 10^11
9
8
7
6
5
4
3
2
1
ELECTRON DENSITY(cm^-3)
10 μ sec.
20 μ sec.
30 μ sec.
40 μ sec.
50 μ sec.
60 μ sec.
0
1/8
2/8
3/8
4/8
5/8
6/8
DISTANCE FROM ANTENNA (INCHES)

Figure 8

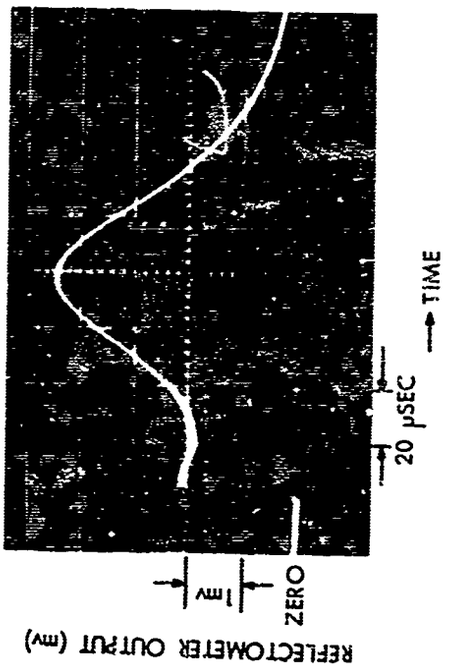

Figure 9

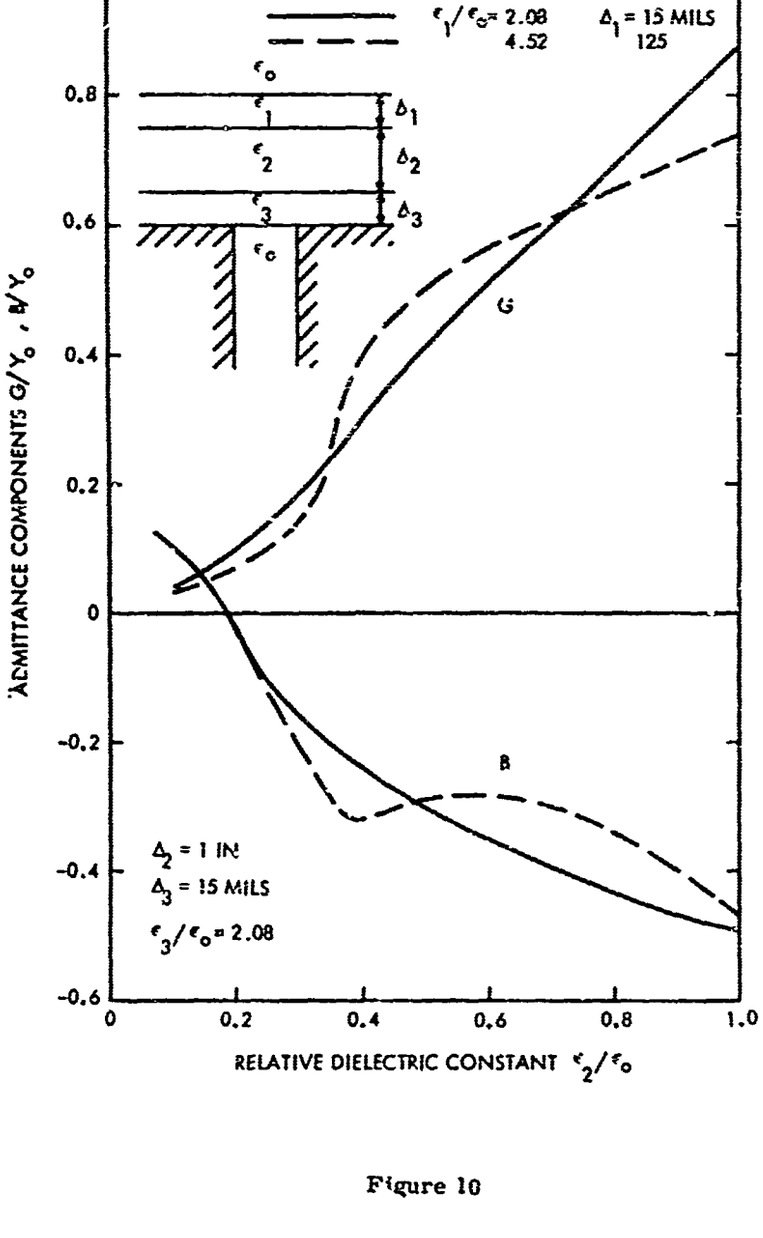
1.0
0.8
0.6
0.4
0.2
0
-0.2
-0.4
-0.6
0
0.2
0.4
0.6
0.8
1.0
ADMITTANCE COMPONENTS G/Y₀ , B/Y₀
RELATIVE DIELECTRIC CONSTANT ε₂/ε₀
ε₁/ε₀ = 2.08
4.52
Δ₁ = 15 MILS
125
ε₀
ε₁
ε₂
ε₃
Δ₁
Δ₂
Δ₃
ε₀
G
B
Δ₂ = 1 IN
Δ₃ = 15 MILS
ε₃/ε₀ = 2.08

Figure 10

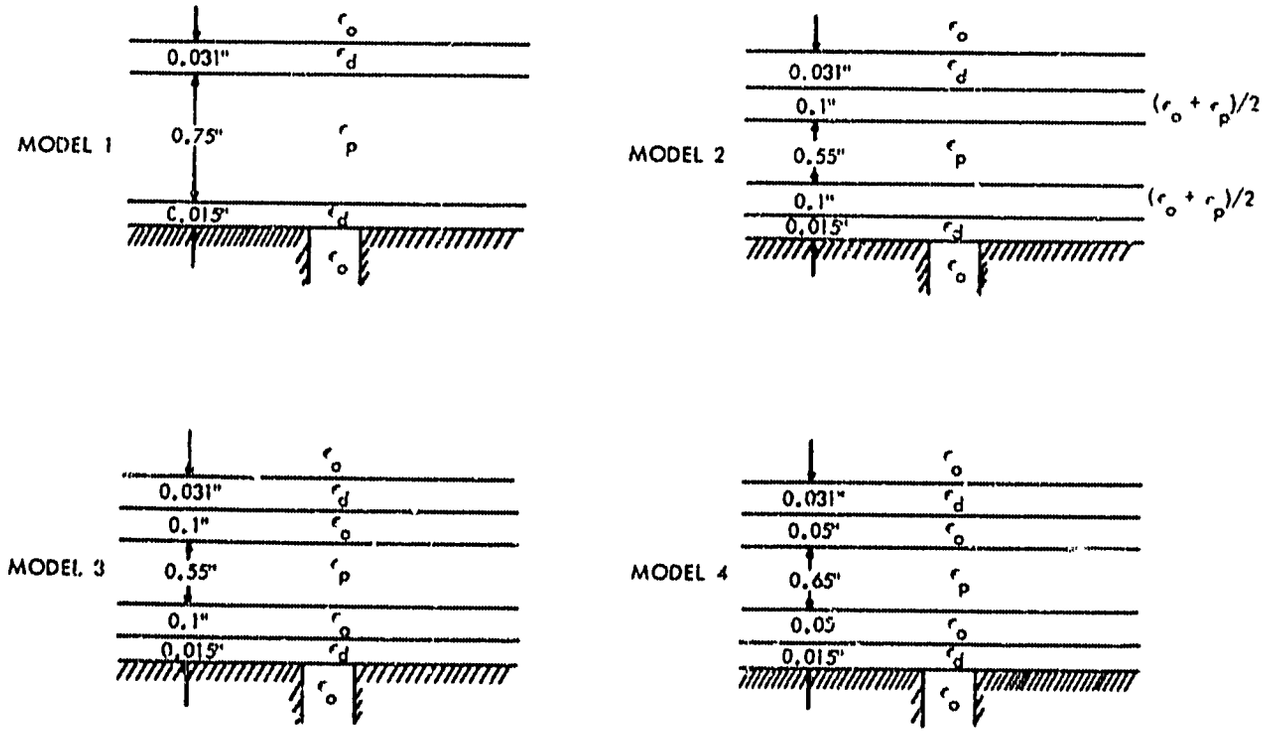
MODEL 1
0.031"
0.75"
0.015"
MODEL 2
0.031"
0.1"
0.55"
0.1"
0.015"
$(r_o + r_p)/2$
$(r_o + r_p)/2$
MODEL 3
0.031"
0.1"
0.55"
0.1"
0.015"
MODEL 4
0.031"
0.05"
0.65"
0.05
0.015"

Figure 11

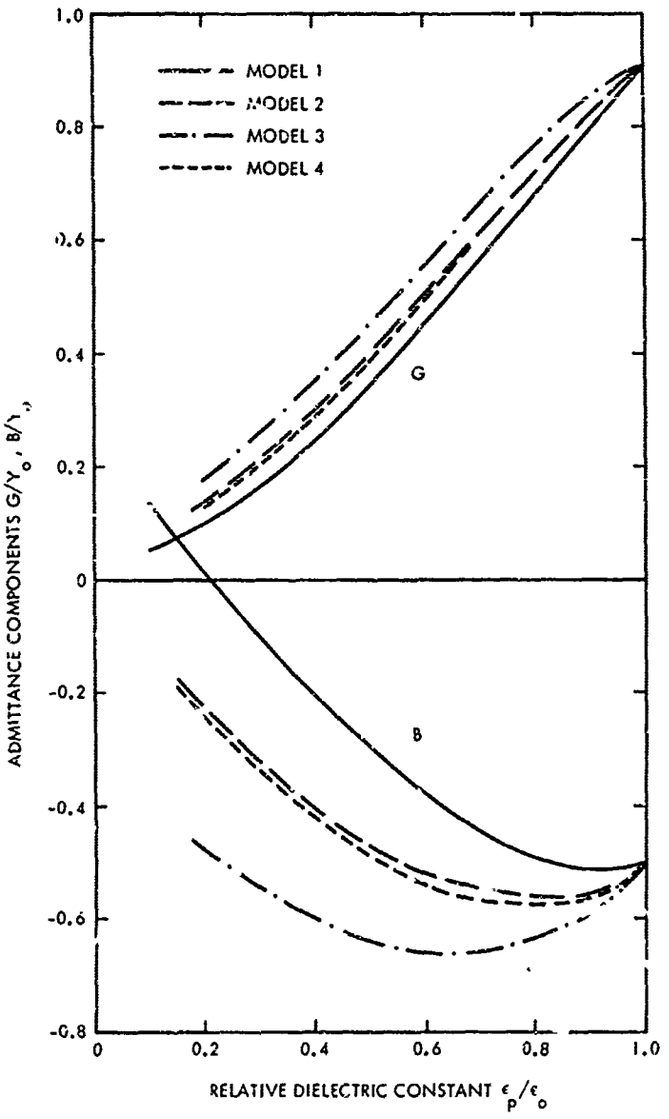
MODEL 1
MODEL 2
MODEL 3
MODEL 4
G
B
1.0
0.8
0.6
0.4
0.2
0
-0.2
-0.4
-0.6
-0.8
0
0.2
0.4
0.6
0.8
1.0
ADMITTANCE COMPONENTS G/Y$_o$, B/Y$_o$
RELATIVE DIELECTRIC CONSTANT ϵ_p/ϵ_o

Figure 12

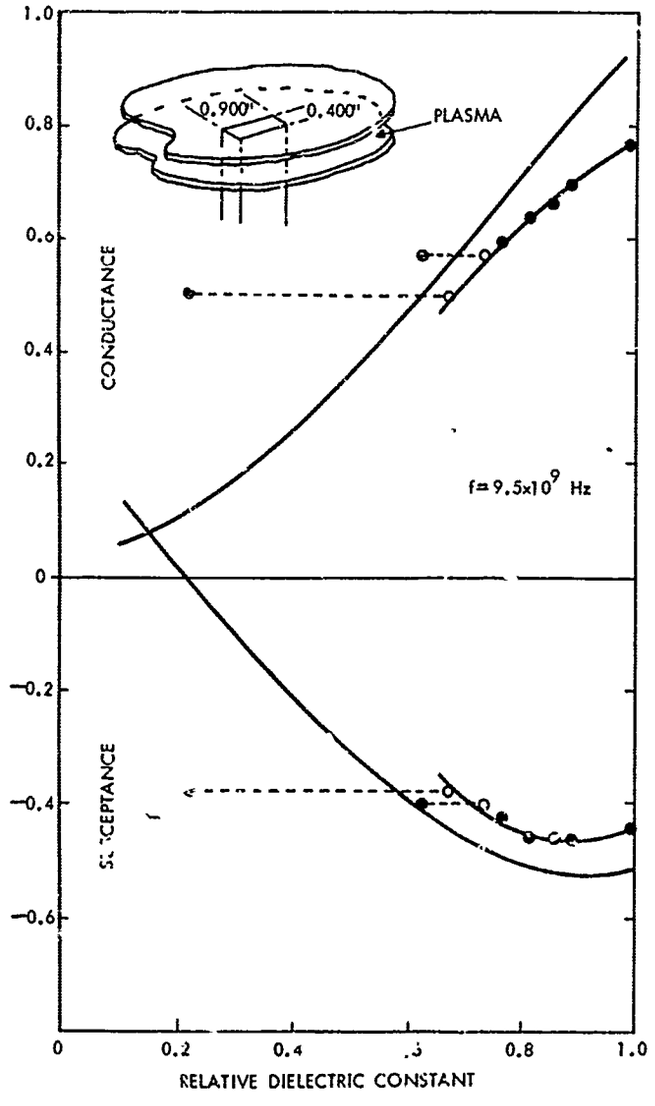
1.0
0.8
0.6
0.4
0.2
0
−0.2
−0.4
−0.6
0.900"
0.400"
PLASMA
CONDUCTANCE
f=9.5x10^9 Hz
0
0.2
0.4
.3
0.8
1.0
RELATIVE DIELECTRIC CONSTANT

Figure 13

RADIO SCIENCE, Vol. 2 (New Series), No 2, February 1967

II. ADMITTANCE OF A PLASMA-COVERED CYLINDRICAL ANTENNA *

G. Meltz, P. J. Freyheit, and C. D. Lustig
Sperry Rand Research Center, Sudbury, Mass., 01776, U.S.A.

Abstract

Based on a variational formulation, an expression is derived for the admittance of a circumferential gap in an infinite cylinder covered by a set of coaxial dielectric or plasma layers. The gap is fed by the dominant TEM mode in a narrowly-spaced, parallel-plate, radial waveguide. Numerical computations are presented for a multiple-layer model of a lossy plasma and for a dielectric layer which supports surface waves. These computations are compared with admittance measurements of a similarly excited metal cylinder surrounded by an annular plasma. The plasma is produced in a long double-wall cylindrical vessel by a pulsed d-c discharge in argon at 0.4 Torr. In the experiment, the radial guide is excited by a small axial probe fed by a conventional coaxial air line. The admittance viewed in the coaxial line is related to the gap admittance by an experimentally determined two-port network representing the junction region. The measurements are in fair agreement with calculated values based on a three-layer model of the inhomogeneous plasma and the discharge tube.

* The paper presented at the Third Plasma Sheath Symposium by G. Meltz, P.J. Freyheit, and C.D. Lustig "The Admittance of a Plasma-Covered Cylindrical Antenna" has been extensively modified by the authors. Due to the modifications the authors have requested that this paper be presented only in Abstract. Interested readers are referred to Radio Science Vol. 2 (New Series), No. 2, February 1967, pp. 203-224 for the complete version of the paper.

III. RADIATION PATTERNS AND ADMITTANCE OF AN AXIAL SLOT ON A PLASMA COVERED CYLINDER*

*This work was partially supported by Contract NAS1-4623

C. M. Knop†
Andrew Corporation
Orland Park, Illinois

†Formerly of NESCO, Pasadena, California

C. T. Swift
NASA Langley Research Center
Langley Station, Hampton, Va.

H. Hodara
National Engineering Science Company
Pasadena, California

INTRODUCTION

The admittance characteristics of three types of slotted-cylinder antennas are considered, namely, the long axial slot, the finite axial slot, and the gap antenna backed by a short-circuited radial cavity.

Most of the present effort is confined to a study of the long slot on the cylinder. This was done because the computational requirements are not too severe, yet the results should be indicative of the trends experienced by finite apertures in a reentry environment. Systematic computations of the admittance per unit length are made for various coating conditions.

First, the case of no coating is considered, and results are compared with those for identical slots on flat ground planes. Second, the special case of the plasma resonant ($\omega = \omega_p$, $\nu = 0$) coating is analyzed to determine whether or not a measurement of the input admittance at resonance will yield diagnostic information. Finally, the case of a general coating is treated to ascertain the effects of losses and plasma inhomogeneities on the admittance.

The exterior portion of finite apertures on coated cylinders are not too difficult to analyze but can lead to computational difficulties, even in the far field where asymptotic expansions may be made to simplify the field expressions. In the near field, no such expansions are allowed; therefore, the computational requirements of the external admittance are more severe. Furthermore, the size of the cylinder chosen for the present analysis (based on adaptability to feed with the slotted line) was so large that additional difficulties were introduced into the computations due to the large arguments of the Bessel and Hankel functions involved.

The work on the large cylinder includes specific computations of the conductance for the uncoated cylinder, and experimental results for both coated and uncoated cylinders. Admittance expressions for the coated cylinder are given and preliminary calculations of the conductance are discussed. Experimental and theoretical results for radiation patterns are also discussed.

Finally, the gap antenna, backed by a short circuited radial cavity and fed by a current element at the periphery is briefly discussed. Specific computations of the impedance for the case of no coating are made, and expressions with coating are given.

THE INFINITE SLOT ON A COATED CYLINDER

The geometry of the structure considered is shown in figure 1. A long slot is cut into an infinite conducting cylinder, and is excited by an electric field which is uniform along the axis, and across the slot, and which varies in time as $e^{+j\omega t}$. The structure is coated with a dielectric, whose complex index of refraction, N may vary in the radial direction.

The tangential fields, H_z and E_ϕ, at any point exterior to the cylinder are described by a Fourier series in azimuth, i.e.,

$$H_z(\rho,\phi) = \sum_{m=-\infty}^{\infty} \bar{H}_{mz}(\rho)e^{-jm\phi} \tag{1a}$$

$$E_\phi(\rho,\phi) = \sum_{m=-\infty}^{\infty} \bar{E}_{m\phi}(\rho)e^{-jm\phi} \tag{1b}$$

Note that equations (1) are independent of the axial coordinate, and that the modal coefficients $H_{mz}(\rho)$ and $E_{m\phi}(\rho)$ depend only on the radial coordinate. These coefficients are determined by a straightforward application of the boundary conditions (appendix II).

The complex power per unit length radiated from the aperture is found by integrating the radial component of the Poynting vector across the slot, i.e.,

$$P = \int_{-\phi_o/2}^{\phi_o/2} S_\rho a\, d\phi = \frac{a}{2} \int_{-\phi_o/2}^{\phi_o/2} E_\phi^*(a,\phi)H_z(a,\phi)d\phi \tag{2}$$

The substitution of equations (1) into equation (2) gives

$$P = \frac{a}{2} \sum_{m'=-\infty}^{\infty} \sum_{m=-\infty}^{\infty} \bar{E}_{m'\phi}^*(a)\bar{H}_{mz}(a) \int_{-\pi}^{\pi} e^{-j(m-m')\phi}d\phi$$

$$= \pi a \sum_{m'=-\infty}^{\infty} \sum_{m=-\infty}^{\infty} \bar{E}_{m'\phi}^*(a)\bar{H}_{mz}(a)\delta_{mm'} = \pi a \sum_{m=-\infty}^{\infty} \bar{E}_{m\phi}^*(a)\bar{H}_{mz}(a) \tag{3}$$

which is nothing more than Parseval's theorem in cylindrical coordinates.[1]

The external or radiation admittance is defined by[2]

$$Y_{cl} = \frac{2P}{|V_o|^2} = 2\pi a \sum_{m=-\infty}^{\infty} \frac{\bar{E}_{m\phi}^{*}(a)\bar{E}_{m\phi}(a)}{|V_o|^2} \tag{4}$$

where V_o is the applied potential across the slot. Suppose, now that the slot is fed by a parallel-plate waveguide excited in the TEM mode. It is assumed that all higher modes are negligible so that E_η is the only component of tangential electric field across the aperture, and is of the form

$$E_\eta = \frac{V_o}{a} \tag{5}$$

If the slot is sufficiently thin, then $E_\eta \cong E_\phi$ and $d_\eta \cong a\, d\phi$. Therefore the following transform pair exists:

$$E_\eta \cong E_\phi = \frac{V_o}{a}$$

$$E_{m\phi} = \frac{V_o}{2\pi a} \frac{\sin(m\phi_o/2)}{(m\phi_o/2)} \tag{6b}$$

Having specified the electric field at the aperture, the external admittance may be computed.

NO COATING

If the antenna radiates into free space, the normalized external admittance per unit length as derived in appendix II is

$$\lambda_w Y_{cvl} = \frac{Y_{cvl}\lambda_w}{Y_o} = \frac{-j2}{\pi C} \sum_{m=0}^{\infty} \frac{a_m}{(1 + a_{om})} \frac{H_m^{(2)}(C)}{H_m^{(2)\prime}(C)} \tag{7}$$

Equation (7) was programed on an electronic computer and results were obtained for two cylinders having different gaps whose circumference-to-wavelength ratio ranged from 8.4 to 45.4. The results are given in

figure 2. For reference, the admittance of a slot of the same width on a flat ground plane as given by Harrington[3] is also plotted in figure 2. To the accuracy with which one could read Harrington's graph, the admittance of the slot on the cylinder throughout the whole range of C was very close to that of a slot on a flat ground plane.

RESONANT COATING

It has been shown (ref. 4) that only the $m = 0$ mode is supported at the plasma resonant condition, $N = 0$, $\left(\text{i.e., } \nu = 0, \ \omega_p = \omega\right)$; therefore, the radiation patterns of an infinitely long slot (or the equatorial patterns of a finite slot) are circular, regardless of the size of the cylinder and thickness of the sheath as long as each are finite. Since the sudden deformation of the radiation pattern into a circle suggests a method of diagnosing a reentry plasma, the admittance was also investigated to determine its behavior at plasma resonance for possible means of diagnostics. At the resonant condition, this admittance per unit length (appendix II) is:

$$Y_{R1}\lambda_v \underset{W>1}{=} \left.\frac{Y_{R1}\lambda_v}{Y_o}\right|_{W>1} = -j\,\frac{1}{C\left[\dfrac{H_o^{(2)\prime}(C)}{H_o^{(2)}(C)} + \dfrac{C}{2}\left(W - \dfrac{1}{W}\right)\right]} \tag{8}$$

The results of equation (8) are plotted in figure 3 as a function of C and W. Again two cylinders were chosen with C ranging between 8.4 and 45.4. Note that for $W = 1.00 + \epsilon$, which corresponds to a vanishing plasma thickness, the conductance decreases from the free-space value by an order of magnitude. Also, the susceptance can change from a large capacitative to a small inductive value or zero when the structure is

coated with this resonant plasma. As the plasma becomes thicker, the admittance per unit length approaches zero. This tendency for the admittance to drop at resonance suggests that a measurement of admittance could also be used for diagnostics.

The admittance of the slot has not yet been computed as the index of refraction increases from zero to some small finite value. However, based upon calculated changes in the radiation patterns due to a small departure from resonance,[4] one concludes that additional azimuthal modes (m = 1, 2, 3, etc.) are rapidly introduced into the field dependence, at least for C ranging between 22.7 and 45.4. As such, one can expect that these modes will alter, perhaps significantly, the input admittance from what it is at resonance; the extent of the alteration increasing with increasing C. However, for small C, this alteration may still be sufficiently small to cause a measurement of the input admittance near and at plasma resonance to be a useful plasma diagnostic tool. This remains to be investigated.

GENERAL COATING

The method described by Swift[5] was used to analyze the slotted cylinder coated with a dielectric having a complex index of refraction. In this approach, the wave equation is numerically integrated through the plasma, thereby avoiding the computational problem of evaluating Bessel and Hankel functions of complex arguments, which describe the functional behavior of the fields within the coating. Furthermore, if this method is used, the case of a coating whose dielectric properties vary radially may also be treated.

Using Swift's notation, the normalized admittance for either homogeneous or inhomogeneous coatings (see appendix II for an outline) is:

$$y_{cl} = \frac{Y_{cl}\lambda_v}{Y_o} = -j\,\frac{2}{a}\,\frac{\epsilon(a)}{\epsilon_o}\sum_{m=0}^{\infty} a_m\,\frac{t_m(a) + ju_m(a)}{t_m'(a) + ju_m'(a)} \qquad (9)$$

where the prime indicates differentiation with respect to the radial parameter.

Computations of equation (9) are plotted in figures 5 and 6 as a function of complex index of refraction for coating thickness corresponding to $\frac{2\pi(b-a)}{\lambda_v} = 0.25$ and a slot width corresponding to $\frac{2\pi w}{\lambda_v} = 0.25$ for cylinders of size $C = 4$, 8, and 12. It is important to note that the admittance is relatively insensitive to variations in C. One is therefore tempted to conclude that the admittance of identical slots on cylinders and flat ground planes are, for all practical purposes, the same* if $C \geq 4$ and if the loss angle δ of the coating is between 90° and 180°, and if the magnitude of $N \geq 1$.

Flow field analysis shows that the electron density and collision frequency may vary considerably within the plasma sheath. A typical example of the distribution along a normal to the vehicle is shown in figure 7, and was chosen as a coating for a cylinder of physical radius 4.152 cm and an aperture width of 1.016 cm†. The admittance was computed as a function of the exciting frequency, and the results are given in figure 8.

---

*A more general conjecture of this type was suggested during conversations with one of the writers (CHT) by W. Rotman of AFCRL prior to the time these extensive computations were performed.

†This width corresponds to the width of a standard X-band waveguide.

Nineteen admittance points were computed in the frequency interval of 10.0 to 11.8 kmc, yet this number was insufficient to establish a smooth curve because of small-scale fluctuations. Nonetheless, some interesting features are revealed. The most striking effect occurs in the region of peak plasma frequency (10.76 kmc), where the conductance decreases sharply and susceptance begins to decrease monotonically.

This seems to be consistent with the results of the resonant plasma coating. At frequencies above resonance, the conductance rises rapidly, but the susceptance remains relatively constant. As the frequency increases, the admittance should approach the no coating values. Below resonance, the curves are fluctuating too much to suggest any general conclusions.

For the types of distributions shown in figure 7, the peak plasma frequency seems to be a sharp dividing point for the admittance properties of slots on cylinders. Whether this is true in general remains to be seen.

THE AXIAL SLOT ON A COATED CYLINDER

The geometry is shown in figure 9. A waveguide, excited in the TE_{01} mode opens onto a cylindrical ground plane, with the long dimension of the waveguide parallel to the axis of the cylinder. Higher-order modes are neglected in the waveguide, and the slot is assumed to be thin enough so that over the slot $E_\eta \sim E_\phi$ and $a\,d\phi = d\eta$.

Since the aperture is finite, and since the tangential fields vary with z, the fields are described by continuous modes in axis and discrete modes in azimuth, i.e.,

$$E_z(\rho,\phi,z) = \sum_{m=-\infty}^{\infty} \int_{-\infty}^{\infty} \bar{\bar{E}}_{mz}(\rho) e^{-jhz} e^{-jm\phi}\,dh \qquad (10a)$$

$$E_\phi(\rho,\phi,z) = \sum_{n=-\infty}^{\infty} \int_{-\infty}^{\infty} \overline{\overline{E}}_{n\phi}(\rho) e^{-jhz_e} e^{-jn\phi} dh \qquad (10b)$$

And the complex power radiated by the aperture is

$$P = \frac{1}{2} \int_{-z_0/2}^{z_0/2} \int_{-\phi_0/2}^{\phi_0/2} E_\phi^*(a,\phi,z) H_z(a,\phi,z) a \, d\phi \, dz \qquad (11)$$

Using Parseval's theorem, equation (11) can be rewritten in the following form

$$P = \frac{1}{2}(2\pi)^2 a \sum_{n=-\infty}^{\infty} \int_{-\infty}^{\infty} \overline{\overline{E}}_{n\phi}^*(a) \overline{\overline{H}}_{nz}(a) dh \qquad (12)$$

And, the external admittance is:

$$Y_c = \frac{2P}{|V_0|^2} = 4\pi^2 a \sum_{n=-\infty}^{\infty} \int_{-\infty}^{\infty} \frac{E_{n\phi}^*(a) \overline{\overline{H}}_{nz}(a)}{|V_0|^2} dh \qquad (13)$$

If the tangential field is $E_\eta \cong E_\phi$ the following transform pair exists:

$$E_\phi(a,\phi,z) = \frac{V_0}{w} \cos\left(\frac{\pi z}{l}\right) \qquad (14a)$$

$$\overline{\overline{E}}_{n\phi}(a) = \frac{-V_0}{2\pi a} \frac{\cos\left(\frac{hl}{2}\right)}{l\left(h^2 - \frac{\pi^2}{l^2}\right)} \frac{\sin\left(n\phi_0/2\right)}{\left(n\phi_0/2\right)} \qquad (14b)$$

The external admittance can now be computed using equations (13) and (14b) in connection with the solution of the boundary-value problem, which gives $\overline{\overline{H}}_{nz}(a)$.

NO COATING

For this case of no coating, the normalized external conductance and susceptance are

$$g_{cv} = \frac{G_{cv}}{Y_o} = \frac{1}{2\pi^5 k^4 p^2} \sum_{m=0}^{\infty} \frac{a_m}{(1 + \delta_{om})} I_{mg} \tag{15a}$$

$$b_{cv} = \frac{B_{cv}}{Y_o} = \frac{1}{2\pi^3 pk^3} \sum_{m=0}^{\infty} \frac{a_m}{(1 + \delta_{om})} (I_{1m} - I_{2m}) \tag{15b}$$

where

$$I_{mg} = \int_0^1 \frac{\cos^2(\pi k y)\,dy}{\left(y^2 - \frac{1}{4k^2}\right)^2 \left|H_m(2)'\left[2\pi pk\sqrt{1 - y^2}\right]\right|^2} \tag{16a}$$

$$I_{1m} = \int_1^{\infty} \frac{\sqrt{y^2 - 1}\,\cos^2(\pi k y) K_m\left[2\pi p\sqrt{y^2 - 1}\right] dy}{\left(y^2 - \frac{1}{4k^2}\right)^2 K_m'\left[2\pi pk\sqrt{y^2 - 1}\right]} \tag{16b}$$

$$I_{2m} = \int_0^1 \frac{\sqrt{1 - y^2}\,\cos(\pi k y)\left\{J_m(x)J_m'(x) + Y_m(x)Y_m'(x)\right\} dy}{\left(y^2 - \frac{1}{4k^2}\right)^2 \left|H_m(2)'(x)\right|^2} \tag{16c}$$

Equation (15a) was computed over the X-band range of 6.56 to 13.12 kmc corresponding to a range of slot lengths of 1/2 to 1 wavelength for the TE_{01} mode, and the results are shown in figure 10. For this range of frequencies and the 13-inch-diameter cylinder used ($2a = 13$ in.) the parameter C increases from 22.7 at $k = 0.5$ to 45.4 at $k = 1.0$.

As a partial check of the computations, the width of the slot at $k = 0.5$ was allowed to approach zero in order to compare the results with those of Wait (ref. 5) for the thin resonant slot. The computations performed here give $g_{cv} = 0.383$ compared to Wait's $g_{cv}\big|_{Wait} = 0.384$. This partial check served as a go-ahead for proceeding with the other cases.

EXPERIMENTAL RESULTS - NO COATING

The particular size of aperture and range of cylinder size C considered in most of the computations were chosen with X-band experiments in mind. The cylinder shown in figure 11 is 13 inches in diameter and 24 inches long, and is just large enough to contain a Hewlett-Packard slotted line. The aperture size is 0.4 inch × 0.9 inch, which corresponds to the inner dimensions of a standard RG-52U waveguide. The short circuit was realized by placing a small brass plate curved to fit the cylinder surface and held in place by a strap. Photographs of the end view showing the feed arrangement and the measurement setup is shown in figures 11 and 12.

The experimental and theoretical results are shown in figure 13. The measured and calculated values of the input conductance differ by, at most, 5 percent. The agreement is sufficiently close to conclude that the effect of higher-order modes and/or computational errors are negligible for the large-sized uncoated cylinder used here. Agreement between first-order theory and experiment can also be expected to be good for smaller cylinders with correspondingly thinner slots.

EXPERIMENTAL RESULTS - POLYETHYLENE COATING

The cylinder used above for the noncoated condition was coated with a polyethylene coating (representing, electrically, an ablative coating) of a quarter-inch thickness, i.e., $T = b - a = 0.25$ inch, and measurements of input waveguide admittance were made. The dielectric constant of this coating material was first measured over the X-band frequency range to ascertain the correctness of the published value of $\epsilon_r = 2.25$. Four samples were cut out of the polyethylene stock sheet and their dielectric constant was measured by both the Von-Hippel method and by directly

measuring the guide wavelength in a slotted line completely filled with the sample material. Both methods of measurement gave an ϵ_r which was within approximately ±1 percent of the published value of 2.25. This is within the accuracy of the measurements; thus, one can justifiably take the dielectric constant as 2.25 within this accuracy.

The polyethylene sleeve was "heat fitted" on the cylinder so as to make a snug fit, and it is estimated that the accuracy of concentricity of the outer surface and inner surface of the dielectric coating was within ±0.010 inch. The slip fitting of the dielectric sleeve on the metal cylinder is depicted in the photograph of figure 14.

The measurements of admittance were made in the conventional manner as with the condition of no coating. To realize the short circuit condition and to avoid the necessity of removing the dielectric sleeve and then replacing it at each frequency used, the short was first placed on the non-coated cylinder at each of the frequencies to be used and the frequency setting was accurately determined by means of a frequency meter accurate to within $\pm 2\frac{1}{2}$ mc (Hewlett-Packard Model X532B). These exact frequencies were then reused with the short removed and the dielectric sleeve in position.

Plots of g_{in} and b_{in} are shown in figures 15 and 16, respectively.

Measurements were then repeated for four different circumferential positions of the dielectric sleeve at each of several frequencies, as shown in table I and figures 15 and 16. The dielectric positions were separated by increments of 90° and designated by positions A, B, C, and D as defined in table I. It is seen from figures 15 and 16 that the resultant admittance differs for each position of the dielectric even though the frequency was held constant. This can be attributed to one or both of the following

reasons: for each position the "effective dielectric constant" of the coating differs due to the approximately ±1 percent deviation in the circumferential variation of dielectric constant which exists; for each position the effective thickness of the dielectric coating differs due to the inner and outer radial variation of approximately ±0.010 inch. In either case, such changes influence the mean electrical circumferential length of the coating, $\bar{C}$, here defined by:

$$\bar{C} = \frac{2\pi\bar{a}}{\lambda_V}\bar{N} = \frac{C}{2}(W + 1)\bar{N} \tag{17}$$

where $\bar{a}$ is the mean radius $\left(\bar{a} = \frac{a + b}{2}\right)$ and $\bar{N}$ is the mean refractive index. It is seen that the change in $\bar{C}$ due to changes in $\bar{a}$ (i.e., W) and/or $\bar{N}$ is

$$\Delta\bar{C} = \frac{C}{2}(W + 1)\Delta\bar{N} + \bar{N}\,\Delta W \tag{18}$$

which since $W \approx 1$ and $\Delta W = \Delta T/a$, $\Delta T = \Delta(b-a)$, is

$$\Delta\bar{C} = \frac{C}{2}\,2\,\Delta\bar{N} + \bar{N}\,\frac{\Delta T}{a} \tag{19}$$

It is recognized that the first term contributing to $\Delta\bar{C}$ is the change in circumferential electrical length due to the change in the refractive index of the coating whereas the second is due to the change in thickness of the coating. Now, here upper limits of $\Delta\bar{N}$ and $\Delta T/a$ are approximately $\Delta\bar{N}_{max} = \pm 0.02$ and $\Delta T/a = \pm 0.004$ so that $\Delta\bar{C} \approx C\ (0.024)$, $\Delta\bar{C}_{max} \approx 0.024 C_{max}$. For the cylinder used at X-band, $C_{max} \approx 45$, therefore, the maximum change in C can be $\Delta C_{max} \approx 1.0$; i.e., the mean circumferential electrical length of the coating can approach the order of a wavelength in the coating material. Intuitively, one would expect that such a

change would very well lead to a large change in input admittance. It is seen that the major contribution to $\overline{\Delta Y}$ is from $\Delta \overline{H}$. Thus, for large cylinders (large C's) small changes in the refractive index may be expected to account for the observed changes in admittance.

To make meaningful measurements of the input admittance and to compare them with computed results, it follows that stricter tolerances on the refractive index and coating thickness will be necessary if one uses electrically large cylinders. These tolerances will be correspondingly reduced (as seen from eq. (19)) for smaller cylinders. It would seem then that for an initial test of theory it may be more appropriate to use smaller cylinders.

The radiation patterns also seemed to be sensitive to small changes in the electrical parameters. The measured equatorial plane patterns are shown in figures 17(a) to 17(f) along with the corresponding computed patterns (using expression 335 of Wait[2]). It is seen that the agreement between theory and experiment in the forward direction is quite satisfactory; however, at the higher frequencies (k = 0.80, 0.85, and 0.90) the radiation level measured in the rear was considerably higher than that predicted, although for the lower frequencies (k = 0.65, 0.70, and 0.75) agreement at the rear is still satisfactory. The poor agreement in the rear direction may also be attributed to the critical dependence on the parameters of H and W.

ADMITTANCE OF A COATED AXIAL SLOT

From the work of Wait[2] the pertinent fields established in region 1 ($a \leq \rho \leq b$) and region 2 ($b \leq \rho \leq \infty$) of figure II-1 are given by (336), (337), (339), (340), and (342), (343), (345), (346) of Wait, respectively.

For the sake of brevity, these expressions will not be rewritten here but it is noted that the following difference in notation is used:

Wait's notation	Notation of this report
μ	μ_v
u_o	u_v
k_o	β_v

Furthermore, it is noted here that in table I of Wait[2] (p. 128) that the coefficient b_{m1} should be multiplied by u, and the coefficient a_{m5} is lacking a minus sign.

Here again the tangential electric fields on the cylindrical surface $\rho = a$ are assumed to be

$$E_\phi(a,\phi,z) = \begin{cases} 0 & \text{off slot} \\ E_o \cos\left(\frac{\pi z}{l}\right) & \text{on slot} \end{cases} \tag{20a}$$

$$E_z(a,\phi,z) = 0 \tag{20b}$$

From equation (20a) it follows that the transform of E_ϕ is

$$\bar{E}_{\phi m}(h,a) = \frac{1}{(2\pi)^2} \int_{-\pi}^{\pi} \int_{-\infty}^{\infty} E_\phi(a,\phi,z) e^{jhz} e^{jm\phi} dz\, d\phi \frac{-\sqrt{a_m}\, V_o \cos\left(h\frac{l}{2}\right)}{2\pi\left(\frac{a}{l}\right)\left(h^2 l^2 - \pi^2\right)} \tag{21}$$

and from (339) of Wait the transform of H_z is

$$\bar{H}_{zm}(h,a) = u^2\left[b_m H_m^{(2)}(ua) + B_m J_m(ua)\right] \tag{22}$$

From Parseval's theorem the external (radiation) admittance is

$$Y_c = \frac{2P_c}{|V_0|^2} = \frac{1}{2}(2\pi)^2 \sum_{m=-\infty}^{m=+\infty} \int_{-\infty}^{\infty} \bar{E}_{\phi m}(h,c)\bar{H}_{zm}(h,a)dh \qquad (23)$$

Using the six tangential boundary conditions (continuity of E_ϕ, E_z, H_ϕ, H_z at $\rho = b$, and continuity of E_ϕ and E_z at $\rho = a$) and determinants gives expressions for B_m, b_m, and D_m, respectively, where D_m is the determinant formed by the coefficients a_{mp}, etc., in table I, p. 128, of Wait.

Explicitly solving for B_m, b_m, and D_m and substituting the expressions into equation (23) then gives

$$Y_c = \frac{\pi}{\omega_0(\mu)^2} \sum_{m=-\infty}^{m=+\infty} \int_{-\infty}^{\infty} \frac{\omega^2\left(\frac{\mu}{\omega}\right)\left(\epsilon_1^2\mu_1^2\left[\frac{\omega}{\omega_1}\right]^2 J_m(\omega) - \omega J_m^{(1)}(\omega)\right]\left[\omega J_m^{(2)}(\omega) - \omega J_m^{(2)'}(\omega)\right] - \left(\frac{\mu}{\omega}\right)^2(\mu^2 - \omega^2)^2 J_m^2\left[J_m^{(2)}(\omega)\right]^2\right) d\omega}{(\omega^2 - \mu^2)^2\left(\epsilon_1^2\mu_1^2\left[\frac{\omega}{\omega_1}\right]^2 J_m(\omega) - \omega J_m^{(1)}(\omega)\right]\left[\omega J_m^{(2)}(\omega) - \omega J_m^{(2)'}(\omega)\right] - \left(\frac{\mu}{\omega}\right)^2(\mu^2 - \omega^2)^2 J_m^2\left[J_m^{(2)}(\omega)\right]^2\right)}$$

(24)

where:

$$U_m = J_m(ua)H_m^{(2)'}(ub) - J_m'(ub)H_m^{(2)}(ua) \qquad (25a)$$

$$V_m = J_m(ua)H_m^{(2)}(ub) - J_m(ub)H_m^{(2)}(ua) \qquad (25b)$$

$$I_m = J_m(ub)H_m^{(2)'}(ua) - J_m'(ua)H_m^{(2)}(ub) \qquad (25c)$$

$$T_m = J_m'(ub)H_m^{(2)'}(ua) - J_m'(ua)H_m^{(2)'}(ub) \qquad (25d)$$

As a partial check on equation (24), consideration of the special case of no coating (b = a) or an air coating (N = 1) each cause equation (24) to reduce to equation (15a) and (15b) as should be

Rationalization and normalization of equation (25) then gives

$$\sigma_{\theta\theta} = \frac{2\pi}{(k_1 a)^2 \left(\frac{b}{a}\right)^2 \pi^2} \sum_{m=0}^{\infty} \frac{\epsilon_m}{(1+\delta_{0m})} \int_0^1 \left[\frac{\begin{array}{l} (x^2-y^2)(1-y^2)\cos^2\left(\frac{b}{2}\sqrt{x^2-y^2}\right)\left[(x^2-y^2)(1-y^2)(cw)^2\left|x^2\sqrt{1-y^2}\,\bar{U}_m Y_m^{(2)}(\chi)\right.\right. \\ \left. - \sqrt{x^2-y^2}\,\bar{V}_m Y_m^{(2)\prime}(\chi)\right|^2 + (cw)^2(x^2-1)^2\bar{V}_m^2\left|Y_m^{(2)}(\chi)\right|^2\Big] \end{array}}{\begin{array}{l} \left[y^2 - \frac{x^2}{(k_1 a)^2}\right]\Big|(cw)^2(x^2-y^2)(1-y^2)\left[x^2\sqrt{1-y^2}\,\bar{U}_m Y_m^{(2)}(\chi)\right. \\ \left. - \sqrt{x^2-y^2}\,\bar{V}_m Y_m^{(2)\prime}(\chi)\right]\left[\sqrt{1-y^2}\,\bar{U}_m Y_m^{(2)}(\chi)\right. \\ \left. - \sqrt{x^2-y^2}\,\bar{L}_m Y_m^{(2)\prime}(\chi)\right] - (cw)^2(x^2-1)\bar{V}_m Y_m\left[Y_m^{(2)}(\chi)\right]^2\Big|^2 \end{array}} \right] dy \tag{26}$$

where $\chi_y \equiv cw\sqrt{1-y^2}$, $\qquad \chi \equiv cw\sqrt{\epsilon_r - y^2}$

$$\left.\begin{aligned} \bar{L}_m &= \left[J_m(\chi)Y_m'\left(\frac{\chi}{w}\right) - J_m'\left(\frac{\chi}{w}\right)Y_m(\chi)\right] \\ \bar{T}_m &= \left[J_m'(\chi)Y_m'\left(\frac{\chi}{w}\right) - J_m'\left(\frac{\chi}{w}\right)Y_m'(\chi)\right] \\ \bar{U}_m &= \left[J_m\left(\frac{\chi}{w}\right)Y_m'(\chi) - J_m'(\chi)Y_m\left(\frac{\chi}{w}\right)\right] \\ \bar{V}_m &= \left[J_m\left(\frac{\chi}{w}\right)Y_m(\chi) - J_m(\chi)Y_m\left(\frac{\chi}{w}\right)\right] \\ L_m &= -j\bar{L}_m \\ T_m &= -j\bar{T}_m \\ U_m &= -j\bar{U}_m \\ V_m &= -j\bar{V}_m \end{aligned}\right\} \tag{27}$$

It is important to note that the above expression was also derived independently by integrating the Poynting vector over a spherical surface of radius r in the far field. As a partial check on equations (27) the case

of no coating ($b = a$, i.e., $W = 1$) or an air coating ($W = 1$) both reduce equations (27) to equation (18a) as should be.

It is noted that the above reduction of y_2 shows that only the integration from $0 \leq y \leq 1$ contributes to the conductance (which may be anticipated if one considers that the conductance can also be obtained using Poynting's vector and the radiation fields).

However, the expression for b_c will be of the form

$$b_c\Big|_{W \geq 1} = \int_0^1 + \int_1^W + \int_W^\infty \tag{28}$$

for the general case of an arbitrary homogeneous coating. As yet the explicit form for the integrands of equation (28) has not been obtained.

An attempt was made to program a modified form of equation (27) in order to compute the conductance of the axial slot on the 13-inch-diameter coated cylinder. However, the results seemed to be in error by at least 6 percent. Possible errors in this computation are still being investigated by examining a plot of the integrand of equations (27).

THE CYLINDRICAL GAP ANTENNA

The antenna under discussion, shown in figures 18, 19, and 20, is essentially a cylindrical geometry version of a spherical slot antenna described by Musiake and Webster[7]. Such an antenna has interesting features that make it extremely useful as a diagnostic tool for reentry plasma sheaths. To name a few:

1. Its cylindrical structure with no protruding part allows it to be an integral part of the reentry vehicle.

2. The feed system consisting of the inner conductor of a coaxial cable across a gap much smaller than a wavelength supports a uniform current; as a result, solutions are possible without assuming an aperture field distribution.

3. In spite of such a narrow gap, the antenna is an excellent radiator when its circumference is approximately equal to 2 wavelengths. At VHF frequencies, the physical size of the antenna is competible with the size of many small reentry vehicles.

4. An additional feature of the narrow gap is to rule out the existence of axial magnetic fields at the aperture and inside the gap. Consequently, only azimuthal E_{z_m} modes are excited and this field distribution is maintained even in the presence of radially nonhomogeneous plasmas.

5. The antenna is a resonant structure whose radiation and impedance properties are determined only by one significant azimuthal mode. From the number of lobes in the radiation pattern, it is possible to determine the significant modal impedance.

6. Finally, this is an antenna which is amenable to simple mathematical analysis, permitting accurate prediction of both far and near field performance.

In this paper the antenna input impedance both with and without plasma coating is discussed. Experimental checks are only given for no coating, and are correlated to the radiation patterns.

INPUT IMPEDANCE WITH NO PLASMA COATING

Consider the cylindrical gap antenna depicted in figure 18. The gap width d is narrow compared to the free-space wavelength $\lambda_o \left(d \ll \lambda_o\right)$ and is formed by a radial waveguide short-circuited at its center by a spacer of radius $\rho = \rho_o$. The gap is fed by a coaxial line located at the rim of the guide at $\rho = a$. The coax center conductor makes electrical contact with the guide top plate and its outer conductor is shorted out against the bottom plate. Because the gap width is small, with respect to the wavelength, the current along the coax inner conductor across the gap can be taken to be constant and equal to I. If the voltage in the coax is V_c, the antenna input impedance presented by the gap to the coax is

$$Z_{in} = -\frac{V_c}{I} \tag{29}$$

This is not merely a definition but also a measurable quantity related to the reflection coefficient Γ in the coax via its characteristic impedance Z_c,

$$Z_{in} = Z_c \frac{1 + \Gamma}{1 - \Gamma} \tag{30}$$

In order to calculate Z_{in}, refer to figure 21 which shows the feed region grossly enlarged. The voltages V_c and V_a in the coax and in the aperture, respectively, are related by Maxwell's equations to the magnetic flux

enclosed by the line integral of the electric field yielding these voltages, that is,

$$V_a - V_c = -\frac{\partial}{\partial t} \iint \bar{B} \cdot d\bar{S} \tag{31}$$

for a perfectly conducting wire. The integration is over the surface defined by the loop boundary just described. The right-hand side of equation (31) is the inductive reactance of the loop, $i\omega_o L_l$ times the total current I flowing in the wires and spreading through the radial guide plates. Equation (29) can thus be rewritten after dividing by I

$$-\frac{V_c}{I} = -\frac{V_a}{I} + i\omega_o L_l \tag{32}$$

$\frac{-V_c}{I}$ is immediately recognized as the input impedance Z_{in} being sought. The ratio $\frac{-V_a}{I}$ has the dimensions of an impedance and is <u>defined</u> as the antenna aperture impedance. It will be shown that the aperture impedance is not in general directly measurable, but in some cases it can be calculated from a knowledge of the fields in the aperture. The quantity $i\omega_o L_l$ can be considered to be solely due to the reactance of the loop.

Equation (32) may now be expressed as follows*

$$Z_{in} = \left(Z_a + Z_{af}\right) + \left(Z_{fa} + Z_f\right) \tag{33}$$

where the first term in parenthesis is equal to $\frac{-V_a}{I}$ and the second to $i\omega_o L_l$. Each parenthesis consists of two parts, the self-impedances Z_a, Z_f, and the mutual $Z_{af} = Z_{fa}$. (The f and a subscript denote, respectively, feed and aperture impedances.) The two impedances, aperture and

*Dr. George I. Cohn made the analysis described by equations (33) to (38).

feed, can sometimes be calculated and/or measured independently of each other if the interaction caused by the mutual impedances is negligible. This is the case if the fields can be divided on a spatial basis into subvolumes such that the fields in any one subvolume can be attributed only to sources not producing fields in any other subvolume. Thus, if

$$|Z_{af}| \ll |Z_a| \tag{34a}$$

or

$$|Z_{af}| \ll |Z_f| \tag{34b}$$

then $Z_a = \frac{-V_a}{I}$ is directly calculable from the fields in the gap which are obtained by solving the electromagnetic boundary value problem. Z_f is the wire inductive reactance in the absence of the gap.

The flux common to two subvolumes is always less than the self-linking flux; therefore,

$$|Z_{af}| \leq |Z_a| \tag{35a}$$

or

$$|Z_{af}| \leq |Z_f|$$

One way to insure separability of impedances as given by equation (33) is to demand

$$|Z_a| \ll |Z_f| \tag{36a}$$

or

$$|Z_f| \ll |Z_a| \tag{36b}$$

that is, either the wire inductive reactance is much smaller than the aperture impedance or vice versa. It will be shown that the feed wire inductive reactance can be made to fulfill the inequality equation (36b) for the gap antenna in question and vanishes as the gap goes to zero. The feed

impedance Z_f and the aperture impedance Z_a (in the absence of coupling between them) will now be calculated, keeping in mind that as long as equation (36b) is satisfied, the antenna input impedance Z_{in} is the sum of these two contributions.

An upper bound on the feed wire inductive reactance is established by calculating the inductance of a coaxial line of length d with inner and outer radii r_1 and r_2. Using the geometrical approximation, it is easily shown that

$$Z_f = 377 \frac{d}{\lambda_o} \ln \frac{r_2}{r_1} \Omega \tag{37}$$

If $\frac{d}{\lambda_o} \sim \frac{1}{30}$ and $\frac{r_2}{r_1} \sim 10$.

$$|Z_f| \sim 30\Omega \tag{38}$$

Since the antenna is to have an input impedance of 50Ω resistive in order to match the coax characteristic impedance, equation (36) is not fulfilled and the input impedance is not separable into feed and aperture. Changing the outer to inner coax radii ratio in equation (37) is not as effective as reducing the gap width since the logarithm varies slowly with the ratio in question. However, if the gap width is reduced by 1/2 or 1/3 corresponding to d/λ_o of the order of 1/60 to 1/100, equation (36) is fulfilled and the impedance is separable.

The solution of the electromagnetic fields subject to the boundary conditions yields the aperture admittance, $Y_m = \frac{I}{-V_m}$ for each peripheral mode m, where $V_m = E_{zm} d$, is the voltage across the gap for the mth mode as shown in figure 22. The total aperture impedance is in turn related to Y_m by

$$Z_a = \sum_m \frac{1}{Y_m} = \sum_m \frac{1}{G_m + i\left(B_m^i + B_m^e\right)} \tag{39}$$

where B_m^i is the susceptance presented at the feed by the interior region, and G_m and B_m^e is the admittance contributed by the exterior region. For a narrow gap, with uniform feed current, the resultant modal admittance Y_m normalized with respect to the wave impedance in the exterior space Y_o $\left((120\Omega)^{-1}\right.$ for free space$\left.\right)$ has been found to be

$$Y_m = G_m + i\left(B_m^e + B_m^i\right)$$

$$G_m = \frac{1}{\pi}\left\{\int_0^1 \frac{\sin^2 \frac{\pi d_o x}{2}}{\left|H_m^{(2)}\left(a_o\sqrt{1-x^2}\right)\right|^2} \frac{dx}{1-x^2} + \left(\frac{\pi}{a_o}\right)^2 \int_0^1 \frac{\sin^2 \frac{\pi d_o x}{2}}{\left|H_m^{(2)'}\left(a_o\sqrt{1-x^2}\right)\right|^2} \frac{x^2}{(1-x^2)^{3/2}}\, dx\right\}$$

$$B_m^e = 12a_o\left\{\int_0^1 \frac{J_m\left(a_o\sqrt{1-x^2}\right)J_m'\left(a_o\sqrt{1-x^2}\right) + Y_m\left(a_o\sqrt{1-x^2}\right)Y_m'\left(a_o\sqrt{1-x^2}\right)}{\left|H_m^{(2)}\left(a_o\sqrt{1-x^2}\right)\right|^2} \sin^2 \frac{\pi d_o}{2} \frac{dx}{\sqrt{1-x^2}} - \int_1^\infty \frac{K_m'\left(a_o\sqrt{x^2-1}\right)}{K_m\left(a_o\sqrt{x^2-1}\right)} \sin^2 \frac{\pi d_o}{2} \frac{dx}{\sqrt{x^2-1}}\right.$$
$$\left. - \left(\frac{\pi}{a_o}\right)^2\left[\int_0^1 \frac{J_m\left(a_o\sqrt{1-x^2}\right)J_m\left(a_o\sqrt{1-x^2}\right) + Y_m\left(a_o\sqrt{1-x^2}\right)Y_m'\left(a_o\sqrt{1-x^2}\right)}{\left|H_m^{(2)'}\left(a_o\sqrt{1-x^2}\right)\right|^2} \sin^2 \frac{\pi d_o}{2} \frac{x^2 dx}{(1-x^2)^{3/2}} - \int_1^\infty \frac{K_m\left(a_o\sqrt{x^2-1}\right)}{K_m'\left(a_o\sqrt{x^2-1}\right)} \sin^2 \frac{\pi d_o}{2} \frac{x^2 dx}{(x^2-1)^{3/2}}\right]\right\}$$

$$\chi_m^i = -i\frac{2\pi a_o}{d_o} \frac{\left[J_m'(a_o)Y_m(r_o) - J_m(r_o)Y_m'(a_o)\right]}{\left[J_m(a_o)Y_m(r_o) - J_m(r_o)Y_m(a_o)\right]} \qquad \sin c\, \frac{\pi d_o}{2} = \frac{\sin\left(\frac{\pi d_o}{2}\right)}{\left(\frac{\pi d_o}{2}\right)}$$

(40)

x, a_o, d_o, r_o being respectively normalized: wave number k/k_o, cylinder radius $k_o a$, gap width $k_o d$, spacer radius $k_o \rho_o$. Y_m was derived by calculating the fields in both regions, matching them at the boundaries between antenna and exterior region taking into account the discontinuity in current.

For each mode m, there exists a current sheath J_{zm} around the gap periphery which is independent of z (fig. 22). The electric field across the gap resulting from this current density is also independent of z at the interface. It follows that the locally induced magnetic field at the interface does not vary along the gap width. Pursuing this reasoning

reasoning further, only a z-dependent H_ϕ could produce an E_ρ component and this one in turn would produce an H_z. One therefore concludes that, in the absence of z-dependent field components, no H_z component is generated at the gap interface.

EVALUATION OF APERTURE IMPEDANCE Z_a

Equation (40) for g_m, b_m^e, and b_m^i was used to calculate the various modal impedances for a frequency scaled up model of the cylindrical gap antenna under study. The model shown in figures 19 and 20 was designed to operate around 1090 mc with the following parameters:

Gap width, $d = \frac{7}{32}$ inch, $d_o = 0.156$

Spacer radius, $\rho_o = 1$ inch

Gap radius, $a = 3$ inches, $a_o = 2.13$

Operating wavelength, $\lambda_o = 8.81$ inches

Graphs showing pertinent calculations of g_o, b_o^e, and b_1^m are shown in figures 23, 24, and 25. The calculated normalized conductance and susceptance for the above parameters as well as the unnormalized corresponding impedances are shown in table II for mode numbers ranging from $m = 0$ to $m = 9$. The important feature of these results is the fact that for an antenna circumference approximately two wavelengths, the first order mode ($m = 1$) contributes most significantly to the impedance. The modes below ($m = 0$) have a reactance that tends to cancel the reactance of the modes above it ($m \geq 2$). In essence, for each value of a_o the antenna is a resonant structure, with one contributing mode. (For $a_o \sim 1$ it can be shown that Z_o is the resonant impedance.) The resonant mode determines both the impedance as well as the radiation characteristics. For the

specific choice of parameters above $a_o = 2.13$, the measured radiation pattern shown in figure 26 exhibits the two lobes that one would expect from the $m = 1$ cosinusoidal aperture distribution of figure 22. Therefore, the size of the antenna establishes only one specific mode as the contributing one and this mode in turn determines uniquely both the input impedance and the radiation fields.

APERTURE IMPEDANCE IN THE PRESENCE OF A NONHOMOGENEOUS PLASMA

The plasma model under consideration is represented by a radially varying dielectric uniform, in the ϕ- and z-direction.

The approach followed is the one developed by C. T. Swift[8]. The plasma is subdivided in n-concentric cylindrical sheaths. Each sheath is taken to have a uniform plasma and collision frequency equal to its average through the sheath.

The fields in the radial waveguide are matched at the interface to those in the first sheath. The field transforms in each sheath are no longer forward traveling waves expressed in terms of Hankel functions. They are standing waves consisting of the linear superposition of Hankel and Bessel functions. The fields in Region I and the first sheath of Region II are

Region I

$$\left.\begin{aligned} E_{zm}{}^{I} &= \frac{V_m}{d} \\ H_{\phi m}{}^{I} &= -iY_o \frac{V_m}{d} \frac{F_m{}'(k_o\rho)}{F_m(k_o\rho)} \\ H_{\rho m}{}^{I} &= -iY_o \frac{m}{k\rho} \frac{V_m}{d} \end{aligned}\right\} \qquad (41)$$

Region II (1st layer)

$$\left.\begin{aligned}
\bar{E}_{zm}^{II1} &= u_1^2 \bar{\mathcal{J}}_m^1 \\
\bar{H}_{\phi m}^{II1} &= -iY_{o1}k_{o1}u_1\bar{\mathcal{J}}_m^{1\prime} - \frac{km}{\rho}\bar{\mathcal{S}}_m^1 \\
\bar{H}_{\rho m}^{II1} &= -Y_{o1}k_{o1}\frac{m}{\rho}\bar{\mathcal{J}}_m^1 + iku_1\bar{\mathcal{S}}_m^1
\end{aligned}\right\} \qquad (42)$$

$$\left.\begin{aligned}
\bar{H}_{zm}^{II1} &= u_1^2\bar{\mathcal{J}}_m^1 \\
\bar{E}_{\phi m}^{II1} &= -\frac{km}{\rho}\bar{\mathcal{J}}_m^1 + iZ_{o1}k_{o1}u_1\bar{\mathcal{S}}_m^{1\prime} \\
\bar{E}_{\rho m}^{II1} &= iku_1\bar{\mathcal{J}}_m^{1\prime} + Z_{o1}k_{o1}\frac{m}{\rho}\bar{\mathcal{S}}_m^1
\end{aligned}\right\} \qquad (43)$$

The foregoing expressions for Region I were obtained after making the substitution

$$u_o^2 = k_o^2$$

$$u_o^2 a_{mo}F_{mo}(u_o\rho) = \frac{V_m}{d}$$

In Region II, forward traveling waves are replaced by the standing waves, i.e.,

$$\left.\begin{aligned}
c_m(k)H_m^{(2)}(u\rho) \to \bar{\mathcal{J}}_m^1(k_1u\rho) &= a_m^1(k)J_m(u_1\rho) + A_m^1(k)H_m^{(2)}(u_1\rho) \\
d_m(k)H_m^{(2)}(u\rho) \to \bar{\mathcal{S}}_m^1(k_1u\rho) &= b_m^1(k)J_m(u_1\rho) + B_m^1(k)H_m^{(2)}(u_1\rho)
\end{aligned}\right\} \qquad (44)$$

$\bar{\mathcal{J}}_m^{1\prime}$ and $\bar{\mathcal{S}}_m^{1\prime}$ are derivatives with respect to the argument $(u_1\rho)$.

The modal aperture admittance Y_m is now expressed in terms of these unknown coefficients by demanding that

$$H_{\phi m}^{III} - H_{\phi m}^{I} = \frac{I}{2\pi a} \qquad 0 \leq z \leq d \qquad (45)$$

Using the expressions (41) and (42), it follows that

$$-iY_o k_{o1} \int_{-\infty}^{\infty} a_m^1 J_m'(u_1 a) + A_m^1 H_m^{(2)'}(u_1 a) u_1 e^{ikz} dk - \frac{m}{a} \int_{-\infty}^{\infty} b_m^1 J_m(u_1 a)$$

$$+ B_m^1 H_m^{(2)}(u_1 a) e^{ikz} k\, dk + iY_o \frac{F_m'(k_o a)}{F_m(k_o a)} \frac{V_m}{d} = \frac{I}{2\pi a} \qquad 0 \leq z \leq d \qquad (46)$$

In order to eliminate the dependence on z, both sides of equation (46) are integrated from 0 to d. And, use of the relation

$$\frac{1}{d} \int_0^d e^{ikz} dk = C_o(k)$$

results in

$$-iY_o k_{o1} \int_{-\infty}^{\infty} \left[a_m^1 J_m^1(u_1 a) + A_m^1 H_m^{(2)'}(u_1 a) \right] u_1 C_o(k) dk - \frac{m}{a} \int_{-\infty}^{\infty} \left[b_m^1 J_m(u_1 a) \right.$$

$$\left. + B_m^1 H_m^{(2)}(u_1 a) \right] k C_o(k) dk + iY_o \frac{F_m'(k_o a)}{F_m(k_o a)} \frac{V_m}{d} = \frac{I}{2\pi a} \qquad (47)$$

In order to find Y_m the four coefficients a_m^1, A_m^1, b_m^1, and B_m^1 must be expressed in terms of V_m. This is done as follows.

As shown by Swift* a Transfer Function can be developed which relates via a 4×4 matrix the unknown coefficients, a_m^1, A_m^1, b_m^1, and B_m^1 in the first sheath to the free-space coefficients c_m, d_m beyond the last sheath. The transfer function depends only on the values of $J_m(u_1\rho_1)$ and $H_m(u_1\rho_1)$ at each sheath and the corresponding plasma parameters. The matrix coefficients are labeled C_{jk}. Their values are given in the cited reference. The following relation holds among these coefficients

$$\begin{bmatrix} a_m^1 \\ A_m^1 \\ b_m^1 \\ B_m^1 \end{bmatrix} = \begin{bmatrix} C_{11} & C_{12} & C_{13} & C_{14} \\ C_{21} & C_{22} & C_{23} & C_{24} \\ C_{31} & C_{32} & C_{33} & C_{34} \\ C_{41} & C_{42} & C_{43} & C_{44} \end{bmatrix} \begin{bmatrix} 0 \\ c_m \\ 0 \\ d_m \end{bmatrix} \tag{48}$$

The preceding equations reduce the number of unknowns from 4 to 2. Application of the two tangential boundary conditions at the antenna surface, i.e.,

$$\left.\begin{aligned} \bar{E}_{zm} &= \frac{V_m}{2\pi} C_o^*(k) \\ \bar{E}_{\phi m} &= 0 \end{aligned}\right\} \tag{49}$$

---

*The field expressions are different from Swift because the factor $\frac{1}{i\omega\mu_o\epsilon_1}$ is absorbed in the coefficients $a_m^1(k)$, $A_m^1(k)$, $b_m^1(k)$, and $B_m^1(k)$. Furthermore, the fields are constructed from $e^{im\phi}e^{ikz}$ while Swift uses negative exponents. The above expressions can be converted to Swift's by dividing all field transforms by $\omega\mu_o\epsilon_1$ and changing m and k into -m and -k.

allows the unknown coefficient c_m and d_m and, consequently, a_m^1, A_m^1, b_m^1, and B_m^1 to be expressed in terms of V_m. The derivation now follows.

Equation (48) can be written as

$$\left.\begin{aligned} a_m^1 &= C_{12}c_m + C_{14}d_m \\ A_m^1 &= C_{22}c_m + C_{24}d_m \\ b_m^1 &= C_{32}c_m + C_{34}d_m \\ B_m^1 &= C_{42}c_m + C_{44}d_m \end{aligned}\right\} \tag{50}$$

Therefore, from equations (47), (49), and (43), after using equation (50), it follows that

$$\left.\begin{aligned} &\left\{C_{12}J_n + C_{22}H_n^{(2)}\right\} c_n + \left\{C_{14}J_n + C_{24}H_n^{(2)}\right\} d_n = \frac{V_n}{2\pi a_1^2}\, c_0^*(k) \\ &\left\{C_{32}J_n' + C_{42}H_n^{(2)} + i\pi_{01}\frac{n}{\eta_1^2}\frac{k}{k_{01}}\left[C_{12}J_n + C_{22}H_n^{(2)}\right]\right\} c_n + \left\{C_{34}J_n' + C_{44}H_n^{(2)\prime} + i\pi_{01}\frac{n}{\eta_1^2}\frac{k}{k_{01}}\left[C_{14}J_n + C_{24}H_n^{(2)}\right]\right\} d_n = 0 \end{aligned}\right\} \tag{51}$$

Solving for c_m and d_m in terms of V_m and expressing a_m^1, A_m^1, b_m^1, and B_m^1 in terms of V_m via equation (49) and substituting into equation (41) results in the following expression for the modal antenna aperture admittance covered with plasma.

$$\frac{Y_n}{i\pi_{01}} = \epsilon_{01}\int_{-\infty}^{\infty}\left[(C_{12}C_{34} - C_{14}C_{32})(J_n')^2 + (C_{22}C_{44} - C_{24}C_{42})\left(H_n^{(2)\prime}\right)^2 + (C_{12}C_{44} - C_{14}C_{42} + C_{22}C_{34} - C_{24}C_{32})J_n'H_n^{(2)\prime}\right]\frac{\zeta_0}{\Delta}\frac{k_0}{\eta_1}\,d\xi$$

$$-\frac{\epsilon_{01}^2}{k_{01}^2}\int_{-\infty}^{\infty}\left[(C_{12}C_{34} - C_{14}C_{32})(J_n)^2 + (C_{22}C_{44} - C_{24}C_{42})\left(H_n^{(2)}\right)^2 + (C_{12}C_{44} - C_{14}C_{42} + C_{22}C_{34} - C_{24}C_{32})J_nH_n^{(2)}\right]\frac{\zeta_0}{\Delta}\frac{k^2}{\eta_1^2}\frac{k_0}{\eta_1} - \frac{2n^2}{\pi}\frac{Y_n'}{r_0} \tag{52}$$

where Δ the determinant of the 4×4 matrix in equation (51) is given by:

$$\Delta = \left(C_{12}C_{34} - C_{14}C_{32}\right)J_m J_m' + \left(C_{12}C_{44} - C_{14}C_{42}\right)J_m H_m^{(2)\prime}$$

$$+ \left(C_{22}C_{34} - C_{24}C_{32}\right)J_m' H_m^{(2)} + \left(C_{22}C_{44} - C_{24}C_{42}\right)H_m^{(2)} H_m^{(2)\prime} \quad (53)$$

It is understood that the arguments of the cylindrical functions are $u_1 a = \sqrt{\left(k_{01}^2 - k^2\right)}a$. The quantity k_{01} is the wave number in the first plasma sheath adjacent to the antenna.

As a partial check on the validity of expression (52), the plasma is removed, in which case

$$C_{12} = C_{14} = C_{24} = C_{32} = C_{34} = C_{42} = 0$$

$$C_{22} = C_{44} = 1$$

$$k_{01} = k_0$$

$$u_1 = u$$

The admittance now reduces to

$$\frac{Y_m}{iY_{01}} = \left\{ k_0 a \int_{-\infty}^{\infty} \frac{H_m^{(2)\prime}}{H_m^{(2)}} C_0^* C_0 \, dk - \frac{m^2}{k_0 a} \int_{-\infty}^{\infty} \frac{H_m^{(2)}}{H_m^{(2)\prime}} C_0^* C_0 \frac{dk}{u} - \frac{2\pi a}{d} \frac{F_m'(k_0 a)}{F_m(k_0 a)} \right\} \quad (54)$$

where $C_0^* C_0 = \sin c^2 \frac{\pi d}{2}$.

Equation (54) is equivalent to equation (40) prior to breaking it into real and imaginary parts.

CONCLUDING REMARKS

This investigation of slotted cylinders has led to the following conclusions:

(1) For the case of resonant coating $(\omega = \omega_p, \quad \nu = 0)$, the admittance approaches zero as the thickness of the coating increases. At intermediate thicknesses, the susceptance can change from a large capacitative to a small inductive value or to zero.

(2) For all practical purposes, the admittance of identical slots on cylinders and ground planes is equivalent if the circumference-to-wavelength ratio of the cylinder is greater than four and if the loss angle of the plasma lies between 90° and 180°, and the magnitude of $N \gtrsim 1$.

(3) For the reentry plasma distribution shown in figure 7, the admittance undergoes pronounced changes when the propagating frequency approaches the peak plasma frequency.

(4) The admittance of apertures on large coated cylinders ($C \gtrsim 20$) seems to be sensitive to slight changes in the electrical and mechanical tolerances of the coating. As such, one is led to conclude that theoretical results will be difficult to realize experimentally unless electrically small cylinders are used ($C \lesssim 10$).

(5) The resonant properties of the cylindrical gap antenna indicate that it may be useful for plasma diagnostics. The presence of plasma or any change of antenna parameters brings one azimuthal mode into prominence which determines both the shape of the radiation pattern and the value of the antenna input impedance. As the plasma varies in density, it would be expected that various modes would be successively excited; therefore, one could expect the pattern and the input impedance to change accordingly.

APPENDIX I

LIST OF SYMBOLS USED IN THE ANALYSIS OF THE AXIAL SLOT

a	radius of conducting cylinder
a_m	$\dfrac{\sin\left(\frac{m\phi_o}{2}\right)}{\left(\frac{m\phi_o}{2}\right)}$
B	susceptance
b	radial distance to air-plasma interface
C	circumference of cylinder in wavelengths $= \frac{2\pi a}{\lambda_v}$
E	electric field
$\bar{E}, \tilde{\bar{E}}$	Fourier transforms of electric field
E_o	amplitude of electric field at aperture
$\vec{E_o}$	amplitude of incident TE_{ol} wave
G	conductance
H	magnetic field
$\bar{H}, \tilde{\bar{H}}$	Fourier transforms of the magnetic field
h	axial mode number
k	length of slot in wavelengths $= l/\lambda_v$
l	length of slot
m	azimuthal mode number
N	index of refraction
P	power
p	a/l
S	Poynting vector
u	radial mode number
V_o	applied potential on slot

$W = b/a$	
w	width of slot
Y	admittance
Y_o	admittance of free space
Y_{ol}	waveguide admittance of TE_{ol} mode
β	wave number
β_{ol}	wave number for the TE_{ol} wave guide mode
Γ	reflection coefficient
δ_{mn}	Kronecker delta $= \begin{cases} 0 & m \neq n \\ 1 & m = n \end{cases}$
ϵ	dielectric constant
ϵ_o	permittivity of free space
ϵ_r	real part of the dielectric constant
η, ξ	transverse components within a rectangular waveguide
λ	wavelength
λg_{ol}	guide wavelength
μ_o	permeability of free space
ν	electron collision frequency
ρ, ϕ, z	cylindrical coordinates
ϕ_o	angular width of slot
ω	exciting frequency
ω_p	plasma frequency
Subscripts:	
c	external
in	input
l	per unit length

R	plasma resonant
v	vacuum
η	vector component along narrow dimension of waveguide
ρ,ϕ,z	vector components along the three principal directions in cylindrical coordinates

APPENDIX II

ADMITTANCE EXPRESSIONS FOR LONG SLOTS ON CYLINDERS

The pertinent fields in regions I and II of the structure shown in figure 1 are:

$$H_z^{I}(\rho,\phi) = \sum_{m=-\infty}^{\infty} A_m\left[J_m(\beta\rho) + B_m H_m^{(2)}(\beta\rho)\right] e^{-jm\phi} \qquad \text{(II-1)}$$

$$H_z^{II}(\rho,\phi) = \sum_{m=-\infty}^{\infty} C_m H_m^{(2)}\left(\beta_v\rho\right) e^{-jm\phi} \qquad \text{(II-2)}$$

$$E_\phi^{I}(\rho,\phi) = \frac{j}{Y_o}\sqrt{\frac{\epsilon_o}{\epsilon}} \sum_{m=-\infty}^{\infty} A_m\left[J_m'(\beta\rho) + B_m H_m^{(2)'}(\beta\rho)\right] e^{-jm\phi} \qquad \text{(II-3)}$$

$$E_\phi^{II}(\rho,\phi) = \frac{j}{Y_o} \sum_{m=-\infty}^{\infty} C_m H_m^{(2)'}\left(\beta_v\rho\right) e^{-jm\phi} \qquad \text{(II-4)}$$

where the prime denotes differentiation of the Bessel and Hankel functions with respect to the argument.

If it is assumed that the aperture field is of the form:

$$E_\phi(a,\phi) = \frac{V_o}{a} = \sum_{m=-\infty}^{\infty} \bar{E}_{m\phi}(a) e^{-jm\phi} = \frac{V_o}{2\pi a} \sum_{m=-\infty}^{\infty} \frac{\sin\left(\frac{m\phi_o}{2}\right)}{\left(\frac{m\phi_o}{2}\right)} e^{-jm\phi} \qquad \text{(II-5)}$$

then the boundary conditions at $\rho = a$ and $\rho = b$ give the following algebraic relationships

$$\frac{V_o}{2\pi a} \frac{\sin\left(\frac{m\phi_o}{2}\right)}{\left(\frac{m\phi_o}{2}\right)} = \frac{j}{NY_o} A_m\left[J_m'(NC) + B_m H_m^{(2)'}(NC)\right] \qquad \text{(II-6)}$$

$$\frac{1}{N} A_m\left[J_m'(NCW) + B_m H_m^{(2)'}(NCW)\right] = C_m H_m^{(2)'}(CW) \qquad \text{(II-7)}$$

$$A_m\left[J_m(NCW) + B_m H_m^{(2)}(NCW)\right] = C_m H_m^{(2)}(CW) \qquad \text{(II-8)}$$

Solving the above equations for A_m and B_m gives:

$$A_m = -j\bar{E}_{m\phi} NY_o \frac{NH_m^{(2)}(NCW)H_m^{(2)'}(CW) - H_m^{(2)}(CW)H_m^{(2)'}(NCW)}{H_m^{(2)}(CW)T_m - NH_m^{(2)'}(CW)L_m} \qquad \text{(II-9)}$$

$$B_m = \frac{H_m^{(2)}(CW)J_m'(NCW) - NJ_m(NCW)H_m^{(2)'}(CW)}{NH_m^{(2)}(NCW)H_m^{(2)'}(CW) - H_m^{(2)}(CW)H_m^{(2)'}(NCW)} \qquad \text{(II-10)}$$

where

$$\left.\begin{aligned} T_m &= J_m'(NCW)H_m^{(2)'}(NC) - J'(NC)H_m^{(2)'}(NCW) \\ L_m &= J_m(NCW)H_m^{(2)'}(NC) - J_m'(NC)H_m^{(2)}(NCW) \end{aligned}\right\} \qquad \text{(II-11)}$$

Therefore:

$$\bar{H}_{mz} = A_m\left[J_m(NC) + B_m H_m^{(2)}(NC)\right]$$

$$= -j\bar{E}_{m\phi} NY_o \left\{\frac{NH_m^{(2)'}(CW)V_m - H_m^{(2)}(CW)U_m}{H_m^{(2)}(CW)T_m - NH_m^{(2)'}(CW)L_m}\right\} \qquad \text{(II-12)}$$

where

$$\left.\begin{aligned} U_m &= J_m(NC)H_m^{(2)'}(NCW) - J_m'(NCW)H_m^{(2)}(NC) \\ V_m &= J_m(NC)H_m^{(2)}(NCW) - J_m(NCW)H_m^{(2)}(NC) \end{aligned}\right\} \qquad \text{(II-13)}$$

From Parseval's theorem, the external admittance per unit length is given by

$$Y_{cl} = \frac{2P}{|V_o|^2} = 2\pi a \sum_{m=-\infty}^{\infty} \frac{\bar{E}_{m\phi} \bar{H}^*_{mz}}{|V_o|^2} \qquad \text{(II-14)}$$

And the substitution of equations (II-5) and (II-12) into equation (II-14) results in the following admittance expression

$$Y_{cl} = -\frac{j}{2\pi a} NY_o \sum_{m=-\infty}^{\infty} \frac{\sin^2\left(\frac{m\phi_o}{2}\right)}{\left(\frac{m\phi_o}{2}\right)^2} \left\{ \frac{NH_m^{(2)'}(CW)V_m - H_m^{(2)}(CW)U_m}{H_m^{(2)}(CW)T_m - NH_m^{(2)'}(CW)L_m} \right\} \qquad \text{(II-15)}$$

For the case of no coating ($m = 1$ or $b = a$), equation (II-15) becomes:

$$Y_{cl} = -\frac{jY_o}{2\pi a} \sum_{m=-\infty}^{\infty} \frac{\sin^2\left(\frac{m\phi_o}{2}\right)}{\left(\frac{m\phi_o}{2}\right)^2} \frac{H_m^{(2)}(C)}{H_m^{(2)'}(C)} \qquad \text{(II-16)}$$

It has been shown[1] that at plasma resonance, the fields, hence the admittance, are indepent of the azimuthal coordinate, ϕ. Therefore, only the $m = 0$ mode is supported, and equation (II-15) reduces to

$$Y_{cl} = -\frac{jY_o}{2\pi a} \lim_{N \to 0} N \left\{ \frac{NH_o^{(2)'}(CW)V_o - H_o^{(2)}(CW)U_o}{H_o^{(2)}(CW)T_o - NH_o^{(2)'}(CW)L_o} \right\} \qquad \text{(II-17)}$$

In order to evaluate the above equation, the following expansions are necessary:

$$\left.\begin{aligned} J_o(x) &\cong 1 - \frac{x^2}{4} & J_o'(x) &\cong -\frac{x}{2} \\ Y_o(x) &\cong \frac{2}{\pi} \log x & Y_o'(x) &\cong \frac{2}{\pi x} \end{aligned}\right\} \qquad \text{(II-18)}$$

to give

$$\left.\begin{aligned} T_o &\cong \frac{j}{\pi}\left[W - \frac{1}{W}\right] & U_o &\cong -j\,\frac{2}{\pi NCW} \\ L_o &\cong -j\,\frac{2}{\pi NC} & V_o &\cong -j\,\frac{2}{\pi}\log W \end{aligned}\right\} \qquad \text{(II-19)}$$

Therefore, for $N = 0$ and $W > 1$

$$Y_{CR} = -\frac{jY_o}{2\pi a}\,\frac{H_o^{(2)}(CW)}{\left[WH_o^{(2)\prime}(CW) + \frac{CW}{2}H_o^{(2)}(CW)\left(W - \frac{1}{W}\right)\right]} \qquad \text{(II-20)}$$

To analyze the inhomogeneous plasma, a method described by Swift[4] is used. Using Swift's notation, the axial magnetic field with the plasma expressed as follows:

$$H_z^I(r,\phi) = \sum_{m=-\infty}^{\infty}\left[\frac{G_{mz}(r)}{C_m}\right]C_m e^{-jm\phi} \qquad \text{(II-21)}$$

where the ratio $\frac{G_{mz}(r)}{C_m} = t_m(r) + ju_m(r)$ is numerically evaluated to give solutions of t_m and u_m at the surface of the conducting cylinder, $r = a$. The details of the technique are adequately described in the reference and will not be repeated here.

At $r = a$ the boundary condition at the aperture gives

$$\tilde{E}_{m\phi}(a,\phi) = \frac{V_o}{2\pi a}\,\frac{\sin\left(\frac{m\phi_o}{2}\right)}{\left(\frac{m\phi_o}{2}\right)} = -\frac{C_m\left[t_m'(a) + ju_m'(a)\right]}{jm\varepsilon(a)} \qquad \text{(II-22)}$$

which allows C_m, hence $H_z^I(a,\phi)$ to be computed. Therefore, use of Parseval's theorem gives the following admittance expression

$$Y = -\frac{jk_o}{2\pi a}\frac{\epsilon(a)}{\epsilon_c}\sum_{m=-\infty}^{\infty}\frac{\sin^2\left(\frac{m\phi_o}{2}\right)}{\left(\frac{m\phi_o}{2}\right)^2}\left[\frac{t_m(a) + ju_m(a)}{t_m'(a) + ju_m'(a)}\right] \qquad \text{(II-23)}$$

The prime in the above equation denotes differentiation with respect to r.

APPENDIX III

RELATIONSHIP BETWEEN INTERNAL AND EXTERNAL ADMITTANCE

Computation of the external admittance is only half the story since the external admittance as such is not a measurable quantity; when an experiment is performed, the input admittance is referred through a measurement of the reflection coefficient. This input admittance (or reflection coefficient) as seen in the feed structure must be related to the external admittance. To do this, however, flow conservation immediately inside and outside the slot is used.

The pertinent fields which exist in the waveguide, due to the waveguide opening onto the ground plane, are

$$E_\eta = \vec{E_o} e^{-j\beta_{o1}z} \cos\left(\frac{\pi\xi}{l}\right)\left[1 + \Gamma e^{j2\beta_{o1}z}\right] + (\text{h.t.})_E \qquad \text{(III-1a)}$$

$$H_\xi = -\vec{E_o} Y_{o1} e^{-j\beta_{o1}z} \cos\left(\frac{\pi\xi}{l}\right)\left[1 - \Gamma e^{j2\beta_{o1}z}\right] + (\text{h.t.})_H \qquad \text{(III-1b)}$$

Assuming that higher-order terms vanish, i.e., $(\text{h.t.})_E = (\text{h.t.})_H = 0$ the complex power flow expressed in terms of the fields inside the slot is

$$P_{c\eta} = \left|\vec{E_o}\right|^2 (1 + \Gamma^*)(1 - \Gamma) Y_{o1} \frac{wl}{4} \qquad \text{(III-2)}$$

But,

$$\vec{E_o} = \frac{V_o}{w} \frac{1}{1 + \Gamma} \qquad \text{(III-3)}$$

Therefore,

$$Y_c = \frac{2P}{|V_o|^2} = \frac{1}{w^2} \frac{(1 + \Gamma^*)(1 - \Gamma)}{|1 + \Gamma|^2} \frac{wl}{2} Y_{o1} = \frac{l}{2w}\left(\frac{1 - \Gamma}{1 + \Gamma}\right) Y_{o1} \qquad \text{(III-4)}$$

But, the input admittance is defined as

$$Y_{in} = -\frac{H_z}{E_\eta} = Y_{ol}\left(\frac{1 - \Gamma}{1 + \Gamma}\right) \qquad \text{(III-5)}$$

Therefore, the following relationship exists between the external and input admittance

$$Y_{in} = 2\left(\frac{w}{l}\right)Y_c \qquad \text{(III-6)}$$

or, in normalized form,

$$y_{in} = \frac{Y_{in}}{Y_{ol}} = g_{in} + jb_{in} = 2\left(\frac{w}{l}\right)\left(\frac{\lambda g_{ol}}{\lambda_w}\right)y_{cv} \qquad \text{(III-7)}$$

Therefore equation III-7 relates a calculated normalized external admittance $\left(y_{cv}\right)$ to the measurable normalized input admittance y_{in}.

REFERENCES

1. C. M. Knop and C. T. Swift, "A Note on the Radiation Conductance of an Axial Slot on a Cylinder," Radio Science, Journal of Research, NBS/USNC-URSI, vol. 69, No. 3, pp. 447-451, March 1965.

2. J. R. Wait, Electromagnetic Radiation From Cylindrical Structures, Pergamon Press, New York, New York, 1959.

3. R. F. Harrington, Time Harmonic Electromagnetic Fields, McGraw-Hill Book Company, New York, New York, 1961.

4. C. T. Swift, and C. M. Knop, "Equatorial Patterns of an Axially Slotted Cylinder Coated with a Critical Dense Plasma," IEEE, PTGAP, vol. AP-12 (Communications), pp. 498-502, July 1964.

5. C. T. Swift, "Radiation Patterns of a Slotted-Cylinder Antenna in the Presence of an Inhomogeneous Lossy Plasma," IEEE, PTGAP, vol. AP-12, no. 6, pp. 728-738, Nov. 1964.

6. J. R. Wait, "Radiation Characteristics of Axial Slots on a Conducting Cylinder," Wireless Engineer, vol. 32, no. 12, December 1955.

7. Y. Musiake and R. E. Webster, "Radiation Characteristics with Power Gain for Slots on a Sphere," IRE Transactions on Antenna and Propagation, vol. AP-5, no. 1, January 1957.

8. C. T. Swift, "Radiation from Slotted-Cylinder Antennas Coated with Concentric Layers of Dielectric Material," M. Sc. Thesis, Virginia Polytechnic Institute, April 1965.

TABLE I.- MEASUREMENTS OF INPUT ADMITTANCE FOR DIFFERENT DIELECTRIC SLEEVE POSITIONS

Sleeve position	Frequency, kmc	VSWR	D_c, cm	D_{sl}, cm	$\Delta = D_{sl} - D_c$, cm	$\frac{\Delta}{\lambda g}$	g_{in}	b_{in}
		With coating		With short				
A	10.60	1.92	14.41	14.51	0.10	0.028	1.78	0.44
B	10.60	1.77	14.43	14.51	.09	.025	1.58	.50
C	10.60	1.77	14.46	14.51	.05	.014	1.75	.20
D	10.60	1.38	14.50	14.51	.01	.003	1.60	.03
A	10.80	2.35	14.78	14.89	0.11	0.031	2.02	0.76
B	10.80	2.00	14.79	14.89	.10	.028	1.84	.50
C	10.80	1.68	14.86	14.89	.03	.009	1.68	.12
D	10.80	1.37	14.96	14.89	-.07	-.020	1.37	-.11
A	11.00	2.4	15.21	15.23	0.02	0.006	2.4	0.20
B	11.00	2.1	15.12	15.23	.11	.032	1.86	.61
C	11.00	1.60	15.16	15.23	.07	.020	1.57	.20
D	11.00	1.72	15.27	15.23	-.04	-.012	1.72	-.16
A	11.20	1.85	13.91	13.90	-0.01	+0.003	1.88	-0.03
B	11.20	1.86	13.86	13.90	+.64	+.012	1.85	+.20
C	11.20	1.65	13.91	13.90	-.01	-.003	1.67	-.03
D	11.20	1.40	13.98	13.90	-.08	-.024	1.37	-.13

Position of Dielectric Sleeve	A	B	C	D
Seam location, Degrees from Slot	180	270	0	90

TABLE II.- TABLES OF MODAL IMPEDANCE OF GAP ANTENNA

m	G_m^e	$b_m^e + b_m^i$	Z_m, ohms
0	8.23	27.1	3.9 - j12.7
1	7.06	-.66	53 + j5.1
2	4.02	48.8	.6 + j7.7
3	1.11	-107	j3.5
4	.149	-168	j2.3
5	.011	-229	j2.0
6		-292	j1.6
7		-355	j1.4
8		-420	j.9
9		-486	j.8

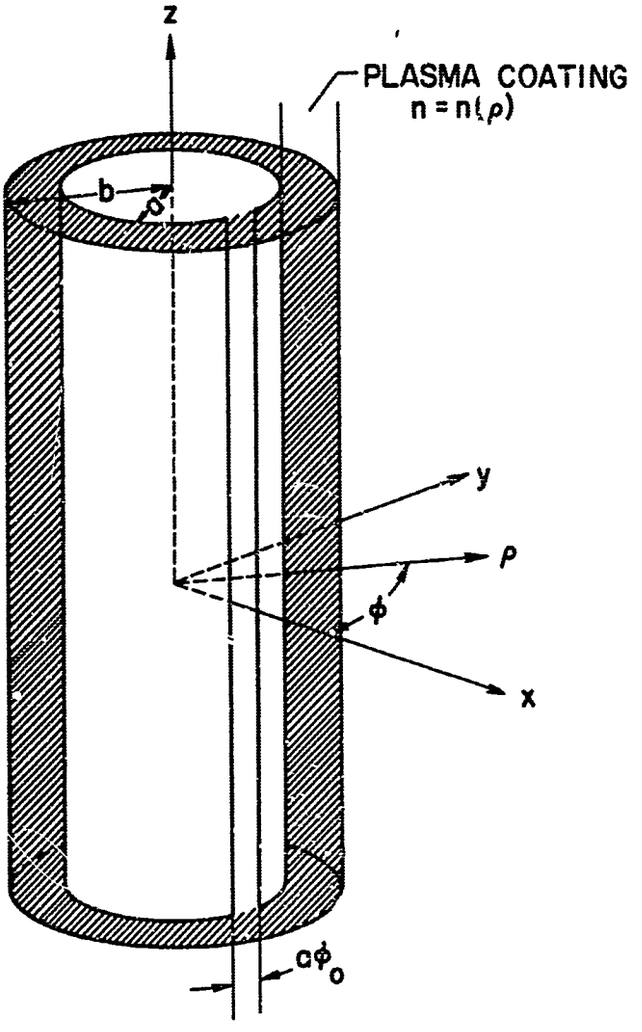

NASA

Figure 1.- Geometry of coated slotted cylinder.

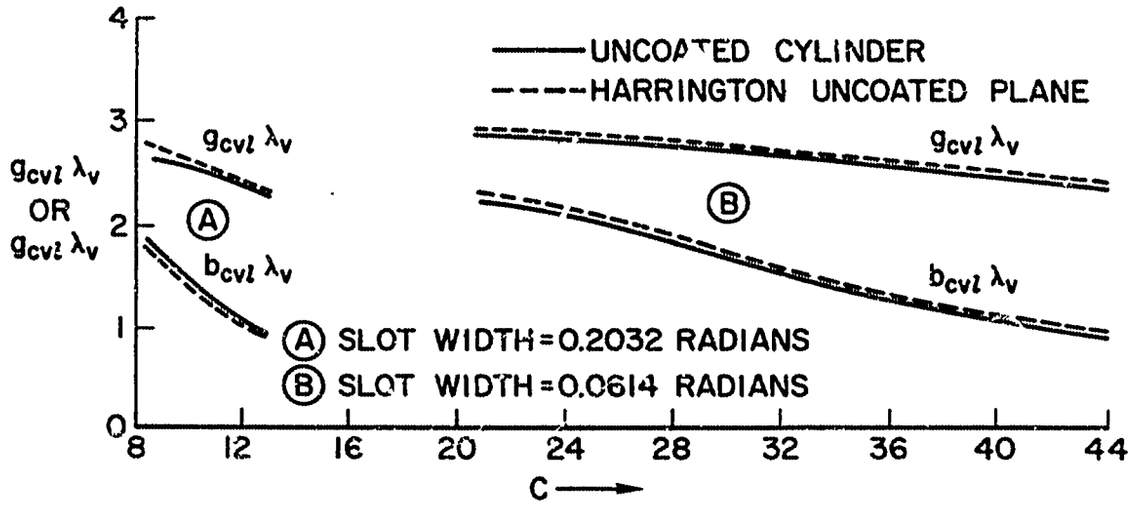

NASA

Figure 2.- Admittance of uncoated cylinder.

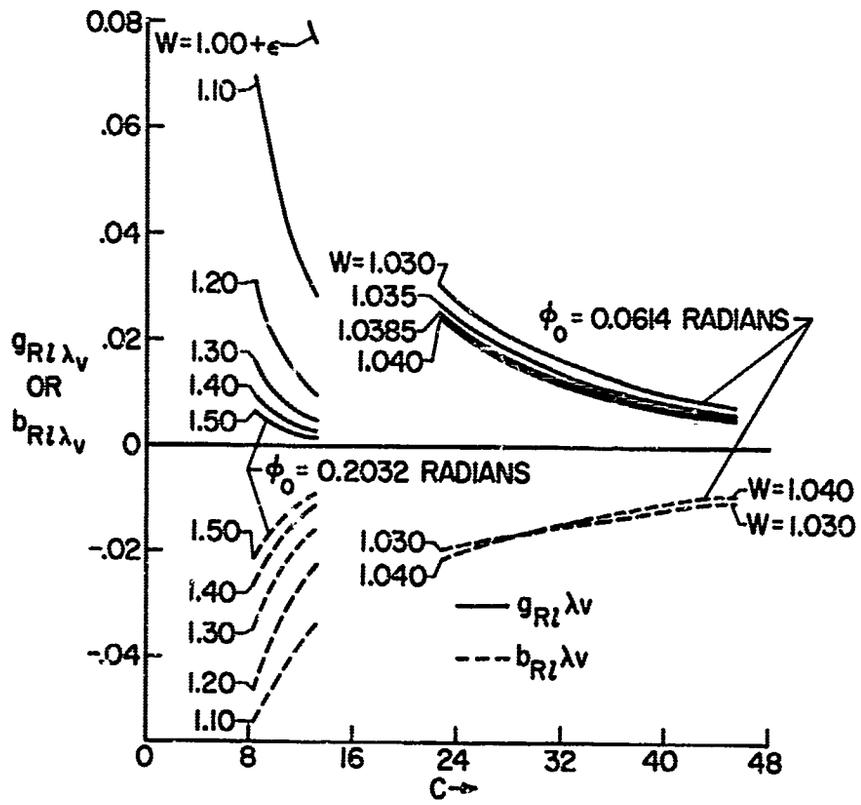

NASA

Figure 3.- Admittance at plasma resonance.

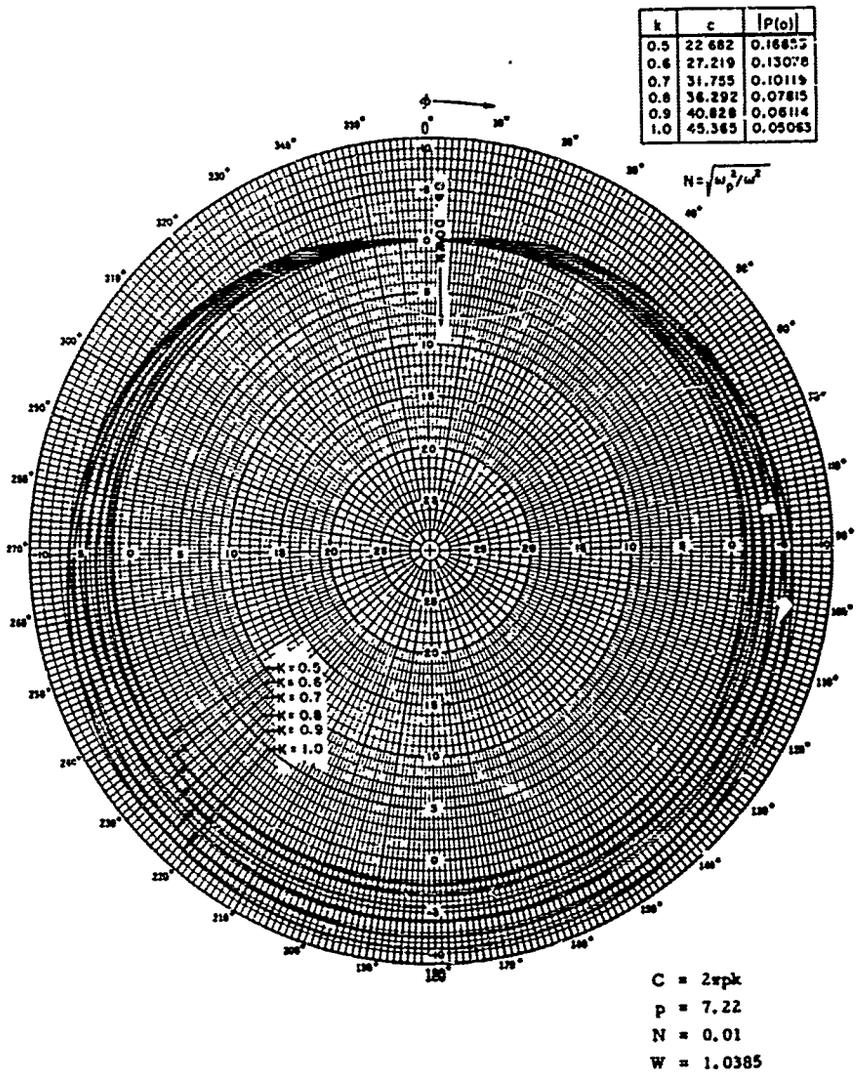

NASA

Figure 4.- Equatorial radiation patterns near plasma resonance.

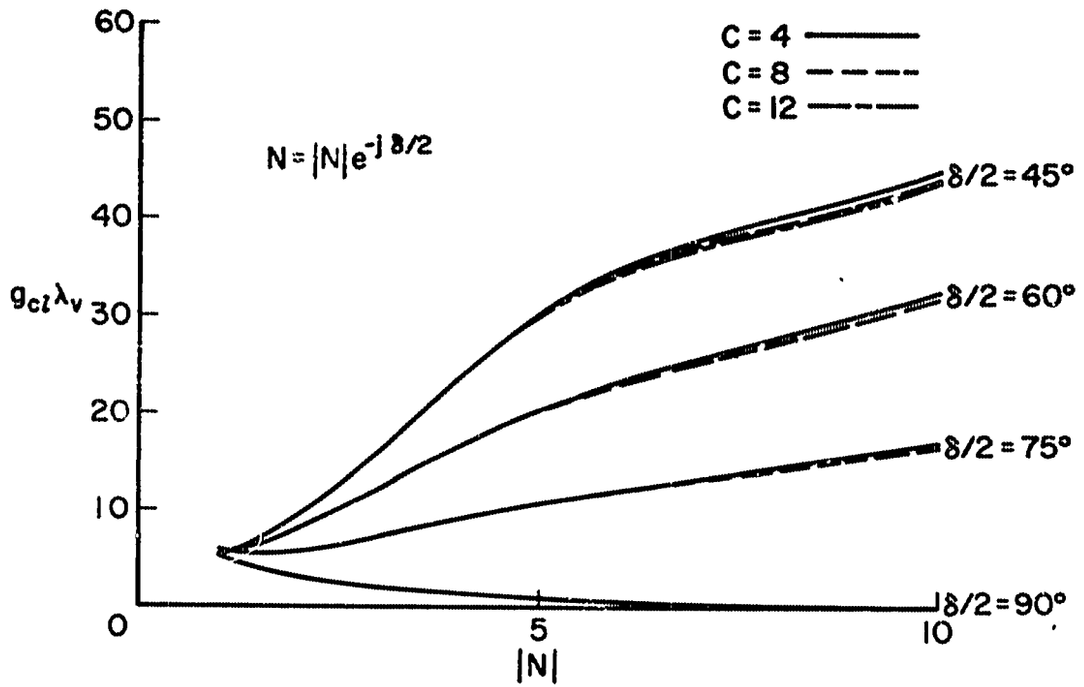

NASA

Figure 5.- Conductance with lossy coating.

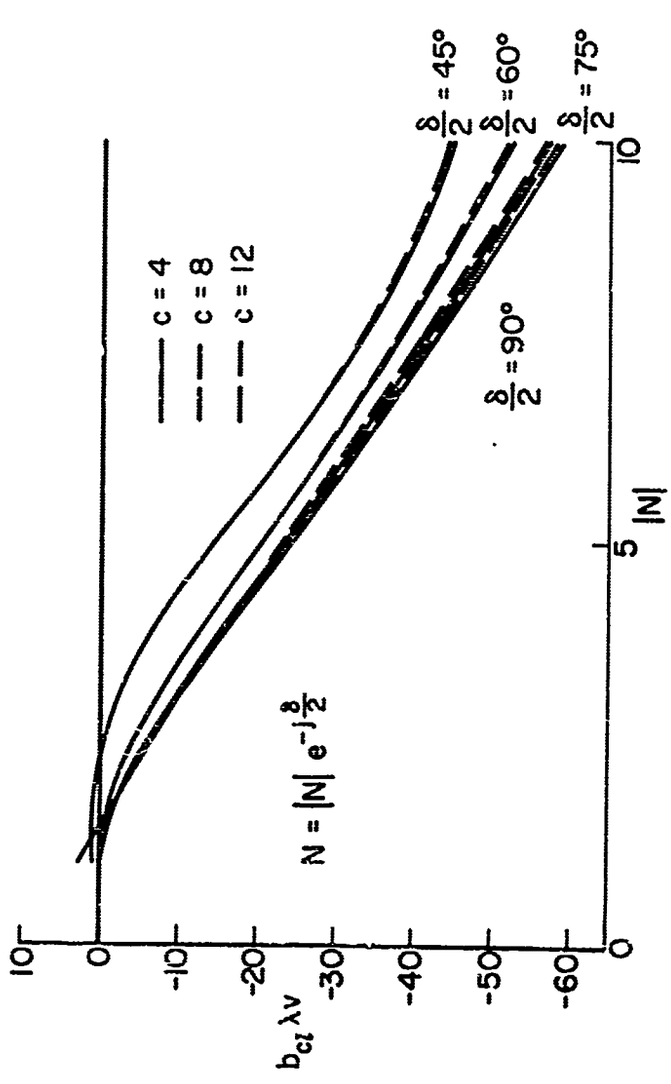

NASA

Figure 6.- Susceptance with lossy coating.

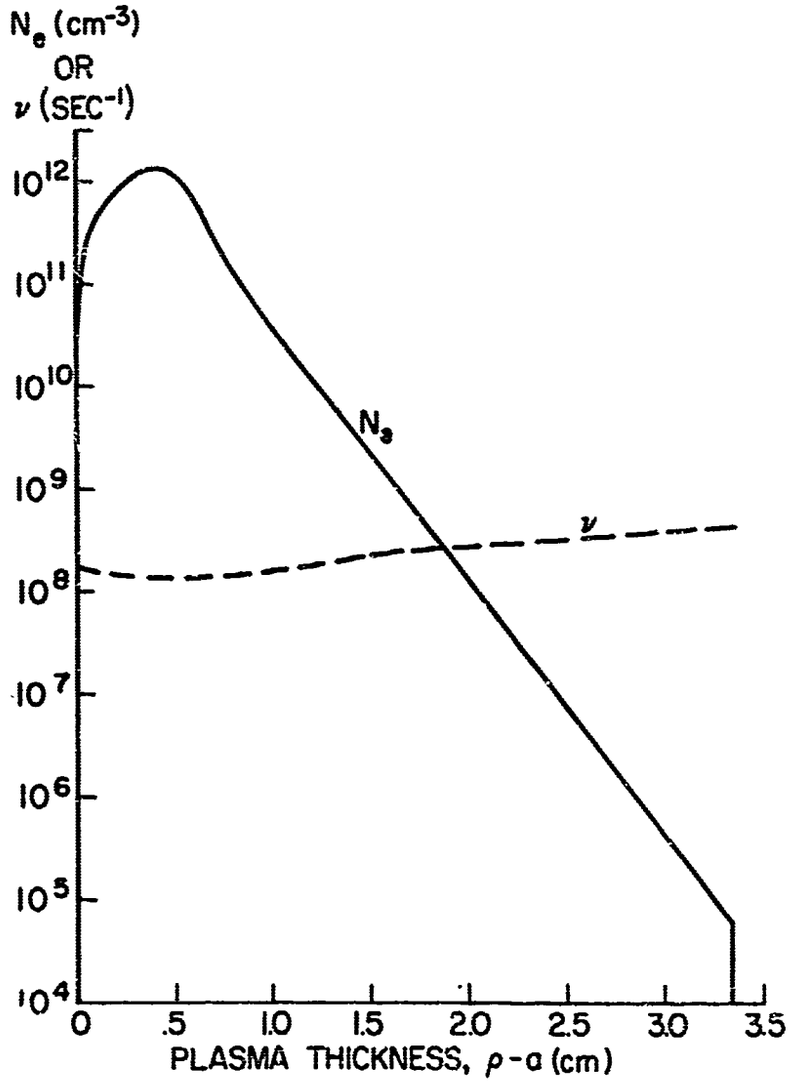

NASA

Figure 7.- Typical reentry plasma profile.

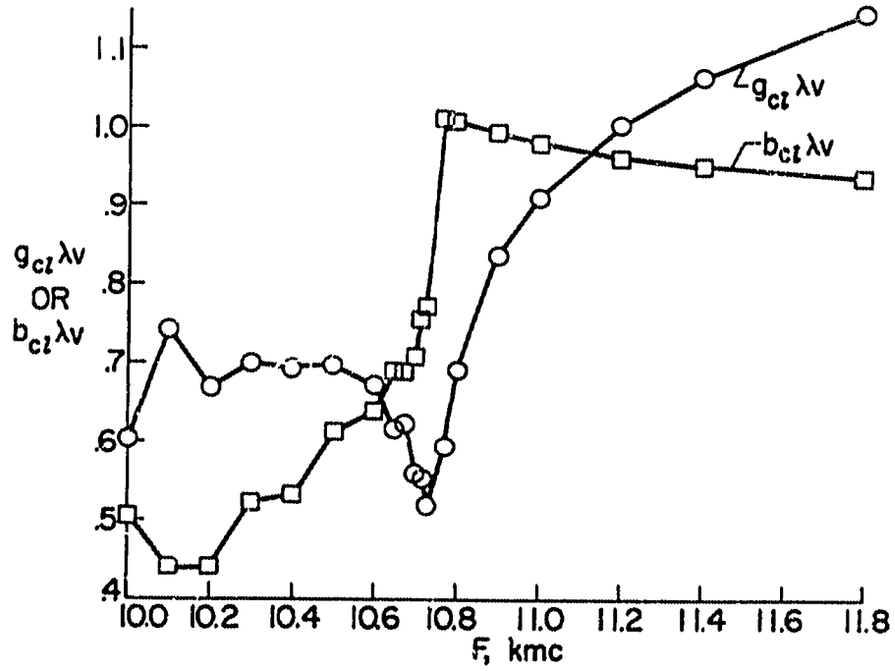

Figure 8.- Admittance of coated slots.

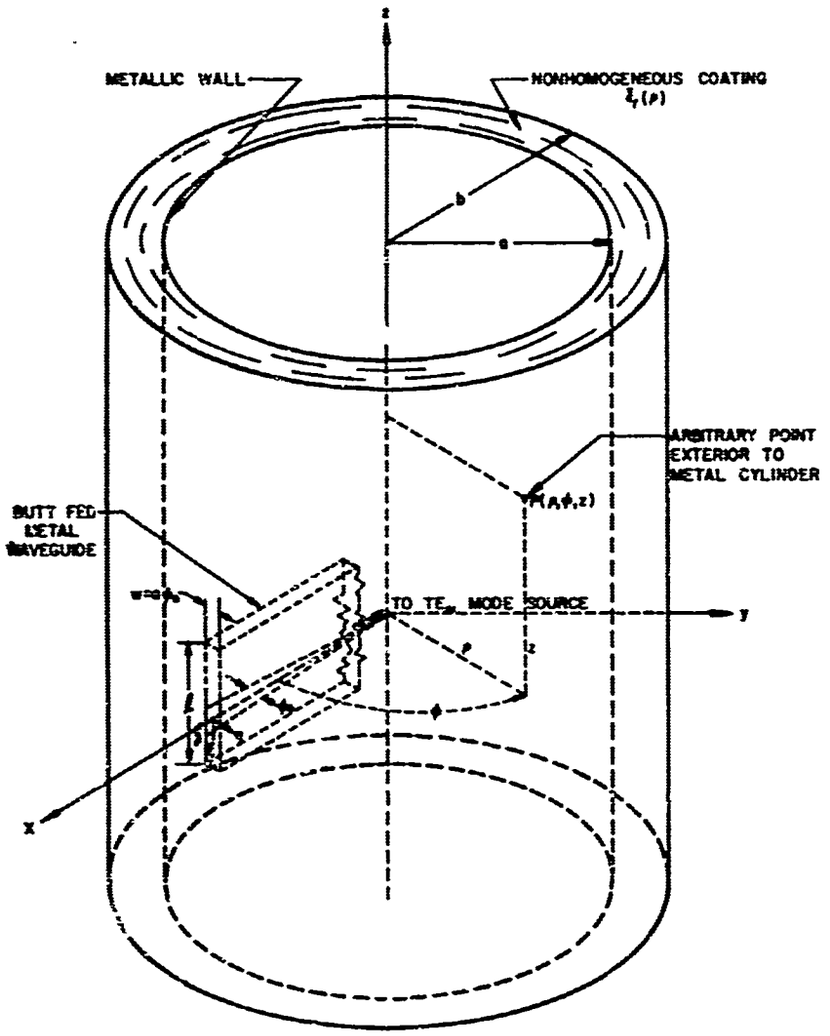

NASA

Figure 9.- Waveguide excited axial slot.

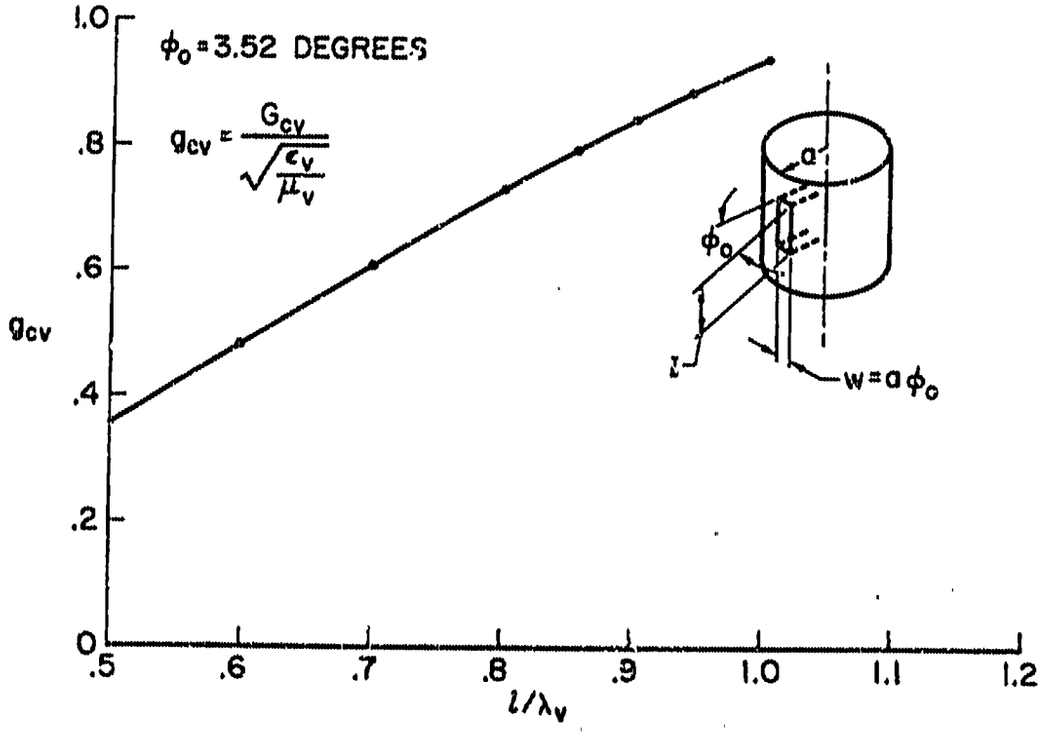

NASA

Figure 10.- External conductance of uncoated axial slot.

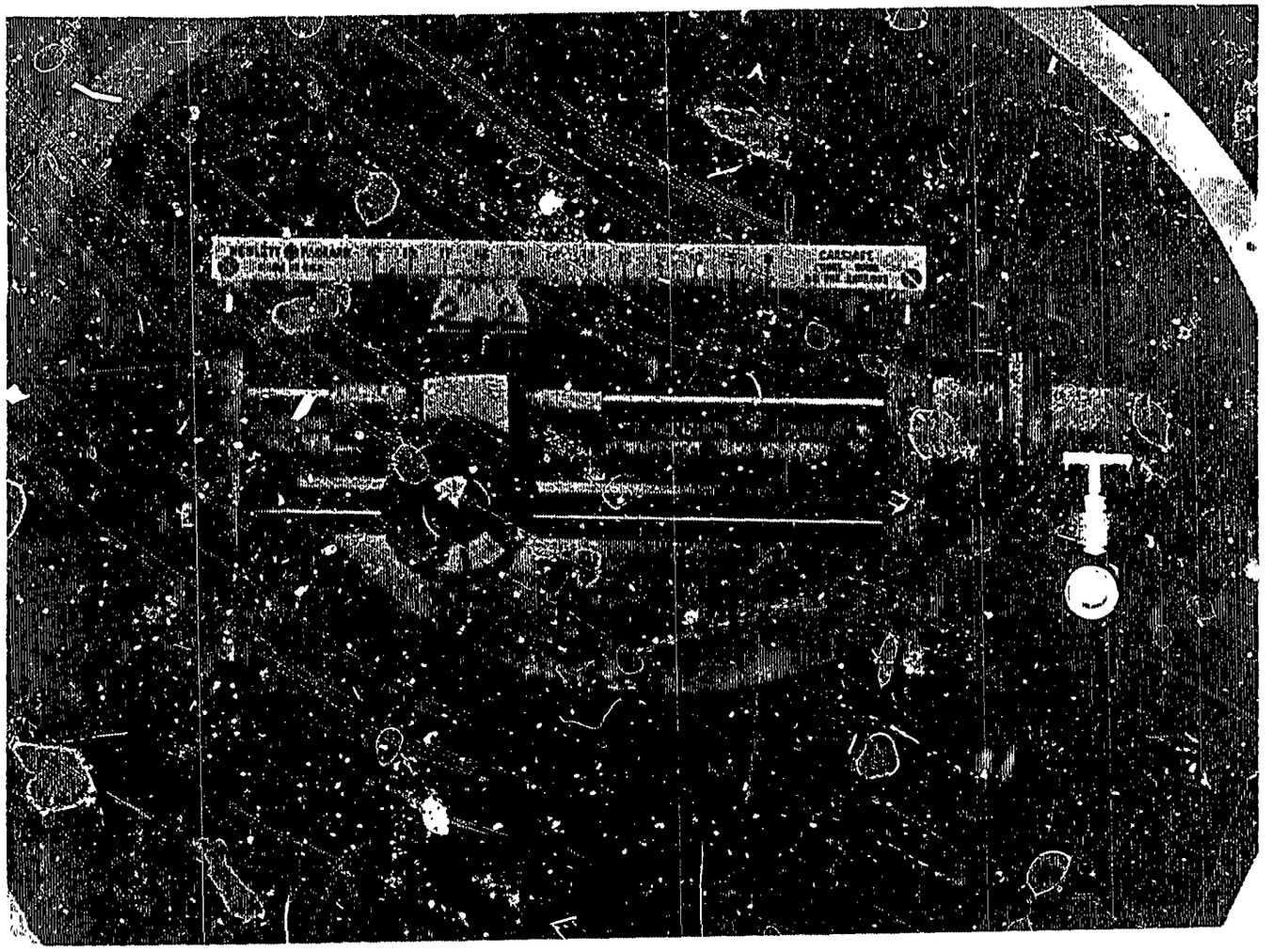

NASA

Figure 11.- Slotted line mounted inside cylinder.

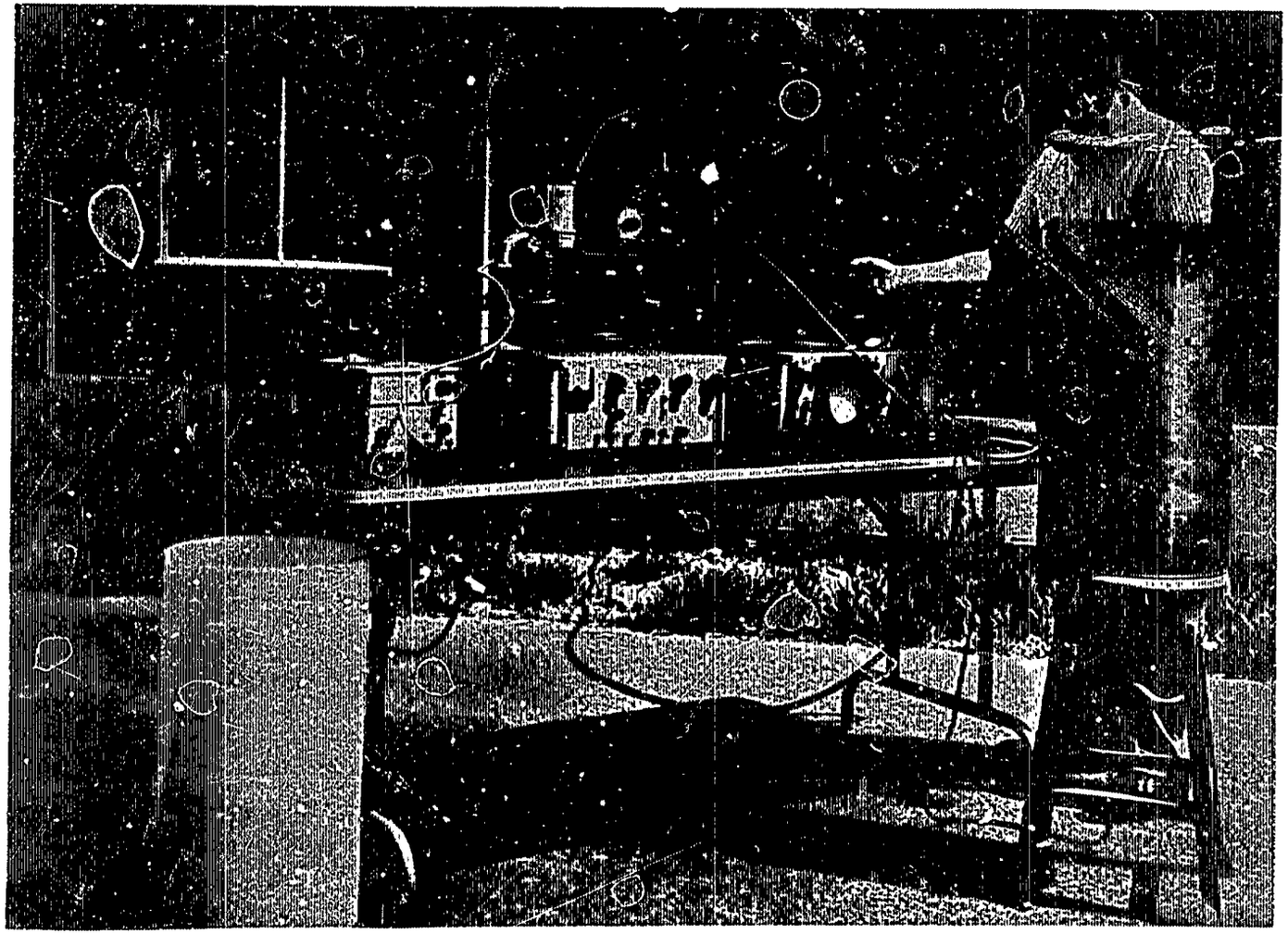

NASA

Figure 12.- Experimental setup.

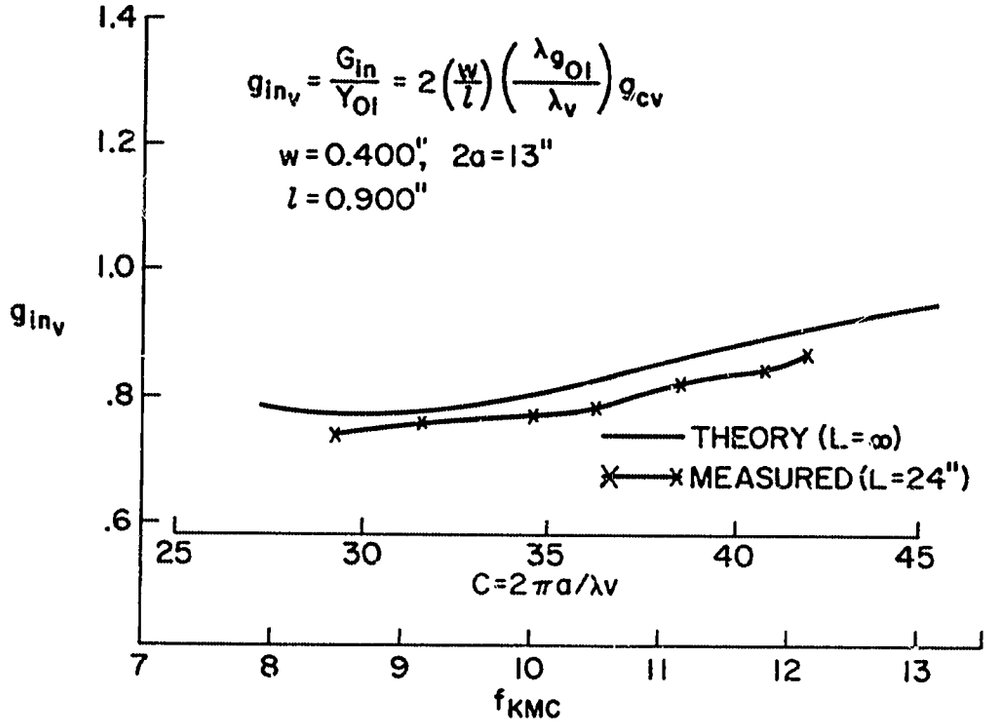

NASA

Figure 13.- Waveguide conductance of uncoated axial slot.

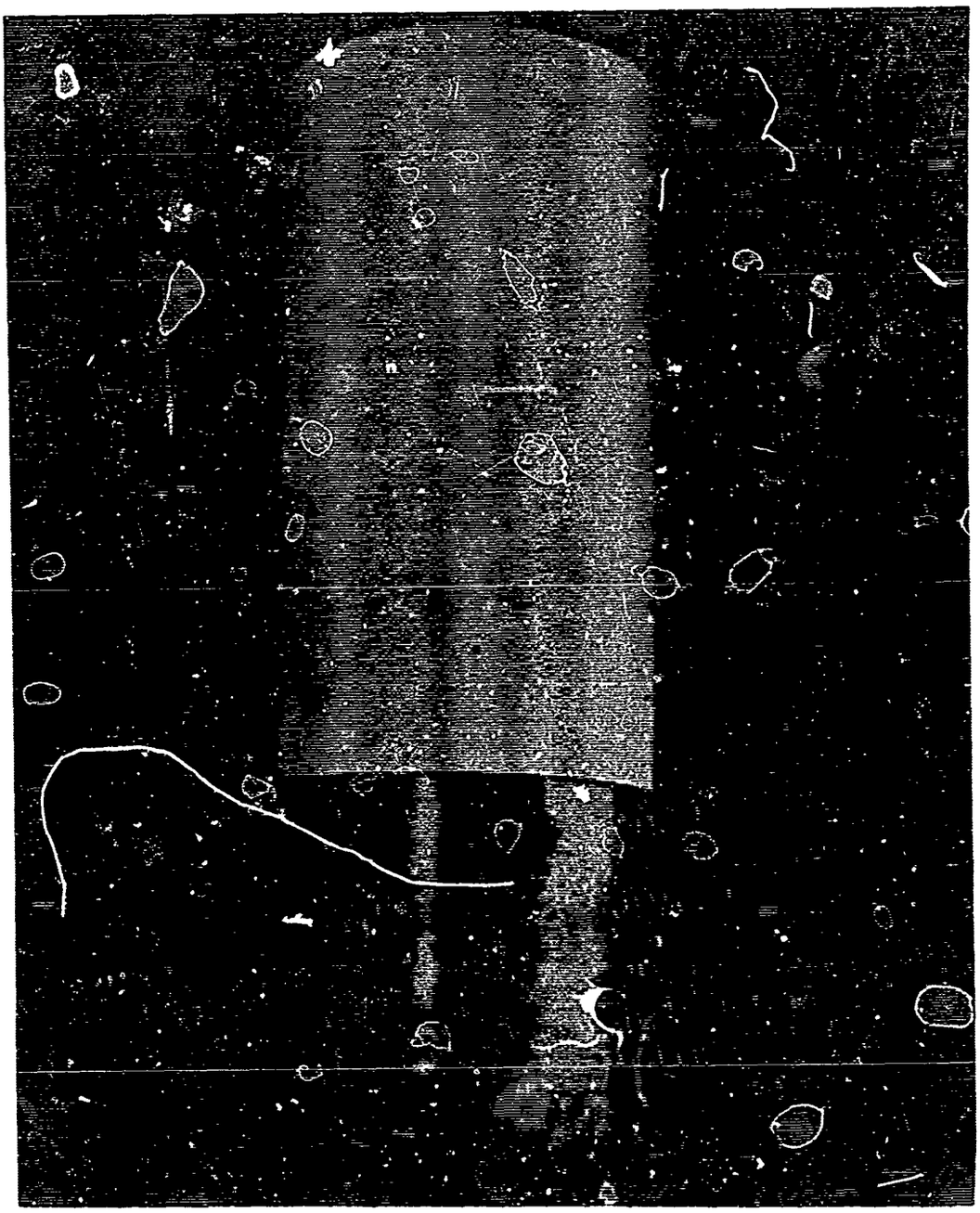

NASA

Figure 14.- Dielectric sleeve on metal cylinder.

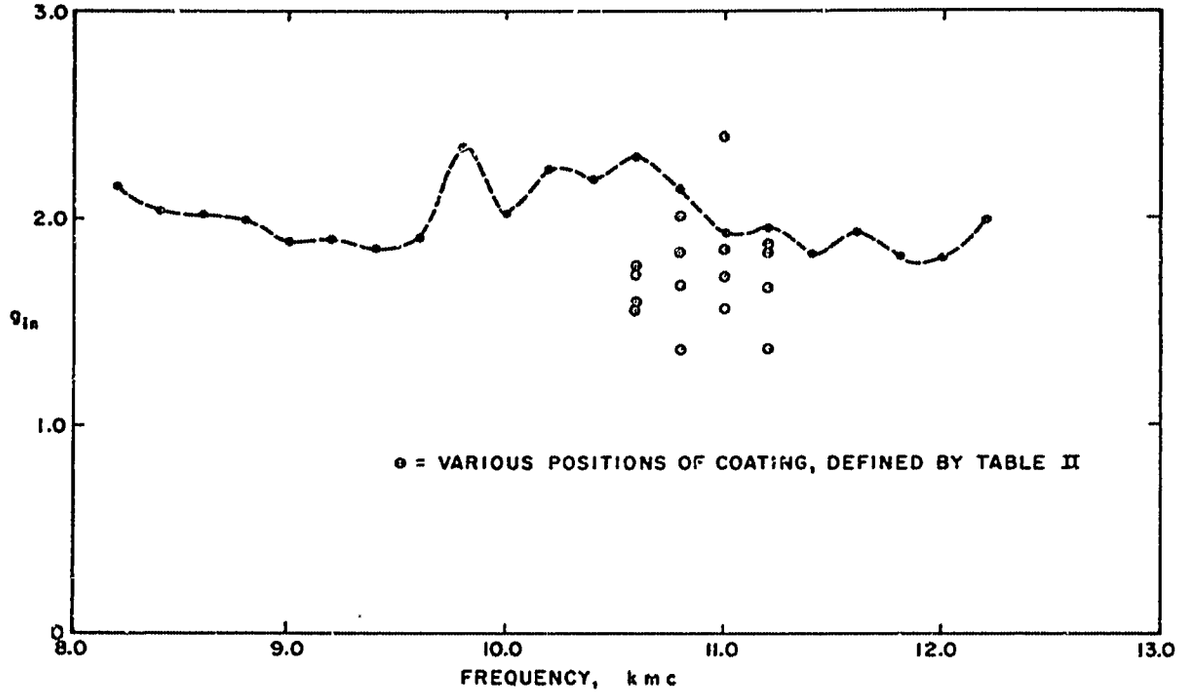

Figure 15.- Waveguide conductance of coated axial slot.

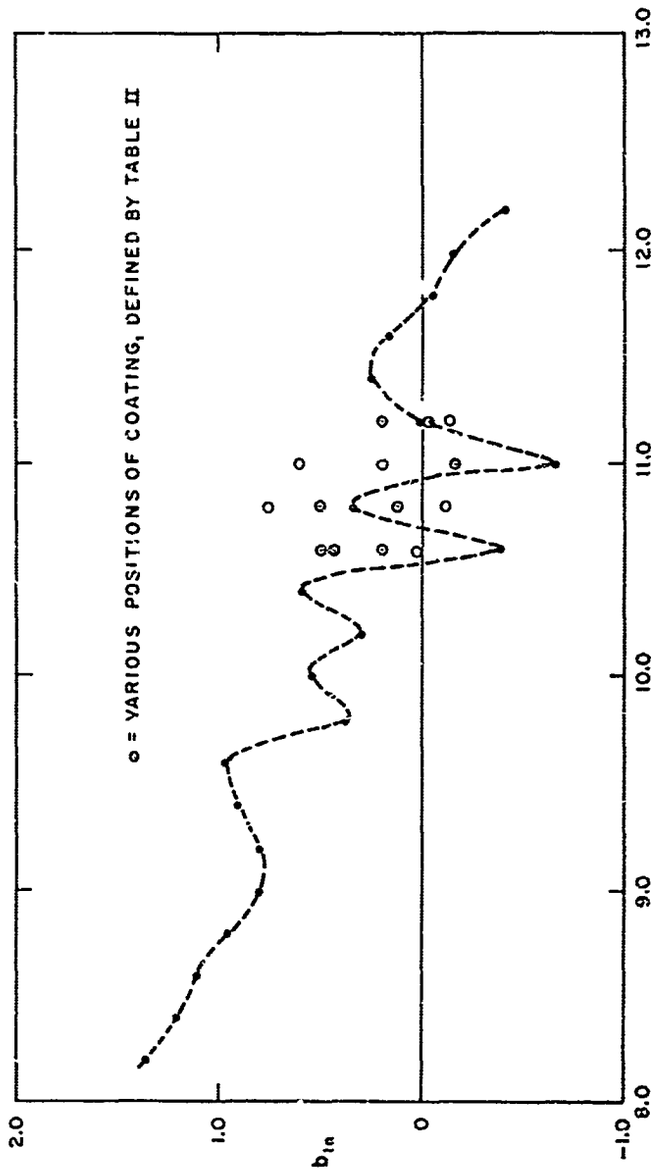

NASA

Figure 15.- Waveguide susceptance of coated axial slot.

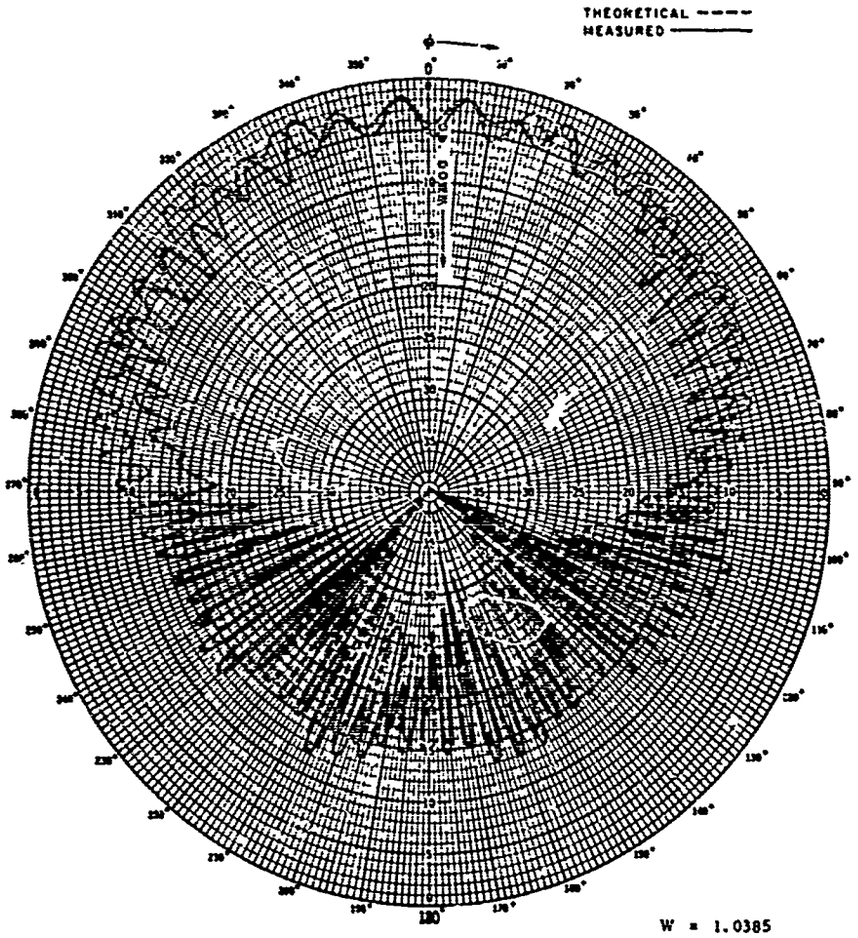

(a) k = 0.65.

NASA

Figure 17.- Measured (and computed) equatorial plane radiation patterns.

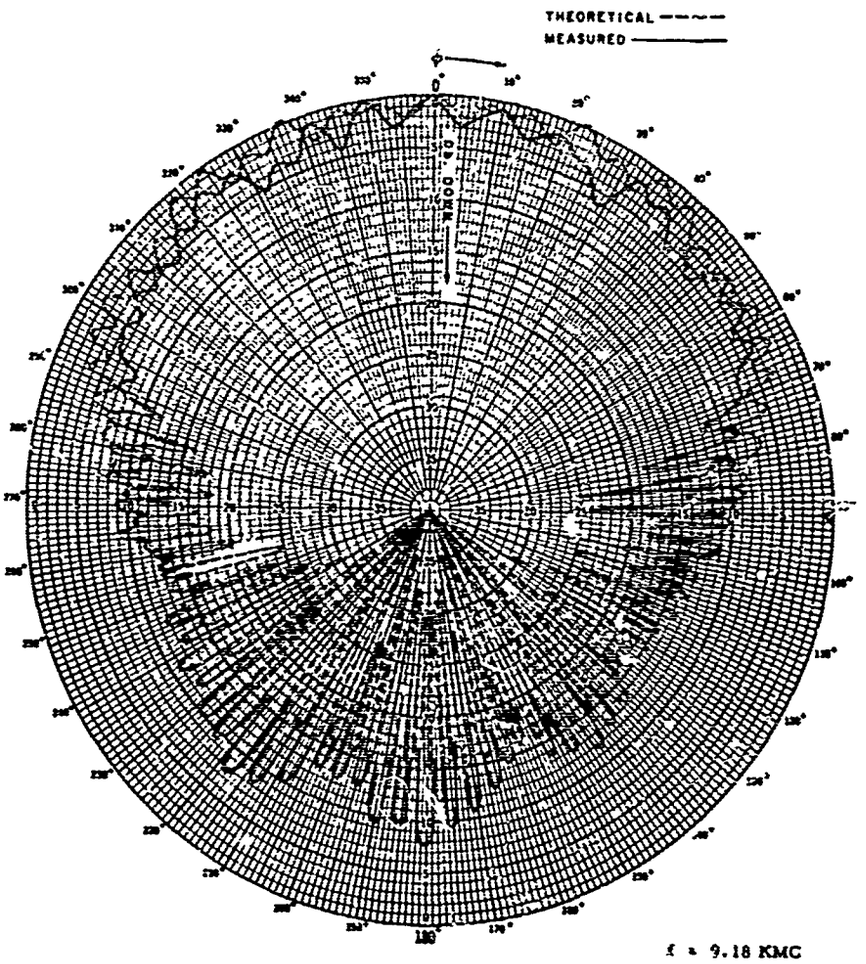

(b) k = 0.7.

NASA

Figure 17.- Continued.

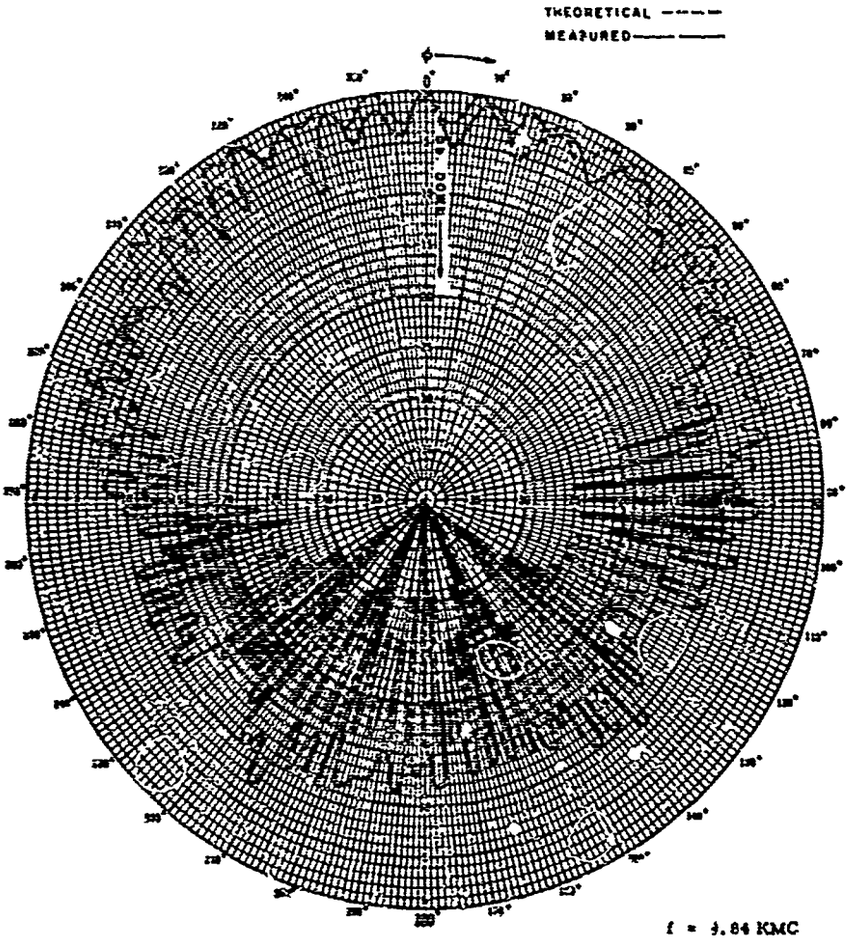

(c) k = 0.75.

NASA

Figure 17.- Continued.

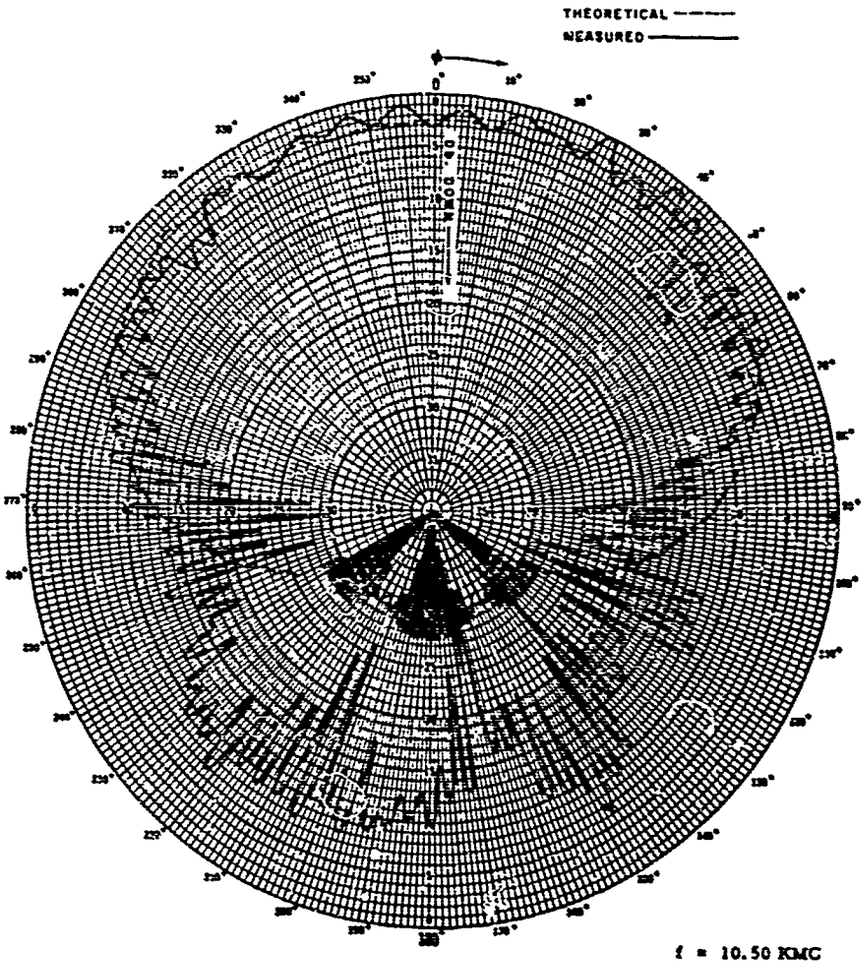

(d) $k = 0.80$.

NASA

Figure 17.- Continued.

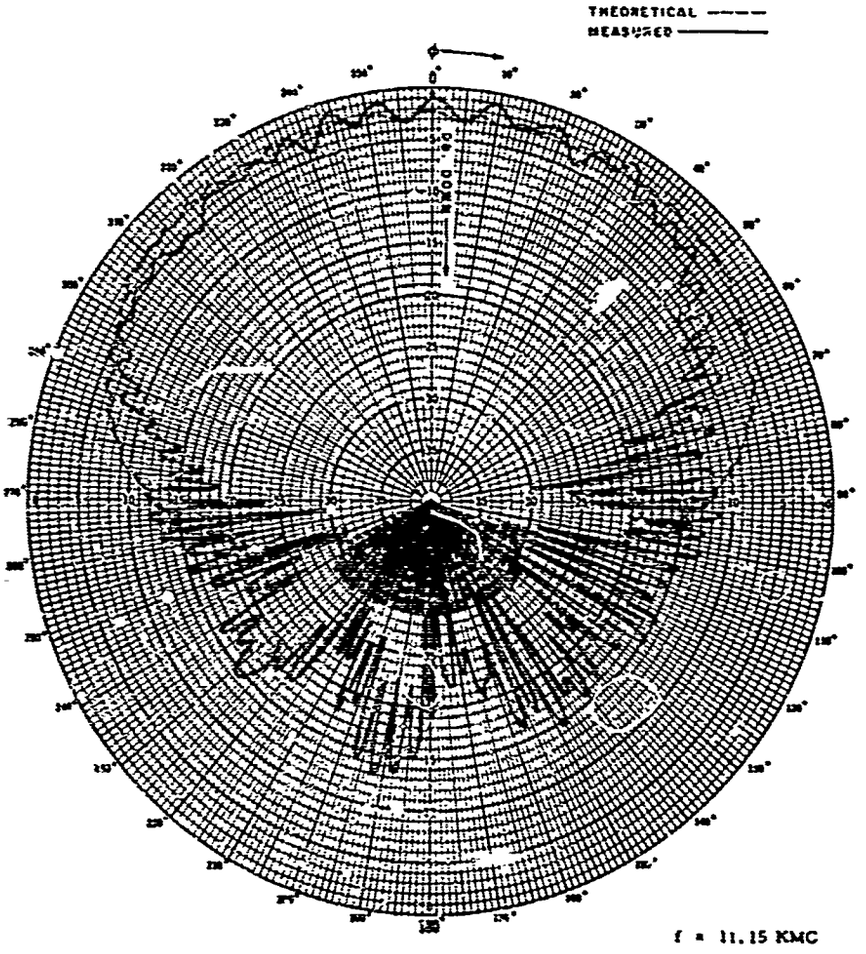

(e) k = 0.85.

Figure 17.- Continued.

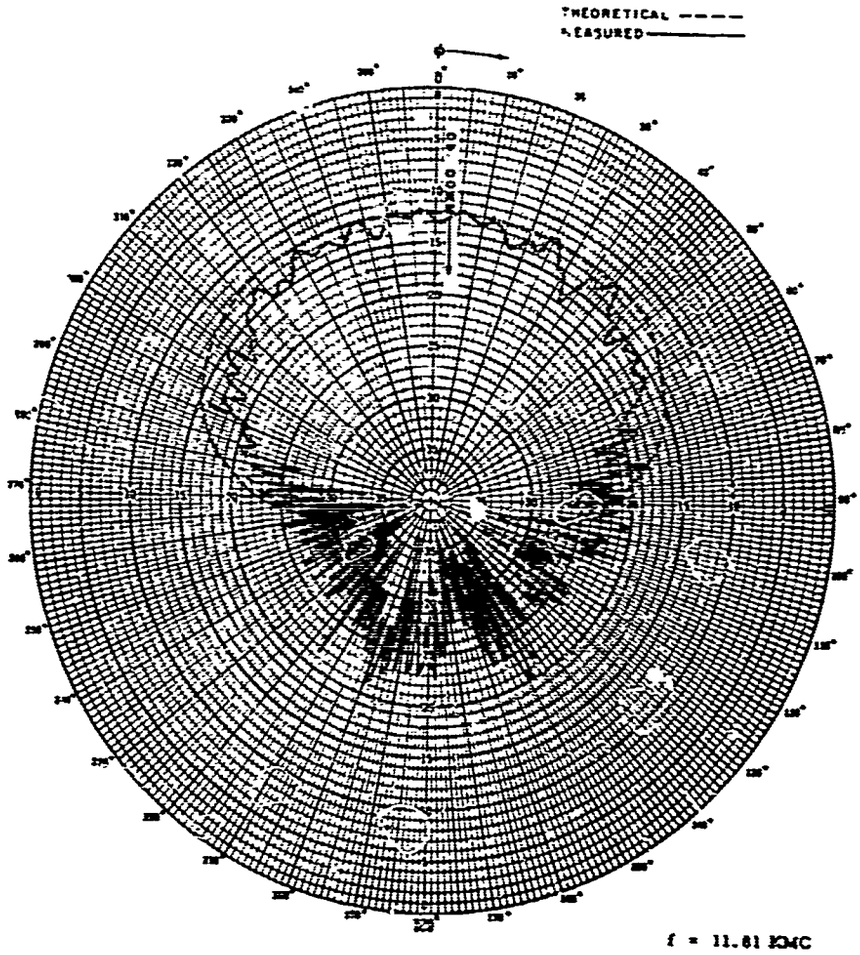

(f) k = 0.90.

E423A

Figure 17.- Concluded.

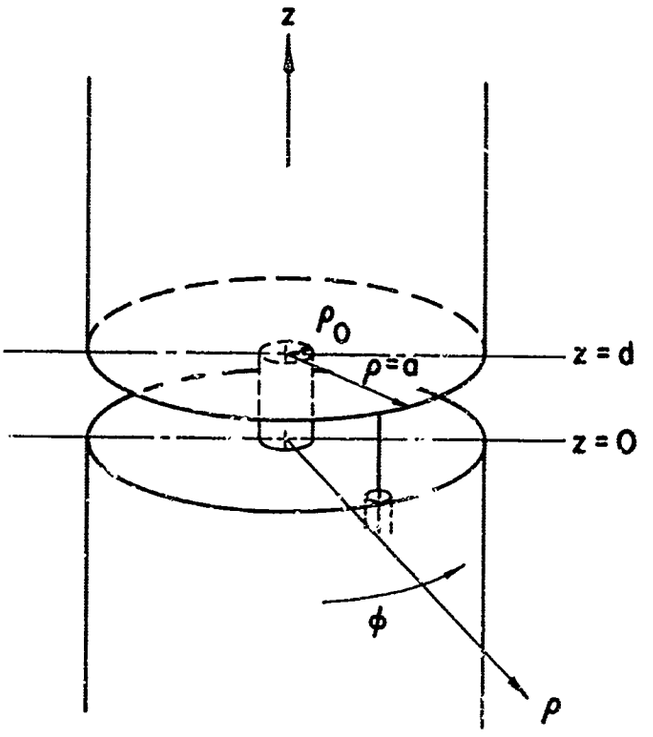

NASA

Figure 10.- Cylindrical gap antenna.

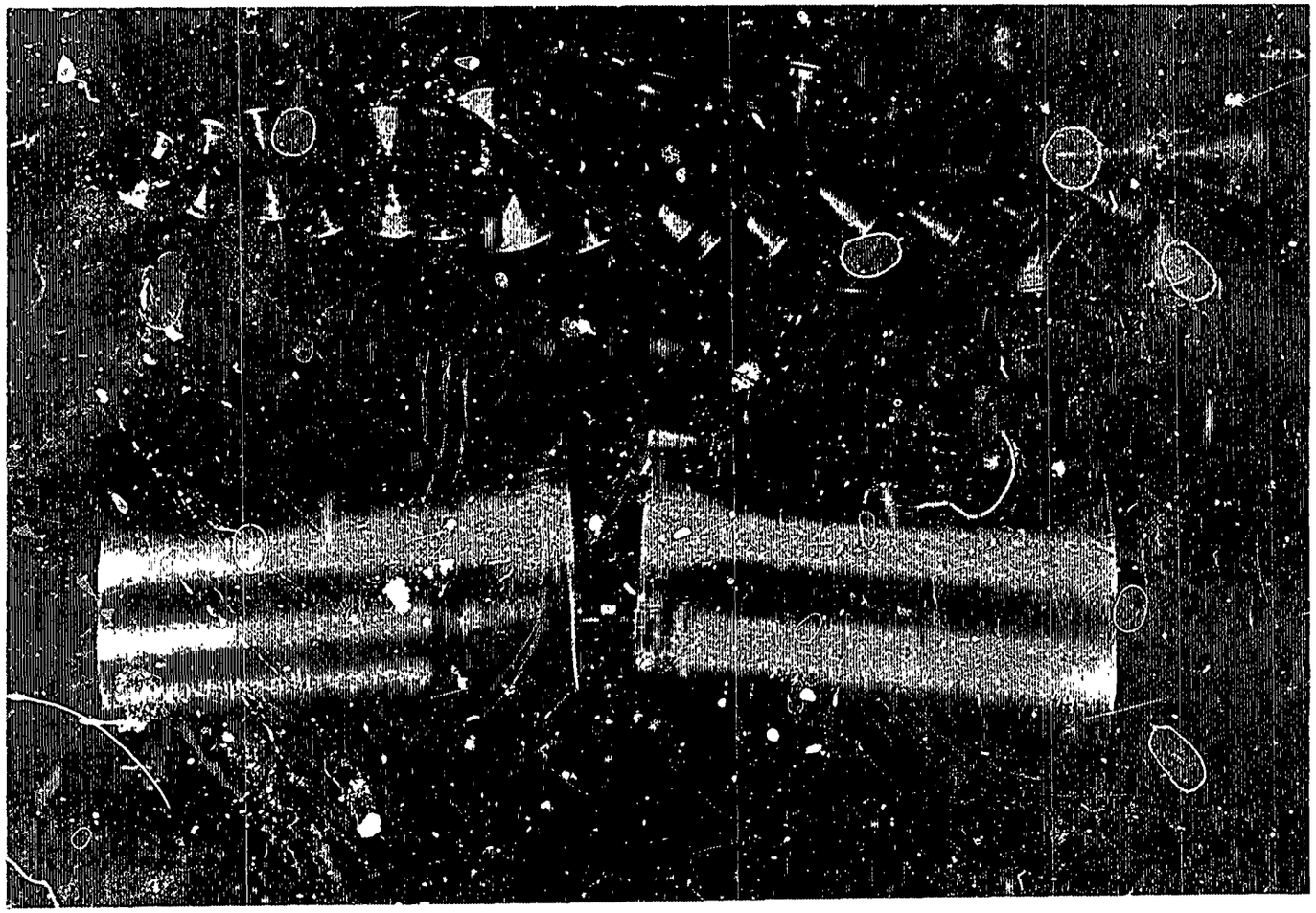

NASA

Figure 19.- Exploded view of the gap antenna with spacers.

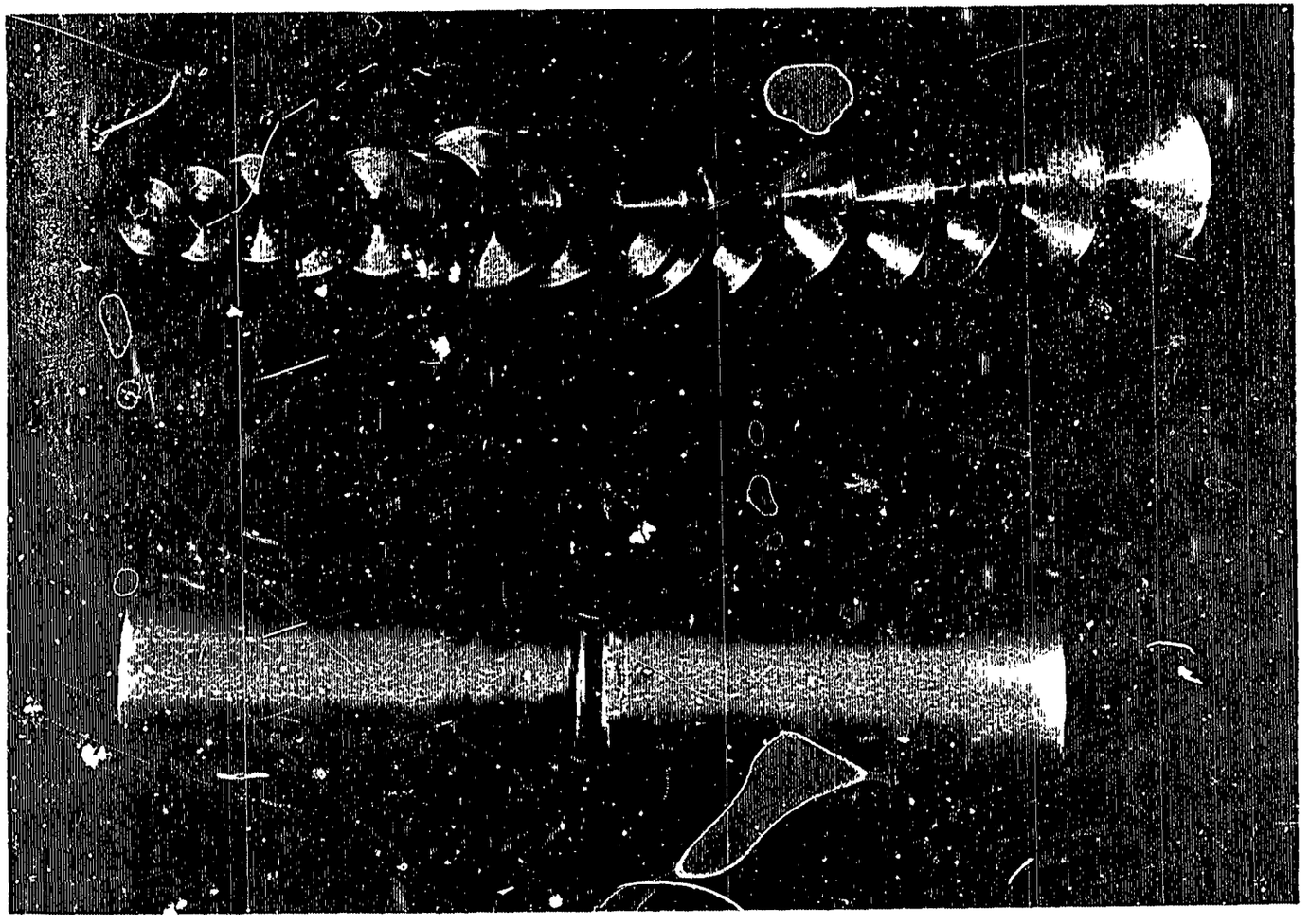

NASA

Figure 20.- Assembled gap antenna with spacers.

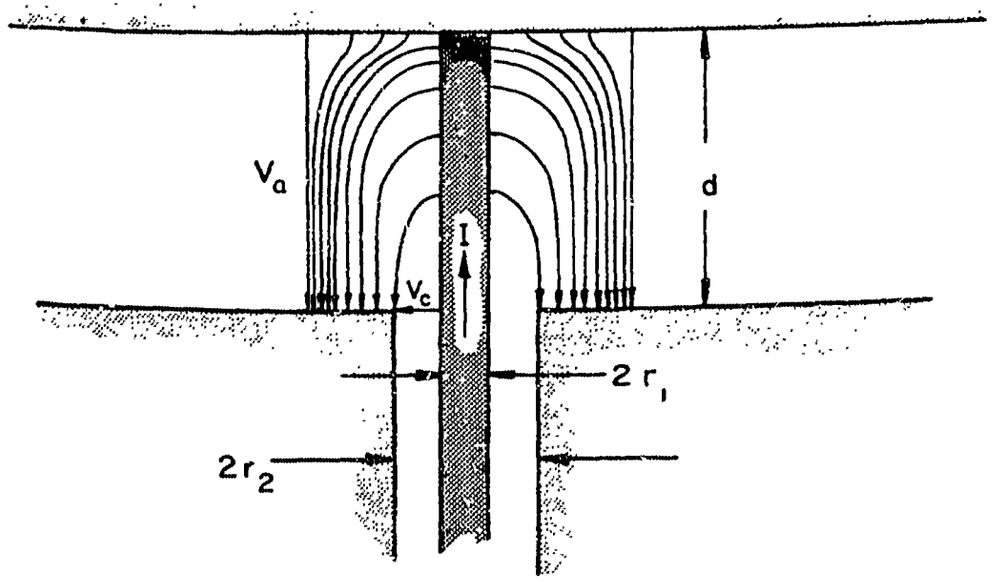

NASA

Figure 21.- Gap antenna feed.

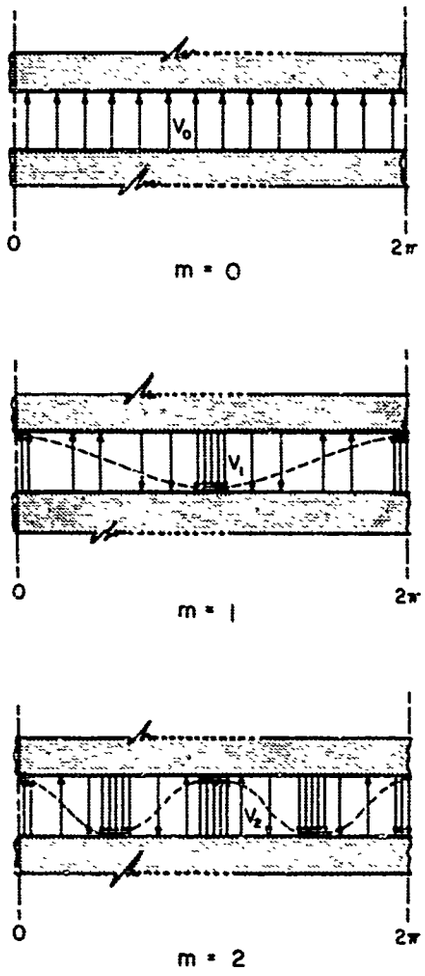

NASA

Figure 22.- Gap modal electric field distribution.

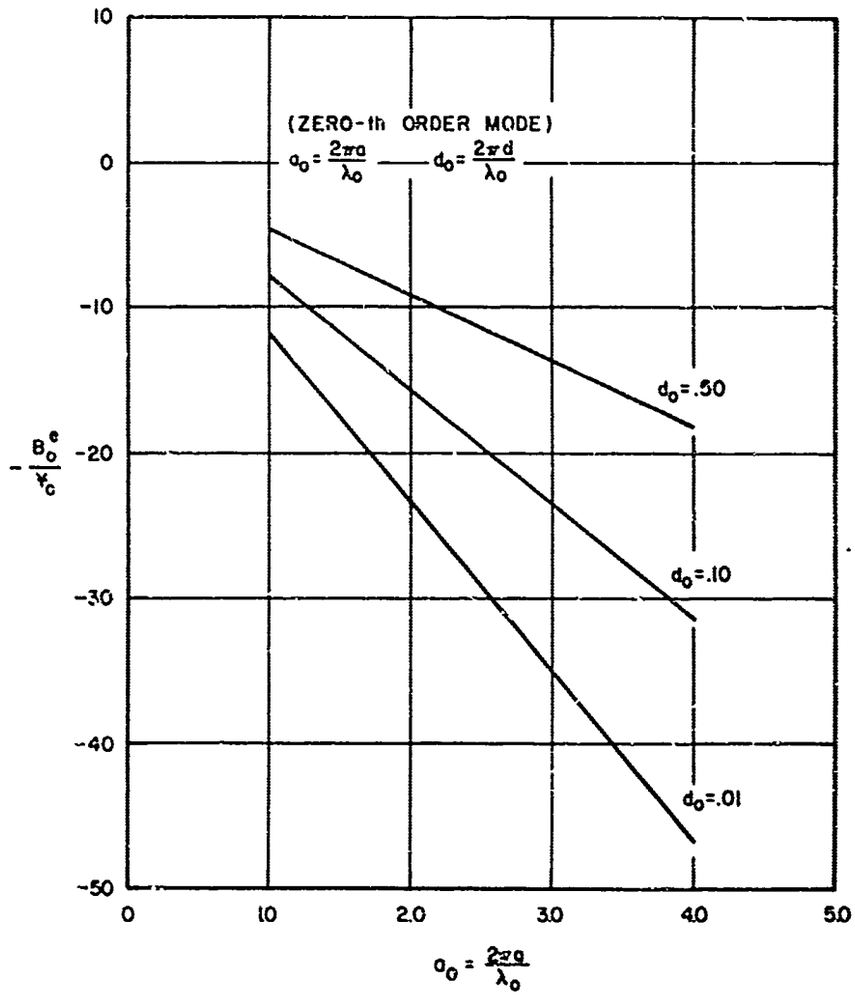

NASA

Figure 23.- Normalized aperture external susceptance as a function of cylinder circumference and gap width.

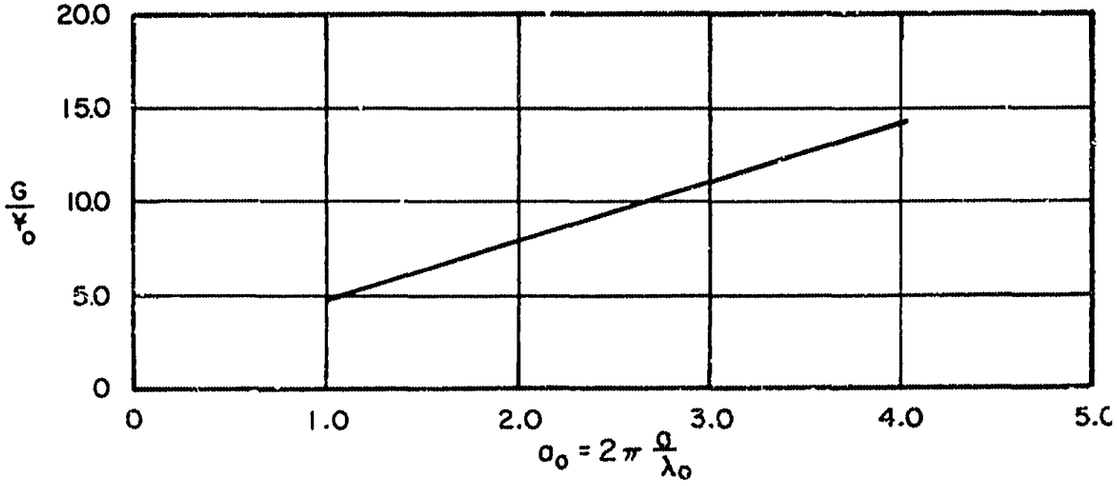

NASA

Figure 24.- Normalized aperture input conductance vs. cylinder circumference in wavelengths.

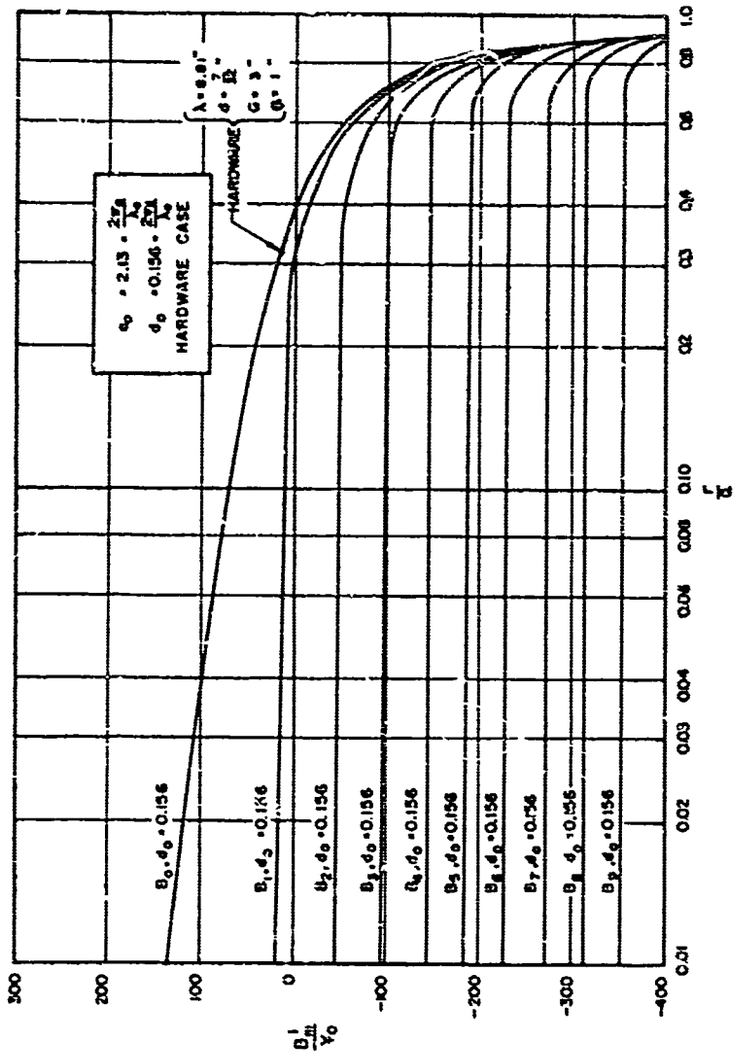

NASA

Figure 25.- Internal susceptance of gap antenna as a function of r/a.

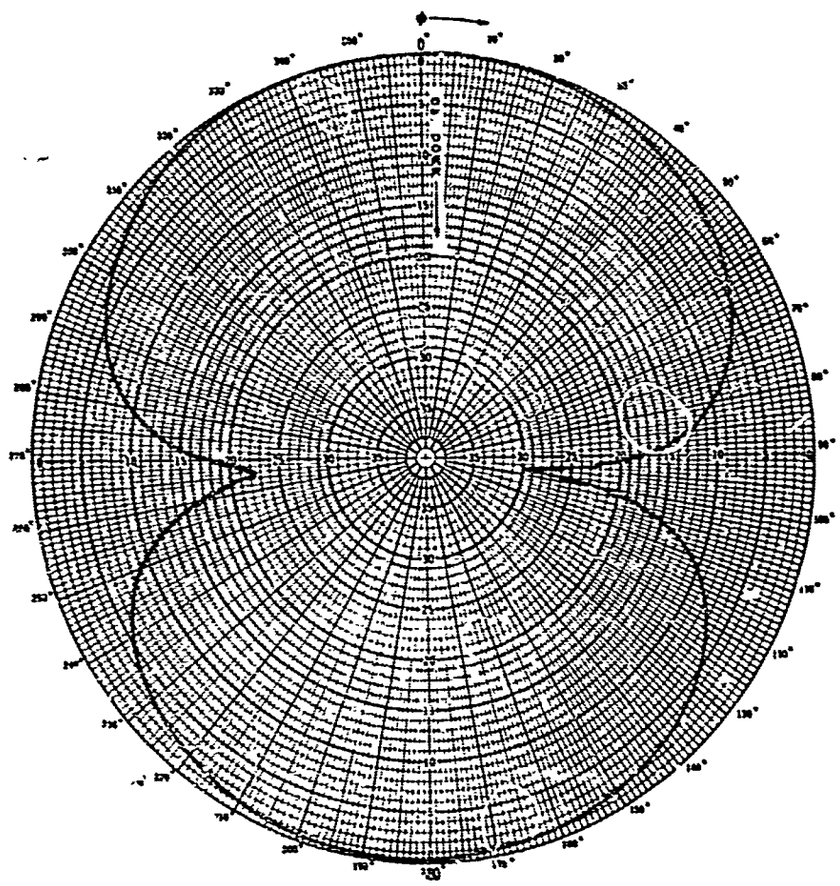

NASA

Figure 26.- Measured equatorial pattern of gap antenna.

NASA-Langley, 1961

IV. THE RADIATION PATTERN OF AN ELECTRIC LINE CURRENT ENCLOSED BY AN AXIALLY SLOTTED PLASMA SHEATH

Andrejs Olte

The University of Michigan
Department of Electrical Engineering
The Radiation Laboratory
Ann Arbor, Michigan 48108

ABSTRACT

A circular uniform plasma sheath of complex conductivity is enclosing a unit electric line source at the origin. The plasma sheath has an infinite axial slot of arbitrary cross section. The problem has been reduced to a Fredholm integral equation of the second kind in which the unknown function is the electric current in the plasma. An approximate solution of the integral equation has been obtained in the case of a locally partially transparent plasma sheath. On the basis of this solution a formula for the radiation pattern is derived. As an example, the radiation patterns are computed for a 35° wedge slot in the plasma sheath of three different thicknesses. In addition, attenuation calculations have been performed on the unslotted plasma sheath.

I. INTRODUCTION

A homogeneous plasma sheath of inside radii a and outside radii b is taken to enclose a unit electric line current at the origin of the coordinate system (r, ϕ, z) as shown in Fig. 1. The z-axis coincides with the line source. The plasma sheath may contain an axial slot of area A_s. The area of the plasma sheath we have indicated by A_p. The structure is uniform in the z-direction. The free space permittivity ϵ_o and the permeability μ_o is taken throughout, including the plasma. The electric conduction properties of the plasma (Rose and Clark, 1961) are accounted for by a complex conductivity

$$\sigma = \frac{\epsilon_o \omega_p^2}{\nu + j\omega} \tag{1}$$

where ω, ν and ω_p are the frequencies of field, collision and plasma respectively.

Since the primary current source as well as the plasma sheath does not depend on the z-coordinate, it follows that the electric and the magnetic fields depend only on the r and ϕ coordinates. Furthermore, the electric field is tangential to the line source, and the magnetic field is transverse to it. That is to say, we are dealing only with the electric field component $E_z(r, \phi)$ and the magnetic field components $H_r(r, \phi)$ and $H_\phi(r, \phi)$. The other field components are zero. If we let the plasma fill in the slot, then $E_z(r, \phi) \to E_z(r)$, $H_r(r, \phi) \to 0$, and $H_\phi(r, \phi) \to H_\phi(r)$. Thus we have only one component each of the electric and the magnetic fields, and they depend only on the radial variable r.

In this report we are concerned with the problem of finding the radiation pattern of the electric line source enclosed by a uniform plasma sheath that contains an infinite axial slot. That is to say, we wish to discover the ϕ variation of $E_z(r, \phi)$. This field may be found from the line current and the electric current induced in the plasma. The latter is the unknown quantity for which we derive a Fredholm

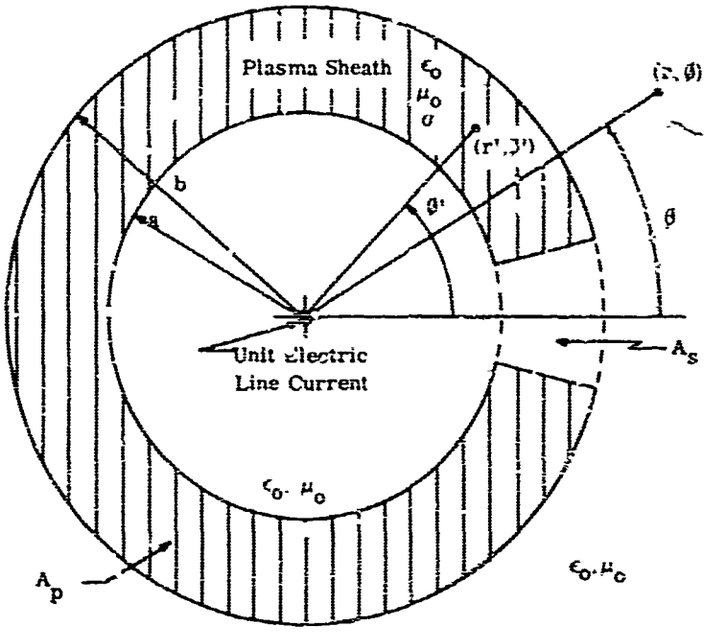

FIG. 1: COORDINATE SYSTEM AND SLOTTED PLASMA SHEATH

integral equation of the second kind in Section II. We may solve this equation only under restrictions which make the solution of very limited practical value. Setting out in search of a better solution, we first solve the unslotted plasma sheath in Section III. Defining the sheath current with a slot as the unslotted sheath current plus a correction current, we are able, in Section IV, to derive an integral equation for the correction current. We use the unslotted sheath current as an approximate current from which we compute the radiation pattern for the slotted plasma sheath. An approximate solution for the correction current serves as a basis for checking the reliability of the radiation pattern calculations. The rationalized MKS system of units has been used with time dependence of $e^{j\omega t}$ understood. In section V we present numerical results and conclusions and indicate the direction of the future work.

II REDUCING THE PROBLEM TO A FREDHOLM INTEGRAL EQUATION OF THE SECOND KIND

The unit electric line source induces conduction currents $i_z(r', \phi')$ in the plasma sheath. The electric field (Harrington, 1961) of both currents is given by

$$E_z(r, \phi) = -\frac{1}{4}\omega\mu_o\left[H_o^{(2)}(k_o r) + \iint_{A_p} i_z(r', \phi') H_o^{(2)}(k_o |\bar{r}-\bar{r}'|) dA'\right] \qquad (2)$$

where $H_o^{(2)}$ is the Hankel function of the second kind, $k_o = \omega\sqrt{\mu_o \epsilon_o}$, and $|\bar{r}-\bar{r}'|$ is the distance from the field point to the source point. We assume that Ohm's law holds in the plasma, i.e.

$$i_z(r, \phi) = \sigma E_z(r, \phi) \qquad . \qquad (3)$$

We are neglecting thereby any space charge effects in the plasma. Eliminating

$E_z(r, \phi)$ between (2) and (3), we obtain an integral equation of the form

$$i_z(r,\phi) + \frac{1}{4}\omega\mu_o\sigma \iint_{A_p} i_z(r', \phi') H_o^{(2)}(k_o|\bar{r}-\bar{r}'|) dA' = -\frac{1}{4}\omega\mu_o\sigma H_o^{(2)}(k_o r) \quad . \tag{4}$$

We recognize that this is a Fredholm integral equation of the second kind with the kernel $H_o^{(2)}(k_o|\bar{r}-\bar{r}'|)$.

We put the integral equation in a more convenient form by defining

$$\tau \equiv \frac{\mu_o \omega \sigma}{4k_o^2} \tag{5}$$

and

$$k_o^2 i(\rho, \phi) \equiv i_z(r,\phi) \tag{6}$$

where $\rho = k_o r$, and hence

$$i(\rho,\phi) + \tau \iint_{A_p} i(\rho', \phi') H_o^{(2)}(|\bar{\rho}-\bar{\rho}'|) dA' = -\tau H_o^{(2)}(\rho) \tag{7}$$

where now $dA' = \rho' d\rho' d\phi'$. This is the fundamental equation of the problem.

The integral equation may be solved by the method of successive approximation (Mikhlin, 1964) provided that

$$|\tau| < \frac{1}{B} \tag{8}$$

where

$$B^2 = \iint_{A_p} \iint_{A_p} \left| H_o^{(2)}(|\bar{\rho}-\bar{\rho}'|) \right|^2 dA\, dA' \quad . \tag{9}$$

By considering unslotted plasma sheath and a Hankel asymptotic form for $H_o^{(2)}$, we obtain from (9) that

$$B \simeq 2\pi k_o (b-a) \quad , \tag{10}$$

and hence from (6) that

$$\frac{\omega_p^2}{|\nu+j\omega|} < \frac{\lambda_o}{\pi^2(b-a)} \tag{11}$$

This estimate of the conditions of convergence is on the pessimistic side. Nevertheless, Eq. (11) gives us a good indication that the successive approximation method of solving the Fredholm integral equation is of value only for either very thin plasma sheath or very low plasma density.

III THE CASE OF UNIFORM PLASMA SHEATH

The situation is as in Fig. 1, with the slot filled in by the plasma. An exact solution to this problem can be obtained in an elementary manner. The electric field may be expressed in the form;

$$E_z(r) = -\frac{1}{4}\omega\mu_o H_o^{(2)}(k_o r) + A_1 J_o(k_o r), \qquad 0 < r < a, \tag{12}$$

$$= A_2 J_o(kr) + B_2 N_o(kr), \qquad a < r < b, \tag{13}$$

$$= A_3 H_o^{(2)}(k_o r) \qquad b < r, \tag{14}$$

where J_o and N_o are Bessel and Neumann functions of order zero, respectively, and

$$k = k_o\sqrt{1-j\sigma/(\omega\epsilon_o)} \tag{15}$$

Then from the Maxwell's equations the corresponding magnetic field is given as

$$H_\phi(r) = -j\frac{1}{4}k_o H_1^{(2)}(k_o r) + j\frac{k_o}{\omega\mu_o} A_1 J_1(k_o r), \qquad 0 < r < a, \tag{16}$$

$$= j\frac{k}{\omega\mu_o}\left[A_2 J_1(kr) + B_2 N_1(kr)\right], \qquad a < r < b, \tag{17}$$

$$= j\frac{k_o}{\omega\mu_o} A_3 H_1^{(2)}(k_o r), \qquad b < r, \tag{18}$$

the cylindrical functions being of order 1.

From the continuity of $E_z(r)$ and $H_z(r)$ at r=a and r=b, we obtain four algebraic equations. By solving them we obtain the complex amplitudes of the waves:

$$A_1 = \frac{\omega\mu_o}{4Dk_o^2}\Big\{ k_oJ_o(ka)H_1^{(2)}(k_oa)\left[k_oN_o(kb)H_1^{(2)}(k_ob)-kN_1(kb)H_o^{(2)}(k_ob)\right] + k_oN_o(ka)H_1^{(2)}(k_oa)\left[kJ_1(kb)H_o^{(2)}(k_ob)-k_oJ_o(kb)H_1^{(2)}(k_ob)\right] + kN_1(ka)H_o^{(2)}(k_oa)\left[k_oJ_o(kb)H_1^{(2)}(k_ob)-kJ_1(kb)H_o^{(2)}(k_ob)\right] + kJ_1(ka)H_o^{(2)}(k_oa)\left[kN_1(kb)H_o^{(2)}(k_ob)-k_oN_o(kb)H_1^{(2)}(k_ob)\right]\Big\}, \quad (19)$$

$$A_2 = \frac{j\omega\mu_o}{2\pi aDk_o^2}\left[k_oN_o(kb)H_1^{(2)}(k_ob)-kN_1(kb)H_o^{(2)}(k_ob)\right], \quad (20)$$

$$B_2 = \frac{j\omega\mu_o}{2\pi aDk_o^2}\left[kJ_1(kb)H_o^{(2)}(k_ob)-k_oJ_o(kb)H_1^{(2)}(k_ob)\right] \quad (21)$$

$$A_3 = \frac{j\omega\mu_o}{\pi^2k_o^2abD} \quad (22)$$

where

$$D = J_1(k_oa)H_1^{(2)}(k_ob)\left[J_o(ka)N_o(kb)-J_o(kb)N_o(ka)\right] + \frac{k}{k_o}\Big\{J_1(k_oa)H_o^{(2)}(k_ob)\left[J_1(kb)N_o(ka)\ J_o(ka)N_1(kb)\right] + J_o(k_oa)H_1^{(2)}(k_ob)\left[J_o(kb)N_1(ka)-J_1(ka)N_o(kb)\right]\Big\} + \left(\frac{k}{k_o}\right)^2 J_o(k_oa)H_o^{(2)}(k_ob)\left[J_1(ka)N_1(kb)-J_1(kb)N_1(ka)\right]. \quad (23)$$

The current induced in the uniform plasma sheath $i_z(r)$ is given by

$$i_z(r) = \sigma E_z(r), \qquad a < r < b$$
$$= \sigma\left[A_2 J_o(kr) + B_2 N_o(kr)\right]. \tag{24}$$

By a similar definition as in (6) we introduce

$$I(\rho) = \frac{\sigma}{k_o^2}\left[A_2 J_o(kr) + B_2 N_o(kr)\right]. \tag{25}$$

The electric field outside the plasma sheath is given by (14) is rewritten in the form

$$E_z(r) = -\frac{1}{4}\omega\mu_o H_o^{(2)}(k_o r)\left[-\frac{4}{\omega\mu_o} A_3\right]. \tag{26}$$

The first factor gives the electric field of the unit electric line source in the free space, the second factor introduces the effect of the plasma sheath on the radiation field. We define the latter factor as the radiation pattern for the electric line source radiating through a concentric uniform plasma sheath, i.e.

$$P_o = -\frac{4}{\omega\mu_o} A_3 \tag{27}$$

This pattern is a constant; it does not depend either on r or ϕ. However, it is rather difficult to calculate because of the involved denominator in A_3. However, in the case $k_o a \gg 1$ and $|ka| \gg 1$, P_o can be reduced with a good approximation to an elementary form by using the Hankel asymptotic form for the cylindrical functions. Taking two terms in the Hankel asymptotic series, we obtain

$$P_o \simeq \frac{2kc\, e^{-j\left[k(b-a)-k_o b-(8k_o b)^{-1}+\frac{3}{4}\pi\right]}}{k_o\left[d_o+d_1(8k_o a)^{-1}+\ldots\right]} \tag{28}$$

where

$$d_o = \left[1+\frac{k}{k_o}+\left(-1+\frac{k}{k_o}\right)e^{-j2k(b-a)}\right]\sin\left(k_o a-\frac{\pi}{4}\right) +$$
$$j\frac{k}{k_o}\left[-1-\frac{k}{k_o}+\left(-1+\frac{k}{k_o}\right)e^{-j2k(b-a)}\right]\cos\left(k_o a-\frac{\pi}{4}\right), \tag{29}$$

and

$$d_1 = j\left(\frac{k}{k_o} - \frac{k_o(b-a)}{kb}\right)\left[-1-\frac{k}{k_o}+\left(-1+\frac{k}{k_o}\right)e^{-j2k(b-a)}\right]\sin\left(k_o a-\frac{\pi}{4}\right) +$$

$$\sqrt{\frac{a}{b}}\left[-1-\frac{k}{k_o}-\left(-1+\frac{k}{k_o}\right)e^{-j2k(b-a)}\right] . \qquad (30)$$

From (1) and (15) we find that $k=k'-jk''$ where

$$k' = k_o\left[\frac{1}{2}A+\frac{1}{2}\sqrt{A^2+B^2}\right]^{1/2} \qquad (31)$$

$$k'' = k_o\left[-\frac{1}{2}A+\frac{1}{2}\sqrt{A^2+B^2}\right]^{1/2} \qquad (32)$$

and

$$A \equiv 1-\frac{X^2}{1+Y^2}\ ; \qquad B \equiv \frac{YX^2}{1+Y^2} \qquad (33)$$

with

$$X \equiv \frac{\omega_p}{\omega}\ ; \qquad Y \equiv \frac{\nu}{\omega}\ . \qquad (34)$$

From (28) we observe that the amplitude of P_o is determined principally by the factor $\exp\left[k''(b-a)\right]$ as would also be the corresponding case of a normally incident plane wave radiation through a plasma slab.

The asymptotic current distribution in the plasma associated with (28) is given by

$$i(r) \simeq \frac{j\tau\sqrt{\frac{2}{\pi k_o r}}}{d_o+d_1(8k_o a)^{-1}}\left\{\left[\left(1+\frac{k}{k_o}\right)-j\frac{1}{8}\left(\frac{1}{k_o b}+\frac{1}{k_o r}\right)\left(1+\frac{k_o}{k}\right)\right]e^{-jk(r-a)} +\right.$$

$$\left.\left[\left(\frac{k}{k_o}-1\right)+j\frac{1}{8}\left(\frac{1}{k_o b}-\frac{1}{k_o r}\right)\left(1-\frac{k_o}{k}\right)\right]e^{jk\left[r-2(b-a)\right]}\right\} \qquad (35)$$

The first term in the $\{\ \}$ brackets represents outward propagating current wave and the second term the reflected current wave. Again the exponentials are the dominant factors in this formula.

The approximate forms of P_o and $I(z)$ for the case $k_o a \gg 1$ and $|k|b \ll 1$ are given by

$$P_o \simeq \frac{e^{j(k_o b - \frac{3\pi}{4})}}{k_o\sqrt{ab}} \left\{ \left[\frac{1}{k_o b} + j\ell n\left(\frac{b}{a}\right) \right] \sin\left(k_o a - \frac{\pi}{4}\right) - j \frac{1}{k_o a} \cos\left(k_o a - \frac{\pi}{4}\right) \right\}^{-1} \tag{36}$$

and

$$I(z) \simeq \frac{X^2(1+jk_o b\ell n\frac{b}{r})}{(1-jY)2\sqrt{2\pi k_o a}} \left\{ \left[1+jk_o b\ell n\frac{b}{a} \right] \sin\left(k_o a - \frac{\pi}{4}\right) - j\frac{b}{a}\cos\left(k_o a - \frac{\pi}{4}\right) \right\}^{-1} \tag{37}$$

The two formulas have been obtained using the small argument approximation for the cylindrical functions of argument kr and the first term in the Hankel asymptotic series for those of argument $k_o r$. That is to say, these formulas are valid approximations for a plasma sheath of sufficiently large radius and $\omega \sim \omega_p$.

IV AN APPROXIMATE SOLUTION TO THE CURRENT INTEGRAL EQUATION AND THE RADIATION PATTERN

We recognize that the normalized current of the uniform plasma sheath, (25), is a solution of the integral equation (7) with $A_p \rightarrow (A_p + A_s)$, i.e.

$$I(\rho) + \tau \iint_{A_p+A_s} I(\rho') H_o^{(2)}(|\bar{\rho} - \bar{\rho}'|) dA' = -\tau H_o^{(2)}(\rho) . \tag{38}$$

We define a current $I_c(\rho, \psi)$ by

$$I(\rho, \psi) \equiv I(a) + I_c(\rho, \psi) \tag{39}$$

and thus from (7) obtain

$$i_c(\rho,\phi)=\tau\iint_{A_p} i_c(\rho',\phi')H_o^{(2)}(|\bar{\rho}-\bar{\rho}'|)dA'=-i(\rho)=\tau H_o^{(2)}(\rho) - \tau\iint_{A_p} i(\rho')H_o^{(2)}(|\bar{\rho}-\bar{\rho}'|)dA' \quad . \tag{40}$$

However, from (38) we see that the right-hand side of (40) reduces to

$$\tau\iint_{A_s} i(\rho')H_o^{(2)}(|\bar{\rho}-\bar{\rho}'|)dA'$$

and thus

$$i_c(\rho,\phi)+\tau\iint_{A_p} i_c(\rho',\phi')H_o^{(2)}(|\bar{\rho}-\bar{\rho}'|)dA'=\tau\iint_{A_s} i(\rho')H_o^{(2)}(|\bar{\rho}-\bar{\rho}'|)dA' \quad . \tag{41}$$

By opening a slot A_s in the uniform plasma sheath, we change the sheath current by $i_c(\rho,\phi)$ and the integral equation (41) defines this current. Integral equations (7)and (41) differ only in their right-hand sides. Thus the condition (8) on the convergence of the resolvent applies also to the latter. The zeroth order approximation to $i_c(\rho,\phi)$ is given by

$$i_c^{(o)}(\rho,\phi)=\tau\iint_{A_s} i(\rho')H_o^{(2)}(|\bar{\rho}-\bar{\rho}'|)dA' \quad . \tag{42}$$

By opening the slot we reduce $i(\rho)=0$ in the slot area A_s and assuming that we may neglect $i_c(\rho,\phi)$ we obtain by a simple transformation from (2) and (14)

$$E_z(r,\phi)\simeq A_3H_o^{(2)}(k_or)+\frac{1}{4}\omega\mu_o\iint_{A_s} i(r')H_o^{(2)}(k_o|\bar{r}-\bar{r}'|)dA' \quad , \; r>b \; . \tag{43}$$

Using the asymptotic forms for the Hankel functions, we obtain

$$E_z(r,\phi) \simeq -\frac{1}{4}\omega\mu_o\sqrt{\frac{2}{\pi k_o r}}\, e^{-j(k_o r-\frac{\pi}{4})}\left[P_o - \iint_{A_s} i(r')e^{jk_o r'\cos(\phi-\phi')}\,dA'\right], \quad r >> b \tag{44}$$

and the radiation pattern $P_s(\phi)$, consistent with the earlier definition in (27), is then

$$P_s(\phi) \simeq P_o - \iint_{A_s} i(r')e^{jk_o r'\cos(\phi-\phi')}\,dA' \quad . \tag{45}$$

It is clear that including the current $i_c^{(o)}(r,\phi)$ in the approximation we obtain for the radiation pattern

$$P_{sc}(\phi) \simeq P_o - \iint_{A_s} i(r')e^{jk_o r'\cos(\phi-\phi')}\,dA' + \iint_{A_p} i_c^{(o)}(r',\phi')e^{jk_o r'\cos(\phi-\phi')}\,dA' . \tag{46}$$

Equation (45) shows us that opening a slot amounts to adding to the existing current its negative, i.e. to make the total current in the slot area zero. For overdense plasmas $|P_o| \ll 1$ and the negative current in the slot area then dominates the radiation pattern. We believe that (45) gives a good approximation to the radiation pattern whenever i(r) penetrates into the sheath. The adding of $i_c^{(o)}(r,\phi)$ to the radiation pattern $P_s(\phi)$ in (46) is not so much to improve the approximation in (45) as to provide perhaps a means of feeling out its bounds of validity. Whenever

$$P_s(\phi) \simeq P_{sc}(\phi) \tag{47}$$

one can reasonably say that (45) gives a good approximation to the radiation pattern.

If the slot is a wedge slot of width $2\psi_o$, then the double integral in (45) may be transformed into a series, and we obtain for the radiation pattern

$$P_s(\phi) \simeq P_o - 2\phi_o \sum_{n=0}^{\infty} \epsilon_n \frac{\sin(n\phi_o)}{n\phi_o} R_n \cos n\phi \qquad (48)$$

where

$$\epsilon_n = 1, \quad n = 0$$
$$= 2, \quad n = 1, 2, 3, \ldots$$

and

$$R_n = -j^n \int_{k_o a}^{k_o b} i(\rho) J_n(\rho) \rho d\rho . \qquad (49)$$

It is clear that the pattern is an even function in ϕ. The ϕ variable is measured from the center of the slot.

V NUMERICAL RESULTS AND CONCLUSIONS

In Figs. 2, 3 and 4 we present the radiation through a uniform plasma sheath for Y=0.01, 0.1 and 1.0 respectively. With Y=0.01 the plasma is only slightly lossy. With Y=1.0 the plasma is very lossy. The inside radius of the plasma sheath has been kept at one free space wavelength λ_o, and the sheath thickness has been taken up to $3\lambda_o$. The plasma parameter X is varied in steps from 0.25 to 2.0.

In Figs. 2 and 3 the calculations have been carried out using the exact formula (27) for all X values except X=2. For X=2 calculation we used the asymptotic form (28) with d_1 set to zero. The same asymptotic form was used for all calculations in Fig. 4. The asymptotic form for P_o gave excellent agreement with the exact results in Figs. 2 and 3 where it was applicable, and surprisingly little disagreement, even for cases (e.g. Y=0.01, X=1) where the arguments of the cylinder functions were far too small for the Hankel asymptotic expansion to be valid.

The processes that inhibit radiation through the sheath are reflections, absorptive attenuation, and reactive attenuation by the plasma. The attenuation of the radiation for $0 < X < (\sqrt{2}$ approx.) is due to reflections and absorptive attenuation, and for $X > (\sqrt{2}$ approx.) due mainly to both reactive and absorptive attenuation. In

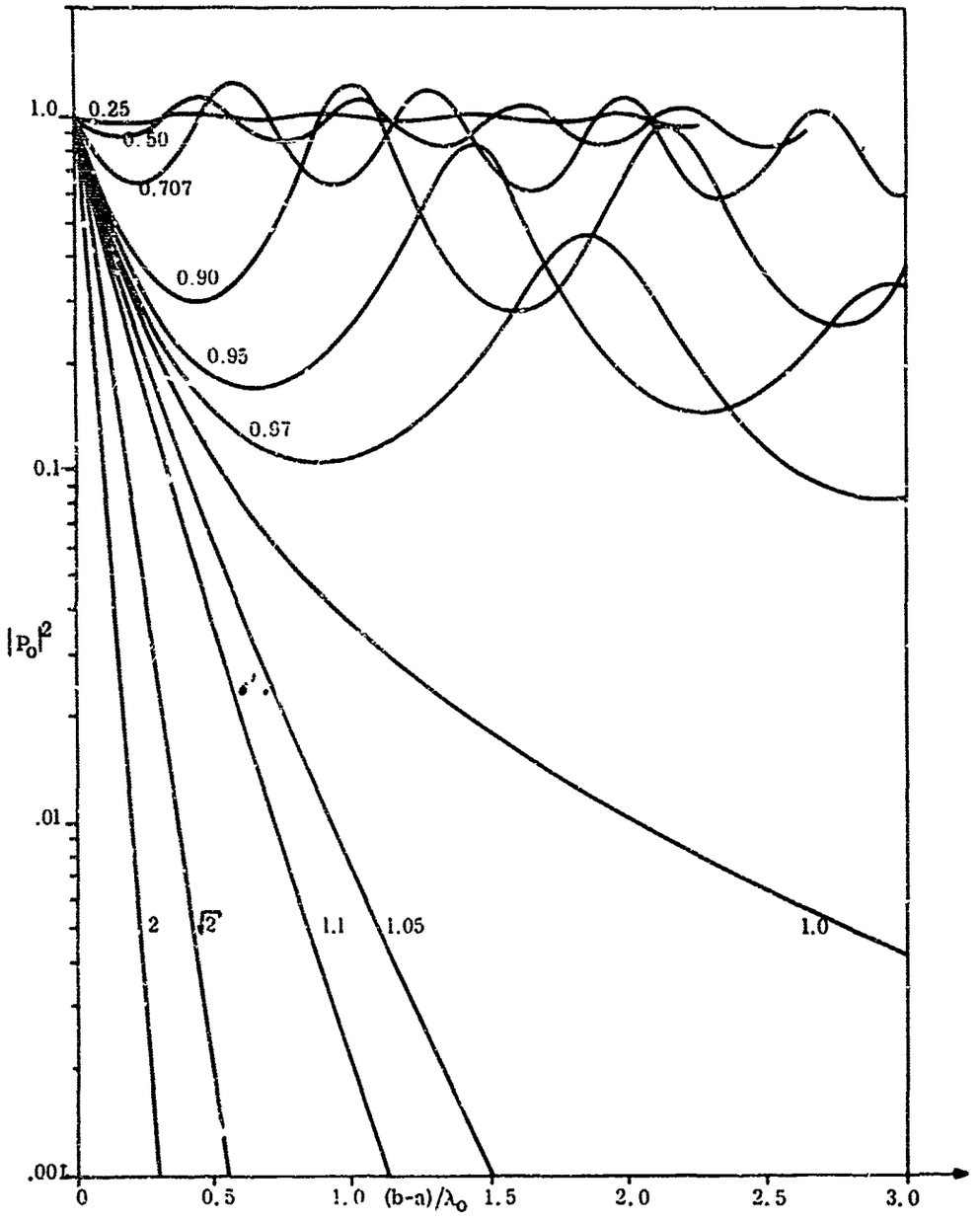

FIG. 2: RADIATION GRAPHS THROUGH UNIFORM PLASMA SHEATH VS SHEATH THICKNESS FOR $a=1\lambda_0$, Y=0.01 AND X AS A PARAMETER.

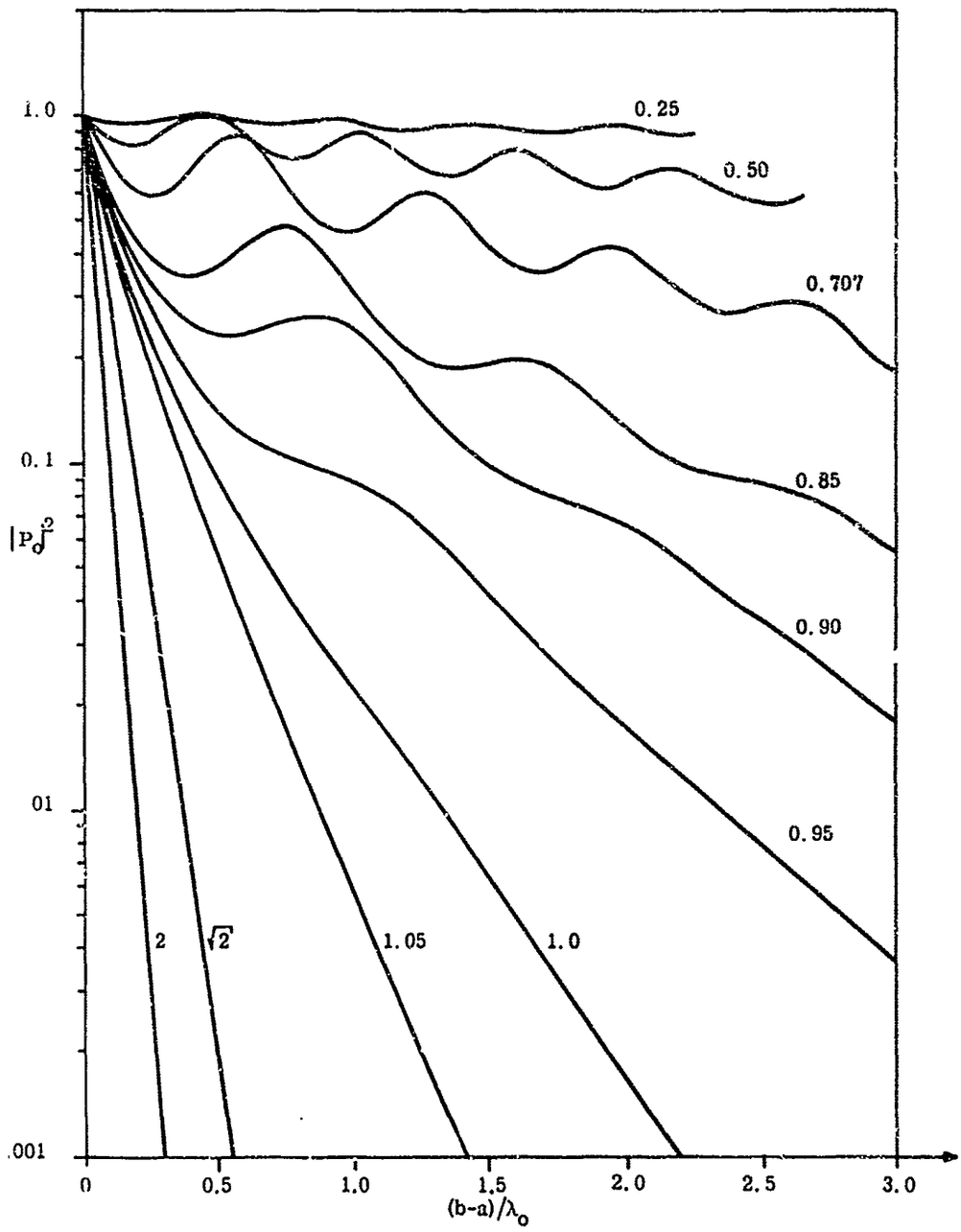

FIG. 3: RADIATION GRAPHS THROUGH UNIFORM CIRCULAR PLASMA SHEATH VS SHEATH THICKNESS FOR $a=1\lambda_o$, Y=0.1, AND X AS A PARAMETER

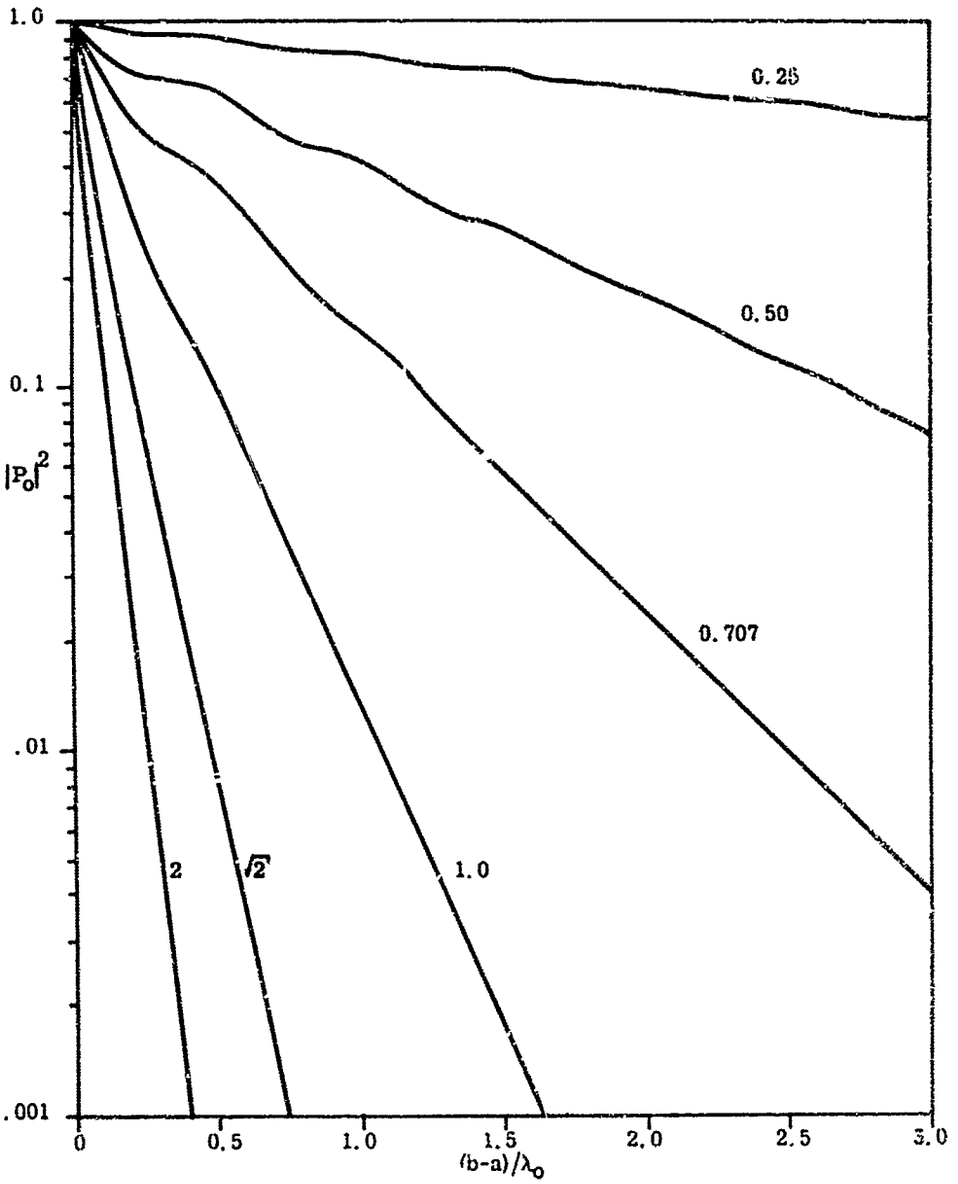

FIG. 4: RADIATION GRAPHS THROUGH UNIFORM CIRCULAR PLASMA SHEATH VS SHEATH THICKNESS FOR $a=1\lambda_o$, Y=1.0 AND X AS A PARAMETER

each case we may identify conditions where only one process is primarily causing the attenuation. Thus for $X < \sqrt{2}$ and Y=0.01 we see, in Fig. 2, the radiation graphs oscillating because of the reflections. As Y increases to 0.1 in Fig. 3, the amplitude of the oscillations decreases, and for Y=1 in Fig. 4, the oscillations are practically gone; but now the graphs have assumed a downward slope. This is caused by the absorptive attenuation in the plasma taking over and eliminating the reflections. Also, we see that we get quite a bit more attenuation for very lossy plasma (Y=1) than for very low loss plasma (Y=0.01). For the case of $X > \sqrt{2}$ the opposite is true; low loss plasma causes more attenuation than a very lossy plasma. This is due to the effectiveness of the reactive attenuation.

In Fig. 5, we show a 36° wedge slot in the plasma sheath, and in Figs. 6 to 14 we present the radiation power pattern $|P_s(\phi)|^2$ calculated from (48) for the sheath thickness of $0.5\lambda_0$, $1.0\lambda_0$ and $2.0\lambda_0$, respectively. The inside sheath radius is kept at $1.0\lambda_0$. The graphs have been arranged in sets of three: Y=1.0, 0.1 and 0.01, and X is a parameter in each set. Since the power patterns are even functions in ϕ, we have plotted them only from 0° to 180°. By the constant lines we show the attenuation in the power radiated before the plasma slot is introduced, i.e. the radiation power pattern for the unslotted plasma sheath. These lines are obtained from Figs. 2 to 4. In some cases the attenuation is so large that it is off scale. These values we will give in a note. As a way of calibration we mention that the radiation power pattern of unit amplitude would correspond to the electric line source radiating in the free space.

In Figs. 6, 7 and 8 we present the set Y=1. By opening a slot in this very lossy plasma we have, for all practical purposes, re-established radiation in the forward direction, i.e. ϕ=0, independent of the sheath thickness. Outside of the front lobe there is no significant recovery of the signal strength. Increased slot width, the calculations will show, narrows the front lobe with some additional gain

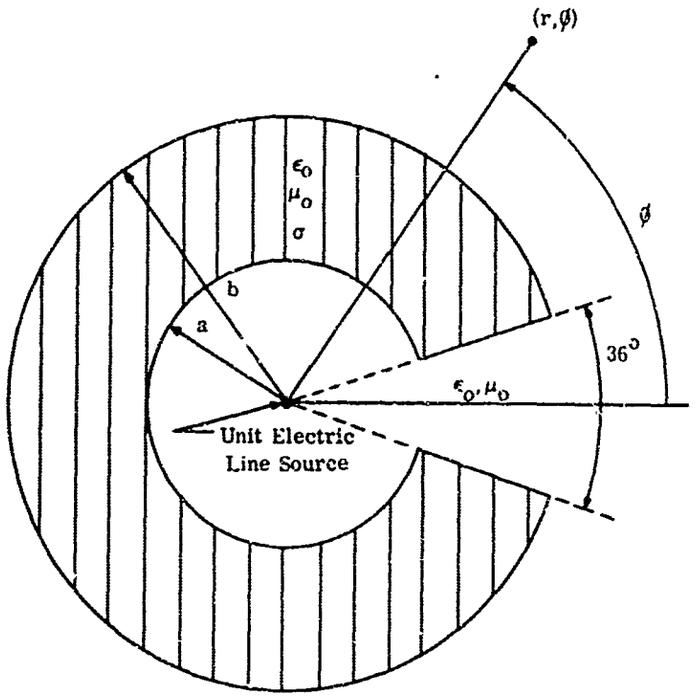

FIG. 5: PLASMA SHEATH WITH $a=1\lambda_o$, $b=2\lambda_o$, AND A 36^o WEDGE SLOT

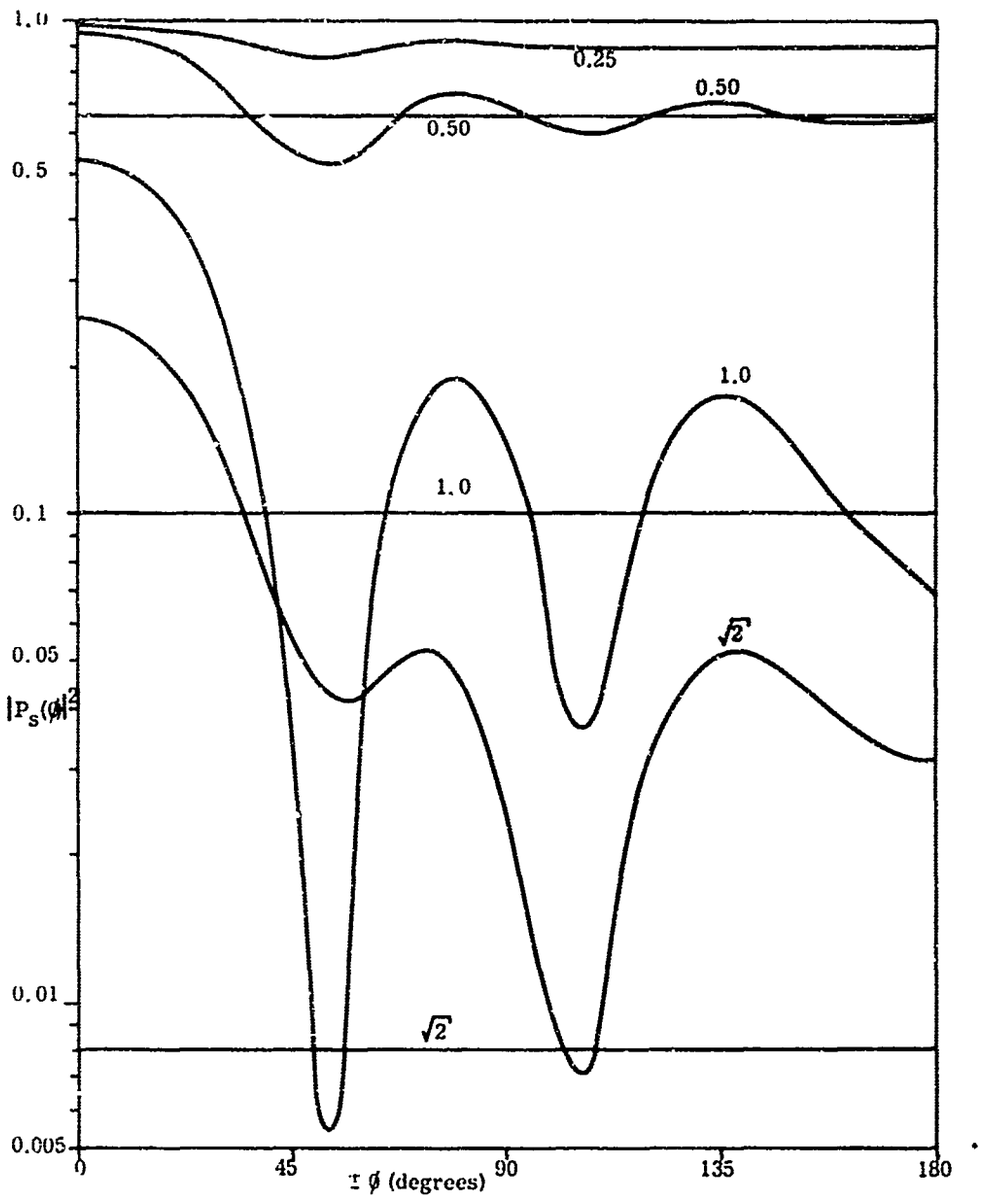

FIG. 6: RADIATION POWER PATTERNS FOR $0.5\lambda_0$ THICK PLASMA SHEATH WITH 36° WEDGE SLOT, Y=1, AND X AS A PARAMETER. The parallel lines are the corresponding patterns for the unslotted case.

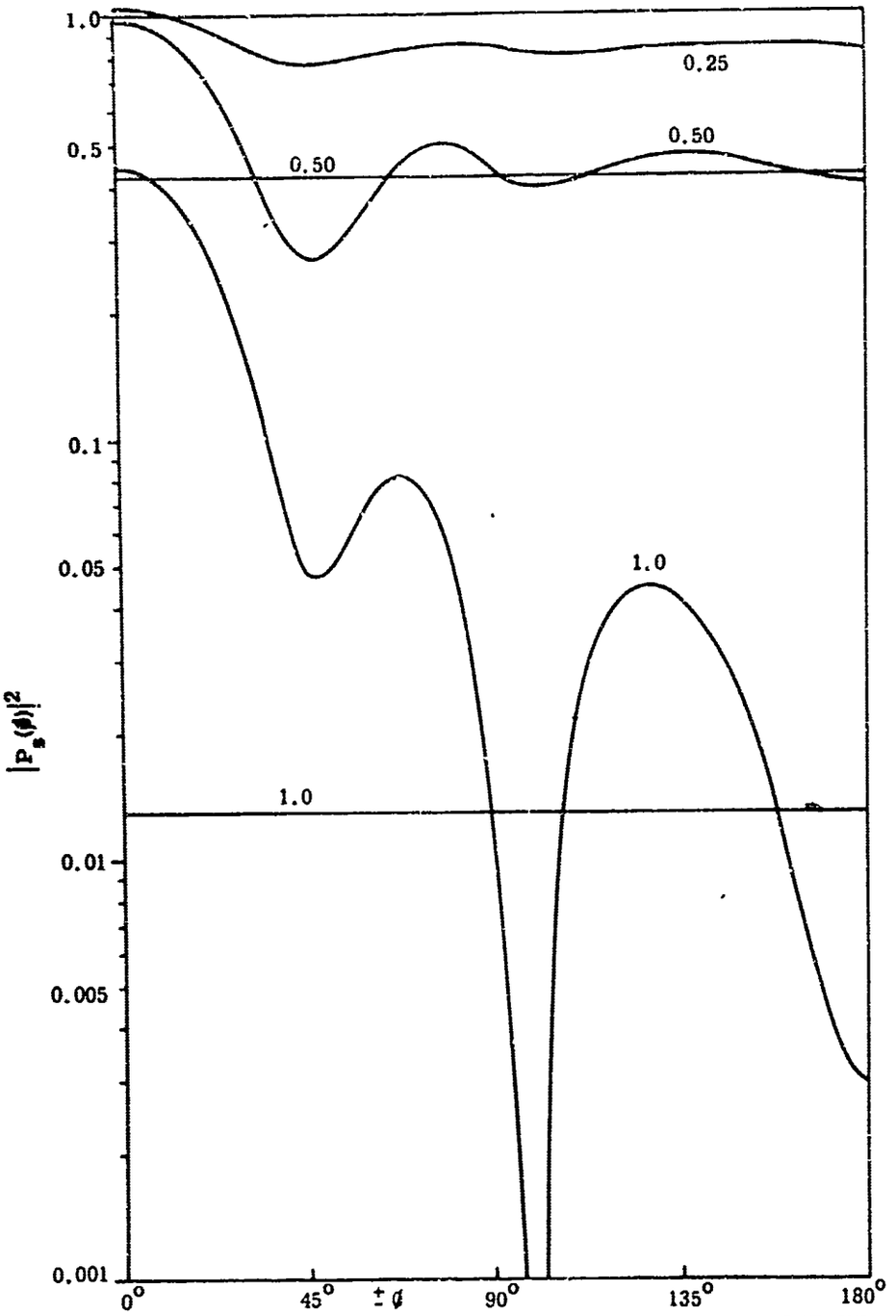

FIG. 7: RADIATION POWER PATTERN FOR 1.0λ_0 THICK PLASMA SHEATH WITH 36° WEDGE SLOT; Y=1, AND X AS A PARAMETER. Parallel lines are corresponding patterns for unslotted case.

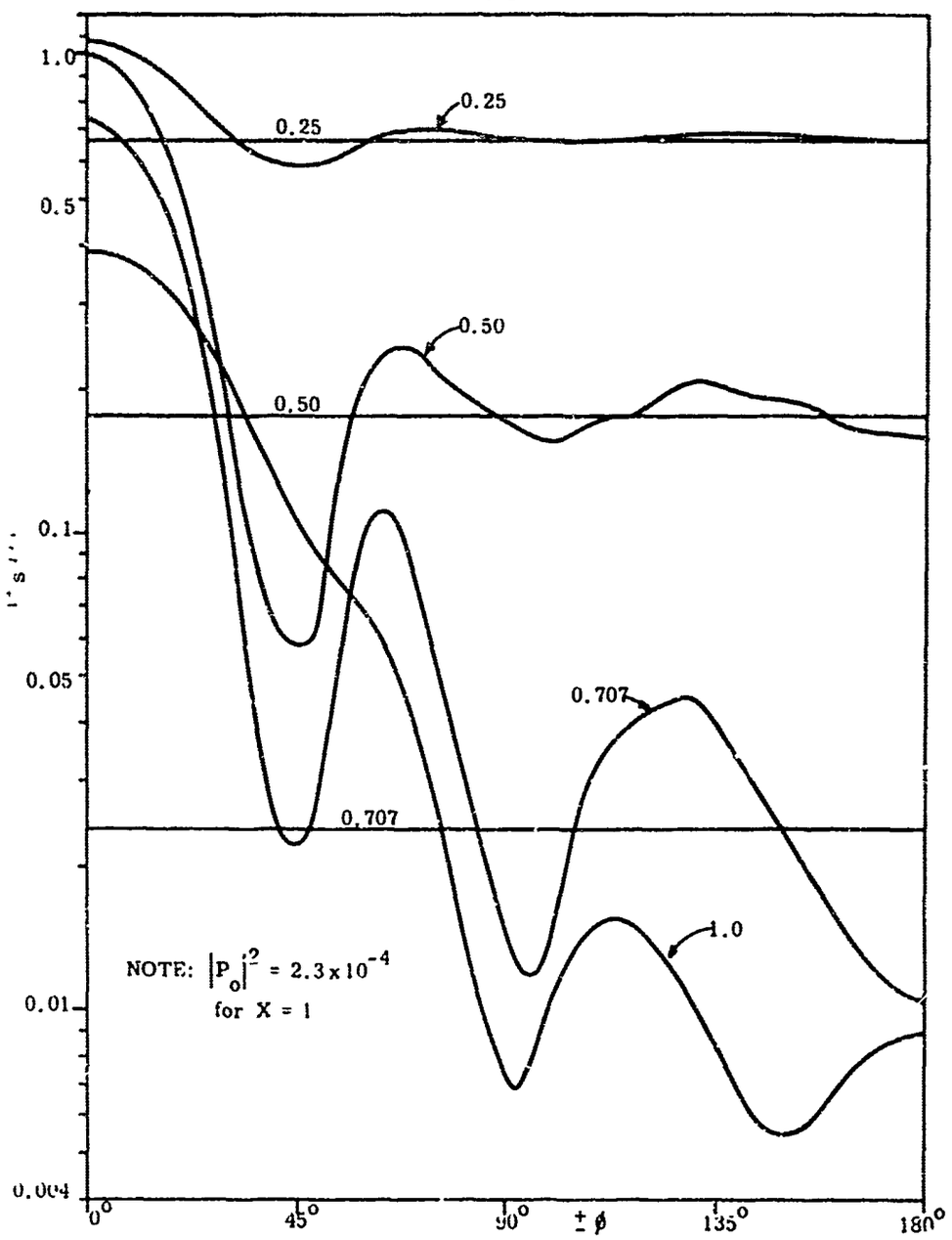

FIG. 8: RADIATION POWER PATTERN FOR 2.0λ THICK PLASMA SHEATH WITH A 36° WEDGE SLOT, Y = 1, AND X° AS A PARAMETER. The parallel lines are the corresponding patterns for the unslotted case.

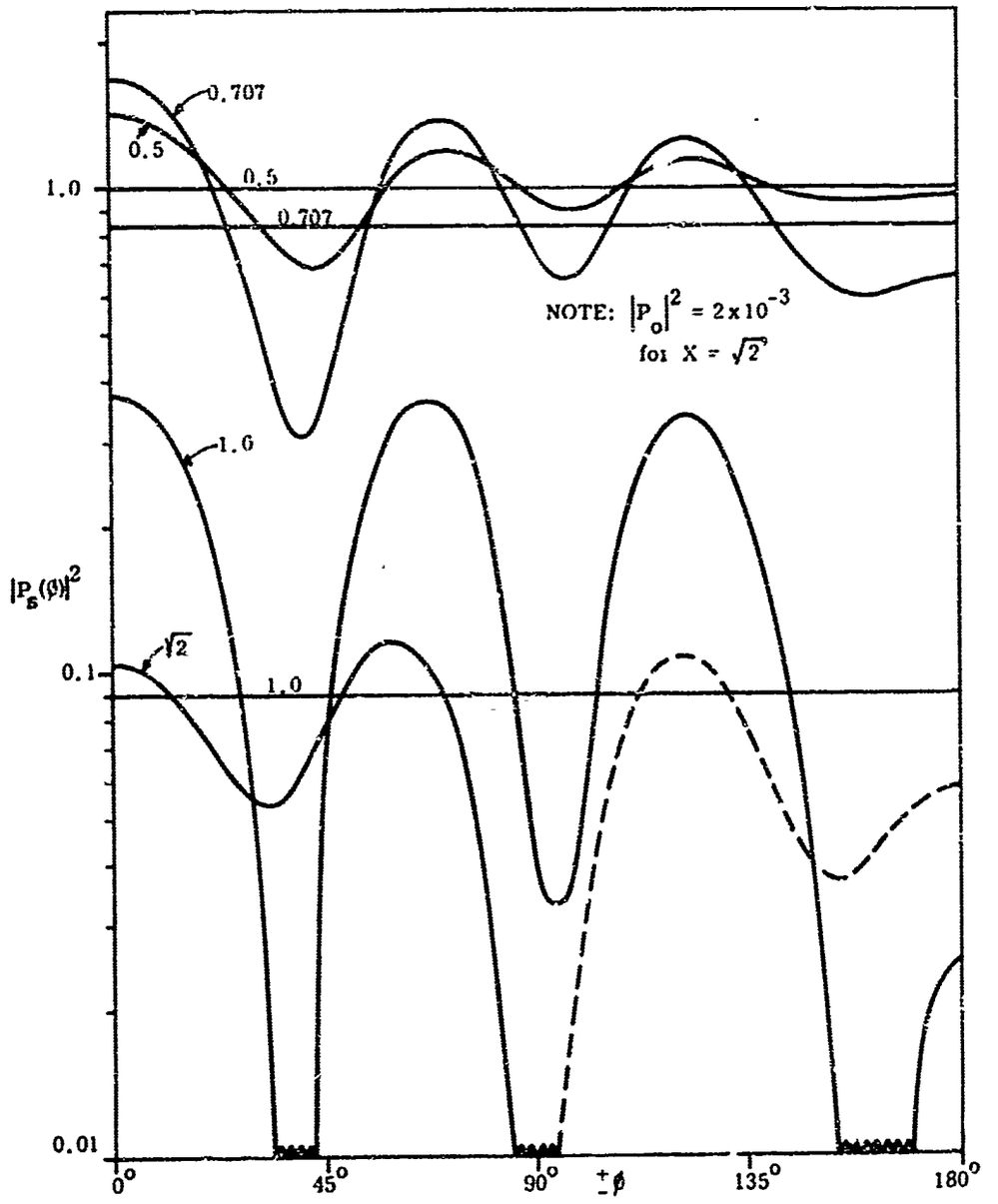

FIG. 9: RADIATION POWER PATTERN FOR 0.5λ THICK PLASMA SHEATH WITH A 36° WEDGE SLOT, Y=0.1, AND X AS A PARAMETER. The parallel lines are the corresponding patterns for the unslotted case.

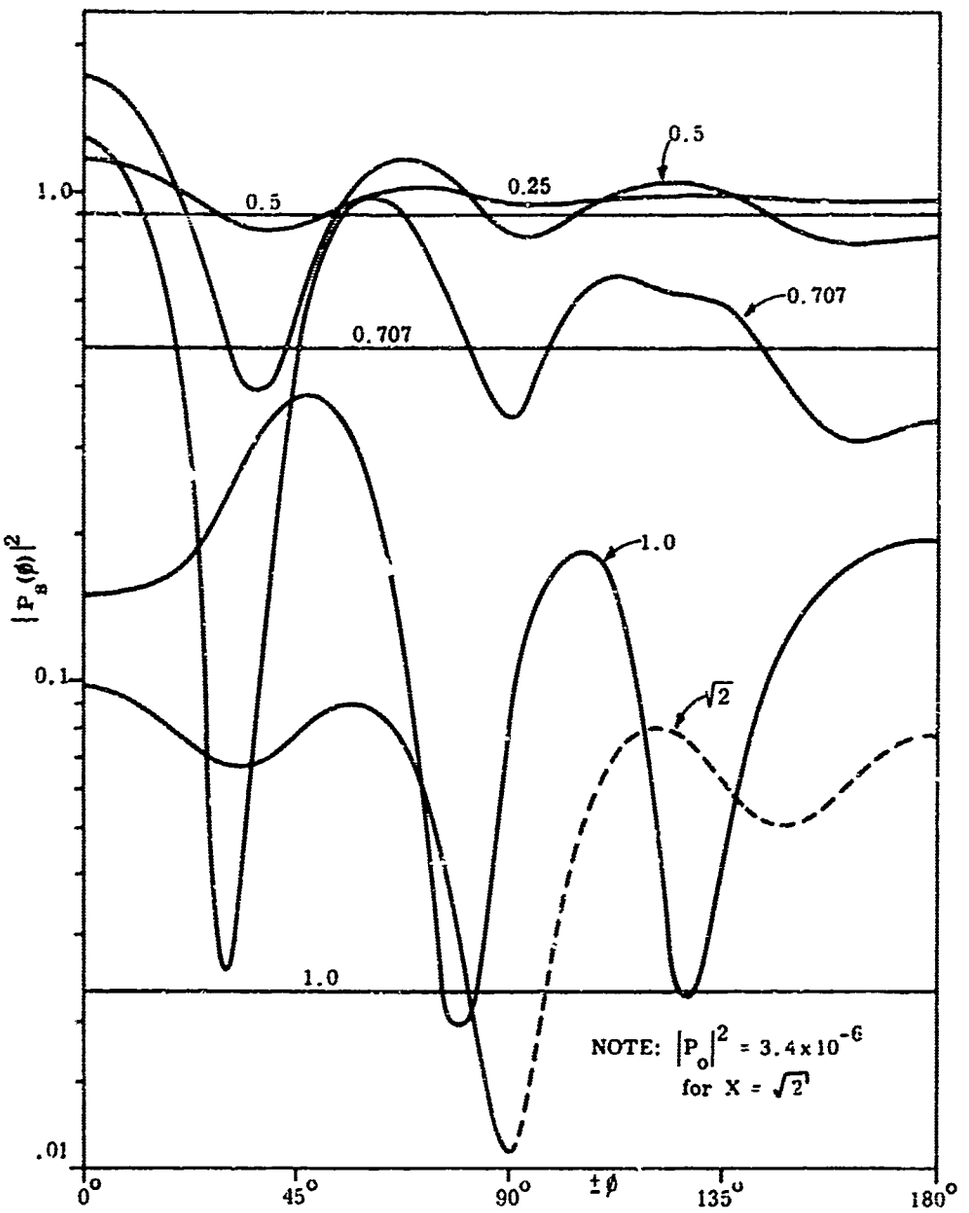

FIG. 10: RADIATION POWER PATTERN FOR 1.0λ THICK PLASMA SHEATH WITH A 36° WEDGE SLOT, Y = 0.1, AND X AS A PARAMETER. The parallel lines are the corresponding patterns for the unslotted case.

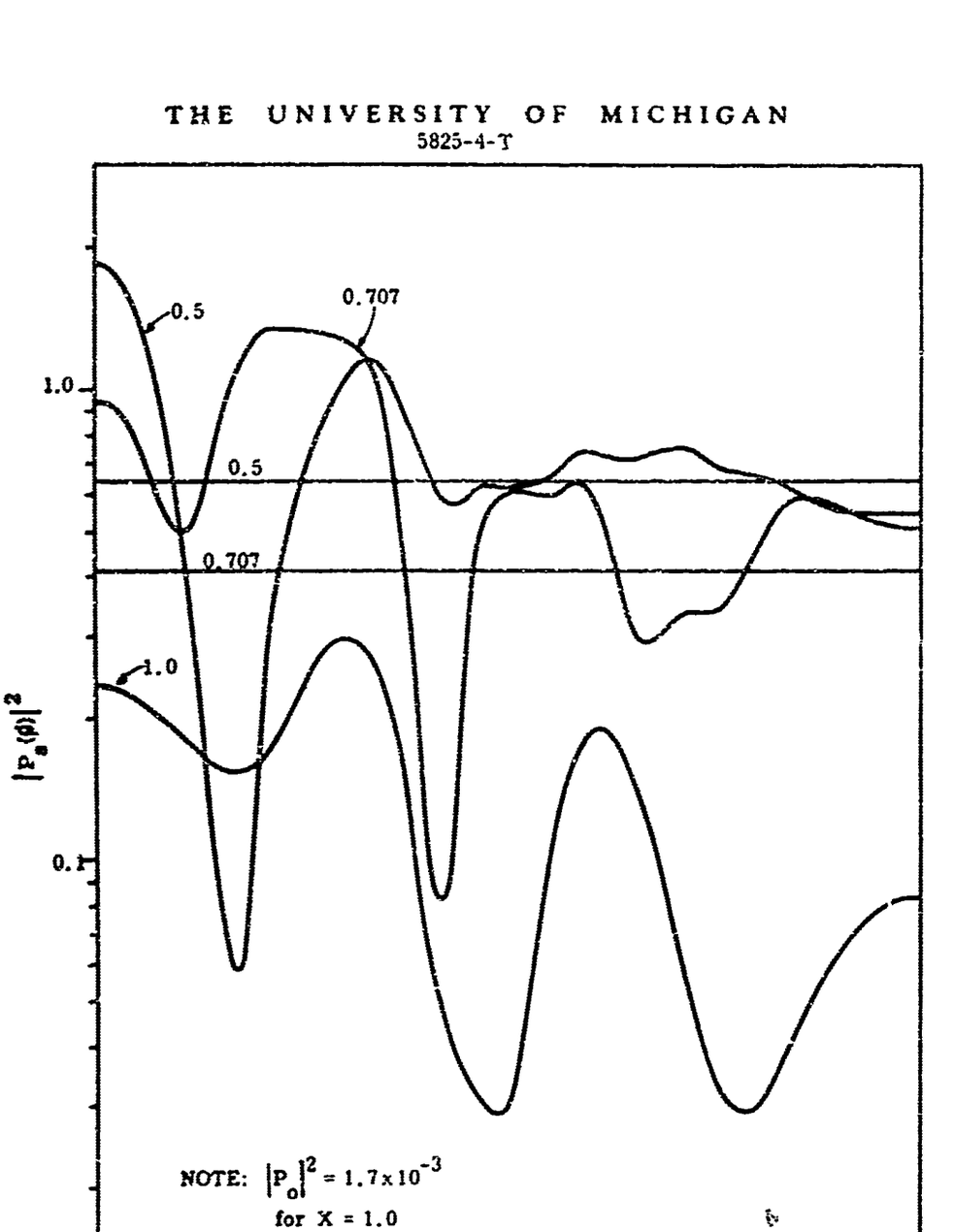

FIG. 11: RADIATION POWER PATTERN FOR $2.0\lambda_o$ THICK PLASMA SHEATH WITH 36° WEDGE SLOT; Y=0.1, AND X AS A PARAMETER. Parallel lines are corresponding patterns for unslotted case

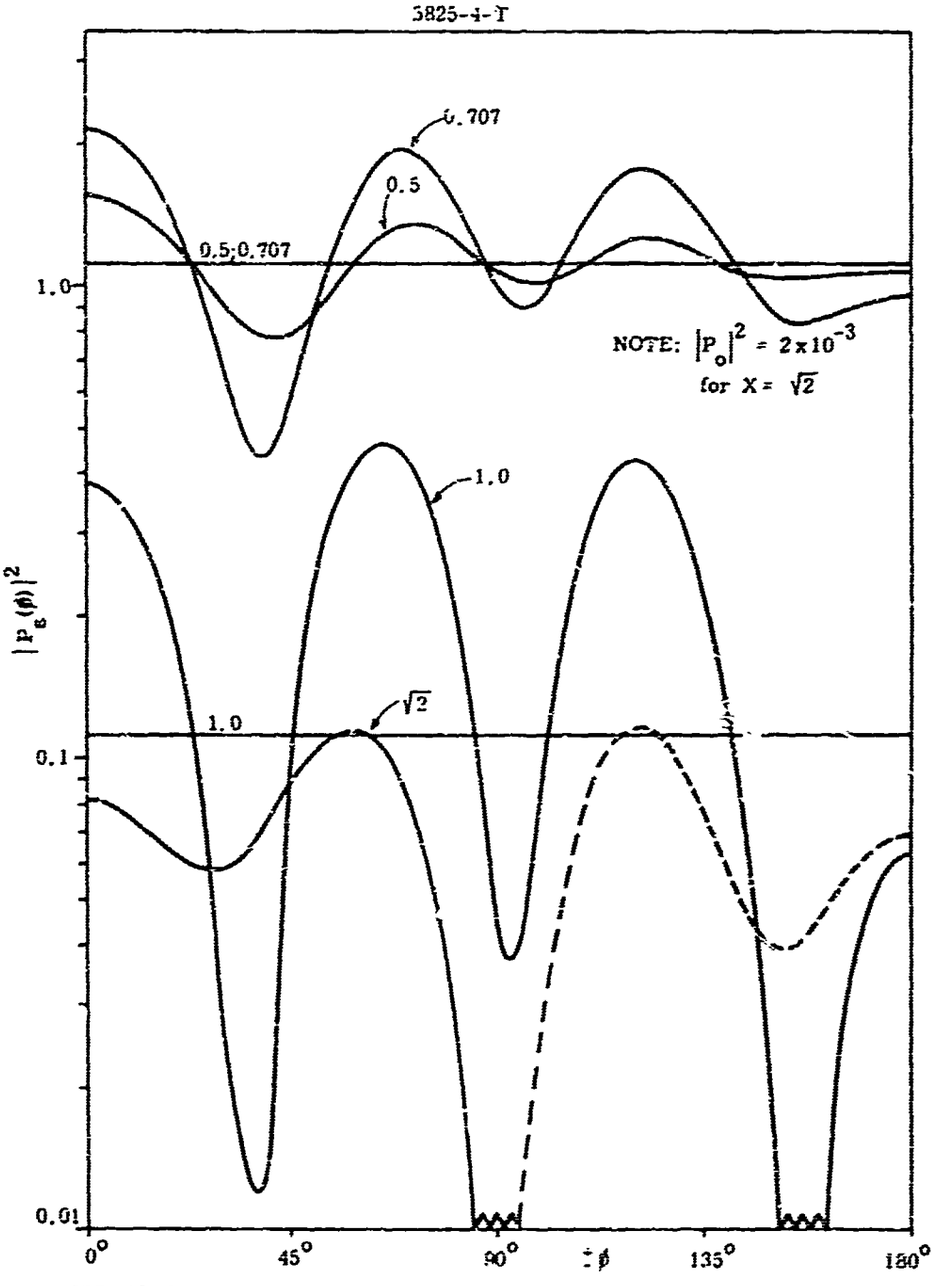

FIG. 12: RADIATION POWER PATTERN FOR $0.5\lambda_o$ THICK PLASMA SHEATH WITH A 36° WEDGE SLOT, Y = 0.01, AND X AS A PARAMETER. The parallel lines are the corresponding patterns for the unslotted case.

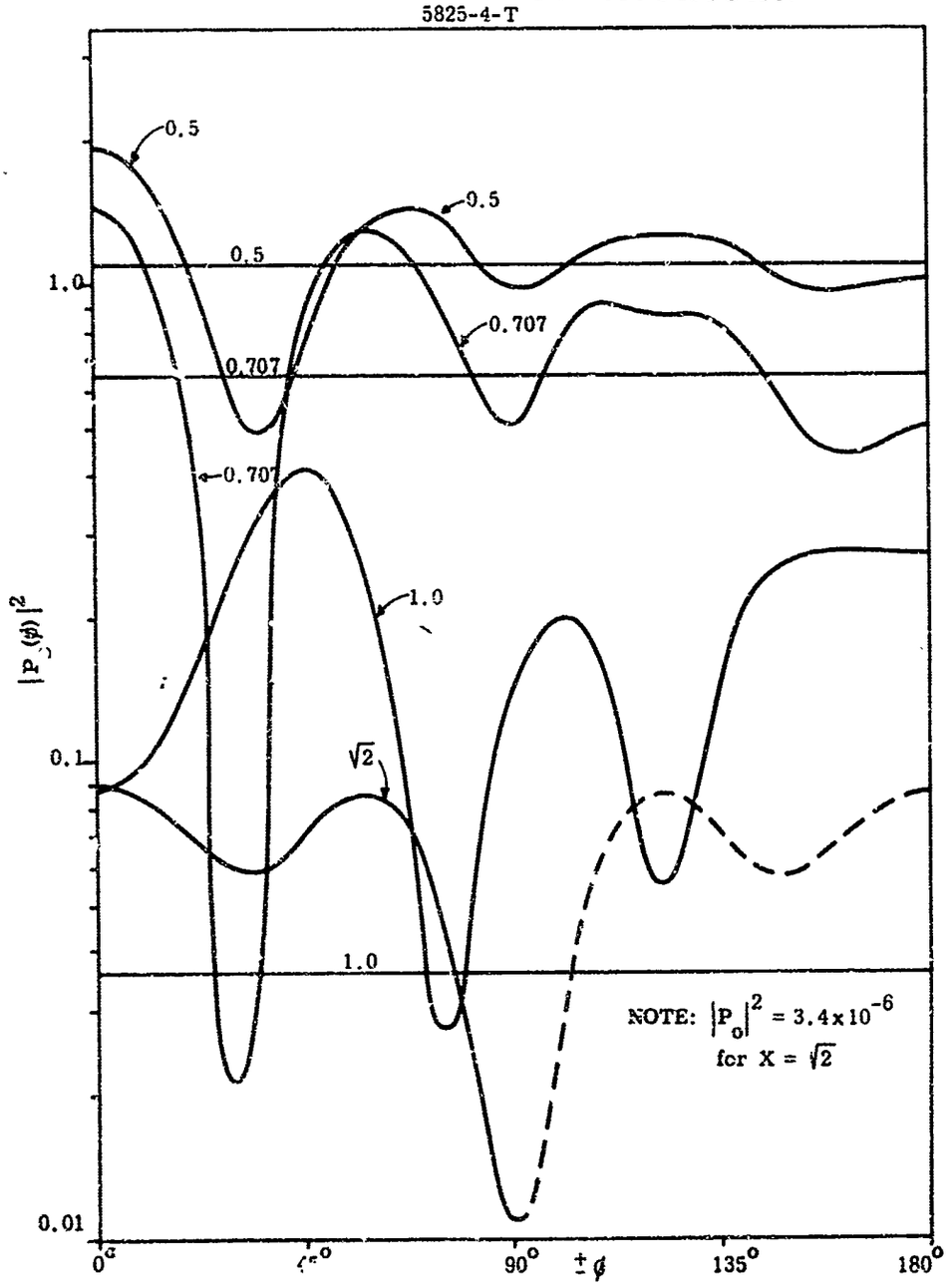

FIG. 13: RADIATION POWER PATTERN FOR $1.0\lambda_0$ THICK PLASMA SHEATH WITH A 36° WEDGE SLOT, Y = 0.01, AND X AS A PARAMETER. The parallel lines are the corresponding patterns for the unslotted case.

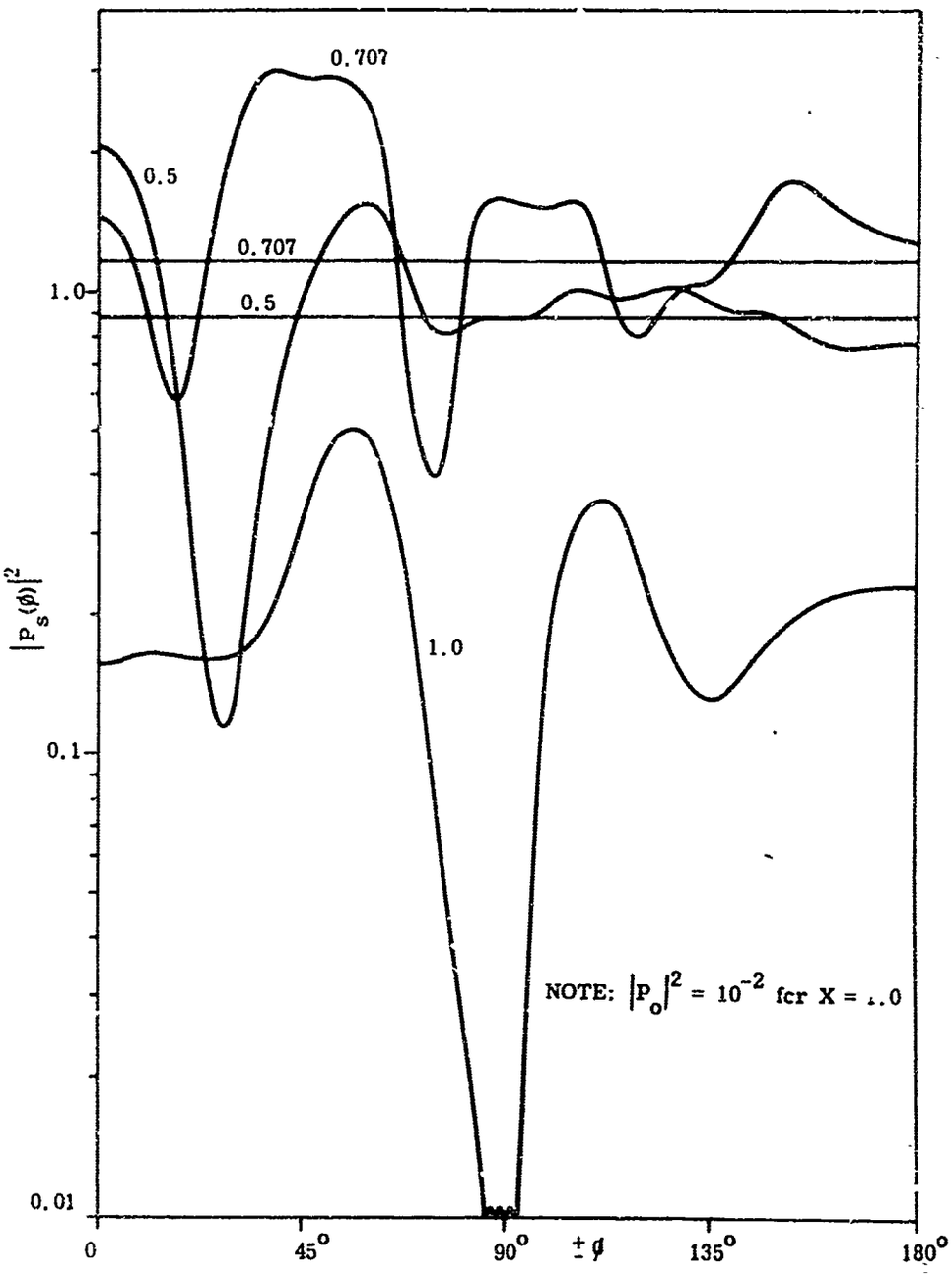

FIG. 14: RADIATION POWER PATTERN FOR 2.0λ THICK PLASMA SHEATH WITH A 36° WEDGE SLOT, Y = 0.01, AND X AS A PARAMETER. The parallel lines are the corresponding patterns for the unslotted case.

in the signal strength for $\beta=0$. If we halve the slot width, the forward lobe is considerably reduced with no benefit for the rest of the pattern.

In Figs. 9, 10 and 11 we present the set Y=0.1. By opening a slot in this sheath of "medium" lossy plasma we observe that for $X < 0.707$ the formerly uniform pattern breaks into oscillations. The radiation is enhanced slightly in the forward direction. The oscillating character for the pattern persists as X is increased, i.e. a dominant forward mode is not formed in the range of the validity of approximation, in contrast to the case of the very lossy plasma sheath. Sections of graphs for which the approximations are expected to break down are shown in the dotted line. For $X > 0.707$ the slot improves the radiation very substantially as compared to the sheath without a slot.

In Figs. 12, 13 and 14 we present the set Y=0.01, i.e. a very "low" loss plasma sheath. The comments for this one are substantially the same as for the previous case.

The sets of data have been presented as they were calculated. A dominating forward lobe formed for the Y=1 set. It came as a surprise that for Y=0.1 and 0.01 sets no such dominance was found. However, there is no doubt that a dominant forward lobe would develop as X is increased beyond $\sqrt{2}$. Only (48) is not then a valid approximation in the case of our thick sheath.

The method we have presented for calculating the radiation pattern for the slotted plasma sheath makes use of the electric currents in the plasma before the slot is opened. It is an approximate method which is expected to give the radiation pattern with good accuracy only if the electric currents sufficiently penetrate the plasma sheath. If the attenuation of the unslotted plasma sheath is more than 20 db, i.e. $|P_0|^2 < 0.01$, then we are approaching the bounds of validity of the approximation for the pattern as a whole. However, one expects that the forward lobe will be given to a good order of approximation even for somewhat larger attenuation

than 20 db, as was shown by calculations performed in (46)

If the attenuation of the unslotted plasma sheath is such that the radiation through it is practically insignificant, we then find that the electric currents penetrate the plasma only a small fraction of the free space wavelength. If we open a slot in the plasma under these conditions, the slot in fact becomes a waveguide which connects the source with the outside space. For suitable slot boundaries one can show that a finite number of modal fields can propagate in the slot waveguide. These modes may be used as a basis for calculating the radiation pattern. Work is in progress to exploit this waveguide approach for these cases where the integral equation method becomes too cumbersome. This work will be reported as Part II of this study.

The two significant conclusions indicated by this study are:

1) Opening a slot in the plasma sheath re-establishes radiation in the forward direction to a substantial level.

2) The plasma slot should be at least one-half wavelength wide at its narrowest cross section when the electric field is polarized tangential to the slot walls. Increasing the slot width beyond one-half wavelength brings only diminishing returns as far as the radiation enhancement in the forward direction is concerned.

VI REFERENCES

Harrington, R. F. (1961) Time-Harmonic Electromagnetic Fields, McGraw-Hill, pp. 223-232.

Mikhlin, S. G. (1964), Integral Equations, The MacMillan Co., p. 13.

Rose, D. R. and M. Clark, Jr. (1961), Plasmas and Controlled Fusion, MIT Press, p. 150.

ACKNOWLEDGEMENT

The author has benefited from discussions with Wm. F Croswell, F. Russo and T. E. Sims of the NASA-Langley Research Center and their colleagues. For the computations he thanks J. Klebers and E. K. Miller of the Radiation Laboratory.

V. THE EFFECT OF A FINITE CONICAL PLASMA SHEATH ON THE RADIATION FIELD OF A DIPOLE*

D. C. Pridmore-Brown
Aerospace Corporation, Los Angeles, California

ABSTRACT

The plasma sheath that forms about a reentry vehicle is simulated by a cone of finite slant height and negligible thickness. This cone can support surface currents that are induced in it by a Hertzian dipole antenna situated on its axis. The radiation pattern of such a structure at wavelengths long compared to the slant height is calculated using a Lobedev-Kontorovich integral transform together with the Wiener-Hopf technique. In the opposite limit, the radiation pattern is obtained by a perturbation technique. Plots are presented showing the effects of sheath strength, slant height, and antenna frequency on the patterns.

---

* This research was supported by the U.S. Air Force under Contract AF 04(695)-469.

I. INTRODUCTION

The present study is one of a series[1,2] undertaken to gain a better understanding of the role of diffraction effects or antenna pattern distortion in the so-called blackout problem. This term is commonly used to describe a sharp reduction in the effective transmission of information by radio between a reentry vehicle and a ground station. This reduction is observed as the vehicle enter he earth's atmosphere and becomes enveloped in a sheath of partially ionized gas or plasma. It is due partly to the ability of this plasma sheath to reflect electromagnetic waves and so alter the radiation impedance of the antenna; partly to the sheath's ability to spread waves into new directions, thus causing antenna pattern distortion; and partly to the fact that the plasma responds differently to different frequency components, which results in phase distortion. There will also be an additional damping of the signal by ohmic losses in the sheath, but this effect should be small in the case of plasma sheaths that are very thin compared to a wavelength.

As in previous studies, we shall restrict ourselves to a point-dipole antenna that is driven by a constant-current source at a single frequency. Thus we shall be mainly concerned with antenna pattern distortion. Two previous studies considered the case of a magnetic dipole antenna[1] and an electric dipole antenna[2] located axisymmetrically within a thin conical plasma sheath of infinite extent. The plasma was represented by a current sheet whose strength was calculated on the basis of a cold electron plasma. The results of these two cases showed that the electric dipole antenna generates a strong surface wave that carries most of the radiated energy out along the surface of the conical sheath, whereas no such wave is produced by the magnetic dipole antenna. In fact, it is clear that the magnetic dipole induces purely azimuthal currents in the conical sheath that are confined to the vicinity of the source for long wavelengths,

whereas the currents induced by the electric dipole run up and down along the generators of the cone. These facts suggest that the adoption of a more realistic model, consisting of a cone of finite slant height, may profoundly modify the radiation pattern in the electric dipole case, particularly if the wavelength is comparable to, or longer than, the cone's slant height. The present work is concerned with this case.

The problem is solved by Wiener-Hopf techniques using a Lebedev-Kontorovich integral transform. It reduces to an infinte set of algebraic equations which can be solved by iteration in the low-frequency limit. This method has already been employed in the problem of determining the scattering of plane acoustic waves by a rigid disc[3] and the impedance of a biconical antenna.[4] In the opposite limit, when the slant height is long compared to a wavelength but still finite, the problem is solved by a perturbation technique based on the known infinite-cone solution. These two techniques are used to calculate radiation patterns that show the manner in which the distortion fades and the radiation resistance gradually resumes its free-space value as the slant-height is reduced from infinity to zero.

II. ANALYSIS

We consider the radiation field of an elementary electric Hertzian dipole that is located on the axis of a thin partially-conducting conical sheath of finite slant height b. We adopt spherical coordinates centered at the apex of the cone, which then becomes the surface $\theta = \theta_0$, $0 \leq r \leq b$ (Fig. 1). The dipole source is at $r = a$, $\theta = 0$ and is oriented along the cone's axis so that the problem is axisymmetric. Since then all currents are purely radial, it is easily verified from Maxwell's equations that we can express the fields in terms of a single scalar potential $\Pi(r,\theta)$ such that

$$\underline{E} = \nabla \times \nabla \times (\underline{r}\Pi) \tag{1}$$

Using MKS units and suppressing a common time factor $e^{-i\omega t}$ we then find that $\Pi(r,\theta)$ satisfies the wave equation

$$(\nabla^2 + k^2)\,\Pi(r,\theta) = \frac{J(r,\theta)}{i\omega\varepsilon_0 r} \tag{2}$$

where $k^2 = \omega^2\mu_0\varepsilon_0$. The nonvanishing field components are

$$E_r = -\frac{1}{r}\left[\frac{1}{\sin\theta}\,\frac{\partial}{\partial\theta}\left(\sin\theta\,\frac{\partial}{\partial\theta}\right)\right]\Pi \tag{3}$$

$$E_\theta = \frac{1}{r}\,\frac{\partial^2}{\partial r\partial\theta}\left(r\Pi\right) \tag{4}$$

$$H_\phi = i\omega\varepsilon_0\,\frac{\partial\Pi}{\partial\theta} \tag{5}$$

Now the current density $\underset{\sim}{J} = J(r,\theta)\,\hat{c}_r$ is made up of the antenna current and the current induced in the sheath.

$$J(r,\theta) = -i\omega p\,\delta(r - a) + \sigma(r,\theta)E_r \tag{6}$$

Here p is the dipole moment of the antenna and $\sigma(r,\theta)$ the conductivity of the sheath; $\sigma(r,\theta)$ is taken to be zero everywhere except at the sheath itself, where it is assumed to be infinite in such a way as to allow induced sheet currents. Thus, we write it as follows

$$\sigma(r,\theta) = (i\omega\epsilon_0 r)\,\frac{2g}{\pi \sin\theta_0}\,\frac{1}{r}\,U(b - r)\delta(\theta - \theta_0) \tag{7}$$

in terms of a dimensionless sheath parameter g, the step function $U(b - r)$ ($= 1$ for $r < b$, 0 for $r > b$) and the delta function $\delta(\theta - \theta_0)$. It can be shown that, in terms of plasma parameters,[2]

$$g = \frac{\pi d}{2r}\,\sin\theta_0\,\frac{\omega_p^2}{\omega(\omega + i\nu_c)} \tag{8}$$

where ω_p and ν_c are plasma and electron collision frequencies, respectively, and d is the sheath thickness. In the calculations we shall assume that $\nu_c = 0$ and $\omega_p^2\,(d/r) = \text{const.}$, which makes g a positive real constant. The representation of a thin plasma slab by a current sheet in this way was first used by Wait.[5]

The solution to Eq. (2) can be represented formally as the solution to an integral equation

$$\Pi(r,\theta) = -\frac{1}{4\pi}\int_{\text{vol.}} \frac{e^{ik|\underset{\sim}{r}-\underset{\sim}{r}'|}}{|\underset{\sim}{r}-\underset{\sim}{r}'|}\left(\frac{J}{i\omega\varepsilon_0 r}\right) d^3r$$

$$= \frac{e^{ikR}}{R} + \frac{a}{\pi}\int_0^b dr' \int_0^{2\pi} \frac{d\phi}{2\pi} \frac{e^{ik|\underset{\sim}{r}-\underset{\sim}{r}'|}}{|\underset{\sim}{r}-\underset{\sim}{r}'|} \mathcal{L}\Pi(r',\theta_0) \qquad (9)$$

Here we have substituted for J from Eqs. (6) and (7); R is the source-to-receiver distance shown in Fig. 1, $\mathcal{L} = \frac{1}{\sin\theta}\frac{\partial}{\partial\theta}\left(\sin\theta\,\frac{\partial}{\partial\theta}\right)$ and we have suppressed a factor $(p/4\pi\varepsilon_0 a)$ for convenience.

A. LONG WAVELENGTH LIMIT

Although the integral equation (9) can be inverted exactly in the case of an infinite cone $(b = \infty)$[2], it does not appear to be possible to do so in general. In this part we present an analysis which yields the solution in the limit of long wavelengths, $\lambda >> b > a$. Part B will be devoted to the case $b > \lambda > a$.

We introduce the notation

$$\psi(r) = (ra)^{1/2}\mathcal{L}\Pi(r,\theta_0)\ , \quad \psi_0(r) = (ra)^{1/2}\mathcal{L}\left(\frac{e^{ikR}}{R}\right) \qquad (10)$$

$$\mathcal{H}(r,\theta|r',\theta') = (rr')^{1/2}\int_0^{2\pi}\frac{d\phi}{2\pi}\,\frac{e^{ik|\underset{\sim}{r}-\underset{\sim}{r}'|}}{|\underset{\sim}{r}-\underset{\sim}{r}'|} \qquad (11)$$

$$\Pi_0(r,\theta) = \frac{e^{ikR}}{R} = (ra)^{-1/2}\,\mathcal{H}(r,\theta|a,0) \qquad (12)$$

in terms of which Eq. (9) becomes

$$\Pi(r,\theta) = \Pi_0(r,\theta) + (ra)^{-1/2}\,\frac{a}{\pi}\int_0^b \mathcal{H}(r,\theta|r',\theta_0)\,\psi(r')\,\frac{dr'}{r'} \qquad (13)$$

This equation expresses $\Pi(r,\theta)$ at any point in terms of the values of $\psi(r)$ on the sheath. Notice that $\psi(r) = -r^{3/2}\, a^{1/2}\, E_r(r,\theta_o)$, so $g\psi(r)$ is proportional to the induced current. If we operate on both sides of Eq. (13) by $\mathcal{L}$ and let $\theta \to \theta_o$ we obtain the following integral equation for $\psi(r)$

$$\psi(r) = \psi_o(r) + \frac{g}{\pi}\int_0^b G(r|r')\ \psi(r')\ \frac{dr'}{r'} \tag{14}$$

where we have introduced $G(r|r') = \mathcal{L}\mathcal{H}(r,\theta_o|r',\theta_o)$.

1. Spectral Analysis of the Integral Equation

We now obtain the Lebedev transform of Eq. (14) by multiplying both sides of it by $K_\nu(\gamma r)dr/r$ and then integrating over r from 0 to ∞. Here $K_\nu(\gamma r)$ is a hyperbolic Bessel function and $\gamma = -ik$. The result is, formally

$$\int_0^\infty \psi(r)\ K_\nu(\gamma r)\ \frac{dr}{r} = \int_0^\infty \psi_o(r)\ K_\nu(\gamma r)\ \frac{dr}{r} + \frac{g}{\pi}\int_0^\infty \frac{dr}{r}\, K_\nu(\gamma r)\int_0^b \frac{dr'}{r'}\ G(r|r')\ \psi(r') \tag{15}$$

These integrals will converge provided $r^{-1}\ \psi(r)\ K_\nu(\gamma r)$ is integrable at the origin. We return to this point later.

We next introduce the following integral representation

$$\mathcal{H}(r,\theta|r',\theta') = \frac{1}{i}\int_{c-i\infty}^{c+i\infty} \frac{\nu d\nu}{\cos\nu\pi}\, P_{\mu-1/2}(\cos\theta_<)P_{\mu-1/2}(-\cos\theta_>)I_\mu(\gamma r)K_\mu(\gamma r')$$

$$(|c| < 1/2) \tag{16}$$

which can be deduced from the well-known expansion for the potential of a ring source[6]

$$\mathcal{G}(r,\theta|r',\theta') = \sum_{n=0}^{\infty} (2n+1)\, P_n(\cos\theta)\, P_n(\cos\theta')\, I_{n+1/2}(\gamma r_<)\, K_{n+1/2}(\gamma r_>) \tag{17}$$

This expansion converges for all γ (real or imaginary). Here $\theta_<$, $\theta_>$ stand respectively for the lesser and the greater of θ and θ', and similarly for $r_<$ and $r_>$. To establish the equivalence of Eqs. (16) and (17), notice that as $|\mu| \to \infty$ ($\mu \neq \pm 0, \pm 1, 2, \ldots$)

$$\mu I_\mu(x)\, K_\mu(y) \sim \frac{1}{2}\left[\left(\frac{x}{y}\right)^\mu + \frac{\Gamma(-\mu)}{\Gamma(\mu)}\left(\frac{1}{4}\,xy\right)^\mu\right] \tag{18}$$

$$\left|\sec \mu\pi P_{\mu-1/2}(\cos\theta_<)\, P_{\mu-1/2}(-\cos\theta_>)\right| \sim |\mu|^{-1} \exp\left[-|\mathrm{Im}(\mu)|(\theta_>-\theta_<)\right] \tag{19}$$

[see Appendix A, Eqs. (A-1), (A-2) and (A-13)], so Eq. (16) converges absolutely, provided we assume (temporarily) that $\gamma = -ik$ is real. Furthermore the integration path can be closed by a semicircle at infinity in the right-hand plane if $r' > r$. If this is not the case, one can appeal to the relation [see Eq. (A-3)] which exists between the hyperbolic Bessel functions to show that for any even function $f(\mu)$ [such that $f(\mu) = -f(-\mu)$]

$$\int_{-i\infty}^{i\infty} f(\mu)\left[I_\mu(x)\, K_\mu(y) - I_\mu(y)\, K_\mu(x)\right]\mu\, d\mu = 0 \tag{20}$$

Consequently r and r' can be freely interchanged in Eq. (16) provided the integration path is taken along the imaginary axis ($c =$). Finally use of Cauchy's theorem together with Eq. (A-11) leads to Eq. (17).

From Eq. (16) we deduce also the integral representations for $G(r|r')$ and $\psi_o(r)$

$$G(r|r') = -\frac{1}{i}\int_{c-i\infty}^{c+i\infty} \frac{\mu d\mu}{\cos\mu\pi}\,(\mu^2 - 1/4)P_{\mu-1/2}(\cos\theta_o)P_{\mu-1/2}(-\cos\theta_o)I_\mu(\gamma r)K_\mu(\gamma r') \tag{21}$$

$$\psi_o(r) = -\frac{1}{i}\int_{c-i\infty}^{c+i\infty} \frac{\mu d\mu}{\cos\mu\pi}\,(\mu^2 - 1/4)P_{\mu-1/2}(-\cos\theta_o)I_\mu(\gamma r)K_\mu(\gamma r')$$

$$(|c| < 1/2) \tag{22}$$

Here we have used the fact that $(\mathcal{L} + \mu^2 - 1/4)P_{\mu-1/2}(\cos\theta) = 0$.

Let us now introduce Eq. (21) into Eq. (15) and reverse the order of the μ and r integration. The integration over r can then be carried out immediately by virtue of Eq. (A-8), and we find

$$\int_0^\infty \frac{dr}{r} K_\nu(\gamma r)G(r|r') = -\frac{1}{i}\int_{c-i\infty}^{c+i\infty} \frac{\mu d\mu}{\cos\mu\pi}\,\frac{\mu^2-1/4}{\mu^2-\nu^2}\,P_{\mu-1/2}(\cos\theta_o)P_{\mu-1/2}(-\cos\theta_o)K_\mu(\gamma r')$$

$$(1/2 > c > |\mathrm{Re}(\nu)|$$

$$= -\pi\,\frac{\nu^2-1/4}{\cos\nu\pi}\,P_{\nu-1/2}(\cos\theta_o)P_{\nu-1/2}(-\cos\theta_o)K_\nu(\gamma r') \tag{23}$$

Similarly,

$$\int_0^\infty \frac{dr}{r} K_\nu(\gamma r)\psi_o(r) = -\pi\,\frac{\nu^2-1/4}{\cos\nu\pi}\,P_{\nu-1/2}(-\cos\theta_o)K_\nu(\gamma a) \tag{24}$$

Here the integration over u was performed by noticing that because the integrand is odd in μ the integration path can be closed on the imaginary axis. Introducing these expressions into Eq. (15) we find

$$\frac{D(\nu)}{\cos\nu\pi}\int_0^b \psi(r)\, I_\nu(\gamma r)\,\frac{dr}{r} + \int_b^\infty \psi(r)\, K_\nu(\gamma r)\,\frac{dr}{r} = \int_0^\infty \psi_0(r)\, K_\nu(\gamma r)\,\frac{dr}{r} \tag{25}$$

where

$$D(\nu) = \cos\nu\pi + \frac{\pi}{2}\left(\nu^2 - \frac{1}{4}\right) P_{\nu-1/2}(\cos\theta_0)\, P_{\nu-1/2}(-\cos\theta_0) \tag{26}$$

This is an integral equation involving two unknown functions of ν, viz., $\int_0^b \psi(r) K_\nu(\gamma r) r^{-1}\, dr$ and $\int_b^\infty \psi(r)\, K_\nu(\gamma r) r^{-1}\, dr$. In general we must resort to complex variable techniques to solve it, but first let us consider the limiting case of an infinite cone ($b \to \infty$).

2. Infinite Cone Limit

Denoting this case by the subscript ∞ we have from Eqs. (24) and (25)

$$\int_0^\infty \psi_\infty(r)\, K_\nu(\gamma r)\,\frac{dr}{r} = -\pi\,\frac{\nu^2 - 1/4}{D(\nu)}\, P_{\nu-1/2}(-\cos\theta_0)\, K_\nu(\gamma a) \tag{27}$$

Introducing Eq. (16) into Eq. (13) and making use of Eq. (27) we find

$$\Pi_\infty(r,\theta) = \Pi_0(r,\theta) + (ra)^{-1/2}\,\frac{g}{\pi}\int_{-i\infty}^{i\infty}\frac{dr'}{r'}\,\psi_\infty(r') \cdot \frac{1}{I}\int_{-i\infty}^{i\infty}\frac{\mu d\mu}{\cos\mu\pi}\,P_{\mu-1/2}(\cos\theta_<)$$

$$\cdot\, P_{\mu-1/2}(-\cos\theta_>)\; I_\mu(\gamma r)\; K_\mu(\gamma r')$$

$$= \Pi_0(r,\theta) + (ra)^{-1/2} i g \int_{-i\infty}^{i\infty}\frac{\mu d\mu}{\cos\mu\pi}\;\frac{\mu^2-1/4}{D(\mu)}\,P_{\mu-1/2}(\cos\theta_<)P_{\mu-1/2}(-\cos\theta_>)$$

$$\cdot\, P_{\mu-1/2}(-\cos\theta_0)\cdot I_\mu(\gamma r)\; K_\mu(\gamma a)$$

$$= \Pi_0(r,\theta) + i\,(ra)^{-1/2}\int_{-i\infty}^{i\infty}\mu d\mu\left[\frac{1}{\cos\mu\pi} - \frac{1}{D(\mu)}\right]\frac{P_{\mu-1/2}(\cos\theta_<)P_{\mu-1/2}(-\cos\theta_>)}{P_{\mu-1/2}(\cos\theta_0)}$$

$$\cdot\, I_\mu(\gamma r)\; K_\mu(\gamma a)$$

Here $\theta_<$, $\theta_>$ refer to θ and θ_0. Comparison of the first integral with Eqs. (12) and (16) reveals that it exactly cancels $\Pi_0(r,\theta)$. Thus we are left with

$$\Pi_\infty(r,\theta) = (ra)^{-1/2} \cdot \frac{1}{I}\int_{-i\infty}^{i\infty}\frac{\mu d\mu}{D(\mu)}\;\frac{P_{\mu-1/2}(\cos\theta_<)\;P_{\mu-1/2}(-\cos\theta_>)}{P_{\mu-1/2}(\cos\theta_0)} \cdot I_\mu(\gamma r)\; K_\mu(\gamma a) \tag{28}$$

This solution has already been studied in some detail in a previous paper.[2] There it was shown that it can be expressed as a summation over the roots of $D(\mu) = 0$, these being the orders of those Legendre functions

$P_{\mu-1/2}(\pm\cos\theta)$ that compose the natural eigenfunctions for the infinite cone. One result of that study that we must make use of in the present paper concerns the behavior of the solution in the vicinity of the apex of the cone, namely the fact that $\psi_\infty(r) \sim \text{const } r^\epsilon$ as $r \to 0$ where $\epsilon = |\mathrm{Re}(\nu_0)|$ and $\pm\nu_0$ is that pair of zeros of Eq. (26) which is nearest the imaginary axis. If we allow a small amount of dissipation in the sheath so that $\nu_c > 0$ and consequently $\mathrm{Im}(g) < 0$, then it was shown[2] that $\epsilon > 0$, and, in fact, $\epsilon \to 0$ uniformly as $\nu_c \to 0$. Since $D(\mu)$ is even in μ, this means that there is a strip $|\mathrm{Re}(\mu)| < \epsilon$ containing the imaginary axis where $D(\mu)$ has no zeros. Now the behavior of $\psi(r)$ near the apex must be like that of ψ_∞ from which we conclude that the first integral in Eq. (25) converges within this strip. Thus Eq. (25) is to be considered as defined within the strip $|\mathrm{Re}(\nu)| < \epsilon = |\mathrm{Re}(\nu_0)|$.

We now take up the task of finding a solution to Eq. (27) in the general case of a cone of finite slant height b. To do this we regard Eq. (27) as a Wiener-Hopf problem and try to express each of the terms appearing in it as sums or products of analytic functions of ν that are holomorphic in overlapping half-spaces of the complex ν plane and behave suitably at infinity.

3. Wiener-Hopf Decomposition

Consider first the second term in Eq. (25). Since $K_\nu(\gamma r)$ is an even integral function of ν, it is clear that the same is true of this term. Using the asymptotic form of $K_\nu(\gamma r)$ given in Eq. (A-5) we find as $|\nu| \to \infty$

$$2\int_b^\infty \psi(r)K_\nu(\gamma r)\,\frac{dr}{r} \sim \frac{\Gamma(\nu)}{(\gamma b/2)^\nu}\int_b^\infty \psi(r)\left(\frac{b}{r}\right)^\nu \frac{dr}{r} + \frac{\Gamma(-\nu)}{(\gamma b/2)^{-\nu}}\int_b^\infty \psi(r)\left(\frac{b}{r}\right)^{-\nu}\frac{dr}{r} \qquad (29)$$

Thus the behavior at infinity is determined by that of $\psi(r)$ near $r = b$, and this is given by the edge condition[7]

$$\psi(r) \sim (r - b)^{-p} \text{ as } r \to b^{+} \tag{30}$$

where $p \leq 1/2$, the equality holding for an infinitely conducting cone. Thus we write

$$\int_b^{\infty} \psi(r) K_{\nu}(\gamma r) \frac{dr}{r} = \frac{\Gamma(\nu)}{(\gamma b/2)^{\nu}} \mathcal{E}^{+}(\nu) \tag{31}$$

where $\mathcal{E}^{+}(\nu)$ is an integral function of ν. From Eqs. (29) and (30) we deduce that $\mathcal{E}^{+}(\nu) \to 0$ as $|\nu| \to \infty$ in any right-hand half-plane, $\mathrm{Re}(\nu) > \infty$.

In a similar way consider

$$\int_0^b \psi(r) K_{\nu}(\gamma r) \frac{dr}{r} = \frac{1}{2} \Gamma(\nu)\Gamma(-\nu) \left[\int_0^b \psi(r) \nu I_{-\nu}(\gamma r) \frac{dr}{r} - \int_0^b \psi(r) \nu I_{\nu}(\gamma r) \frac{dr}{r} \right]$$

$$= \frac{\Gamma(\nu)}{(\gamma b/2)^{\nu}} \mathcal{E}^{-}(\nu) + \frac{\Gamma(-\nu)}{(\gamma b/2)^{-\nu}} \mathcal{E}^{-}(-\nu) \tag{32}$$

As pointed out in the last section, this expression is holomorphic in $|\mathrm{Re}(\nu)| > c$ and hence, by symmetry the first and second terms on the right are holomorphic respectively in the overlapping half-planes $\mathrm{Re}(\nu) > -c$ and $\mathrm{Re}(\nu) < c$. Furthermore assuming the edge condition $\psi(r) \sim \text{const}$ as $r \to b^{-}$ we deduce that

$$\mathcal{E}^{-}(\nu) = O(\nu^{-1}) \text{ in } \mathrm{Re}(\nu) < c \tag{33}$$

It remains to consider the coefficient $D(\nu)/\cos\nu\pi$. We should like to be able to write it as a ratio of functions holomorphic respectively in left and right half-planes. Now it has been demonstrated[2] that for real ν $D(\nu)$ has simple zeros along the real axis which are in one-one correspondence with those of $\cos\nu\pi$. In fact, denoting the zeros of $D(\nu)$ by ν_s it was shown that

$$\pm\nu_s = s + 1/2 + \delta_s, \qquad s = 1,2,... \tag{34}$$

where $0 \leq \delta_s < 1$. In addition $D(\nu)$ has a pair of zeros situated near the imaginary axis that we denote by $\pm\nu_0$. Thus $D(\nu)/\cos\nu\pi$ has simple zeros at $\nu = \pm\nu_s$, $s = 0, 1, 2, \ldots$, and simple poles at $\nu = \pm(s + 1/2)$, $s = 1,2,\ldots$. (The zeros of $D(\nu)$ at $\nu = \pm 1/2$ are cancelled by those of $\cos\nu\pi$.) These facts suggest the possibility of writing $D(\nu)/\cos\nu\pi$ in terms of infinite products

$$\frac{D(\nu)}{\cos\nu\pi} = D(0)\left(1 + \nu/\nu_0\right)\mathcal{D}^+(\nu)\cdot\left(1 - \nu/\nu_0\right)\mathcal{D}^+(-\nu) \tag{35}$$

$$\mathcal{D}^+(\nu) = \prod_{s=1}^{\infty}\left[\frac{1 + \nu/\nu_s}{1 + \nu/(s + 1/2)}\right] = \prod_{s=1}^{\infty}\left[1 - \frac{\nu\,\delta_s}{(s + 1/2 + \delta_s)(s + 1/2 + \nu)}\right] \tag{36}$$

It is clear that $\mathcal{D}^+(\nu)$ converges and is non-zero for $\mathrm{Re}\{\nu\} > -3/2$ and, furthermore, that it tends to zero as $|\nu| \to \infty$ in this half-plane. To determine its rate of fall-off at infinity consider the asymptotic

rm of D(ν), given by using Eq. (A10) in Eq. (26)

$$D(\nu) \sim \frac{2g}{\pi \sin\theta_o} \nu \cos(\nu\theta_o - \pi/4) \cos(\nu\pi - \nu\theta_o - \pi/4) \tag{37}$$

· ν tends to infinity along rays making a finite angle with the real
cis

$$\left|\frac{D(\nu)}{\cos\nu\pi}\right| \sim \frac{g}{\pi \sin\theta_o} |\nu| \qquad |\nu| \to \infty, \arg(\nu) \neq 0,\pi \tag{38}$$

rom this we can deduce that

$$\mathcal{D}^+(\nu) = O(|\nu|^{-1/2}) \quad \text{in} \quad \mathrm{Re}(\nu) > -3/2 \tag{39}$$

We now attempt to separate Eq. (25) by multiplying by $(\gamma b/2)^\nu/\Gamma(\nu)$ and making use of Eqs. (24), (31), (32), and (35).

$$(1 - \nu/\nu_o)\mathcal{D}^+(-\nu)\left[\mathcal{E}^-(\nu) + \frac{\Gamma(-\nu)}{\Gamma(\nu)} (\gamma b/2)^{2\nu} \mathcal{E}^-(-\nu)\right]$$

$$+ \left[D(0)\ (1 + \nu/\nu_o)\mathcal{D}^+(\nu)\right]^{-1}\left[\mathcal{E}^+(\nu) + \frac{(\gamma b/2)^\nu}{\Gamma(\nu)} \frac{\pi(\nu^2-1/4)}{\cos\nu\pi} P_{\nu-1/2}(-\cos\theta_o) K_\nu(\gamma a)\right] = 0 \tag{40}$$

The first term in this expression is holomorphic and $O(|\nu|^{-1/2})$ in $\mathrm{Re}(\nu) < c$. The remaining terms will only tend to zero in the right-hand plane provided a > b, but they still miss being holomorphic there because of the simple poles of $\mathcal{D}^+(-\nu)$, $\Gamma(-\nu)$ and $1/\cos\nu\pi$ in this region. Thus it is not possible to transform Eq. (25) into a finite

algebraic equation which can be solved by an appeal to Liouville's theorem. Instead one must subtract out the residues at these poles so as to obtain an algebraic equation with an infinite number of terms.

The restriction a > b according to which the source is excluded from the interior of the conical sheath was necessitated by the fact that the last term in Eq. (40) goes as $|\nu|(b/z)^{\nu}\exp[-|\mathrm{Im}(\nu)\theta_0|]$ as $|\nu| \to \infty$ in the right-hand plane. Fortunately, however, the radial component of the electric field, $E_r = -r^{-1}\mathcal{L}^{-1}\psi$, satisfies a reciprocity principle (see Appendix B). Consequently we can use the results of the present analysis applied to the case r < b < a to obtain as well the fields in the reciprocal case a < b < r, which is the one that interests us. We remark parenthetically that if it is desired to have a formalism which applies to all cases (including the remaining one a < b, r < b), this can be done at the cost of some extra complication by subtracting the quantity

$$\frac{D(\nu)}{\cos\nu\pi}\int_0^b \psi_\infty(r)\, K_\nu(\gamma r)\,\frac{dr}{r} + \int_b^\infty \psi_\infty(r)\, K_\nu(\gamma r)\,\frac{dr}{r}$$

from both sides of Eq. (25) to yield

$$\frac{D(\nu)}{\cos\nu\pi}\int_0^b \tilde{\psi}(r)\, K_\nu(\gamma r)\,\frac{dr}{r} + \int_b^\infty \tilde{\psi}(r)\, K_\nu(\gamma r)\,\frac{dr}{r} = \left[\frac{D(\nu)}{\cos\nu\pi} - 1\right]\int_b^\infty \psi_\infty(r) K_\nu(\gamma r)\,\frac{dr}{r} \tag{41}$$

where $\tilde{\psi}(r) = \psi(r) - \psi_\infty(r)$. When this equation is multiplied through by $(\gamma b/2)^{\nu}/\Gamma(\nu)$ the last term will clearly go to zero as $|\nu| \to \infty$ in the right-hand plane for all b.

We now return to Eq. (40) (with a > b) and put

$$(1 - \nu/\nu_o)\, \mathcal{D}^+(-\nu)\, \frac{\Gamma(-\nu)}{\Gamma(\nu)}\, (\gamma b/2)^{2\nu}\, \mathcal{E}^-(-\nu) = H^+(\nu) + \Sigma_D^- + \Sigma_\Gamma^- \tag{42}$$

$$\frac{(\gamma b/2)^{\nu}\pi\, (\nu^2 - 1/4)}{D(0)(1 + \nu/\nu_o)\, \mathcal{D}^+(\nu)\, \Gamma(\nu)\, \cos\nu\pi}\, P_{\nu-1/2}(-\cos\theta_o) K_\nu(\gamma a) = Q^+(\nu) + \Sigma_Q^- \tag{43}$$

where

$$\Sigma_D^- = \sum_{n=1}^{\infty} a_n\, \mathcal{E}^-(-n - 1/2)\, \frac{(\gamma b/2)^{2n+1}}{\nu - (n + 1/2)} \tag{44}$$

$$\Sigma_\Gamma^- = \sum_{n=1}^{\infty} b_n\, \mathcal{E}^-(-n)\, \frac{(\gamma b/2)^{2n}}{\nu - n} \tag{45}$$

$$\Sigma_Q^- = \sum_{n=1}^{\infty} c_n\, \frac{(\gamma b/2)^{n+1/2}}{\nu - (n + 1/2)} \tag{46}$$

Here

$$a_n = \frac{\Gamma(-n - 1/2)}{\Gamma(n + 1/2)}\, L'(n + 1/2) \tag{47}$$

$$b_n = (-)^{n+1}\, \frac{n}{(n!)^2}\, L(n) \tag{48}$$

$$c_n = -\frac{1}{D(0)}\, \frac{n(n+1)}{\Gamma(n + 1/2)}\, \frac{P_n(\cos\theta_o)}{\Gamma(-n - 1/2)}\, K_{n+1/2}(\gamma a) \tag{49}$$

and we have put $(1 - \nu/\nu_0)\mathcal{D}^+(-\nu) = L(\nu)$. Also

$$L^+(n + 1/2) = \lim_{\nu \to n + 1/2} \left\{[\nu-(n + 1/2)]L(\nu)\right\}$$

Now $H^+(\nu)$, $Q^+(\nu)$ are clearly "plus" functions (holomorphic and tending to zero in $\mathrm{Re}\{\nu\} > -\varepsilon$) while Σ_D^-, Σ_T^- and Σ_Q^- are "minus" functions. Thus we write Eq. (40) in the form

$$J(\nu) = L(\nu)\mathcal{E}^-(\nu) + \Sigma_D^- + \Sigma_T^- + \Gamma_Q^-$$

$$= -H^+(\nu) - \mathcal{E}^+(\nu)/L(-\nu) - Q^+(\nu) \qquad (50)$$

and conclude from Liouville's theorem that $J(\nu) = 0$. Hence we find on reintroducing Eqs. (44) through (46)

$$L(\nu)\mathcal{E}^-(\nu) + \sum_1^\infty a_n \mathcal{E}^-(-n - 1/2)\,\frac{(\gamma b/2)^{2n+1}}{\nu - (n + 1/2)}$$

$$+ \sum_1^\infty b_n \mathcal{E}^-(-n)\,\frac{(\gamma b/2)^{2n}}{\nu - n}$$

$$= -\sum_1^\infty c_n\,\frac{(\gamma b/2)^{n+1/2}}{\nu - (n + 1/2)} \qquad (51)$$

To solve this equation we assume a power series in $(\gamma b/2)$.

$$\mathcal{E}^{-}(\nu) = \sum_{n=1}^{\infty} E_n(\nu)\ (\gamma b/2)^{n+1/2} \tag{52}$$

and then equate successive powers of $\gamma b/2$ to transform it into the following infinite system of equations

$$L(\nu)\ E_n(\nu) + \sum_{m=1}^{n/2-1} \frac{a_m}{\nu - (m+1/2)}\ E_{n-2m-1}(-m-1/2)$$

$$+ \sum_{m=1}^{(n-1)/2} \frac{b_m}{\nu-m}\ E_{n-2m}(-m)$$

$$= \frac{c_n}{\nu - (n+1/2)} \qquad n = 1,2,\ldots \tag{53}$$

Here the integral parts of the upper limits $(n/2-1$ and $(n/2-1/2$ are to be understood. Solving the system of equations by iteration and then substituting into Eq. (52) we find

$$L(\nu)\,\mathcal{E}^{-}(\nu) = \frac{c_1}{\nu-3/2}\,(\gamma b/2)^{3/2} + \frac{c_2}{\nu-5/2}\,(\gamma b/2)^{5/2}$$

$$+\left[\frac{c_3}{\nu-7/2} + \left(\frac{2}{5}\right)\frac{b_1\,c_1}{L(-1)(\nu-1)}\right](\gamma b/2)^{7/2}$$

$$+\left[\frac{c_4}{\nu-9/2} + \left(\frac{2}{7}\right)\frac{b_1\,c_2}{L(-1)(\nu-1)} + \left(\frac{1}{3}\right)\frac{a_1\,c_1}{L(-3/2)(\nu-3/2)}\right](\gamma b/2)^{9/2}$$

$$+ \cdots \qquad (54)$$

Notice that $\mathcal{E}^{-}(\nu)$ is essentially the L-K transform of the induced current in the sheath. We turn next to the task of expressing the radiation field in terms of $\mathcal{E}^{-}(\nu)$

4. The Formal Solution

The scalar potential $\Pi(r,\theta)$ is given formally by Eq. (13). If in this expression we introduce Eq. (16) for $\mathcal{G}(r,\theta|r',\theta_0)$ and make use of Eq. (32) we obtain

$$\Pi(r,\theta) = \Pi_0(r,\theta) + (ra)^{-1/2}\,\frac{g}{i\pi}\int_{-i\infty}^{i\infty}\frac{\mu d\mu}{\cos\mu\pi}\,P_{\mu-1/2}(\cos\theta_<)P_{\mu-1/2}(-\cos\theta_>)I_\mu(\gamma r)$$

$$\left[\frac{\Gamma(\mu)}{(\gamma b/2)^{\mu}}\,\mathcal{E}^{-}(\mu) + \frac{\Gamma(-\mu)}{(\gamma b/2)^{-\mu}}\,\mathcal{E}^{-}(-\mu)\right] \qquad (55)$$

Making use of Eqs. (35), (42), and (50), we can rewrite this result as follows

$$\Pi(r,\theta) = \Pi_0(r,\theta) + (ra)^{-1/2} \frac{g}{i\pi} D(0) \int_{-i\infty}^{i\infty} \frac{\mu d\mu}{D(\mu)} P_{\mu-1/2}(\cos\theta_<) P_{\mu-1/2}(-\cos\theta_>) \cdot$$

$$\cdot I_\mu(\gamma r) L(-\mu) \frac{\Gamma(\mu)}{(\gamma b/2)^\mu} \left[\Sigma_Q^-(\mu) + H^+(\mu)\right] \qquad (56)$$

in which form it is clear that the μ-contour can be closed in the right-hand plane provided $r \leq b$. The only poles are at $\mu = n + 1/2$ due to $\Sigma_Q^-(\mu)$ and at $\mu = \mu_s$ where $D(\mu_s) = 0$. The contribution from those at $n + 1/2$ is

$$(ra)^{-1/2} \frac{g}{i\pi} (-2\pi i) D(0) \sum_{n=1}^{\infty} \frac{n+1/2}{D'(n+1/2)} (-)^n P_n(\cos\theta_0) P_n(\cos\theta) I_{n+1/2}(\gamma r) \cdot$$

$$\cdot L(-n-1/2) \frac{(n+1/2)}{(\gamma b/2)^{n+1/2}} \left\{ \lim_{\nu \to (n+1/2)} \left[(\nu-n-1/2)\, \Sigma_Q^-(\nu)\right] \right\}$$

On making use of Eqs. (46) and (49) it is easily verified that this reduces to the series expansion for $-\Pi_0(r,\theta)$ as given in Eqs. (12) and (17). Thus the contribution from these poles exactly cancels the first term on the right of Eq. (55). As a result the total solution is given by the integral in Eq. (55) evaluated as a sum of residues at the poles $\mu = \mu_s$. Putting $\cos\mu\pi = D(\mu)/[D(0)L(\mu)L(-\mu)]$ in Eq. (55) we have then

$$\Pi(r,\theta) = -(ra)^{-1/2}\, 2g\, D(0) \sum_{\mu} \frac{\mu}{D'(\mu)} P_{\mu-1/2}(\cos\theta_<) P_{\mu-1/2}(-\cos\theta_>) I_\mu(\gamma r) \cdot$$

$$\cdot \frac{\Gamma(\mu_s)}{(\gamma b/2)^\mu} L(-\mu)\, L(\mu)\, \mathcal{E}^-(\mu) \qquad (r \leq b < a) \qquad (57)$$

where the summation is over the roots of $D(\mu) = 0$. Notice that there is no contribution from the second term in the integral in Eq. (55) since $L(\mu_s)\,\mathcal{E}^-(-\mu_s) = 0$.

As a partial check of this result consider the limit $g \to 0$. In this limit it is easily seen from Eq. (26) that for the s^{th} root

$$\delta_s \equiv \mu_s - s - 1/2 \longrightarrow \frac{g}{\pi}\, s(s+1)\left[P_s(\cos C_o)\right]^2$$

and from Eq. (51) (since $a_n \to 0$)

$$L(\mu_s)\,\mathcal{E}^-(\mu_s) \longrightarrow \delta_s^{-1}\, c_s\,(\gamma b/2)^{s+1/2}$$

where c_s is given in Eq. (49). Introducing these results into Eq. (57) it is readily verified that $\Pi(r,\theta) \longrightarrow \Pi_o(r,\theta)$ as it should.

We now have a solution valid for the receiver inside the cone and the source outside. To obtain the solution in the reverse case---source inside and receiver outside---we appeal to the reciprocity theorem (Appendix B) which allows us formally to interchange source and receiver coordinates in the radial component of the electric field. According to Eq. (3) this component can be computed from Eq. (57) as follows

$$E_r = -r^{-1}\mathcal{L}\Pi(r,\theta) = -\frac{p}{4\pi\varepsilon_o}\,(ra)^{-3/2}\,2gD(0)\sum_{\mu}\frac{\mu(\mu^2-1/4)}{D'(\mu)}\,P_{\mu-1/2}(\cos\theta_<)\cdot$$

$$\cdot\, P_{\mu-1/2}(-\cos\theta_>)\; I_\mu(\gamma r)\,\frac{\Gamma(\mu)}{(\gamma b/2)^\mu}\; L(-\mu)\; L(\mu)\,\mathcal{E}^-(\mu)$$

$$(r \le b < a) \qquad (58)$$

Here $\mathcal{L} = \frac{1}{\sin\theta}\frac{\partial}{\partial\theta}\left(\sin\theta\ \frac{\partial}{\partial\theta}\right)$, and we have reinstated the factor $(p/4\pi\epsilon_o a)$ that was suppressed after Eq. (9). In this expression the receiver coordinates are contained in the term $P_{\mu-1/2}(\cos\theta)I_\mu(\gamma r)$ and the source coordinates in $L(\mu)\mathcal{E}^-(\mu)$ and hence ultimately in the coefficients c_n [see Eqs. (49) and (54)]. It now becomes clear that in order to use reciprocity we should have formulated the problem for a ring source instead of a point source. The reader will readily verify that if we had done so the result would have been to replace the source term $K_n(\gamma a)$ in the coefficients c_n in Eq. (49) by $P_n(\cos\alpha)\ K_n(\gamma a)$, where α is the angle subtended by the ring source. (Notice that as the ring shrinks down to a point, $\alpha \to 0$ and $P_n(\cos\alpha) \to 1$.) Once this is done we can formally make the substitutions $r \to a$, $\theta \to \alpha \to 0$ in the receiver coordinates in Eq. (58) and $a \to r$, $\alpha \to \theta$ in the source coordinates. Finally we can operate on the result by $-r\,\mathcal{L}^{-1}$ to obtain the scalar potential

$$\Pi(r,\theta) = \frac{p}{4\pi\epsilon_o a}(ra)^{-1/2}2g\mathcal{D}(0)\sum_\mu A(\mu)\ \mathcal{L}^{-1}\left[L(\mu)\mathcal{E}^-(\mu)\right] \tag{59}$$

where

$$A(\mu) = \frac{\mu^2-1/4}{\mathcal{D}'(\mu)}\ P_{\mu-1/2}(-\cos\theta_o)\ \frac{\mu\,\Gamma(\mu)}{(\gamma b/2)^\mu}\ I_\mu(\gamma a)L(-\mu) \tag{60}$$

This form is now valid in the range $a < b < r$. Here $L(\mu)\mathcal{E}^-(\mu)$ is given by the right-hand side of Eq. (54) so $\mathcal{L}^{-1}$ eventually operates on the c_n (which are now functions of r and θ). Thus if we introduce the coefficients

$$\hat{c}_n = \mathcal{L}^{-1}\,c_n(r,\theta) = -\ \frac{c_n(r,\theta)}{n(n+1)} = \frac{1}{\mathcal{D}(0)}\ \frac{P_n(\cos\theta)\ P_n(\cos\theta_o)\ K_{n+1/2}(\gamma r)}{\Gamma(n+1/2)\left[k+(n+1/2)/\nu_o\right]\mathcal{D}'(n+1/2)} \tag{61}$$

we see that the term $\mathcal{L}^{-1}[L(\mu)\,\mathcal{E}^{-}(\mu)]$ in Eq. (59) is given by the right-hand side of Eq. (54) with c_n replaced by $\hat{c}_n$.

5. The Far-Field Radiation Pattern

To calculate the field at large distances from the cone we use the asymptotic form $K_{n+1/2}(\gamma r) \sim (\pi/2\gamma r)^{1/2}\, e^{-\gamma r}$ for the radial functions appearing in the $\hat{c}_n$. This allows a radial factor $r^{-1}\, e^{-\gamma r}$ to be taken out of the expression for $\Pi(r,\theta)$ which we then write formally as a power series in γb

$$\Pi(r,\theta) = \left(\frac{p}{4\pi\varepsilon_0 a}\right) \frac{e^{-\gamma r}}{r} \sum F_n(\theta)\, (\gamma b)^n \tag{62}$$

The angular coefficients $F_n(\theta)$ can be found by equating successive powers of γb in

$$\sum_{n=1}^{\infty} F_n(\theta)\, (\gamma b)^n = \left(\frac{\pi}{2\gamma a}\right)^{1/2} 2gD(\vartheta) \sum_{\mu} A(\mu)\, \frac{\mathcal{L}^{-1}[L(\mu)\mathcal{E}^{-}(\mu)]}{K_{n+1/2}(\gamma r)}$$

Substituting the right-hand side of Eq. (54) for $\mathcal{L}^{-1}[L(\mu_s)\,\mathcal{E}^{-}(\mu_s)]$ with ν replaced by μ_s and c_n by $\hat{c}_n$ given in Eq. (61) we find for the first few coefficients

$$F_1(\theta) = -\left(\frac{b}{a}\right)^{1/2} \frac{g}{L(-3/2)} \sum \frac{A(\mu)}{\mu - 3/2}\, P_1(\cos\theta_0)\, P_1(\cos\theta)$$

$$F_2(\theta) = -\frac{1}{3}\left(\frac{b}{a}\right)^{1/2} \frac{g}{L(-5/2)} \sum \frac{A(\mu)}{\mu - 5/2}\, P_2(\cos\theta_0)\, P_2(\cos\theta)$$

$$F_3(\theta) = -\frac{1}{15}\left(\frac{b}{a}\right)^{1/2}\frac{g}{L(-7/2)}\sum\frac{A(\mu)}{\mu-7/2}\;P_3(\cos\theta_o)\;P_3(\cos\theta)$$

$$-\frac{1}{10}\left(\frac{b}{a}\right)^{1/2}\frac{g}{L(-3/2)}\;\frac{L(1)}{L(-1)}\sum\frac{A(\mu)}{\mu-1}\;P_1(\cos\theta_o)\;P_1(\cos\theta)$$

$$F_4(\theta) = -\frac{1}{105}\left(\frac{b}{a}\right)^{1/2}\frac{g}{L(-9/2)}\sum\frac{A(\mu)}{\mu-9/2}\;P_4(\cos\theta_o)\;P_4(\cos\theta)$$

$$-\frac{1}{14}\left(\frac{b}{a}\right)^{1/2}\frac{g}{L(-5/2)}\;\frac{L(1)}{L(-1)}\sum\frac{A(\mu)}{\mu-1}\;P_2(\cos\theta_o)\;P_2(\cos\theta)$$

$$+\frac{1}{6}\left(\frac{b}{a}\right)^{1/2}\frac{g\,L'(3/2)}{[L(-3/2)]^2}\sum\frac{A(\mu)}{\mu-3/2}\;P_1(\cos\theta_o)\;P_1(\cos\theta) \qquad (63)$$

The intensity, as given by the radial component of the Poynting flux,

$$S_r = \frac{1}{2}\;\mathrm{Re}(E_\theta H_\phi^*)$$

becomes in the far field

$$S_r = \frac{\omega^2\epsilon_o}{2c}\left|\frac{\partial\Pi}{\partial\theta}\right|^2$$

Introducing Eq. (62) for Π we write this as follows

$$S_r = \frac{\omega^2\epsilon_o}{2c}\left(\frac{p}{4\pi\epsilon_o a}\right)^2\left(\frac{ka}{r}\right)^2 F(\theta) \qquad (64)$$

in terms of an angular distribution factor

$$F(\theta) = \frac{1}{(ka)^2}\left|\sum F_n'(\theta)(-ikb)^n\right|^2 \tag{65}$$

Here we have reintroduced $k = i\gamma$.

In the absence of the sheath, i.e., as $g \to 0$ it is readily verified that

$$\sum F_n(\theta)(\gamma b)^n \longrightarrow (\pi/2\gamma a)^{1/2}\sum (2n+1)P_n(\cos\theta)I_{n+1/2}(\gamma a)$$

which is the expansion of the plane wave $\exp(\gamma a\cos\theta)$ in spherical waves.[6] Thus it follows that in this limit $F(\theta) \to \sin^2\theta$, which is the free dipole distribution.

6. Numerical Work

To compute the angular distribution factor $F(\theta)$ given in Eq. (65) it is necessary to evaluate the coefficients $F_n'(\theta)$, which are the derivatives of the expressions given in Eq. (63). These involve the infinite products $L(-p)$ and the infinite sums $S(p) = \sum A(\mu)/(\mu-p)$ for various integer and half-integer p's. The first 30 roots μ_s of the dispersion equation $D(\mu) = 0$ together with the derivatives $D'(\mu_s)$ and the corresponding Legendre functions $P_{\mu-1/2}(\cos\theta)$ were obtained on an electronic computer by the method outlined in the report of Ref. 2. The infinite products $L(-p) = (1 + p/\mu_0)\mathcal{J}^+(p)$ with $\mathcal{J}^+(p)$ given in Eq. (36) were then computed as follows

$$L(-p) = \left(1 + \frac{p}{\mu_0}\right) \prod_{s=1}^{\infty} \left[\frac{1 + p/\mu_s}{1 + p/(s + 1/2)}\right]$$

$$\approx \left(1 + \frac{p}{\mu_0}\right) \prod_{s=1}^{30} \left[\frac{1 + p/\mu_s}{1 + p/(s + 1/2)}\right] \prod_{s=31}^{48} \left[\frac{1 + p/(s + 1/2 + \delta_s)}{1 + p/(s + 1/2)}\right] (1 - 0.0103p)$$

with $\delta_s = (1/17)(s + 5)_{\text{mod } 18}$; i.e., $\delta_1 = \delta_{19} = \delta_{37} = \cdots = 6/17$, $\delta_2 = \delta_{20} = \cdots = 7/17$, etc. This expression for δ_s is the asymptotic form (for large s) of $\mu_s - (s + 1/2)$ which is obtained from Eq. (37). The last term is an approximation to

$$\prod_{s=49}^{\infty} \left[\frac{1 + p/(s + 1/2 + \delta_s)}{1 + p/(s + 1/2)}\right] \qquad \simeq 1 - (p/2) \sum_{s=49}^{\infty} (1/s^2)$$

$$= \prod \left[1 - \frac{p\delta_s}{(s + 1/2 + \delta_s)(s + 1/2 + p)}\right] \qquad = (1 - p/2)\left[\pi^2/6 - \sum_{s=1}^{48} (1/s^2)\right]$$

$$\simeq \prod \left(1 - \frac{p\delta_s}{s^2}\right) \qquad = 1 - 0.0103p$$

$$\simeq \prod \left(1 - p/2s^2\right)$$

(In the third step we replace δ_s by its average value of 1/2.)

In terms of these quantities the infinite sums $S(p) = \sum_{\mu} A(\mu)/(\mu-p)$ are easily computed using Eq.(60) for $A(\mu)$. Notice in this expression that

$$\frac{\mu\Gamma(\mu)}{(\gamma b/2)^{\mu}} I_{\mu}(\gamma a) = \left(\frac{a}{b}\right)^{\mu}\left[1 - \frac{(ka/2)^2}{\mu+1} + \frac{(ka/2)^4}{2(\mu+1)(\mu+2)} \cdots\right]$$

Computed values of $S(p)$ and $L(-p)$ corresponding to the case $ka = 1/3$, $kb = 1$ and for sheath parameters $g = 0.1$, 1 and 10 are given in Table 1. The series Eq. (65) unfortunately does not converge for larger values of kb so that its use in computing is limited to situations where the wavelength is large compared to the slant height of the cone. For such long wavelengths the radiation pattern turns out to be practically indistinguishable from that of the free dipole, although its level can be considerably different. In fact, for the cases considered, the radiated power levels referred to the free dipole level were computed to be 14.5 db, 9.4 db, and -19 db for $g = 0.1$, 1 and 10, respectively.

5. LONG CONE LIMIT

In this part we make use of the known[2] current distribution along an infinite cone to obtain an approximate radiation pattern for a cone of finite length. It is expected on physical grounds that such an approximation should be good for cones whose slant height is long compared to a wavelength.

Let us return to the fundamental integral equation eq. (9) and rewrite it in an obvious way as follows

$$\Pi(r,\theta) = \Pi_{\infty}(r,\theta) - \frac{g}{\pi}\int_b dr' \int \frac{d\phi}{2\pi} \frac{\exp(ik|\underset{\sim}{r}-\underset{\sim}{r}'|)}{|\underset{\sim}{r}-\underset{\sim}{r}'|} \mathcal{L}\Pi(r',\theta_0) \qquad (66)$$

Here $\Pi_\infty(r,\theta)$ is the solution for $b = \infty$. It is clear that if we introduce $\mathcal{L}\Pi_\infty(r',\theta_o)$ in place of $\mathcal{L}\Pi(r',\theta_o)$ under the integral sign in Eq. (66) the result will be to yield an approximation to $\Pi(r,\theta)$ valid for large b. Physically we are replacing the actual current distribution on the cone by the one which obtains when the cone is infinitely long. This approximation could itself be introduced into the right-hand side of Eq. (66) to yield a second approximation, and so on, but we shall not go beyond the first one.

$\Pi_\infty(r,\theta)$ can be obtained from Eq. (28) by closing the contour at infinity and evaluating the resulting integral as a sum of residues at the zeros of $D(\mu)$ (cf. Ref. 2). The result is

$$\Pi_\infty(r,\theta) = 2\pi i k \sum_\nu \frac{\nu}{D'(\nu)} \frac{P_{\nu-1/2}(\cos\theta_<)P_{\nu-1/2}(-\cos\theta_>)}{P_{\nu-1/2}(\cos\theta_o)} j_{\nu-1/2}(ka)h^{(1)}_{\nu-1/2}(kr) \tag{67}$$

Here we have used Eqs. (A-1) and (A-2) to express the modified Bessel functions in terms of the spherical ones. The summation in Eq. (67) is over the roots of $D(\nu) = 0$ where $D(\nu)$ is defined in Eq. (26). From Eq. (67) we obtain the expression

$$\mathcal{L}\Pi_\infty(r',\theta_o) = -2\pi i k \sum_\nu \frac{\nu(\nu^2 - 1/4)}{D'(\nu)} P_{\nu-1/2}(-\cos\theta_o) j_{\nu-1/2}(ka)h^{(1)}_{\nu-1/2}(kr') \tag{68}$$

which is to be substituted for $\mathcal{L}\Pi(r',\theta_o)$ under the integral sign in Eq. (66).

In the far field ($r \to \infty$) the Green's function in Eq. (66) can be simplified

$$\int_0^{2\pi} \frac{d\phi}{2\pi} \frac{\exp(ik|\underset{\sim}{r}-\underset{\sim}{r}'|)}{|\underset{\sim}{r}-\underset{\sim}{r}'|} \sim \frac{e^{ikr}}{r} \int_0^{2\pi} \exp\left\{-ikr'[\sin\theta\sin\theta'\cos(\phi-\phi')+\cos\theta\cos\theta']\right\} \frac{d\phi}{2\pi}$$

$$= \frac{e^{ikr}}{r} \exp(-ikr'\cos\theta\cos\theta') \, J_0(kr'\sin\theta\sin\theta') \qquad (69)$$

Similarly the Hankel functions appearing in Eqs. (67) and (68) can be replaced by the asymptotic values

$$h^{(1)}_{\nu-1/2}(kr) \sim i^{-\nu-1/2} \frac{e^{ikr}}{kr}$$

This must clearly be done in Eq. (67), and in Eq. (68) it is justified since we are assuming that b is large. With these modifications we introduce Eqs. (67), (68), and (69) into Eq. (66) to obtain

$$\Pi(r,\theta) = -i^{1/2} \frac{e^{ikr}}{r} \sum_\nu c_\nu \left[\frac{P_{\nu-1/2}(\cos\theta_<)P_{\nu-1/2}(-\cos\theta_>)}{P_{\nu-1/2}(\cos\theta_o)} + \gamma_\nu f_b(\theta) \right] \qquad (70)$$

where

$$c_\nu = \frac{2\pi\nu}{D'(\nu)}\, i^{-\nu} j_{\nu-1/2}(ka)$$

$$\gamma_\nu = \frac{\pi}{2}\left(\nu^2 - 1/4\right) P_{\nu-1/2}(-\cos\theta_o)$$

$$f_b(\theta) = \int_{kb}^{\infty} e^{i\alpha x} J_o(\beta x) x^{-1} dx$$

$$\alpha = 1 - \cos\theta_o \cos\theta$$

$$\beta = \sin\theta_o \sin\theta$$

The far-field radiation pattern becomes [cf. Eq. (64)].

$$F(\theta) = \left(\frac{r}{ka}\right)^2 \left|\frac{\partial \Pi}{\partial \theta}\right|^2 = \frac{1}{(ka)^2}\left|\sum_\nu c_\nu F_\nu(\theta)\right|^2 \qquad (71)$$

where $F_\nu(\theta)$ is the derivative with respect to θ of the expression in braces in Eq. (70).

$$F_\nu(\theta) = \begin{cases} \dfrac{P_{\nu-1/2}(-\cos\theta_o)}{P_{\nu-1/2}(\cos\theta_o)} P'_{\nu-1/2}(\cos\theta)\sin\theta + \gamma_\nu f_b'(\theta) & \text{for } \theta \le \theta_o \\ P'_{\nu-1/2}(-\cos\theta)\sin\theta + \gamma_\nu f_b'(\theta) & \text{for } \theta \ge \theta_o \end{cases}$$

$$f_b'(\theta) = \begin{bmatrix} \tan(\theta/2) \\ -\cot(\theta/2) \end{bmatrix} + \int_0^{kb} e^{i\alpha x}\left[\beta J_1(\beta x) - i\alpha J_o(\beta x)\right] dx \quad (\theta \lesssim \theta_o) \qquad (72)$$

Here the discontinuity in $f_b'(\theta)$ has been exhibited explicitly with the help of the Weber-Schafheitlin integrals. It is readily verified that $F_\nu(\theta)$ itself is continuous

$$\left[F_\nu(\theta)\right]_{\theta_o^-}^{\theta_o^+} = -\frac{2}{\pi}\,\frac{\cos\nu\pi}{P_{\nu-1/2}(\cos\theta_o)}\,\frac{1}{\sin\theta_o} - \frac{2\gamma_\nu}{\sin\theta} = 0$$

To show this we have used the Wronskian relation [Eq. (A-12)] and the fact that ν satisfies $D(\nu) = 0$.

Note that $f_b'(\theta)$ depends only on θ_o and on kb and is independent of the sheath parameter g and the source location a. It has been evaluated numerically for kb = 20, $\theta_o = 10°$, and the results are given in Table 2. A table of the Legendre functions $P_{\mu-1/2}(\cos\theta)$ for g = 0.1, 1, and 10 has been furnished in the previous report.[2]

III. RADIATION PATTERNS

Figure 2 is a plot of the radiation pattern of the dipole source in an infinite conical sheath for various values of the sheath parameter g. The dipole is driven at a frequency corresponding to ka = 1/3, and the cone angle is $\theta_o = 10°$. The dotted curve labelled g = 0 is the free-space pattern, $I = \sin^2\theta$. The intensity levels are given in decibels referred to that of the free-space pattern at 90°, that is, to unity. Thus the quantity plotted is $10 \log_{10} F(\theta)$ where $F(\theta)$ is given in Eq. (68) or Eq. (71). It is clear that the presence of the sheath leads to enhanced power output (increased radiation resistance) for low values of g and to a surface wave which is especially pronounced at intermediate values. These effects are discussed at length in the previous report.[2]

Figure 3 shows the effect of increasing frequency on the radiation pattern labelled g = 0.1 of the previous figure. The incipient formation of lobes at the higher frequency is evident. The radiation pattern is fairly insensitive to frequency with the level proportional to $(ka)^{-2}$ for $(ka) \leq 1/3$.

Figures 4 and 5 exhibit the effect of finite slant height on the radiation patterns. They have been drawn for sheath parameters g = 0.1 and g = 10, respectively, and the same cone angle, 10°. The curves labelled kb = 1 (corresponding to $\lambda = 2\pi b$) have, of course, been computed by the scheme described in Part A while the perturbation scheme of Part B was used to obtain the curves labelled kb = 20. In this last case the slant-height is only about 3 wavelengths long, $b = (10/\pi)\lambda$, so the numerical values may be somewhat in error as they are based on the first term only of a perturbation expansion in λ/b.

These plots indicate that truncating the cone has a pronounced effect on the radiation. At a slant height of three wavelengths the surface wave is sharply reduced, and there is some change in the total power output.

At a slant height of one-sixth of a wavelength the surface wave has entirely disappeared although the total power output is still markedly different from that corresponding to the bare dipole. It is interesting that the power output remains high for the weakly reflecting sheath ($g = 0.1$) but it is greatly depressed by the strongly reflecting one.

The tremendous variation in intensity radiated at different angles necessitates the use of a decibel or logarithmic scale to display the entire pattern. However, the distortions this introduces are misleading. Accordingly, different portions of the radiation patterns of Fig. 4 have been reproduced on a linear scale in Fig. 6.

ACKNOWLEDGMENT

The author is indebted to Dr. R. H. Huddlestone and Professor A. Baños for valuable discussions of this problem.

REFERENCES

1. D. C. Pridmore-Brown, J. Math. & Phys. 43, 199-271 (1964).

2. A. Baños, Jr., R.H. Huddlestone, D.C. Pridmore-Brown and E.C. Taylor, Aerospace Technical Report TDR-269(5220-10)-2, (October 1964); also J. Math. & Phys. 44, (1965).

3. A. Leitner and C. P.-Wells, IRE Trans. on Antennas and Propagation, AP-4, 637-640 (1956); also B. Noble, Methods Based on the Wiener-Hopf Technique, Pergamon Press, London (1958), p. 213.

4. J. A. Meier and A. Leitner, Oesterreichisches Ingenieur-Archiv, 13, 141-151 (1959).

5. J. R. Wait, Appl. Sci. Res. 8, Section B, 397-417 (1960).

6. P. Morse and H. Feshbach, Methods of Theoretical Physics, McGraw-Hill, New York (1953), p. 1466.

7. C. J. Bouwkamp, Rep. Progr. Phys. 17, 35-100 (1954).

APPENDIX A. TABLE OF FORMULAE

The modified or hyperbolic Bessel functions $I_\mu(x)$, $K_\mu(x)$ are related to the cylindrical and spherical Bessel functions by

$$I_\mu(x) = i^{-\mu} J_\mu(ix) = i^{-\mu} \left(\frac{2ix}{\pi}\right)^{1/2} j_{\mu-1/2}(ix) \tag{A-1}$$

$$K_\mu(x) = i^{\mu+1} \frac{\pi}{2} H_\mu^{(1)}(ix) = i^{\mu+1} \left(\frac{i\pi x}{2}\right)^{1/2} h_{\mu-1/2}^{(1)}(ix) \tag{A-2}$$

and to each other by

$$K_\mu(x) = -\frac{1}{2} \mu\Gamma(\mu)\Gamma(-\mu)[I_{-\mu}(x) - I_\mu(x)] \tag{A-3}$$

Note that they are integral functions of μ and that $K_\mu(x)$ is even in μ. They have the asymptotic forms

$$I_\mu(x) \sim (2\pi x)^{-1/2} e^x ; \quad K_\mu(x) = (\pi/2x)^{1/2} e^{-x} \tag{A-4}$$

for $x \gg |\mu|$ and

$$\mu\, I_\mu(x) \sim \frac{(x/2)^\mu}{\Gamma(\mu)} ; \quad 2K_\mu(x) \sim \frac{\Gamma(\mu)}{(x/2)^\mu} + \frac{\Gamma(-\mu)}{(x/2)^{-\mu}} \tag{A-5}$$

for $|\mu| \gg x$.

From the differential equations satisfied by $I_\mu(x)$ and $K_\nu(x)$

$$\left(x \frac{d}{dx} x \frac{d}{dx} - x^2 - \mu^2\right) I_\mu(x) = 0$$

$$\left(x \frac{d}{dx} x \frac{d}{dx} - x^2 - \nu^2\right) K_\nu(x) = 0 \qquad \text{(A-6)}$$

it follows, on multiplying the first by $K_\nu(x)$, the second by $I_\mu(x)$, subtracting and integrating, that

$$(\mu^2-\nu^2) \int I_\mu(x)\, K_\nu(x) \frac{dx}{x} = x[K_\nu(x)\, I'_\mu(x) - I_\mu(x)\, K'_\nu(x)] \qquad \text{(A-7)}$$

and hence

$$(\mu^2-\nu^2) \int_0^\infty I_\mu(x) K_\nu(x) \frac{dx}{x} = 1 \qquad \text{(A-8)}$$

provided $\mathrm{Re}\{\mu-|\nu|\} > 0$.

The Legendre $P_{\mu-1/2}(\cos\theta)$ is an integral symmetric function of μ satisfying

$$\left(\frac{1}{\sin\theta} \frac{d}{d\theta} \sin\theta \frac{d}{d\theta} + \mu^2 - 1/4\right) P_{\mu-1/2}(\cos\theta) = 0 \qquad \text{(A-9)}$$

and having the asymptotic behavior

$$P_{\mu-1/2}(\cos\theta) \sim \left(\frac{2}{\pi|\mu|\sin\theta}\right)^{1/2} \cos(\nu\theta-\pi/4) \qquad \text{(A-10)}$$

as $|\mu| \to \infty$ provided $0 < \theta < \pi$.

When $\mu = n + 1/2$, n an integer

$$P_n(-x) = (-)^n P_n(x) \qquad \text{(A-11)}$$

and otherwise ($\mu \neq n + 1/2$)

$$P_{\mu-1/2}(x)P'_{\mu-1/2}(-x) + P_{\mu-1/2}(-x)P'_{\mu-1/2}(x) = -\left(\frac{2}{\pi}\right)\frac{\cos\mu\pi}{1-x^2} \qquad \text{(A-12)}$$

APPENDIX B. THE RECIPROCITY PRINCIPLE

In this Appendix we verify that the usual reciprocity principle holds in the presence of current sheets.

Consider two source distributions of current $\underset{\sim}{J}_1(\underset{\sim}{r})$ and $\underset{\sim}{J}_2(\underset{\sim}{r})$ and their corresponding fields $\underset{\sim}{E}_1$, $\underset{\sim}{H}_1$, $\underset{\sim}{E}_2$, $\underset{\sim}{H}_2$ in a region V enclosed by surfaces S. Then the relation

$$\int_S (\underset{\sim}{E}_2 \times \underset{\sim}{H}_1 - \underset{\sim}{E}_1 \times \underset{\sim}{H}_2) \cdot \underset{\sim}{n}\, dS = \int_V (\underset{\sim}{E}_1 \cdot \underset{\sim}{J}_2 - \underset{\sim}{E}_2 \cdot \underset{\sim}{J}_1)\, dV$$

follows directly from Maxwell's equations on the assumption that the sources have the same harmonic time dependance. If now we take the current sources to be radial and to have the form

$$\underset{\sim}{J}_1 = \underset{\sim}{e}_r\, \delta(\underset{\sim}{r} - \underset{\sim}{r}_1)$$

$$\underset{\sim}{J}_2 = \underset{\sim}{e}_r\, \delta(\underset{\sim}{r} - \underset{\sim}{r}_2)$$

and if we consider the surfaces S to consist of the inner and outer surfaces of the conical sheath together with the surface at infinity, then this equation reduces to

$$\int_{\text{cone}} \left[E_{1r}(H_{2\phi}) - E_{2r}(H_{1\phi}) \right] dS = E_{1r}(\underset{\sim}{r}_2) - E_{2r}(\underset{\sim}{r}_1)$$

where the integration is now taken over just one surface of the cone, and $[H_\phi]$ denotes the jump in H_ϕ across this surface. Imposition of the jump boundary conditions across this surface then causes the integral to vanish. Thus we conclude that the radial component of the electric field is symmetric in source and receiver coordinates.

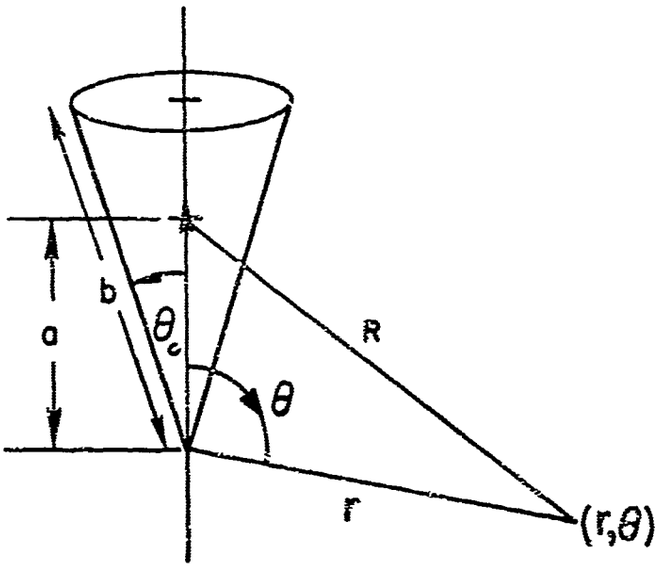

Fig. 1. Schematic diagram of mathematical model showing electric dipole antenna in finite conical sheath.

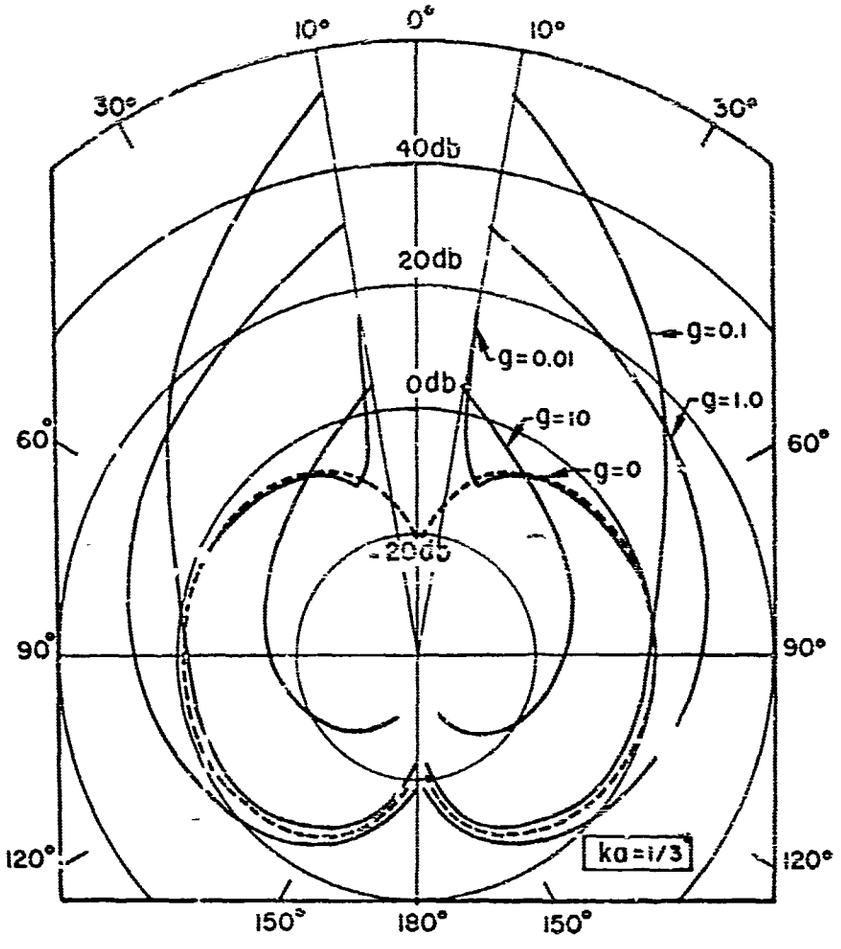

Fig. 2. Radiation pattern of antenna in infinite sheath for different values of sheath parameter g.

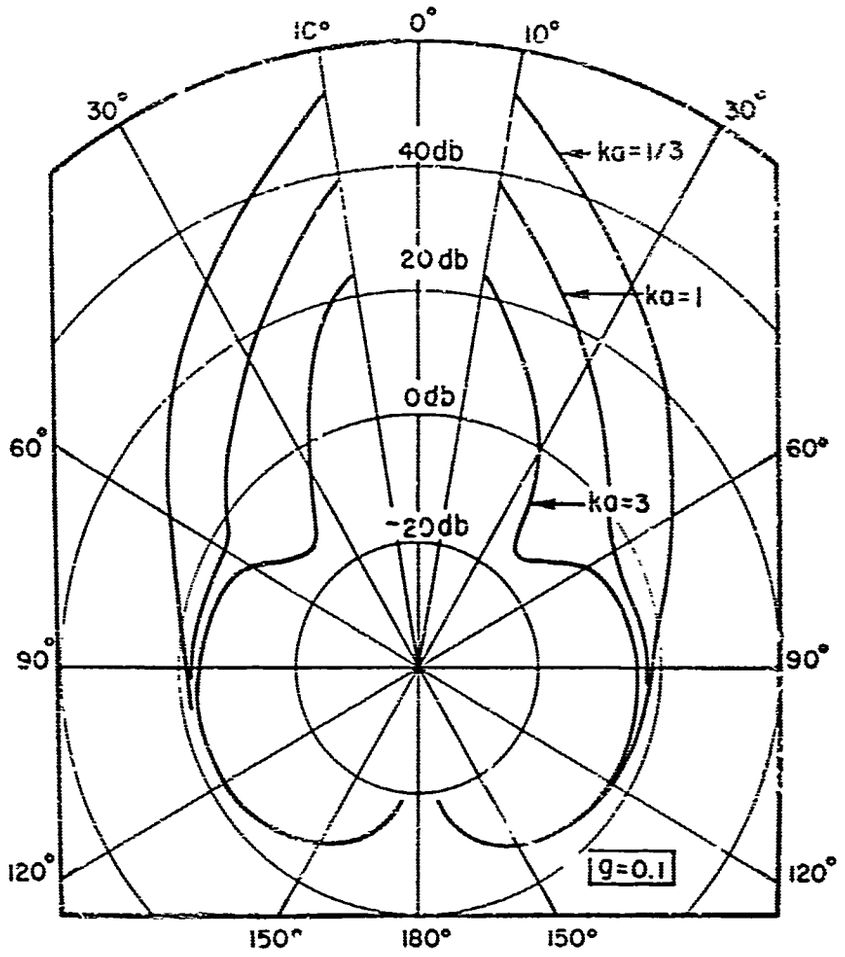

Fig. 3. Radiation pattern of antenna in infinite sheath for different values of frequency parameter ka.

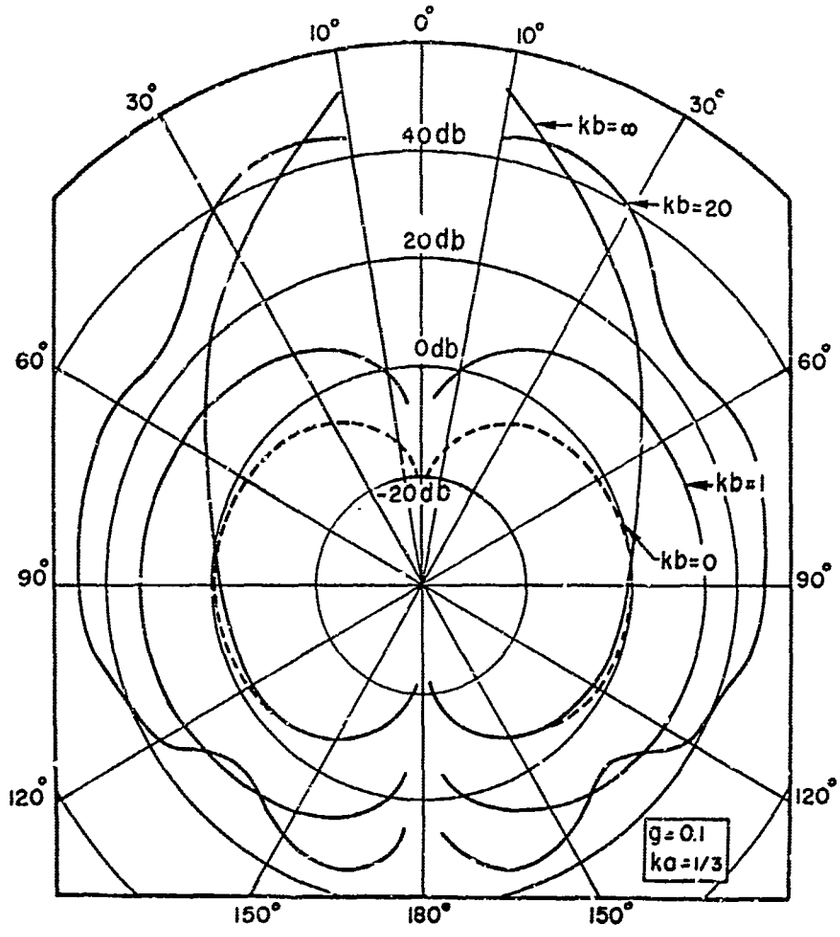

Fig. 4. Radiation pattern of antenna in finite sheath for various slant heights and g = 0.1.

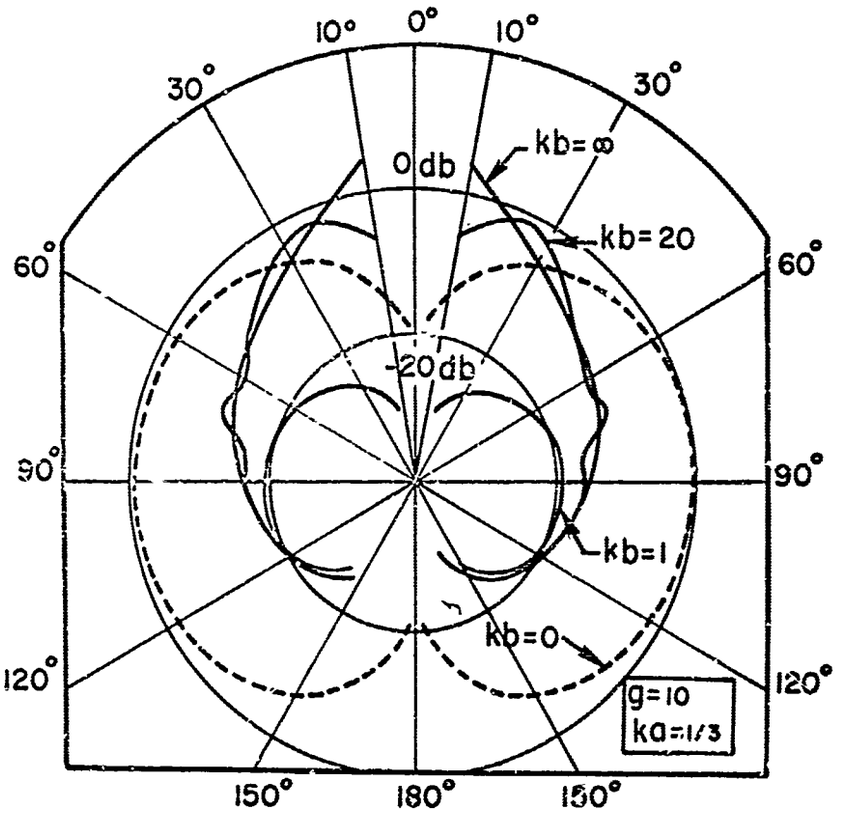

Fig. 5. Radiation pattern of antenna in finite sheath for various slant heights and g = 10.

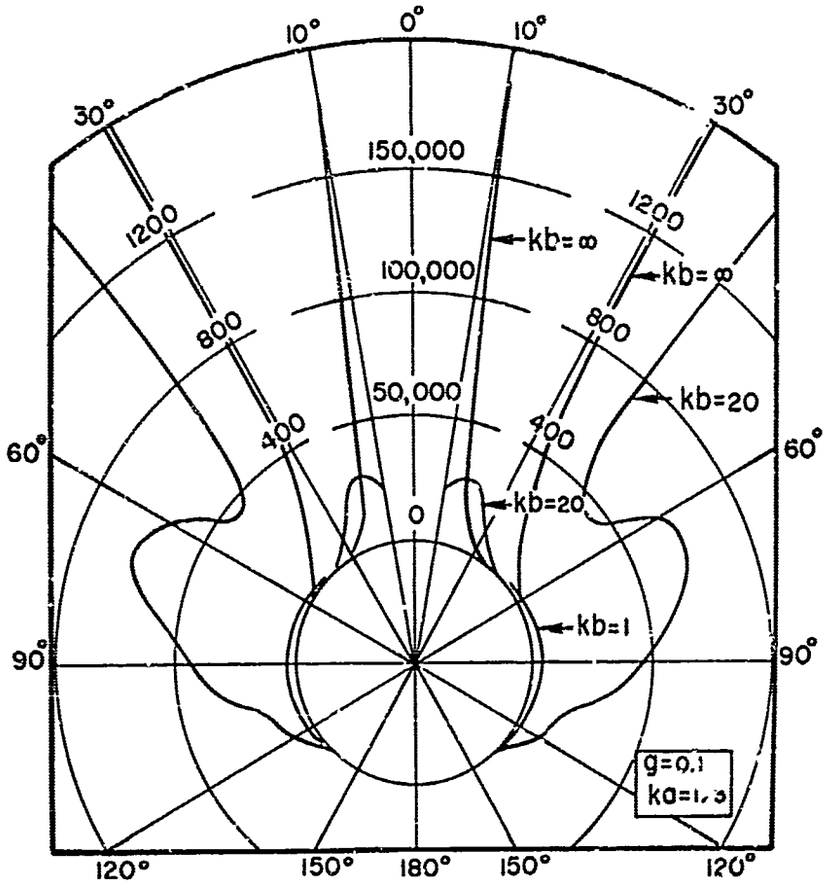

Fig. 6. Reproduction of Fig. 4 on two different linear scales.

able 1. Computed values of quantities discussed in Section A-6.

g = 0.1			g = 1		
p	L(-p)	S(p)	p	L(-p)	S(p)
-1	1.27 - .250i	----	-1	1.63 - 2.66i	----
1	.875 + .172i	11.5 - .903i	1	.799 + 1.30i	-.381 + 1.27i
1.5	.830 + .245i	10.0 - .199i	1.5	.735 + 1.80i	-.446 + .802i
2.5	.760 + .374i	10.2 + 1.88i	2.5	.644 + 2.63i	-.337 + .518i
3.5	.706 + .486i	9.26 + 3.22i	3.5	.579 + 3.31i	-.267 + .367i

g = 10		
p	L(-p)	S(p)
-1	-.939	---
1	1.99	.0128
1.5	2.38	.00445
2.5	3.03	.00272
3.5	3.57	.00184

Table 2. Computed values of the expression defined in Eq. (72).

θ	10°	30°	50°	70°	90°	110°	130°	150°	170°
$\mathrm{Re}\{f_b'(\theta)\}$	-10.0	1.11	-.038	.341	.133	-.038	-.026	-.048	-.015
$\mathrm{Im}\{f_b'(\theta)\}$	-2.93	-.984	.377	.365	.360	.238	.073	.104	-.082

VI. PROPAGATION OF TRANSIENT SIGNALS IN PLASMAS

C. T. Case and R. E. Haskell

Air Force Cambridge Research Laboratories
Bedford, Massachusetts

INTRODUCTION

Most analyses of wave propagation in plasmas are based on the assumption of a monochromatic wave. Although no real signals are truly monochromatic, this assumption is often a very good one for many applications. However, with the advent of very narrow pulses and extremely fast rise-times, the frequency spectra of certain signals are broad enough for a large number of frequency components to interact significantly with the plasma.[1]

The dispersive nature of a lossless, isotropic plasma may be seen from the simple dispersion equation

$$k = \frac{1}{c}\sqrt{\omega^2 - \Pi^2} \qquad (1)$$

where k is the wave number, ω is the angular frequency, c is the free-space velocity of light, and Π is the plasma frequency. This dispersion relation is plotted in Figure 1, where it is observed that no propagation occurs for frequencies below the plasma frequency. As the frequency increases above the plasma frequency the phase velocity decreases

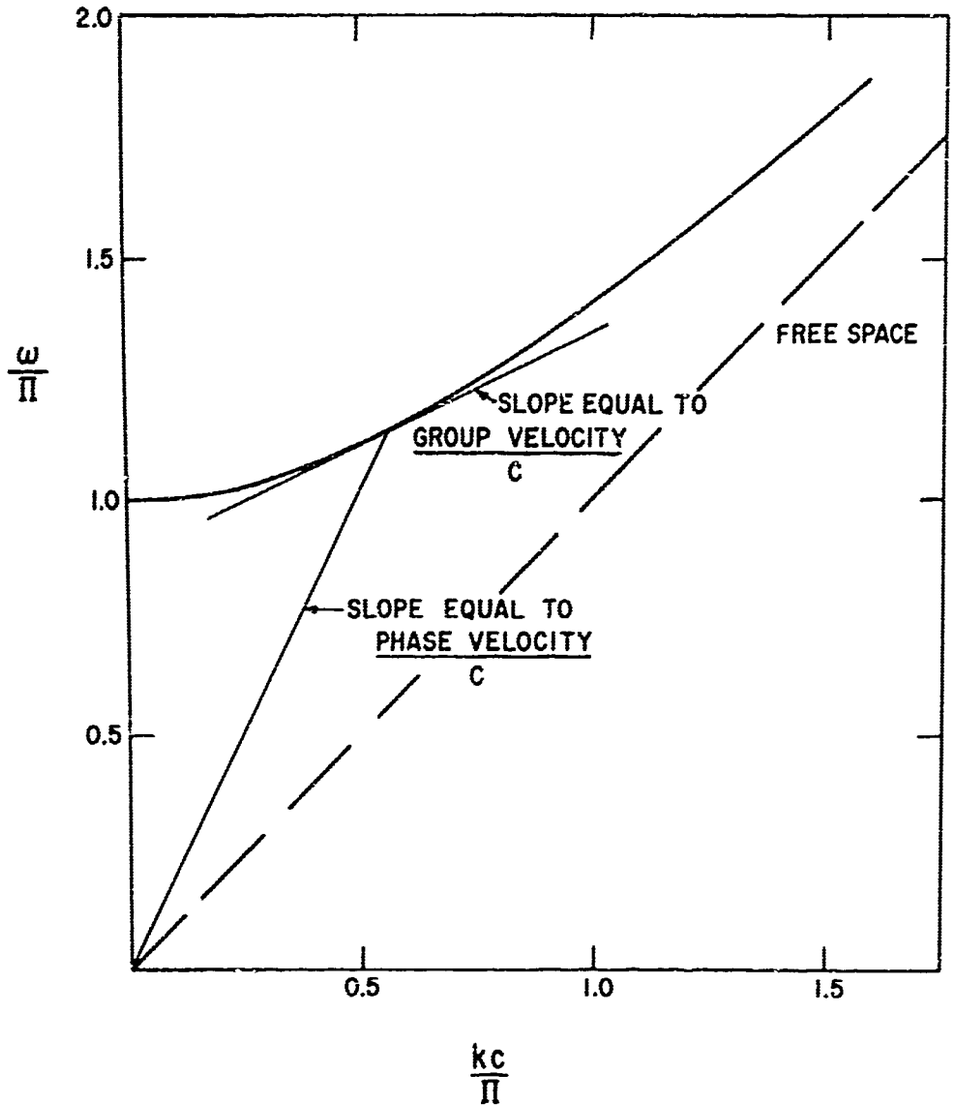

Fig. 1 Dispersion relation for a lossless, isotropic plasma.

from infinity toward c while the group velocity increases from zero toward c.

The response of a nonmonochromatic signal propagating in a dispersive media can in principle be determined by a superposition of all of the Fourier frequency components, each of which propagates according to Figure 1. If the frequency spectrum is sufficiently narrow and peaked about a carrier frequency ω_o, then the signal may be treated as a wave packet and the wave number k given by (1) may be expanded in a Taylor series about ω_o. This technique has been widely used to determine the overall degradation of pulsed signals propagating in dispersive media.[2-5] However, this analysis is not valid if the frequency spectrum is very broad and thus it can not be used for very short pulses, for describing the initial arrival of the signal, or for analyzing with no carrier frequency. In this paper these special cases will be discussed by solving the initial value problem of waves propagating in plasmas using Laplace transform techniques

FORMULATION OF THE PROBLEM

Maxwell's equations which describe the propagation of electromagnetic waves in an isotropic plasma are

$$\begin{aligned} \text{curl } \underset{\sim}{\mathcal{E}} &= -\mu_o \frac{\partial \underset{\sim}{\mathcal{H}}}{\partial t} \\ \text{curl } \underset{\sim}{\mathcal{H}} &= \underset{\sim}{J} + \epsilon_o \frac{\partial \underset{\sim}{\mathcal{E}}}{\partial t} \end{aligned} \tag{2}$$

where

$$\underset{\sim}{J} = -Ne\underset{\sim}{v} \tag{3}$$

and $\underset{\sim}{v}$ is determined from the equation of motion

$$\frac{\partial \underset{\sim}{v}}{\partial t} + \nu \underset{\sim}{v} = -\frac{e}{m}\underset{\sim}{\mathcal{E}}. \tag{4}$$

In these equations N is the electron number density and ν is an effective collision frequency.

Let us consider the one-dimensional problem in which $\underset{\sim}{\mathcal{E}}$ is linearly polarized in the x-direction and is propagating in the z-direction. We shall write the x-component of $\underset{\sim}{\mathcal{E}}(t, z)$ as $\mathcal{E}(t, z)$ and the Laplace transform of $\mathcal{E}(t, z)$ as $E(s, z)$. If we then take a Laplace transform in time of Equations (2)-(4) and solve for $E(s, z)$ setting all initial conditions equal to zero, we readily obtain the equation

$$\frac{\partial^2 E(s, z)}{\partial z^2} - \frac{1}{c^2}\left(s^2 + \frac{s\Pi^2}{s+\nu}\right) E(s, z) = 0. \tag{5}$$

We wish to determine the time response $\mathcal{E}(t, z)$ in the semi-infinite region $z > 0$ when the time response $\mathcal{E}(t, 0)$ is prescribed at $z = 0$. The solution of (5) may then be written

$$E(s, z) = E(s, 0)e^{-\frac{z}{c}\sqrt{s^2 + \frac{s\Pi^2}{s+\nu}}} \tag{6}$$

where $E(s, 0)$ is the Laplace transform of $\mathcal{E}(t, 0)$. The time response $\mathcal{E}(t, z)$ is then obtained by taking the inverse of (6). That is,

$$\mathcal{E}(t, z) = \frac{1}{2\pi i}\int_{\gamma_s} E(s, 0)e^{st - \frac{z}{c}\sqrt{s^2 + \frac{s\Pi^2}{s+\nu}}}\,ds. \tag{7}$$

If collisions can be neglected then (7) reduces to

$$\mathcal{E}(t, z) = \frac{1}{2\pi i}\int_{\gamma_s} E(s, 0)e^{st - \frac{z}{c}\sqrt{s^2 + \Pi^2}}\,ds. \tag{8}$$

We shall investigate various solutions of (8) in the following two sections. Equation (7) will then be investigated in order to determine the role which collisions play in the propagation of transient signals in plasmas. Finally, reflections from a plasma-vacuum interface will be considered.

NUMERICAL SOLUTIONS FOR SHORT DISPERSION LENGTHS

There are very few initial transforms E(s, 0) for which the inverse transform (8) is known. One exception is a unit step magnetic field at z = 0 for which H(s, 0) = 1/s. From Maxwell's equations

$$E(s, z) = \sqrt{\frac{\mu_o}{\epsilon_o}}\ \frac{s}{\sqrt{s^2 + \Pi^2}}\ H(s, z) \quad ,$$

so that

$$E(s, 0) = \sqrt{\frac{\mu_o}{\epsilon_o}}\ \frac{1}{\sqrt{s^2 + \Pi^2}} \quad . \tag{9}$$

Equation (8) may then be written as

$$\mathcal{E}(t, z) = \mathcal{L}^{-1}\left[\frac{\sqrt{\frac{\mu_o}{\epsilon_o}}\ e^{-\frac{z}{c}\sqrt{s^2 + \Pi^2}}}{\sqrt{s^2 + \Pi^2}}\right]$$

which, from tables is

$$\mathcal{E}(t, z) = \begin{cases} 0 & 0 < t < z/c \\ \sqrt{\frac{\mu_o}{\epsilon_o}}\ J_o\left[\Pi\sqrt{t^2 - \frac{z^2}{c^2}}\right] & t > z/c \end{cases} \tag{10}$$

where $J_o(x)$ is the zero order Bessel function of the first kind. Note that no signal arrives prior to the time $t = z/c$.

The solution (10) is a damped oscillatory function whose frequency approaches the plasma frequency for large times. The argument of the Bessel function in (10) may be written as

$$\Phi = \Pi \sqrt{t^2 - z^2/c^2} \quad , \tag{11}$$

If we define the "instantaneous frequency" of the oscillation by $\omega_I = d\Phi/dt$, then from (11) we find that

$$\omega_I = \frac{\Pi}{\sqrt{1 - z^2/c^2 t^2}} \quad , \tag{12}$$

Thus for early times ($t \gtrsim z/c$) the instantaneous frequency is very high and approaches the plasma frequency for very long times. The instantaneous frequency also increases for larger plasma frequencies and longer dispersion lengths.

For other forms of $E(s, 0)$, the inverse transform (8) can not be found from tables and alternate methods for evaluating the integral in (8) must be found. For the particular case of a step sine wave input the solution can be written in terms of a sum of Bessel functions[6-8], which can be expressed in terms of tabulated Lommel functions[9-11].

Integral solutions which may be evaluated numerically for short dispersion lengths may be obtained either by contour integration or by using the convolution theorem.[9, 10, 12] In this section we shall present results obtained by use of the convolution theorem.

The time response given by (8) may be written

$$\mathcal{E}(t, z) = \mathcal{L}^{-1}\left[E(s, 0)\, e^{-\frac{z}{c}\sqrt{s^2 + \Pi^2}}\right] . \tag{13}$$

Since, from tables[13]

$$\mathcal{L}^{-1}\left[e^{-\frac{z}{c}\sqrt{s^2+\Pi^2}}\right] = \delta\left(t - \frac{z}{c}\right) - \frac{z\Pi}{c}\,\frac{J_1\left(\Pi\sqrt{t^2 - z^2/c^2}\right)}{\sqrt{t^2 - z^2/c^2}}\, U(t - z/c)$$

where $U(t - z/c)$ is the unit step function, we can, by using the convolution theorem, write (13) as

$$\mathcal{E}(t, z) = \left[\mathcal{E}(t - z/c, 0) - \frac{z\Pi}{c}\int_{z/c}^{t} \mathcal{E}(t - t', 0)\,\frac{J_1\left(\Pi\sqrt{t'^2 - z^2/c^2}\right)}{\sqrt{t'^2 - z^2/c^2}}\,dt'\right] U(t - z/c) . \tag{14}$$

If a unit step $\mathcal{E}$ field is turned on at $z = 0$, then (14) becomes

$$\mathcal{E}(t, z) = \left[1 - \frac{z\Pi}{c}\int_{z/c}^{t} \frac{J_1\left(\Pi\sqrt{t'^2 - z^2/c^2}\right)}{\sqrt{t'^2 - z^2/c^2}}\, dt'\right] U(t - z/c) \tag{15}$$

Equation (15) has been evaluated numerically and the results are shown in Figure 2. Note that the argument of J_1 in (15) is the same as (11) and that the "instantaneous frequency" shown in Figure 2 is in accord with the discussion following (12).

If a unit step-carrier sine wave is turned on at $z = 0$ then (14) can be written in normalized form as

$$\mathcal{E}(\tau, \eta) = \mathrm{Im}\left[e^{i(\tau - \eta)} - P\eta e^{i\tau}\int_{\eta}^{\tau} \frac{e^{-iu} J_1\left(P\sqrt{u^2 - \eta^2}\right)}{\sqrt{u^2 - \eta^2}}\, du\right] U(\tau - \eta) \tag{16}$$

where

$$\tau = \omega_o t$$
$$\eta = \omega_c z/c \tag{17}$$
$$P = \Pi/\omega_o \quad .$$

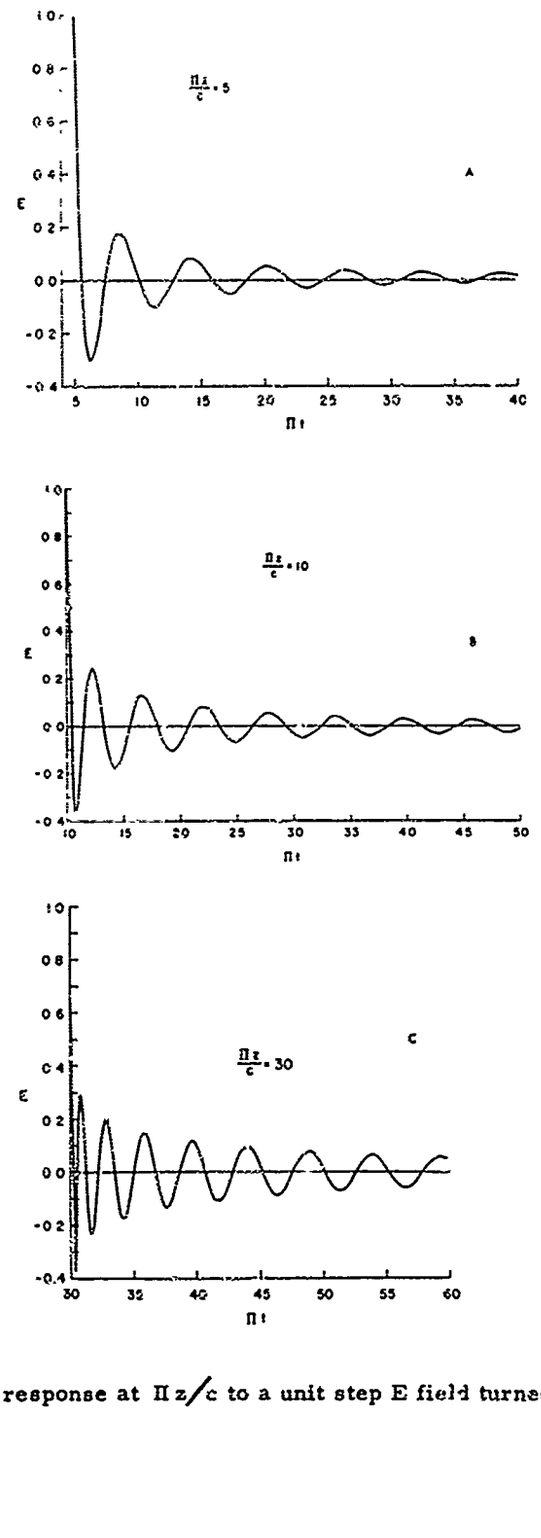

Fig. 2 Time response at $\Pi z/c$ to a unit step E field turned on at $z = 0$.

The results of numerical integration of (16) are shown in Figure 3. Note that the instantaneous frequency of the first cycle is higher for larger values of Π/ω_o and $\omega_o z/c$. Also note that the envelope of the oscillations builds up more slowly as the plasma frequency Π approaches the carrier frequency ω_o. Finally, we see that the peaks of oscillations do not increase monotonically toward unity but rather oscillate about the value one.

For the overdense case, $P > 1$, the waves are evanescent in the steady state with an amplitude given by $e^{-\eta\sqrt{P^2 - 1}}$. A value of $\eta = 2\pi$ corresponds to a propagation distance equal to one free-space wavelength. The response at $\eta = 1$ is shown in Figure 4 where the steady state values of the evanescent waves are reached after only a couple of cycles. On the other hand, the response at $\eta = 5$, which is plotted in Figure 5, shows that the amplitude of the oscillations is still much larger than the steady state value even after many cycles. Of course the steady state amplitude of the evanescent waves decreases drastically as η increases. Note that the instantaneous frequency of the last cycle shown in Figure 5b is still about twice the carrier frequency.

In order to investigate the effects of a finite rise-time on the dispersion of a carrier pulse, let

$$\mathcal{E}(t, 0) = \mathrm{Im}\left[\left(1 - e^{-a\omega_o t}\right)e^{i\omega_o t}\right] U(t) \quad , \tag{18}$$

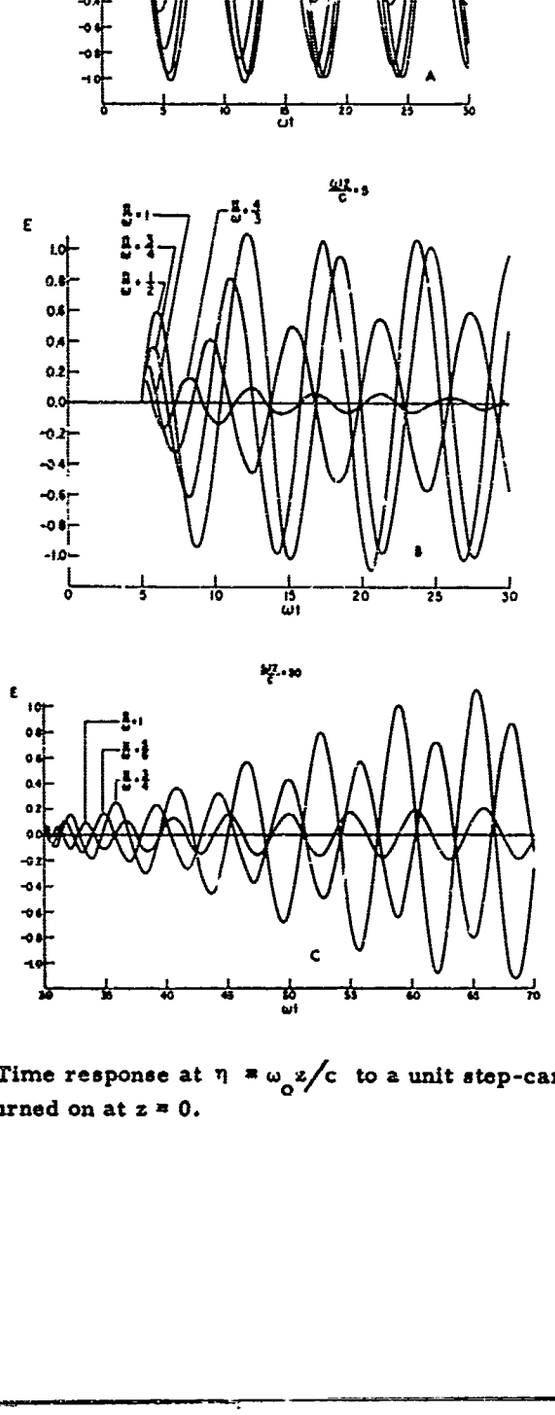

Fig. 3 Time response at $\eta = \omega_o z/c$ to a unit step-carrier sine wave turned on at $z = 0$.

If we substitute (18) into (14) and use (17) we obtain

$$\mathcal{E}(\tau, \eta) = \mathrm{Im}\left[e^{i(\tau - \eta)} - e^{-(\alpha - i)(\tau - \eta)} - P\eta e^{i\tau} \int_{\eta}^{\tau} \frac{e^{-iu} J_1(P\sqrt{u^2 - \eta^2})}{\sqrt{u^2 - \eta^2}} du \right. \qquad (19)$$

$$\left. + P\eta e^{-(\alpha - i)\tau} \int_{\eta}^{\tau} \frac{e^{(\alpha - i)u} J_1(P\sqrt{u^2 - \eta^2})}{\sqrt{u^2 - \eta^2}} du \right] U(\tau - \eta) \, .$$

The results of numerical integration of (19) are shown in Figure 6 where the envelopes of the oscillations are plotted for different values of α.

APPROXIMATE SOLUTIONS FOR LONG DISPERSION LENGTHS

For very long dispersion lengths (i. e., large values of η) the numerical integration method described in the previous section loses its usefulness. This is due to the fact that under these conditions it is necessary to take the difference of two very large numbers in order to obtain a small number leading to possibly large errors. However, it is just in this region of very large η that approximate solutions to the transient propagation problem work very well. We shall consider approximate solutions of the integral in (8) for the propagation of a unit step-carrier sine wave.

The arrival of the signal wavefront at the time $t = z/c$ $(\tau = \eta)$ has been analyzed by Sommerfeld.[14, 15] If the integrand in (8) is expanded for high frequencies, then one finds that under the condition

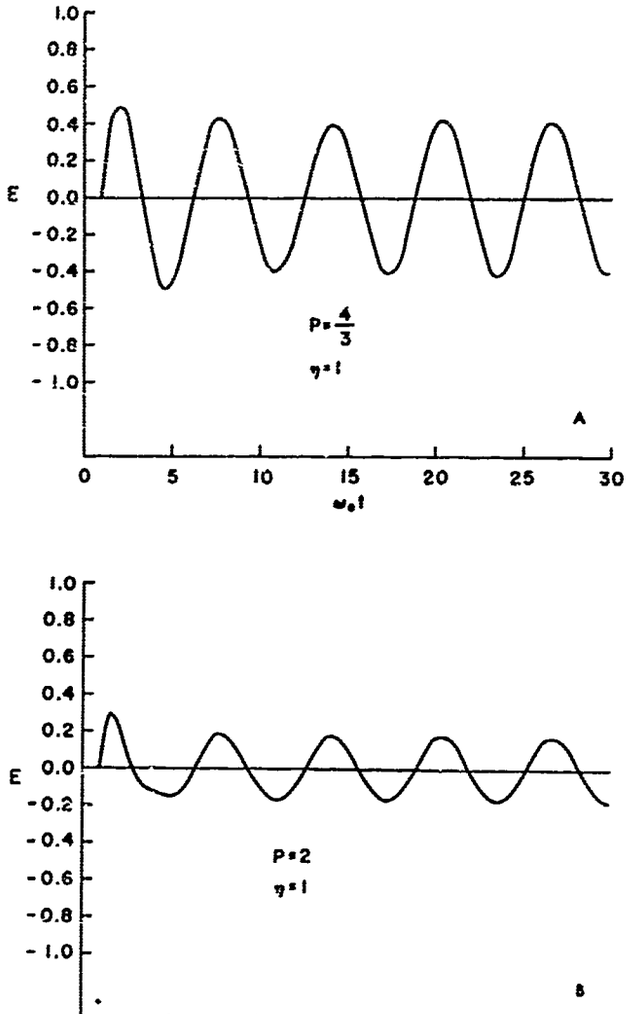

Fig. 4 Propagation of a step-carrier sine wave in an overdense plasma. $\eta = 1$.

$$\tau - \eta << \frac{P^2 \eta}{2} \ , \tag{20}$$

the solution to (8) may be written in the form[10, 15]

$$\mathcal{E}(\tau, \eta) = \frac{1}{P^2 \eta} \sqrt{u} \ J_1\left(\sqrt{u}\right) U(u) \tag{21}$$

where

$$u = 2P^2 \eta(\tau - \eta) \ . \tag{22}$$

This solution is plotted in Figure 7. Note from the condition (20) that this solution is valid for times immediately following the arrival of the wavefront.

After this initial time period it is possible to use the saddlepoint method of integration[15, 16] to evaluate the integral in (8). This method is based on the fact that if the contour of integration can be deformed through the saddlepoints along the lines of steepest descent, then the major contribution to the integral will result from integrating in the vicinity of the saddlepoints. If the second derivative with respect to s of the exponent in (8) is sufficiently large then the saddlepoint solution will be a good approximation to the actual solution.

In the integral in (8) the location of the saddlepoints, found by equating to zero the first derivative with respect to s of the exponent, are

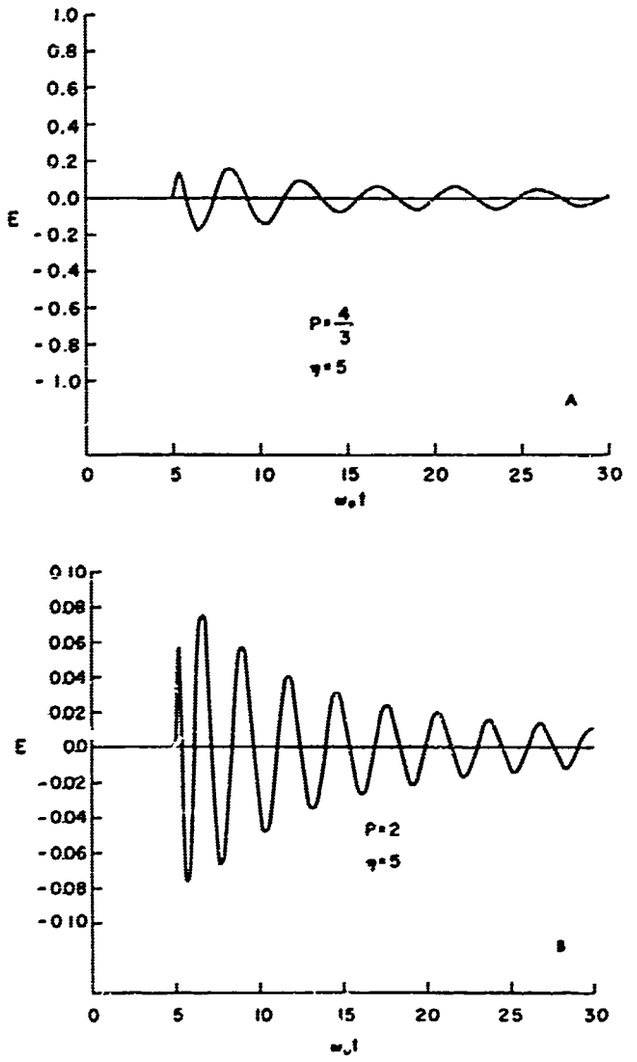

Fig. 5 Propagation of a step-carrier sine wave in an overdense plasma. $\eta = 5$.

given by

$$s_s = \pm \frac{i\Pi}{\sqrt{1 - \left(\frac{z}{ct}\right)^2}} \quad . \tag{23}$$

As time increases after the arrival of the wavefront the two saddlepoints move in from $\pm\infty$ along the imaginary axis approaching $\pm i\Pi$ for long times. These saddlepoints and the paths of steepest descent through them are shown in Figure 8.

The time interval from just after $t = z/c$, until the saddlepoints approach the vicinity of the poles, is called the precursor region. In this region the saddlepoint solution is given by[10]

$$\mathcal{E}(\tau, \eta) = |\mathcal{E}| \cos\left(P\sqrt{\tau^2 - \eta^2} + \pi/4\right) \tag{24}$$

where

$$|\mathcal{E}| = M \left| \frac{\sqrt{w}}{w^2 - 1} \right| \tag{25}$$

and

$$M = \frac{\sqrt{2/\pi}}{P\eta^{1/2}(1 - P^2)^{1/4}}$$

$$w^2 = \frac{(\tau^2 - \eta^2)(1 - P^2)}{\eta^2 P^2} \quad . \tag{26}$$

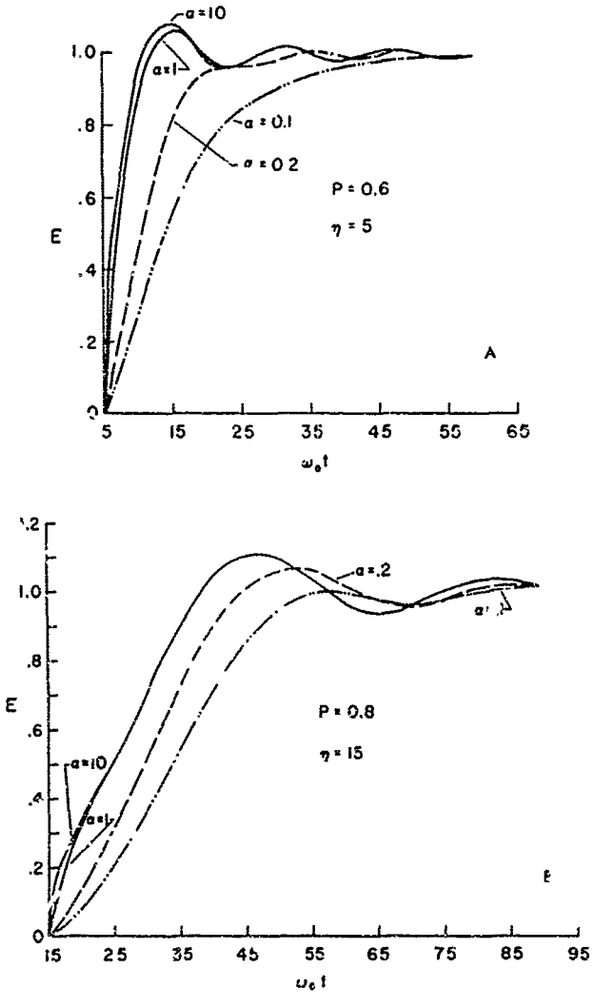

Fig. 6 Oscillation envelopes for various finite rise-times of a turn-on sine wave.

A universal curve representing the envelope of the precursor is plotted from (25) in Figure 9. Note that the amplitude of the precursor increases with increasing τ for $w < 1$ and decreases for increasing τ for $w > 1$. The amplitude becomes infinite at $w = 1$, which occurs when $\tau = \eta \sqrt{1 - P^2}$ and corresponds to a time of arrival at the group velocity (i. e., $t_g = z/v_g$). By setting $s_s = i\omega_o$ in (23) we see that this also corresponds to the time at which the saddlepoint crosses the pole. The standard saddlepoint solution given by (24) breaks down in this region.

This time interval during which the saddlepoint crosses a pole includes the arrival of the main signal at the group velocity. An approximate solution which is valid in this time interval for large η may be obtained by expanding the integrand in (8) about the pole at $s = \pm i\omega_o$. The corresponding solution is given by [10, 16]

$$\xi(\tau, \eta) = A \sin\left(\tau - \eta \sqrt{1 - P^2} + \theta_o\right) \tag{27}$$

where

$$A = \frac{1}{\sqrt{2}} \sqrt{\left[\frac{1}{2} + C(v)\right]^2 + \left[\frac{1}{2} + S(v)\right]^2} \tag{28}$$

$$v = \sqrt{\frac{2}{\pi}} \frac{(1 - P^2)^{3/4}}{\sqrt{2\eta P^2}} \left[\tau - \frac{\eta}{\sqrt{1 - P^2}}\right] \tag{29}$$

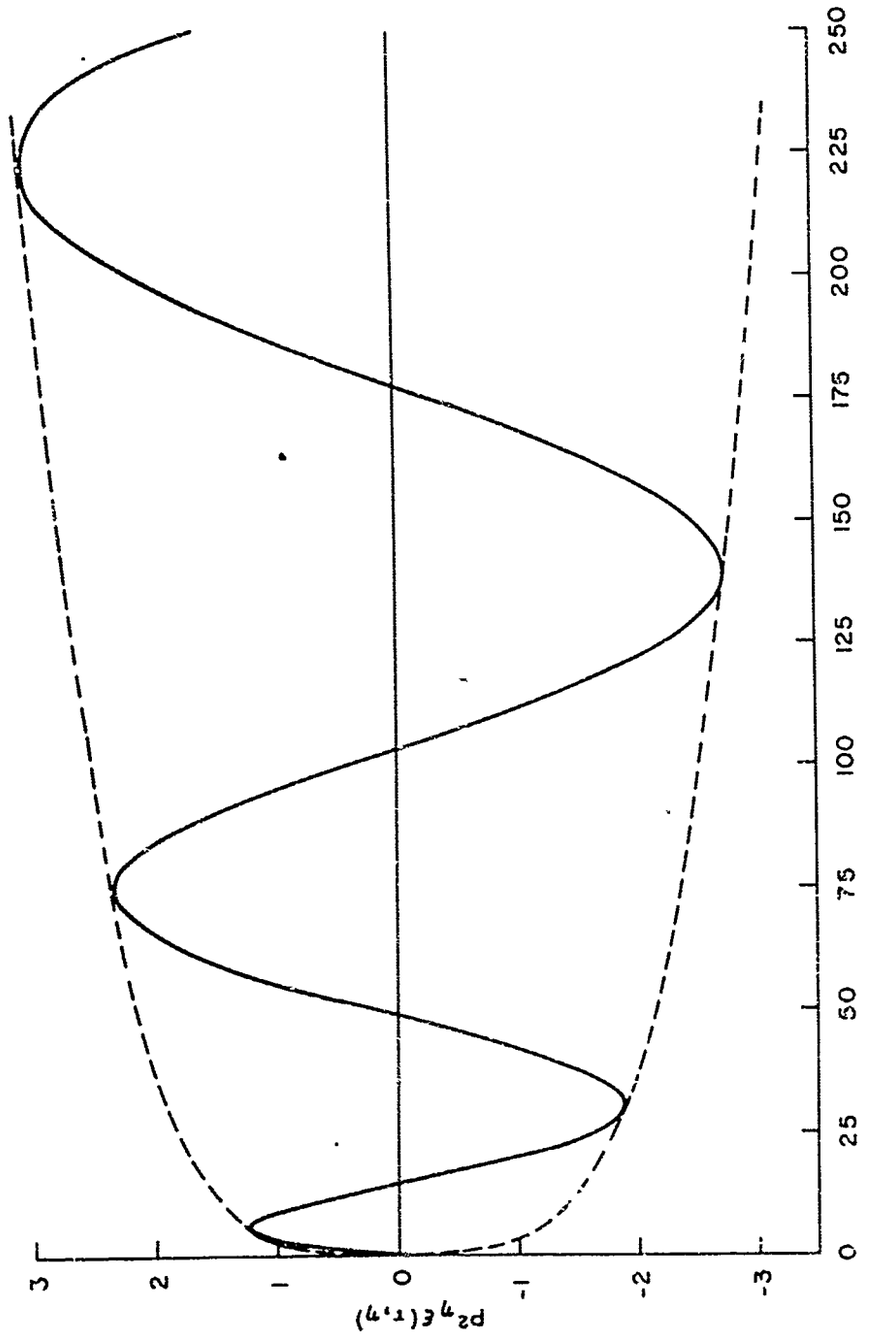

Fig. 7 Universal Sommerfeld solution for the arrival of the signal wavefront. $u = 2P^2\eta(\tau - \eta)$

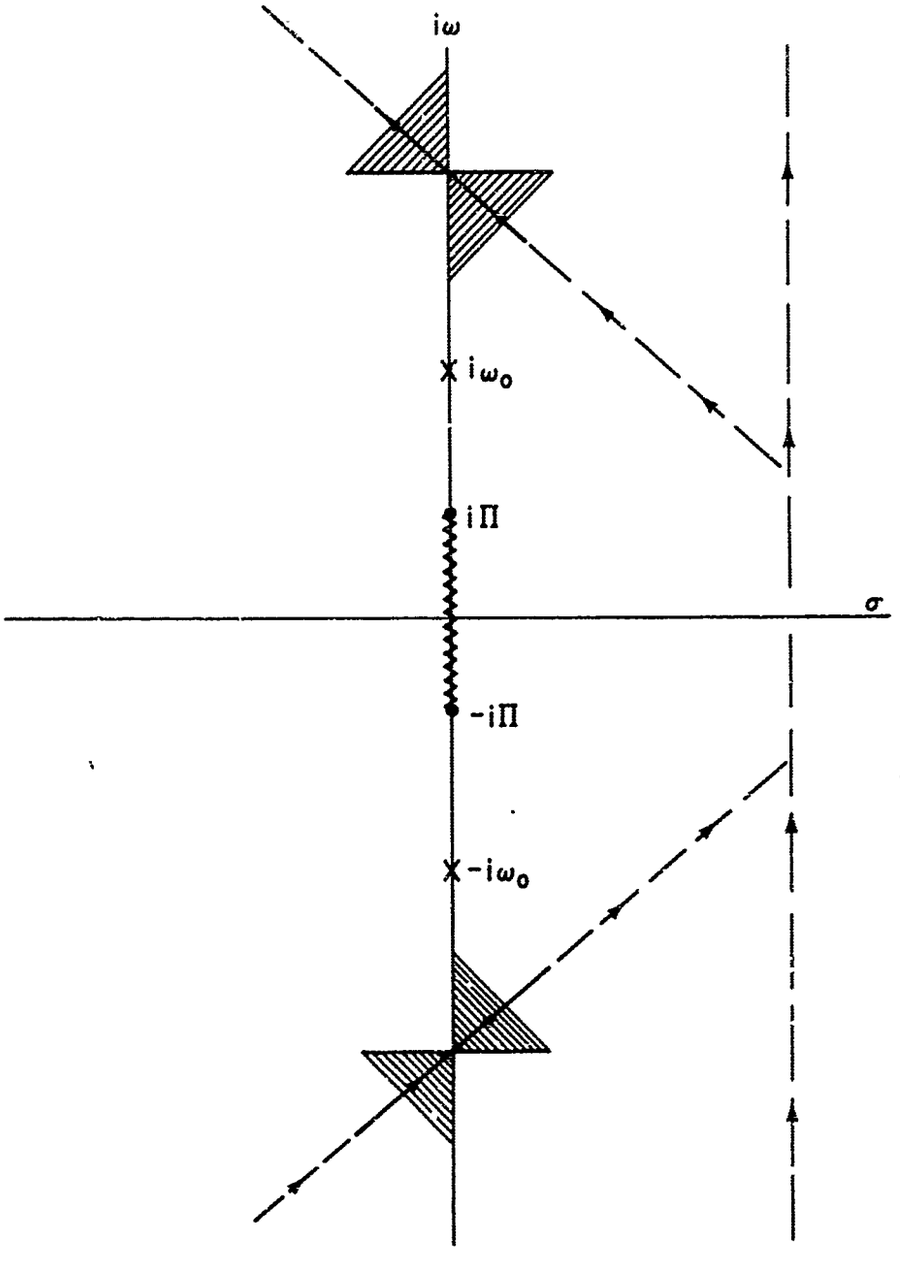

Fig. 8 Location of the saddlepoints and the paths of steepest descent. Saddlepoints move in from $\pm i\omega$ and approach $\pm i\Pi$ for long times.

$$\theta_o = \tan^{-1}\left(\frac{C(v) - S(v)}{1 + C(v) + S(v)}\right)$$

and

$$C(v) = \int_0^v \cos\left(\frac{\pi}{2} x^2\right) dx$$

$$S(v) = \int_0^v \sin\left(\frac{\pi}{2} x^2\right) dx$$

are the Fresnel cosine and sine integrals respectively.

The amplitude function A given by (28) is plotted as a function of v in Figure 10 and will be referred to as a master Fresnel envelope. The time history of the envelope (as a function of τ) for a particular value of P and η is determined by using (29) which acts like a "stretching factor" and simply changes the abscissa scale in Figure 10. Note carefully that the master Fresnel envelope has a value of 0.5 at $v = 0$, which corresponds to $\tau = \eta\sqrt{1 - P^2}$ and is the time of arrival at the group velocity $\tau_g = z/v_g$.

In order to determine the time scale at which the ringing of the master Fresnel envelope occurs we note that on the v scale the ringing occurs for changes of v of the order $\Delta v \sim 1$. Thus from (29) we see that the ringing will occur on a time scale $\Delta t \sim 1/a\omega_o$, where

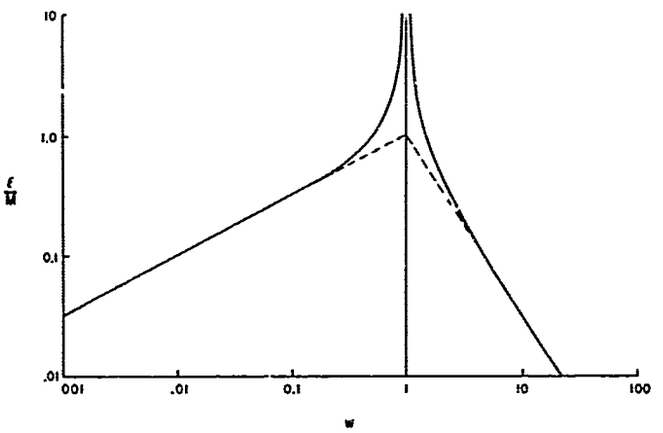

Fig. 9 Amplitude of the precursor solution.

$$w = \left[(\tau^2 - \eta^2)(1 - P^2) / \eta^2 P^2 \right]^{1/2}$$

$$M = \sqrt{\frac{2}{\pi}} \Big/ P \eta^{1/2} (1 - P^2)^{1/4}$$

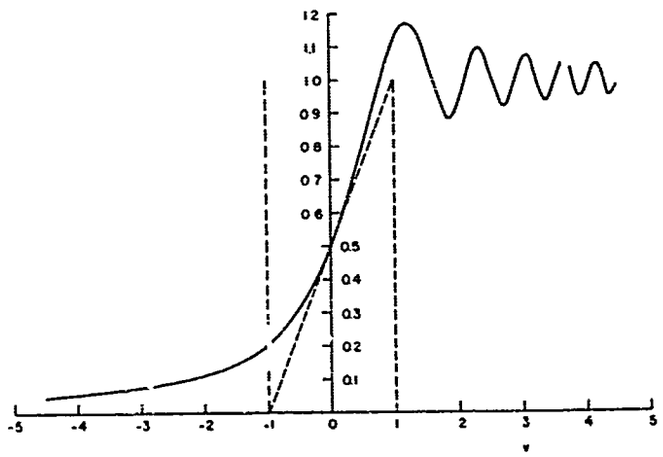

Fig. 10 Master Fresnel envelope describing the arrival of the main signal.

$$v = \sqrt{\frac{2}{\pi}} \; \frac{(1 - P^2)^{3/4}}{\sqrt{2\eta P^2}} \left[\tau - \frac{\eta}{\sqrt{1 - P^2}} \right]$$

$$a = \sqrt{\frac{2}{\pi}} \frac{(1 - P^2)^{3/4}}{\sqrt{2\eta P^2}} \quad .$$

The solution (27) is based on an expansion of the exponent in (8) in a Taylor series about $s = \pm i\omega_o$. Only the first three terms in this expansion are kept and this is justified as long as

$$\eta\left[\sqrt{1 - P^2} \cdot (1 - P^2)\right] >> 1 \quad , \tag{30}$$

This condition is based on the requirement that a large number of cycles occur between the arrival of the wavefront at $t_f = z/c$ and the time of arrival at the group velocity $t_g = z/v_g$. We note from (30) that for times greater than t_g the solution (27) will be a good approximation for very large values of η, depending on the value of P. For values of P greater than .866 the coefficient of η in (30) decreases from .25 toward zero as P approaches unity. The condition (30) therefore becomes more and more difficult to satisfy. This is due in part to the fact that the pole comes very close to the branch point and the expansion fails in this region. This problem can be partially overcome by a suitable conformal transformation[9, 10] which will improve the range of validity of the solution for values of P very close to one (P > .99).

The results of this section are summarized in Figure 11 where the total envelope response to a unit step-carrier sine wave input is plotted for

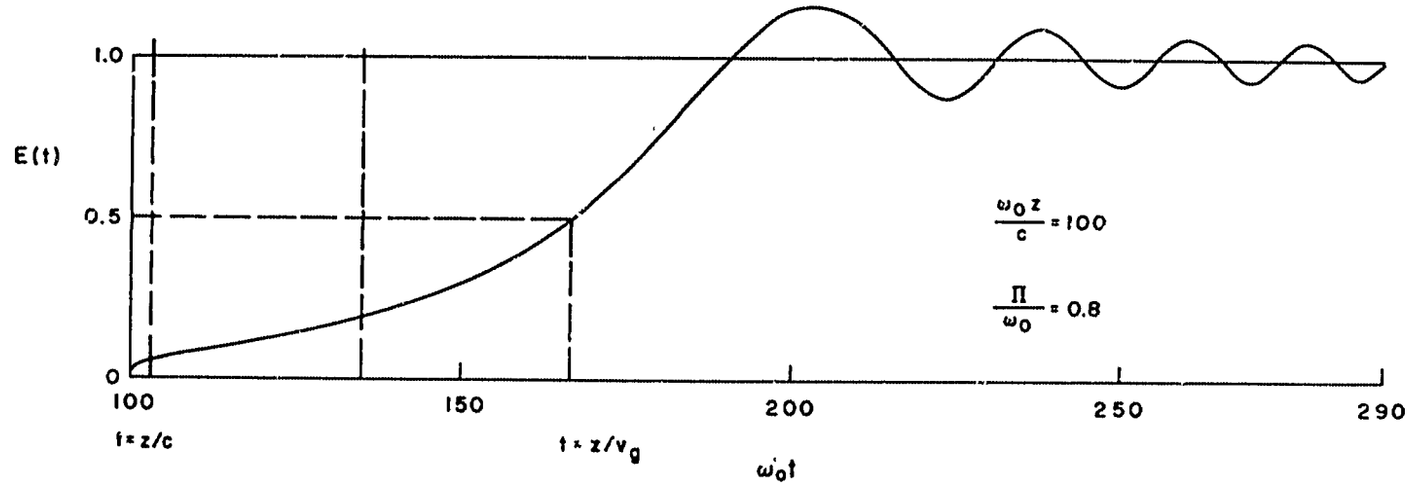

Fig. 11 Total envelope response at $\omega_o z/c = 100$ to a step carrier sinc wave turned on at $z = 0$.

the particular case of P = 0.8 and $\eta = 100$. This total solution is made up of three separate parts. The first is the Sommerfeld solution for the arrival of the signal wavefront. This is then joined to the precursor region which is evaluated by the standard saddlepoint method. As the saddlepoint approaches the pole in the complex s-plane this solution is then joined to the master Fresnel envelope solution. This total solution then approaches the steady state value of 1 for large times.

COLLISIONAL DAMPING OF TRANSIENT SIGNALS IN PLASMAS

In order to determine the effect of collisions on the envelope response found in the previous section, we consider the integral in (7). For this case the trajectories of the saddlepoints move off of the imaginary axis in the complex s-plane. The arrival of the main signal occurs when the saddlepoint moves into the vicinity of the pole. Since we are interested primarily in this part of the solution, we shall consider a modification of the pole expansion of the previous section.

If a step-carrier sine wave of unit amplitude is turned on at t = 0 then the solution given by (7) may be written

$$\mathcal{E}(t, z) = -\mathrm{Im}\left[\frac{1}{2\pi i}\int_{\gamma_s} \frac{1}{s + i\omega_o}\, e^{W(s,\, t)}\, ds\right] \tag{31}$$

where

$$W(s, t) = st - \frac{z}{c}\sqrt{s^2 + \frac{s\Pi^2}{s + \nu}} \tag{32}$$

An approximate solution of (31) may be obtained for the main signal build-up by expanding $W(s, t)$ in a Taylor series about ω_o. The solution may be written in the form[16]

$$\mathcal{E}(t, z) = - \mathrm{Im} \left\{ e^{W(i\omega_o)} \frac{1}{2} \left[1 + \mathrm{erf}\ \Theta(-i\omega_o) \right] \right\} \tag{33}$$

where

$$\Theta(i\omega_o) = \frac{W'(-i\omega_o)}{\sqrt{2W''(i\omega_o)}} = re^{-i\phi} \tag{34}$$

and where ϕ may be shown to be a positive angle between 0 and $\pi/4$.

The envelope of (33) is given by

$$|\mathcal{E}(t, z)| = \left| e^{W(i\omega_o)} \right| \left| \frac{1}{2} \left[1 + \mathrm{erf}\ \Theta(-i\omega_o) \right] \right| .$$

The exponential function, $e^{W(-i\omega_o)}$, is just the attenuation which a steady state wave of frequency ω_o suffers due to collisions. The remaining factor can be written as

$$B(r, \theta) = \frac{1}{2} \left| \left[1 + \mathrm{erf}\ \Theta(-i\omega_o) \right] \right| \tag{35}$$

$$= \frac{1}{2} \sqrt{\left[1 + \frac{2}{\sqrt{\pi}} v(r,\theta) \right]^2 + \left[\frac{2}{\sqrt{\pi}} u(r,\theta) \right]^2}$$

where $\theta = \pi/2 - \phi$ and we have used the relations

$$\operatorname{erf} \theta = -\frac{2i}{\sqrt{\pi}} F(z)$$

where $z = i\theta = re^{i\theta}$ and

$$F(z) = \int_0^z e^{x^2} dx \tag{36}$$

$$= u(r, \theta) + iv(r, \theta) \quad .$$

The function $F(z)$ given by (36) is tabulated for complex arguments.[17]

The behavior of the function $E(r, \theta)$ given by (35) is shown in Figure 12. The trajectory (r, θ) as a function of time depends on the collision frequency ν. When $\nu = 0$, $\theta = 45^\circ$ and the envelope solution is that given by (28) with r equal to the argument (29). If $\nu \neq 0$, the angle θ is not constant as time increases, but rather decreases from 90° approaching some angle between 45° and 90° asymptotically for large times.

It is therefore seen that the effect of collisions is two-fold. First, the entire envelope is attenuated an amount equal to the attenuation of a cw wave with an angular frequency ω_o. Second, the "ringing" of the envelope is inhibited and quickly damps out.

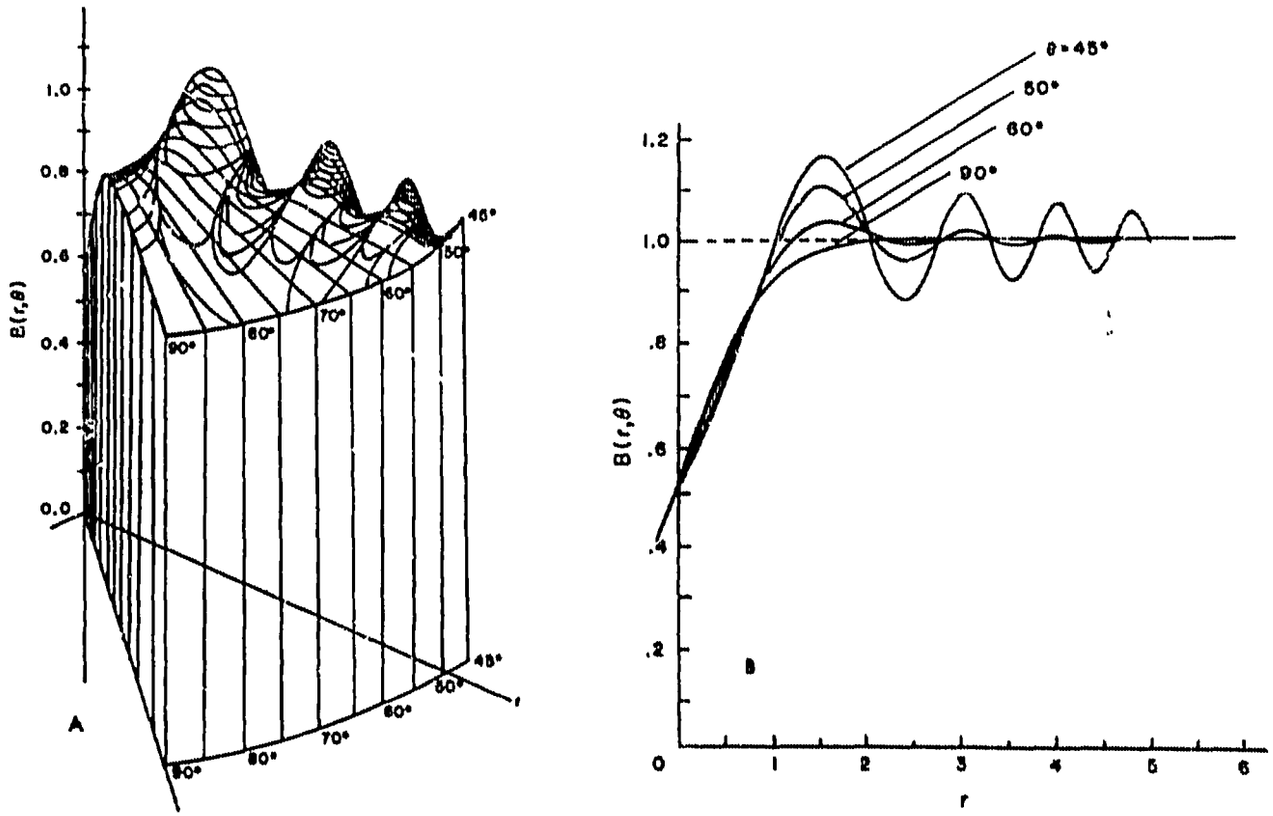

Fig. 12 The function B(r, θ).

REFLECTIONS FROM A PLASMA-VACUUM INTERFACE

An electromagnetic signal which is reflected from or transmitted through a plasma-vacuum interface will be dispersed as a result of the discontinuity in the medium at the interface. Let a lossless, isotropic plasma occupy the half-space $z > 0$, and free-space occupy the half-space $z < 0$. A wave incident on the boundary from the free space side will give rise to a reflected wave in free space and a transmitted wave in the plasma. Applying the boundary conditions by equating the tangential components of the electric and magnetic fields on either side of the boundary, one can readily obtain the complex reflection coefficient

$$R = \frac{s - \sqrt{s^2 + \Pi^2}}{s + \sqrt{s^2 + \Pi^2}} \quad . \tag{37}$$

If the incident wave is a step-carrier sine wave, then the reflected signal at the boundary is given by

$$\mathcal{E}_R(t) = \frac{1}{2\pi i}\int_{\gamma_s}\left(\frac{s - \sqrt{s^2 + \Pi^2}}{s + \sqrt{s^2 + \Pi^2}}\right)\frac{\omega_o e^{st}}{s^2 + \omega_o^2}\,ds \quad . \tag{38}$$

Using the convolution theorem together with the expressions from tables[13]

$$\mathcal{L}^{-1}\left[\frac{s - \sqrt{s^2 + \Pi^2}}{s + \sqrt{s^2 + \Pi^2}}\right] = \mathcal{L}^{-1}\left[\frac{-\Pi^2}{\left(s + \sqrt{s^2 + \Pi^2}\right)^2}\right]$$

$$= -\frac{2J_2(\Pi t)}{t}$$

we obtain

$$\mathcal{E}_R(t) = -2\mathrm{Im}\int_0^t e^{i\omega_0(t-t')}\ \frac{J_2(\Pi t')}{t'}\ dt' \qquad (39)$$

Equation (39) has been evaluated numerically and the results are shown in Figure 13. Reflection from a perfect conductor is indicated by the dashed curve in Figure 13a. The major feature of these curves is the apparent shift or "delay" of the initial cycle of the response which increases as the plasma frequency decreases. This "delay time" has been discussed by Chen[18] and Knop[19, 20], who find it to be related to the time $t_D = 2/\Pi$.

In order to obtain a physical meaning for this time delay t_D, let us write the reflection coefficient R given by (37) in the form

$$\frac{s - \sqrt{s^2 + \Pi^2}}{s + \sqrt{s^2 + \Pi^2}} = \exp\left[\ln\left(s - \sqrt{s^2 + \Pi^2}\right) - \ln\left(s + \sqrt{s^2 + \Pi^2}\right)\right]. \qquad (40)$$

If (40) is substituted into (38), then the saddlepoints of the resulting exponential function are given by

$$s_s = \pm\sqrt{\frac{4}{t^2} - \Pi^2} \qquad (41)$$

Thus at $t = 0$ the saddlepoints are at $\pm\infty$ on the real axis. As time increases they move inward along the real axis. At $t = 2/\Pi$ they merge at the origin to

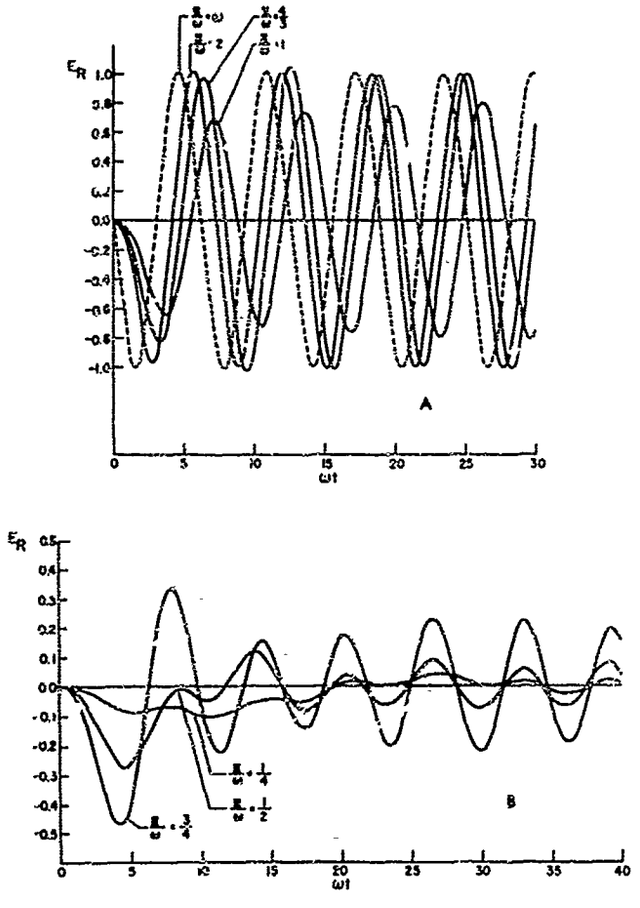

Fig. 17 Reflected signal at the free-space side of a plasma-vacuum boundary.

form a third order saddlepoint. For $t > 2/\Omega$ they move along the imaginary axis and approach the points $\pm i\Omega$ for large times. For times $t < 2/\Omega$ the saddlepoints are located on the real axis and the solution is nonoscillatory in nature, increasing monotonically in the negative direction. The oscillatory nature of the solution occurs for $t > 2/\Omega$. At $t = 2/\Omega$ a transition occurs between these two types of solutions. The saddlepoints moving in along the real axis, therefore, represent the "delay" which occurs before the oscillatory nature of the solution can begin. Unfortunately, the saddlepoint solutions are not good approximations for this problem since the "heights" of the saddlepoints are not sufficient for the integral to be evaluated except in the neighborhood of the saddlepoints. However, the motion of the saddlepoints lends insight into the nature of the "delay time" as described above.

CONCLUDING REMARKS

Two types of transient solutions occur depending upon the distance the wave travels through the plasma. For short dispersion lengths (less than a few free space wavelengths), exact solutions must be used. This usually means some type of numerical integration procedure is required. For long dispersion lengths (a very large number of free space wavelengths), approximate solutions may be used with good accuracy. The wavefront of the signal arrives with the velocity of light c. The signal then builds up slowly in the precursor region until the main signal arrives with the group

velocity. As the propagation distance in the plasma increases, the precursor region becomes longer and the amplitude of the signal in this region becomes smaller.

The nature of the dispersed signal can be divided into two categories. First the envelope of the signal becomes distorted, oscillating about the steady state value. Second, the carrier frequency becomes phase modulated. Where the saddlepoint method of integration can be used, the "instantaneous frequency" of the dispersed signal is equal to the frequency corresponding to the location of the saddlepoint in the s-plane at that instant of time. Whereas the envelope of the distorted signal is a critical function of the envelope of the input signal, the phase modulation characteristic of the dispersed signal is primarily a function only of the nature of the dispersive plasma medium.

REFERENCES

1. H. J. Schmitt, Dispersion of Pulsed Electromagnetic Waves in a Plasma, IEEE Trans. on Microwave Theory and Techniques, Vol. MTT-13, 472, (July 1965).
2. G. I. Cohn, Electromagnetic Transients in Waveguides, Proc. Natl. Electronics Conf. Vol. 8, 284, (1952).
3. R. Elliott, Pulse Waveform Degradation due to Dispersion in Waveguide, IRE Trans. on MTT, Vol. MTT-5, 254 (Oct 1957).
4. M. P. Forrer, Analysis of Millimicrosecond RF Pulse Transmission, Proc. IRE, 46, 1830 (Nov 1958).
5. C. M. Knop and G. I. Cohn, Comments on Pulse Waveform Degradation due to Dispersion in Waveguide, IEE Trans. on MTT, Vol. MTT-11, p. 587 (1963).
6. C. M. Knop, Pulsed Electromagnetic Wave Propagation in Dispersive Media, IEE Trans. on AP Vol. AP-12, No. 4 (July 1964).
7. A. Rubinowicz, Propagation of a Cut-off Train of De Broglie Waves, Acta Physica Polonica, Vol. X, 79, (1950).
8. R. Gajewski, On Transients in Waveguides, Bull. de L'Academie Polonaise Des Sciences, Vol 3, 29 (1955).
9. M. Cerrillo, Transient Phenomena in Waveguides, TR No. 33, Research Laboratory of Electronics, MIT (Jan. 8, 1948).

10. R. E. Haskell and C. T. Case, Transient Signal Propagation in Lossless, Isotropic Plasmas, AFCRL Tech Rept., to be published.

11. E. N. Dekanosidze, Tables of Lommel's Functions of Two Variables, Pergamon Press, New York (1960).

12. C. T. Case, On Transient Wave Propagation in a Plasma, Proc. IEEE (Corr.) 53, 730 (July 1965).

13. Erdelyi, Magnus, Oberhettinger, and Tricomi, Tables of Integral Transforms, Vol. 1, McGraw-Hill Book Co., Inc., New York, 1954.

14. A. Sommerfeld, Ann. Physik, 44, 177-202 (1914).

15. L. Brillouin, Wave Propagation and Group Velocity, Academic Press, New York and London (1960).

16. M. V. Cerrillo, An Elementary Introduction to the Theory of the Saddle-point Method of Integration, Research Laboratory of Electronics, MIT, TR-55:2a, (May 3, 1950).

17. K. A. Karpov, Tables of the Functions $F(z) = \int_0^z e^{x^2} dx$ in the Complex Domain, The Macmillan Co., New York, 1964.

18. S. N. C. Chen, The Transient Phenomenon in an Isotropic Plasma without Collision Loss, Proc. IEEE (Corr.) 51, 1045 (Jul. 1963).

19. C. M. Knop, Comments on the Transient Phenomenon in an Isotropic Plasma without Collision Loss, Proc. IEEE (Corr.) 52, 99, Jan. 1964.

20. C. M. Knop, Further Comments on the Transient Phenomena in an Isotropic Plasma without Collision Loss, Proc. IEEE (Corr.) 53, 751, (July 1965).

Unclassified
Security Classification

DOCUMENT CONTROL DATA - R&D

(Security classification of title, body of abstract and indexing annotation must be entered when the overall report is classified)

1. ORIGINATING ACTIVITY *(Corporate author)* Hq AFCRL, OAR (CRD) United States Air Force Bedford, Massachusetts 01730	2a. REPORT SECURITY CLASSIFICATION Unclassified 2b. GROUP -

3. REPORT TITLE Proceedings of the Third Symposium on the Plasma Sheath-Plasma Electromagnetics of Hypersonic Flight: Volume I. Radiation Characteristics of Plasma-Covered Antennas

4. DESCRIPTIVE NOTES *(Type of report and inclusive dates)*
Proceedings of Symposium

5. AUTHOR(S) *(Last name, first name, initial)*
Rotman, W., Moore, H., Papa, R., Lennon, J.

6. REPORT DATE May 1967	7a. TOTAL NO. OF PAGES 237	7b. NO. OF REFS 46
8a. CONTRACT OR GRANT NO. b. PROJECT AND TASK NO. 4642, all tasks c. DOD ELEMENT 62405394 d. DOD SUBELEMENT 681000	9a. ORIGINATOR'S REPORT NUMBER(S) AFCRL-67-0280 (Volume I) Special Reports No. 64 (I) 9b. OTHER REPORT NO(S) *(Any other numbers that may be assigned this report)* AFCRL-67-0280 (Volume I)	

10. [redacted]

11. SUPPLEMENTARY NOTES -	12. SPONSORING MILITARY ACTIVITY Hq AFCRL, OAR (CRD) United States Air Force Bedford, Massachusetts

13. ABSTRACT

This volume is a collection of the unclassified papers presented at the Third Symposium on the Plasma Sheath-Plasma Electromagnetics of Hypersonic Flight. This symposium consisted of the review of progress in reentry communication studies during the three year period since the prior meeting. The program of this symposium on plasma electromagnetics of hypersonic flight involves a wide range of scientific disciplines, including electromagnetics, aerodynamics, aerothermochemistry, plasma dynamics, electronics, and high-temperature phenomena. The papers were selected to explore as many of these facets of research, including the results of laboratory, flight, and system tests, as time permitted.

DD FORM 1 JAN 64 1473

Unclassified
Security Classification

Unclassified
Security Classification

14. KEY WORDS	LINK A		LINK B		LINK C	
	ROLE	WT	ROLE	WT	ROLE	WT
Plasma Electromagnetics Hypersonic-Flight Reentry Communications						

INSTRUCTIONS

1. ORIGINATING ACTIVITY: Enter the name and address of the contractor, subcontractor, grantee, Department of Defense activity or other organization *(corporate author)* issuing the report.

2a. REPORT SECURITY CLASSIFICATION: Enter the overall security classification of the report. Indicate whether "Restricted Data" is included. Marking is to be in accordance with appropriate security regulations.

2b. GROUP: Automatic downgrading is specified in DoD Directive 5200.10 and Armed Forces Industrial Manual. Enter the group number. Also, when applicable, show that optional markings have been used for Group 3 and Group 4 as authorized.

3. REPORT TITLE: Enter the complete report title in all capital letters. Titles in all cases should be unclassified. If a meaningful title cannot be selected without classification, show title classification in all capitals in parenthesis immediately following the title.

4. DESCRIPTIVE NOTES: If appropriate, enter the type of report, e.g., interim, progress, summary, annual, or final. Give the inclusive dates when a specific reporting period is covered.

5. AUTHOR(S): Enter the name(s) of author(s) as shown on or in the report. Enter last name, first name, middle initial. If military, show rank and branch of service. The name of the principal author is an absolute minimum requirement.

6. REPORT DATE: Enter the date of the report as day, month, year, or month, year. If more than one date appears on the report, use date of publication.

7a. TOTAL NUMBER OF PAGES: The total page count should follow normal pagination procedures, i.e., enter the number of pages containing information.

7b. NUMBER OF REFERENCES: Enter the total number of references cited in the report.

8a. CONTRACT OR GRANT NUMBER: If appropriate, enter the applicable number of the contract or grant under which the report was written.

8b, 8c, & 8d. PROJECT NUMBER: Enter the appropriate military department identification, such as project number, subproject number, system numbers, task number, etc.

9a. ORIGINATOR'S REPORT NUMBER(S): Enter the official report number by which the document will be identified and controlled by the originating activity. This number must be unique to this report.

9b. OTHER REPORT NUMBER(S): If the report has been assigned any other report numbers *(either by the originator or by the sponsor)*, also enter this number(s).

10. AVAILABILITY/LIMITATION NOTICES: Enter any limitations on further dissemination of the report, other than those imposed by security classification, using standard statements such as:

(1) "Qualified requesters may obtain copies of this report from DDC."

(2) "Foreign announcement and dissemination of this report by DDC is not authorized."

(3) "U. S. Government agencies may obtain copies of this report directly from DDC. Other qualified DDC users shall request through

_____."

(4) "U. S. military agencies may obtain copies of this report directly from DDC. Other qualified users shall request through

_____."

(5) "All distribution of this report is controlled. Qualified DDC users shall request through

_____."

If the report has been furnished to the Office of Technical Services, Department of Commerce, for sale to the public, indicate this fact and enter the price, if known.

11. SUPPLEMENTARY NOTES: Use for additional explanatory notes.

12. SPONSORING MILITARY ACTIVITY: Enter the name of the departmental project office or laboratory sponsoring *(paying for)* the research and development. Include address.

13. ABSTRACT: Enter an abstract giving a brief and factual summary of the document indicative of the report, even though it may also appear elsewhere in the body of the technical report. If additional space is required, a continuation sheet shall be attached.

It is highly desirable that the abstract of classified reports be unclassified. Each paragraph of the abstract shall end with an indication of the military security classification of the information in the paragraph, represented as *(TS), (S), (C), or (U).*

There is no limitation on the length of the abstract. However, the suggested length is from 150 to 225 words.

14. KEY WORDS: Key words are technically meaningful terms or short phrases that characterize a report and may be used as index entries for cataloging the report. Key words must be selected so that no security classification is required. Identifiers, such as equipment model designation, trade name, military project code name, geographic location, may be used as key words but will be followed by an indication of technical context. The assignment of links, rules, and weights is optional.

Unclassified
Security Classification